

**Combining Holographic Patterning and Block Copolymer Self-Assembly  
to Fabricate Hierarchical Volume Gratings**

A Dissertation

Submitted to the Faculty

of

Drexel University

by

Michael J. Birnkrant

in partial fulfillment of the

requirements for the degree

of

Doctor of Philosophy

September 2009

## Dedication

---

This work is dedicated to my family and friends. I am grateful for your support and optimism. Without you, this dissertation would have many more split infinitives and lost subjects.

## Acknowledgements

---

I am grateful to everyone who I have met while in graduate school; without whom the experience would have been less pleasant. I would like to thank Professor Christopher Li foremost for his time and energy in preparing me for the future. Without his help I would not have learned so much about polymer science and engineering. In addition, I would like to thank Dr. Timothy Bunning for his insightful and thoughtful discussions on my work.

Special thanks are warranted to my faculty committee members: Dr. Fontecchio, Dr. Schauer and Dr. Elabd for their valuable comments, suggestions, ideas and discussion.

I would like to thank Dr. B.S. Hsiao and Dr. Lixia Rong for facilitating the synchrotron X-ray measurements at the NSLS in Brookhaven National Laboratory. I want to also thank Dr. Lalgudi V. Natarajan, Dr. Vincent P. Tondiglia and Dr. Richard L. Sutherland of SAIC as well as Dr. Pamela F. Lloyd of UES, Inc. for providing me with a crash course in HPDLC.

I would like to thank the members of the Soft Matter Group, Dr. Kishore Tenneti, Dr. Lingyu Li, Dr. Bingbing Wang, Steve Kodjie, Bing Li, Matthew Hood, Eric Laird, Rebecca Chen, Russ Marron, and Molly Stewart, for all of their help and time. I believe we had quite a bit of excitement these past few years.

I am grateful to the NSF-IGERT and NSF-GK12 fellowship administered by Dr. Gogotsi and Dr. Fromm as well as the NSF, Sigma Xi and AFOSR for research funding. I especially want to thank Keiko, Holly, Dorilona, Joanne, Amy and Judy for all of their work.

In this last line I can not understate my gratefulness to my wife Lucy for all of her love and support.

## Table of Contents

---

Dedication . . . . .	i
Acknowledgements . . . . .	ii
List of Tables . . . . .	vii
Abstract . . . . .	viii
Chapter 1. Introduction to Hierarchical Structures on the Nanoscale . . . . .	1
Chapter 2. Background on Manufacturing Hierarchical Nanostructures . . . . .	7
2.1 The Key Elements of Hierarchical Structures . . . . .	7
2.2 Nanofabrication Approaches . . . . .	10
2.2.1 Bottom-Up Approaches . . . . .	11
2.2.2 Top-Down Techniques . . . . .	13
2.2.3 Limitations and Opportunities . . . . .	15
2.3 Self-Assembly Approaches to Obtain Hierarchical Structures . . . . .	19
2.4 Top-Down and Bottom-Up Combined Nanoscale Fabrication . . . . .	31
2.4.1 Fabricating Hierarchical Structures by Combining Nanofabrication Techniques . . . . .	33
2.4.1.1 External-In Methods to Forming Hierarchical Structures	37
2.4.1.2 Internal-Out Methods to Fabricating Hierarchical Structures . . . . .	43
2.4.1.3 Parallel Fabrication of Hierarchical Structures . . . . .	47
2.5 Confinement of Self-Assembling Nanostructures . . . . .	48
2.5.1 Structure . . . . .	49
2.5.2 Placement Accuracy and Registration . . . . .	53

2.5.3	Summary of Hierarchical Structures Formed at the Nanoscale	55
2.6	Objectives of this Dissertation . . . . .	56
Chapter 3. Materials and Methods to Fabricating Hierarchical Volume Gratings		58
3.1	An Introduction to Polymer Based Photonic Crystals . . . . .	58
3.1.1	Coherent Light Scattering from Periodic Media . . . . .	58
3.1.2	Dynamic Polymer Photonic Crystals . . . . .	61
3.1.3	Holographic-Lithography as a Method for Patterning Photonic Crystals . . . . .	66
3.1.4	HP of Liquid Crystals and Nanoparticles . . . . .	69
3.1.5	Summary of Polymer Based Photonic Crystals . . . . .	71
3.2	Materials . . . . .	72
3.2.1	Photopolymerizable Monomers and Initiators . . . . .	72
3.2.2	Homopolymers . . . . .	74
3.2.3	Block Copolymers . . . . .	75
3.3	Method for Fabricating Homopolymer and Block Copolymer Volume Gratings . . . . .	76
3.4	Characterization . . . . .	80
3.4.1	Optical Microscopy . . . . .	80
3.4.2	Electron Microscopy . . . . .	81
3.4.3	Transmission Electron Microscopy Sample Preparation . . . . .	82
3.4.4	X-ray Diffraction and Scattering . . . . .	84
3.4.5	UV-Visible Transmission Spectroscopy . . . . .	86
3.4.6	Thermal Analysis . . . . .	87
3.4.7	Infrared Spectroscopy . . . . .	88

Chapter 4. Volume Gratings by Combining Holographic Patterning and Semicrystalline Homopolymers . . . . .	90
4.1 Introduction . . . . .	90
4.2 Experimental . . . . .	90
4.3 The Structure and Morphology of PEG Volume Gratings . . . . .	91
4.4 Thermal Tuning of PEG Volume Gratings . . . . .	99
4.4.1 Crystallization as a Method for Switching Volume Gratings . . . . .	99
4.4.2 Tuning of the Switching Temperature . . . . .	103
4.5 The morphology of PCL and PLLA Volume Gratings . . . . .	107
4.5.1 A Volume Grating Confining a Blend of PCL and PLLA . . . . .	110
4.6 Summary . . . . .	112
Chapter 5. Hierarchical Volume Gratings from Combined Nanoscale Fabrication Techniques . . . . .	115
5.1 Introduction . . . . .	115
5.2 Experimental . . . . .	115
5.3 The Structure of a PEO-b-PCL Volume Grating . . . . .	116
5.4 Summary . . . . .	125
Chapter 6. Thermally Switching Hierarchical Volume Gratings . . . . .	127
6.1 Introduction . . . . .	127
6.2 Materials and Methods . . . . .	127
6.3 Thermal Tuning of a PEO-b-PCL Volume Grating . . . . .	128
6.4 Thermal Tuning and the Morphology of the Volume Grating . . . . .	132
6.4.1 Thermal Tuning of PCL Volume Gratings . . . . .	139
6.5 On the Structure of the Polymer Protrusions Contained within the PEO-b-PCL . . . . .	144
6.6 The Impact of the Polymer Protrusions on the Diffraction Efficiency . . . . .	145

6.7	The Isothermal Crystallization of PEO-b-PCL Volume Gratings . . .	147
6.8	Conclusion . . . . .	151
Chapter 7. Two-dimensional HP of PEG Photonic Crystals . . . . .		154
7.1	Introduction . . . . .	154
7.2	Experimental . . . . .	154
7.3	The Morphology of a Two-Dimensional PEG Volume Grating . . . . .	155
7.4	Summary . . . . .	159
Chapter 8. Conclusion and Outlook . . . . .		160
8.1	Concluding Remarks . . . . .	160
8.2	Suggestions for the Future of Hierarchical Volume Gratings . . . . .	161
Bibliography . . . . .		163
Vita . . . . .		178

---

**List of Tables**

---

2.1	A list of nanoscale fabrication techniques organized into top-down and bottom-up techniques. . . . .	9
3.1	The vectorial description of a monochromatic plane wave propagation and electric field vectors. . . . .	69
3.2	The components of the prepolymer syrup used in the holographic patterning of polymers and BCP. . . . .	74
3.3	The different PEO-b-PCL BCP volume fractions that were used in this work. . . . .	76

## List of Figures

---

1.1	Nanoscale processing techniques grouped into top-down and bottom-up methods. . . . .	3
1.2	The hierarchical organization of a muscle tendon and the characterization techniques needed to evaluate them [10]. . . . .	4
1.3	The fabrication scheme for combining HP and BCP self-assembly. . .	5
2.1	The experimentally determined phase diagram of a BCP [15]. . . . .	13
2.2	Theoretically determined phase diagram of a BCP with their corresponding morphologies [16,17]. . . . .	14
2.3	Examples of defects that arise in BCP systems [22,23]. . . . .	17
2.4	Moore's second law demonstrates that the cost of manufacturing is growing exponentially. . . . .	18
2.5	The molecular architecture of three types of BCP. In the BCP one part is a coil and the other block is composed of (a) a main chain liquid crystalline polymer, (b) a covalently bound side chain liquid crystalline BCP or (c) a noncovalently bound side chain liquid crystalline BCP.	20
2.6	TEM micrographs of the three morphologies that are formed by PHIC-b-PS rod-coil diBCP at different rod-volume fractions [50,51]. . . . .	22
2.7	The hierarchical structure from a rod-coil BCP [55]. . . . .	23
2.8	The phase diagram for a side-chain liquid crystal BCP predicted by self-consistent field theory [68]. . . . .	25
2.9	The four possible BCP and smectic layer orientations in a cylinder-forming side-chain liquid crystal BCP [57]. . . . .	27
2.10	Comb-coil BCP and their hierarchical self-organization that results from self-assembly of small molecules and BCP (a) is an arbitrarily defined primary structure for the BCP. The resulting molecular recognition and microphase separation results in hierarchical structures (b and c) [79]. . . . .	28

2.11	(a) A comb-coil BCP selected to induce structural hierarchy. (b) At room temperature the small molecules are confined to the PVP and the sample reflects green light. (c) When the sample is heated to above $125^{\circ}\text{C}$ the grating wavelength blue-shifts and the intensity decrease because the small molecule dissociates and becomes a non-specific solvent for PS and P4VP/MSA [81]. . . . .	30
2.12	Examples of hierarchical structures in diatom cell walls as observed with scanning electron microscopy images of cell walls from different diatom species [85]. . . . .	32
2.13	Schematic diagram comparing the procedure for a top-down method before bottom-up(left side) against a bottom-up method before top-down (right side) that was used to arrange nanoparticles from a combined lithography and thin layer of BCP micelles [88]. . . . .	36
2.14	Optical dark-field microscopy image of a square array of BCP micelles on a lithographically defined substrate [89]. . . . .	38
2.15	AFM image and height profile of a square array of BCP micelles on a lithographically defined substrate [89]. . . . .	39
2.16	SEM micrograph of a polymer film that was patterned using the breath figure technique [94,95]. . . . .	40
2.17	The effect of surfactant on the polymer solution to induce the highly ordered arrays of polymer holes confined between domain walls. The SEM images of the hierarchical structure formed by a) 4 wt% polymer solution without polymeric surfactant contains defects, b) 4 wt% polymer solution involving 0.4 wt% polymeric surfactant with less defects, and c) 4 wt% polymer solution and 0.8 wt% polymeric surfactant shows a defect free structure [94]. . . . .	41
2.18	The SEM micrographs demonstrate the impact of confining geometry shape on the self-assembly of breath figures. a) Image of hierarchical structure fabricated using a hexagonal grating, b) a parallel grating and c) a square grating [94]. . . . .	42
2.19	The procedure for hierarchical fabrication of hexagonally arranged BCP droplets by controlled dewetting of PS-b-PEO thin films upon solvent annealing by combining with microcontact printing lithography. The final structure showed order over two length scales, (a) the hexagonal distribution of BCP domains from controlled dewetting, (b) a single BCP domain showing a hexagonal arrangement of cylinders, and (c) a cross section of one of the BCP domains [98]. . . . .	43

2.20	SEM micrographs of a variety of lithographically patterned regions containing gold nanoparticles [100]. . . . .	45
2.21	The sculpting of a colloidal crystal by lift-off microcontact printing. (a) a one-dimensional structure stamped into the colloidal crystal. (b) a two-dimensional structure by rotation of the PDMS stamp in a two step microcontact printing process. (c) and (d) a quasi three-dimensional basket weave pattern obtained by multistep microcontact printing [101]. . . . .	47
2.22	At the top of the figure is an illustration of a two-dimensional surface relief grating covered by a thin film of BCP. Bottom of the figure is an atomic force micrograph and fast fourier transform of a hierarchical two-dimensional in two-dimensional structure in photoresist that resulted from the parallel assembly of nanoscale fabrication techniques.	48
2.23	BCP and colloidal nanoparticles self-assembling inside narrow substrates. [4]. . . . .	49
2.24	SEM images of a single layer of colloidal particles in a lithographically defined substrate. (A) and (C) are the images of a colloidal crystal when the confining geometry is commensurate.(B) and (D) are the images when the size of the well is not commensurate with the dimensions of the colloidal crystals. [93]. . . . .	51
2.25	The confinement of PS-b-polyferrocenyldimethylsilane in A) templates of various widths, B) a plot of the number of rows versus the confinement width of the channel in A, and C) the free energy perpolymer chain of the confined array of spheres with respect to the confinement width of the channel [6]. . . . .	52
2.26	Morphological pattern of a lamellar forming BCP under (A) cylindrical confinement and (B) its cross sectional structure. The morphology of a lamellar BCP under (C) spherical confinement and (D) its cross sectional structure [115]. . . . .	54
2.27	A comparision of the pair distribution fluctuations (PDF) for a thin film of a spherical forming BCP (A) on a flat two-dimensional surface and (B) in a shallow small well [6,123]. . . . .	55
3.1	An illustration of photonic crystals with ordered structures in one-, two-, and three-dimensions. . . . .	60

3.2	Nematic liquid crystals such as 4-cyano-4-pentylbiphenyl tend to align in a direction parallel to $\mathbf{n}$ . The refractive index parallel and perpendicular to the director are different below the nematic to isotropic transition temperature (a). The electro-optical switching of (b) a holographic polymer dispersed liquid crystal diffraction grating [126, 135, 146]. . . . .	64
3.3	Diagram of several layers of a HP, polymer stabilized, liquid crystal structure and the optical response of the same material when exposed to UV and visible light [150]. . . . .	65
3.4	(a) A graph of the diameter and turbidity as a function of temperature for a colloidal crystalline array of poly(N-isopropylacrylamide) (b) the diffraction of the colloidal crystalline array of poly(N-isopropylacrylamide) as a function of temperature [151]. . . . .	67
3.5	A diagram illustrating the vector representation of a plane wave traveling in a direction defined by $\bar{k}_m$ and amplitude $\bar{A}_m$ . $\psi$ is the polarization angle, $\theta$ is the angle between the Z-axis and the vector $\bar{k}_m$ and $\varphi$ is the angle between the projection of $\bar{k}_m$ onto the XY-plane and the X-axis . . . . .	69
3.6	A cross section of a holographic polymer dispersed liquid crystal one-dimensional photonic crystal fabricated from HP [182] . . . . .	72
3.7	SEM images of cross-sectional fracture surfaces of transmission gratings demonstrating that nanoparticles can be sequestered by HP. gold nanoparticles (a), PS spheres (b) and clay powder (c) were all patterned. (d) is a TEM micrograph of the gold nanoparticles patterned using HP. (e) is the evolution of structure shown for two periods. Scale bars correspond to 1.5 micron (a), 1.5 micron (b) and 600 nm (c). [127]	73
3.8	The chemical structure of the components that make-up Norland optical adhesive NOA 65 (a-d) and CIBA-Geigy Inc., Darocure 4265 (e-f).	74
3.9	The chemical structure of the inert homopolymers used in this dissertation: (a) PEG, (b) PCL and (c) PLLA. . . . .	75
3.10	The chemical structure of the BCP used in this dissertation: (a) PEO-b-PCL, (b) PEO-b-PDLA and (c) PEO-b-PE. . . . .	76
3.11	Experimental set up for fabricating a (a) reflection grating and (b) a transmission grating using a single prism. . . . .	78
3.12	The intensity profile for a reflection grating with a prism angle of $18^\circ$ .	79

3.13	A chart displaying the intensity of the interference pattern in the sample (Blue line) and the period of the interference pattern (Black line) dependent on the incident angle of the laser beam relative to the surface normal that are possible for HP in the current setup. . . . .	80
3.14	Schematic of electron beam through TEM for image formation [186].	84
3.15	An image of a JEOL 2000-fx TEM [187]. . . . .	85
3.16	Schematic representation of simultaneous SAXS and WAXD setup at beamline X-27C, NSLS, Brookhaven National Laboratory [190]. . . .	87
4.1	A sample cell containing a mixture of PEG and photocrosslinkable monomers after HP. . . . .	93
4.2	Transmission spectra and TEM image of volume gratings containing PEG formed by HP. . . . .	94
4.3	Two-dimensional X-ray pattern of PEG volume gratings. (a) X-ray geometry for parallel setting, (b) X-ray geometry for perpendicular setting, (c) two-dimensional X-ray pattern for parallel setting PEG $M_w$ 2,000 $\frac{g}{mol}$ , (d) two-dimensional X-ray pattern for perpendicular setting PEG $M_w$ 2,000 $\frac{g}{mol}$ , (e) two-dimensional X-ray pattern for parallel setting PEG $M_w$ 4,600 $\frac{g}{mol}$ , (f) two-dimensional X-ray pattern for perpendicular setting PEG $M_w$ 4,600 $\frac{g}{mol}$ , (g) two-dimensional X-ray pattern for parallel setting PEG $M_w$ 8,000 $\frac{g}{mol}$ , and (h) two-dimensional X-ray pattern for perpendicular setting PEG $M_w$ 8,000 $\frac{g}{mol}$ . . . . .	97
4.4	Azimuthal scans of the two-dimensional X-ray diffraction patterns in figure 4.3. (a) perpendicular setting of PEG volume grating, outer ring d-spacing = 0.398 nm, (b) perpendicular setting of PEG volume grating, inner ring d-spacing = 0.494 nm, (c) parallel setting of PEG volume grating, outer ring d-spacing = 0.398 nm, and (d) parallel setting of PEG volume grating, inner ring d-spacing = 0.494 nm. . . .	98
4.5	PLM image of volume gratings containing PEG. . . . .	99
4.6	Schematic representation of the hierarchical structure of the PEG volume grating. (a) lamellar structures are formed with a periodicity of approximately 200 nm, (b) within the PEG layers, PEG crystals are formed and the lamellar crystals are parallel to the volume grating surface and the PEG chains are parallel to the grating pitch. . . . .	100
4.7	Heating (a) and cooling (b) transmission spectra of a PEG volume grating. The numbers on the right side of both (a) and (b) correspond to the temperatures in Celsius at which the spectra were taken. . . .	101

4.8	Notch position and diffraction efficiency change with respect to temperature for figure 4.7. (a) represents heating and (b) represents cooling.	102
4.9	DSC thermograms of pure PEG and PEG volume gratings. The cooling and heating rates were controlled to be $10 \frac{^{\circ}C}{min}$ .	103
4.10	(a) Transmission spectra of the reflection gratings of PEG and crosslinked resin. The baselines have been offset for clarity in display of the spectra. (b) TEM micrograph of a thin section of a PEG with a $M_w$ $2,000 \frac{g}{mol}$ and crosslinked resin.	105
4.11	Plots of the notch position and diffraction efficiency with respect to temperature in transmission spectra of the PEG volume gratings. (a) PEG $2,000 \frac{g}{mol}$ on heating, (b) PEG $2,000 \frac{g}{mol}$ on cooling, (c) PEG $4,600 \frac{g}{mol}$ on heating, (d) PEG $4,600 \frac{g}{mol}$ on cooling, (e) PEG $8,000 \frac{g}{mol}$ on heating, and (f) PEG $8,000 \frac{g}{mol}$ on cooling.	107
4.12	Transmission spectra in the visible spectrum for mixtures of photocrosslinkable monomers combined with PCL (top) and PLLA (bottom) that were patterned using HP.	109
4.13	TEM of thin cross section of (a) PCL and (b) PLLA confined between layers of crosslinked NOA 65 resin.	110
4.14	A magnified view of the TEM of a thin cross section of a volume grating containing PCL in a mixture with photocrosslinked polymers.	110
4.15	Visible light transmission spectra comparing a volume grating containing a 50:50 weight fraction blend of PCL and PLLA in a mixture with 70% photocrosslinked polymers with the homopolymer spectra of the individual components.	112
4.16	A TEM micrograph of a thin cross section of volume grating containing a 50:50 weight fraction blend of PCL and PLLA in a mixture with 70% photocrosslinked polymers.	114
4.17	The integrated intensity profile parallel (blue-bottom) and perpendicular (red-top) to the patterned layers for a volume grating containing a 50:50 weight fraction blend of PCL and PLLA in a mixture with 70% photocrosslinked polymers.	115

5.1	Schematic representation of hierarchical nanomanufacturing by combining HP and BCP self-assembly. (a) syrup containing photopolymerizable monomers, BCP, and photoinitiator, (b) HP formed ordered structures on a 200 nm scale, (c) BCP self-assembles in nanodomains created by HP structures, and (d) a variety of different BCP structures could be confined in the HP layers. . . . .	117
5.2	Transmission spectrum of a mixture of NOA 65 and PEO-b-PCL patterned using HP. . . . .	119
5.3	TEM image of the cross-section of a PEO-b-PCL volume grating. . . . .	120
5.4	A closer look at the TEM image of the cross section of a PEO-b-PCL volume grating. . . . .	121
5.5	Two-dimensional SAXS (a and b) and two-dimensional WAXD (c and d) of a PEO-b-PCL volume grating. The X-ray beam was parallel (a,c) and perpendicular (b,d) to the grating film, as indicated in the top-right insets of (a) and (b). . . . .	123
5.6	The two-dimensional SAXS of a bulk sample of PEO-b-PCL. . . . .	124
5.7	DSC thermograms of PEO-b-PCL in bulk and in a volume grating. . . . .	125
5.8	Schematic representation of the hierarchical nanostructures formed by combining HP and BCP self-assembly. . . . .	125
6.1	The transmission spectra and TEM of PEO-b-PCL patterned using HP. . . . .	130
6.2	The transmission notch position wavelength and diffraction efficiency of PEO-b-PCL hierarchical grating being heated from $25^{\circ}C$ to $75^{\circ}C$ then cooled down to $0^{\circ}C$ at $1\frac{^{\circ}C}{min}$ . . . . .	131
6.3	DSC thermograms of PEO-b-PCL in bulk and in volume gratings. The cooling and heating rate was $10\frac{^{\circ}C}{min}$ . . . . .	132
6.4	(a) FT-IR at room temperature of a PEO-b-PCL volume grating containing. The change in intensity at $843\frac{1}{cm}$ and $731\frac{1}{cm}$ going from room temperature to $75^{\circ}C$ . . . . .	134
6.5	TEM micrographs of (a) PEO-b-PCL grating quenched from $47^{\circ}C$ and (b) a magnified image of the volume grating. . . . .	136
6.6	TEM micrographs of (a) PEO-b-PCL grating quenched from $75^{\circ}C$ and (b) a magnified image of the volume grating. . . . .	137

6.7	TEM micrographs of (a) PEO-b-PCL grating quenched from $34^{\circ}C$ and (b) a magnified image of the volume grating. . . . .	138
6.8	TEM micrographs of (a) PEO-b-PCL grating after heating and cooling and (b) a magnified image of the volume grating. . . . .	139
6.9	The notch position and diffraction efficiency as a function of temperature. When the PCL volume grating was heated and cooled. . . . .	142
6.10	DSC thermograms of PCL volume gratings with a $10\frac{^{\circ}C}{min}$ heating and cooling rate. . . . .	143
6.11	Transmission optical spectra (left) and TEM micrograph (right) of a cross section of a PCL volume grating after being quenched in liquid nitrogen from $75^{\circ}C$ . . . . .	144
6.12	The TEM micrograph of a PEO-b-PCL grating (a) at $0^{\circ}$ tilt and (b) at $45^{\circ}$ tilt. . . . .	146
6.13	A schematic representation of PEO-b-PCL in a volume grating. . . . .	147
6.14	The visible light transmission spectrums for isothermal crystallization. . . . .	150
6.15	The TEM images of isothermally crystallized hierarchical volume gratings at, (a) $45^{\circ}C$ , (b) $35^{\circ}C$ , (c) quenched in liquid nitrogen, and (d) $25^{\circ}C$ . . . . .	151
6.16	The TEM images of hierarchical volume gratings that were isothermally crystallized at (a) $35^{\circ}C$ , (b) then quenched in liquid nitrogen, (c) followed by annealing at $75^{\circ}C$ then crystallized at $35^{\circ}C$ . . . . .	153
6.17	The transmission spectra of hierarchical volume gratings that were isothermally crystallized at (a) $35^{\circ}C$ , (b) then quenched in liquid nitrogen, (c) followed by annealing at $75^{\circ}C$ then crystallized at $35^{\circ}C$ . . . . .	154
7.1	The schematic of a two-dimensional HP setup and laser intensity profile parallel to the sample cell surface. . . . .	156
7.2	The TEM micrographs of cross sections of the grating formed from HP PEG and NOA 65 in the (a) $45^{\circ}$ plane, (b) YZ-plane, and (c) XZ-plane. The schematic of the cutting planes are shown in (d). . . . .	157
7.3	The PLM images of the two-dimensional PEG photonic crystal (a) before and (b) after recrystallization. . . . .	159

7.4	Light scattering results with narrow peaks of scattered light from a sample of HP PEG in NOA 65 at room temperature and $75^{\circ}C$ . . . .	160
-----	---	-----

## Abstract

---

The top-down nanomanufacturing technique is approaching its theoretic limits and processes such as e-beam lithography are extremely costly. In contrast, the bottom-up method such as self-assembly can easily reach nanometer (even sub-nanometer) feature sizes. One drawback of self assembly, however, is the difficulty to achieve large scale, defect-free structures. Combining the top-down and bottom-up methods in one system can lead to novel hierarchical nanostructures with tailored properties and this approach is generally referred to as “top-down helps bottom-up.” While most of the existing systems deal with (quasi) two-dimensional patterning, partly due to the demands from semiconductor industry, in this dissertation, we demonstrate that three-dimensional, dynamic tunable, optical volume gratings can be manufactured via combining holographic patterning (HP) and block copolymer (BCP) self-assembly into one system.

A number of semicrystalline homopolymers and BCP have been successfully patterned into one-dimensional and two-dimensional optical structures. In the one-dimensional homopolymer case, a Bragg reflector structure with continuous alternating layers of patterned polymer and the crosslinked resin were formed. The result of combining HP and BCP was a hierarchical structure fabricated from a homogeneous solution in one step. HP formed 200 nm periodic lamellar structures, confining a BCP to 100 nm domains. Subsequently, the BCP self-assembles into a lamellar structure with a period of 21 nm. This system provides an interesting basis for studying the thermo-optic behavior of the hierarchical volume grating formed by combining top-down manufacturing and bottom-up self-assembly. Upon heating and cooling a unique thermal switching occurred that can be attributed to the melting/phase separation that the BCP undergoes within the confined region of the volume grating.

There are at least five advantages of this novel nanomanufacturing approach. First, two different nanomanufacturing techniques are seamlessly combined together and the resulting hierarchical structures span from a few nm to the 200 nm scale. Second, by combining these two techniques, the shortcomings of each method can be overcome. Third, this hierarchical structure can be fabricated in a few seconds. Fourth, the HP method enables the fabrication of a multiple layered structure, which is critical for three-dimensional nanodevice applications. Fifth, a variety of two-dimensional and three-dimensional nanostructures can be readily achieved by changing the HP laser set-up and BCP structures.



## Chapter 1. Introduction to Hierarchical Structures on the Nanoscale

A half-century after Richard Feynman gave his “There’s Plenty of Room at the Bottom” talk at Caltech, nanoscale research has expanded. Nanotechnology in its current form has become a household term with the widespread media blitz that has provided the general public with cutting edge research. The drive to use nanoscale materials in electronics, medical, and industrial applications sustains the field. Passive nanostructures such as nanotubes have started to be commercialized by several companies including Arkema, Inc., Zyvex, Inc., and Carbon Nanotechnologies, Inc. Most nanotubes synthesized are being sold back to researchers in order to find new uses, but some nanotubes have found their way into niche applications such as sporting equipment. Nanoparticles and block copolymers (BCP) have also found their way into commercial applications. The applications that use these nanomaterials rely on their passive structures and functions, such as the adsorption of UVA and UVB light by zinc oxide nanoparticles used in sunscreen. The identification of these structures, both organic and inorganic, has spurred new interest in the dynamic properties of nanomaterials. A few examples of dynamic properties of nanomaterials include, the frequency dependent nanotube resonator and polymer actuators [1, 2]. The development of photonic structures, sensors, and active nanomaterials could significantly improve the way the pharmaceutical industry designs drug release agents and the electronic and photonic industries develop transistor and amplifiers.

The culmination of all the advances in nanotechnology has led to constructing more and more complex nanostructures making it quite packed with researchers at these small length scales. Two methods for processing nanoscale materials are available; named after the direction in which the processes occur. These are the top-down and bottom-up nanomanufacturing techniques, as shown in figure 1.1. The terms were

first applied to the field of nanotechnology by the Foresight Institute in 1989 in order to distinguish between molecular manufacturing and conventional manufacturing [3]. The top-down approach also known as, micro- or nano-fabrication, are externally-controlled tools used to shape a material. The bottom-up approach uses the design of molecular interactions to allow a material to spontaneously assemble into ordered structures, this processes is also known as self-assembly. The assembly of a hierarchical material requires two or more processes each with a characteristic length scale. The combination of a process from the top-down column with the bottom-up column would have many advantages over conventional materials processing techniques for the fabrication of advanced materials, shown in figure 1.1. Choosing two or more bottom-up techniques would lead to a hierarchical structure via the culmination of order-disorder transitions. The combination of nanomanufacturing techniques allows for parallel processing, efficient use of volume, and large scale design to specified ends. The driving force to realize the potential of these materials has been two fold. First, biological and bio-inspired materials have been investigated in order to understand the structure-property relationships that exist in nature. The second area of intense research has been in semiconductor chips, where high cost and market demand are driving smaller and faster technologies allowing for new techniques and materials. The potential for fabricating hierarchical structures in one-, two- and three-dimensional structures could benefit filtration, biomedical chip assays, and optical materials.

Hierarchical structures require precise control over ensembles of confined self-assembled nanoparticles or BCP. This can be achieved by either starting at the bottom-up or from the top-down. These routes to fabricate hierarchical structures can be done in parallel or series. Yet, challenges remain when the two technologies are combined including registration of microdomains and self-assembled structures at the interface. In order to maximize the potential of nanomaterials, methods need to be developed that efficiently combine multiple nanomaterials in space.

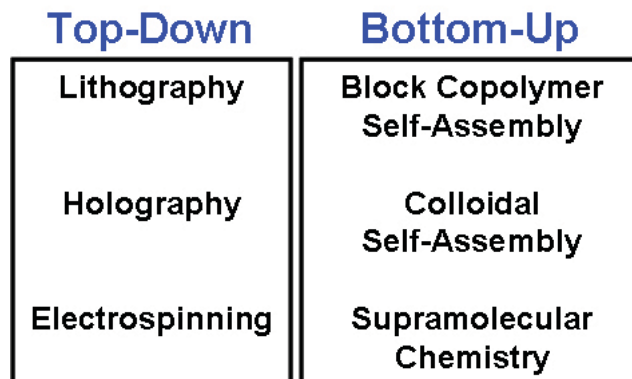


Figure 1.1: Nanoscale processing techniques grouped into top-down and bottom-up methods.

In order to arrange and confine nanoparticles and BCP, top-down microfabrication techniques were introduced as a way to control the self-assembling material. This method of directing self-assembled materials needs to be investigated in order to elucidate methods for obtaining highly ordered defect free nanostructures [4,5]. These methods include molecular epitaxy and confined geometries to control orientation and registration [6, 7]. The importance of controlling self-assembly is evident from the nanoelectronic components currently used in Intel's Inc. chip manufacturing and in photonic crystals [8]. The investigation of epitaxy and confinement of self-assembling materials has added to the understanding and control over single microdomains in soft materials. This information has paved the way for developing hierarchical nanoscale materials by a number of different strategies. These strategies rely on the confinement of self-assembling materials, but it is becoming clear that the combination of self-assembly with microfabrication can result in complex structures.

Polymers have played an integral role in the formation of hierarchically structured materials. Biopolymers such as DNA and proteins can self-assemble over many length scales and synthetic polymers can organize into hierarchical structures [9]. The length scales at which hierarchically structured materials exist requires multiple character-

ization techniques in order to determine the structure, morphology, and behavior. Figure 1.2 is a schematic of a muscle tendon demonstrating the hierarchical nature in polymeric systems. From this image we can see that several different characterization techniques are used including differential scanning calorimetry (DSC), transmission electron microscopy (TEM or EM), scanning electron microscopy (SEM), and optical microscopy (OM) [10,11]. To complement these techniques wide angle X-ray diffraction (WAXD), small angle X-ray scattering (SAXS), light scattering, and Fourier transform-infrared spectroscopy (FT-IR) are employed. This collection of techniques enables construction of the hierarchical material and behavior as a function of an applied stimulus.

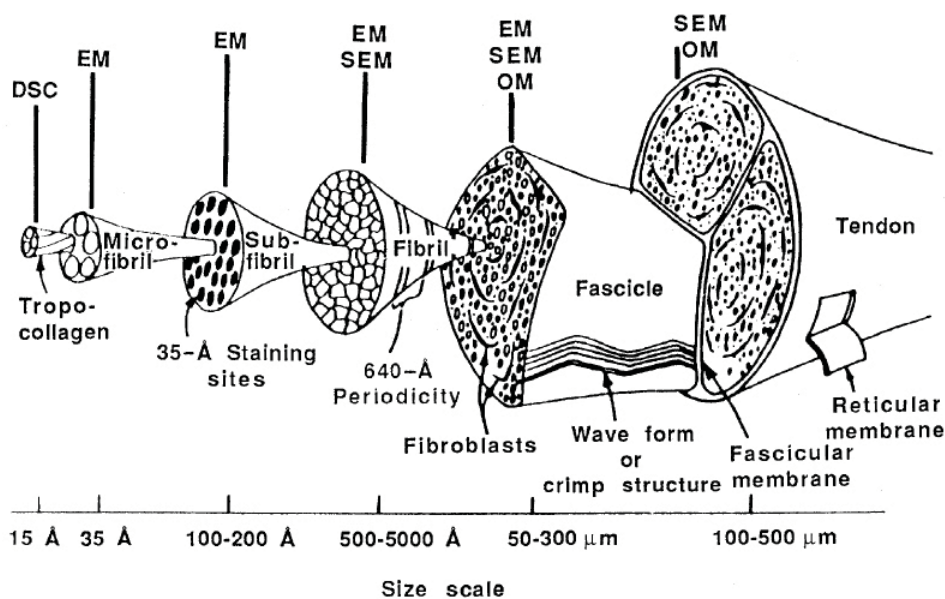


Figure 1.2: The hierarchical organization of a muscle tendon and the characterization techniques needed to evaluate them [10].

This work explores the characteristics of a hierarchical material occupying a volume of space formed from a polymer blend. The structure of a simple one-dimensional hierarchical photonic material from a polymer blend is fabricated and the structure

is explored. Hierarchical nanostructures in a volume of material were fabricated in a bulk system using holographic polymerization (HP) and BCP self-assembly in one step, as shown in figure 1.3. Using HP, a one-dimensional structure on the 200 nm length scale was patterned. The geometry that results from HP provides a nanoconfined space for the BCP. The space approximately 50 nm in size is large enough for the BCP to self-assemble on the 10 nm to 50 nm scale. The two hierarchical structures shown in figure 1.3 represent cylinders-in-lamellae (C-L) and lamellae-in-lamellae (L-L) morphologies. It is anticipated that novel optical properties could be obtained from this unique hierarchical structure and the structures at different length scales also warrant the opportunity to incorporate multiple functionality on the molecular scale as well as microscale.

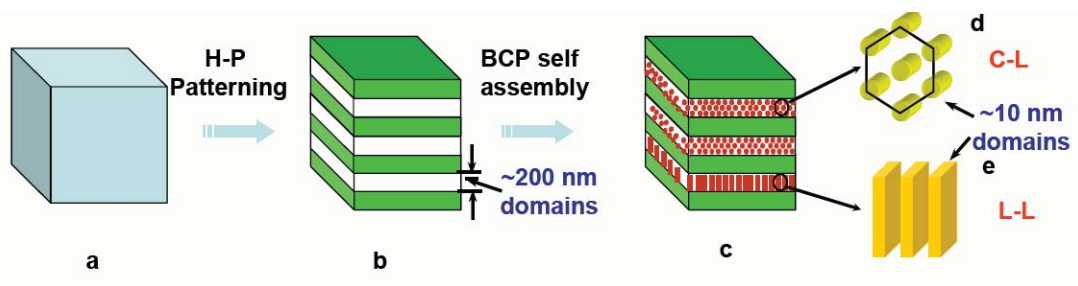


Figure 1.3: The fabrication scheme for combining HP and BCP self-assembly.

Our understanding of hierarchically structured materials and phase changes is not well understood. In order for these materials to become feasible in the next generation of materials a method of measuring and predicting their processability should be investigated. In our case the crystallizable BCP and crosslinked resin will interact depending on the temperature and volume fraction of the components. The temperature modulated volume gratings display interesting optical properties related to the miscibility of the BCP in crosslinked resin. Studying the thermal switching that occurs and relating it to the refractive index changes provides insight into the

soft confinement of the BCP and the phase behavior of the hierarchically structured polymeric material.

The layout of the subsequent chapters is meant to describe the formation and confinement of BCP in a hierarchical volume grating, which was fabricated by combining top-down and bottom-up nanoscale methods in the context of previous work done in the field. A review of the current fabrication techniques and methods for assembling nanoscale hierarchical structures is reviewed in chapter 2. Chapter 3 discusses the methods for characterizing hierarchical structured materials. Chapter 4 presents a nanostructured polymer blend fabricated using a combination of HP and the confinement of the homopolymer. Chapter 5 contains the structure and morphology of hierarchical volume gratings formed from the combination of BCP self-assembly, and HP. In chapter 6, the hierarchical structure is thermally tuned to demonstrate that a unique soft confinement of the BCP occurs in the present system and that the process is reversible and independent of thermal history. Chapter 7 examines the two-dimensional HP of a homopolymer and the thermal switching that the system undergoes. Finally, we summarize the findings and conclude with an outlook of the field of hierarchically structured materials.

## Chapter 2. Background on Manufacturing Hierarchical Nanostructures

### 2.1 The Key Elements of Hierarchical Structures

Hierarchically structured materials offer several potential advantages over conventional materials because they are constructed with multiple levels of ordering, demonstrate complex behaviors, and can be multifunctional. This could lead to compact configurations unattainable in conventional materials that display ordering on only one length scale. Moreover, hierarchical structures can be configured to exhibit single crystal and controlled localized defects at the confined length scale. Templates and selective lithographic techniques can be used to pattern the ordered structures with multiple microdomains at the larger length scales, which limits self-assembly to confined regions. Hierarchical structures can have a diversity of morphologies due to the many structures that can be microfabricated or self-assembled.

In an ideal manufacturing plant the desired product would spontaneously self-assemble from a collection of starting materials using specified chemical interactions. The development of self-assembled hierarchical structures from BCP that have liquid crystalline small molecules and DNA nanotechnology is a promising area of research. However, the design principles to go from molecular recognition and BCP phase separation that have ordered structures on many length scales lacks the design principles to develop manufacturing processes. As is the case in current self-assembled hierarchical structures. In order to get around these limitations, microfabrication, and self-assembly can be combined to provide solutions in the development and manufacturing of DRAM and CMOS chip manufacturing, where high prices and huge technological hurdles need to be overcome. The chip manufacturing industry has laid out their requirements for the incorporation of technology into current manufacturing

process schemes. Even after development of fundamental capabilities it would take another six years to develop new infrastructure and design capabilities [12]. This impose a great challenge on nanotechnology to provide solutions in a timely fashion.

Current chip manufacturing relies on lithography that is part of a larger group of processing techniques classified as top-down microfabrication, these are listed in table 2.1. A top-down approach breaks down or widdles away at the bulk material to gain structure at the nanoscale. In a top-down approach a uniform homogeneous substrate or mixture is formulated. A pattern is then transfered to the mixture during contact or exposure to refine the elements. The unexposed or unpatterned material is then removed leaving behind the desired nanoscale features. Since, the formulation of the starting material can be arbitrarily defined this enables great flexibility in patterning new materials using top-down principles.

Self-assembly is one of many bottom-up approach used to piece together materials to give rise to ordered structures; a list of bottom-up approaches is given in the right hand column of the table 2.1. In a bottom-up approach the individual base materials of the system are first specified in great detail. These elements are then linked together to form larger molecules, which in turn can be linked until a complex structure has been assembled through covalent, electrostatic, and secondary intermolecular forces. The simplicity of not needing to define the substrate for the underlying molecules allows them to quickly assemble without external influences resulting in hierarchical structures.

Nanoscale assemblies fabricated by combining top-down with bottom-up methods could be useful in biomedical and photonic applications. These materials fabricated from combining nanoscale assemblies provides a route to fabricate hierarchical structures. The fabrication of complex three-dimensional hierarchical structures have potential for multilayer photonic crystals, chemical sensors, catalysis, and biotechnology [13]. Xia and coworkers recently demonstrated that DNA could be transported

Top-Down	Bottom-Up
<ul style="list-style-type: none"> <li>• Microcontact printing</li> <li>• Micromolding in capillaries</li> <li>• Microtransfer molding</li> <li>• Micromolding</li> <li>• Soft lithography</li> <li>• UV photolithography</li> <li>• Near-field scanning optical lithography</li> <li>• Contact lithography</li> <li>• Noncontact lithography</li> <li>• Interference lithography</li> <li>• X-ray lithography</li> <li>• Focused ion beam lithography</li> <li>• Zone plate array lithography</li> <li>• Electron beam lithography</li> <li>• Nanografting</li> <li>• Dip-pen lithography</li> <li>• Nano imprint lithography</li> <li>• Layer-by-layer deposition</li> <li>• Electrospinning</li> </ul>	<ul style="list-style-type: none"> <li>• Self-assembled monolayers</li> <li>• BCP microphase separation</li> <li>• Liquid crystal ordering</li> <li>• Particle sedimentation</li> <li>• Crystallization</li> <li>• Supramolecular chemistry</li> <li>• Molecular recognition self-assembly</li> </ul>

Table 2.1: A list of nanoscale fabrication techniques organized into top-down and bottom-up techniques.

through hierarchically structured photonic crystals fabricated from the combination of colloidal particle self-assembly and lithographically patterned substrates. The resulting hierarchical porous structure is analogous to spongy tissue in tree leaves and animal dermis. The authors demonstrated that DNA tagged with fluorescent probes could be transported through the micron-sized channels while the overall structure remained relatively uniform. Using hierarchical structures in developing computer chips, biomedical, and photonic applications, it is evident that much more can come from combining top-down and bottom-up. The challenge for hierarchical structures is building useful materials from the nanoscale to the mesoscale. In the next few years, the combination of top-down and bottom-up nanotechnology could be useful in advancing energy conversion or be incorporated into already present computing

techniques. Advances in fuel cell, solar energy, and information technologies could be made by hierarchically organized materials, which may potentially overcome present hurdles in these systems.

Directed self-assembly is a combined top-down and bottom-up technique that uses microfabrication to limit and control self-assembly. The study of confinement on self-assembled layers has demonstrated that an essential set of sub-lithographic isolated periodic lines and dots can be fabricated. The pitch of the self-assembled structures confined to a region has also been demonstrated. In order to accomplish other goals related to chip manufacturing there is a need to elucidate the principles of directed self-assembly and its impact on hierarchical structures. The main challenge is to understand the limitation and opportunities in this area, which will provide routes to build up from the nanoscale. The rest of this chapter reviews the current fabrication routes to hierarchical structures and directed self-assembly. The unit processes for constructing hierarchical materials is reviewed first, followed by the self-assembly of hierarchical structures. In the rest of the chapter the combination of top-down and bottom-up and the confinement of the self-assembly is discussed.

## **2.2 Nanofabrication Approaches**

Numerous methods for fabricating nanoscale structures are available from both the top-down and bottom-up. The top-down technique employs micro-fabrication to create one-, two-, and three-dimensional geometric or complex structures through electrospinning, lithography and holography. In contrast, bottom-up approaches, use the physical and chemical properties of molecular materials to arrange components by self-organization. The self-organization of nanostructured materials can be achieved by colloidal particle assembly, microphase separation, and molecular processes. In this section we review two methods for nanoscale fabrication, BCP microphase separation

and Lithography.

### 2.2.1 Bottom-Up Approaches

Soft materials are ordered materials built from bottom-up approaches. These techniques include molecular ordering, BCP phase separation, and colloidal crystals. These materials assemble and disassemble based on intermolecular interactions, which are much weaker in comparison to metals and ceramics. The small potential energy barrier from these weak interactions results in phase transitions around room temperature, which gives rise to a rich and diverse number of structures that soft materials possess [14]. However, defects arise due to variations in size, shape, and potential energy of the self-assembling materials. These variations lead to a reduction in the order of the overall structure. One method that has been intensely investigated is BCP microphase separation, which has also been used to form hierarchical nanoscale structures.

The thermodynamics of phase separation described by the Flory-Huggins theory, depends on the molecular weight, volume fraction, and side chain interactions. The length scale of the two phases persists over many orders of magnitude from the nanometer to the millimeter level. Most mixtures of high molecular weight polymers phase separate, yet the chemical bond prevents macrophase separation resulting in a variety of ordered nanostructures at the 10 nm to 100 nm length scale. The chemical bond between the two polymer chains then becomes the boundary of the domains. The size of the domains is dependent on the degree of polymerization. The enthalpy of the system is proportional to the degree of polymerization times the Flory-Huggins segmental interaction parameter or  $\chi$  parameter. Since the magnitude of the  $\chi$  parameter is usually positive, the degree of segregation only needs to be small for the BCP to phase separate. This is due to the large degree of polymerization prevalent in

polymer chains. Though the degree of segregation indicates whether the two blocks are immiscible, the morphology of the BCP is determined by the volume fraction of one block with respect to the total volume. One-dimensional structures of alternating polymer layers stacked together called lamellae are commonly observed at symmetric volume fractions. Assymetry in the volume fraction leads to nonplanar morphologies to accommodate the energy penalty from chain stretching. The degree of curvature increases with the degree of assymetry leading to three different morphologies. In the first phase, a gyroid structure is present in the BCP system when the volume fraction of one component is between 0.28 and 0.34. The second morphology are cylinders that are hexagonally close packed if the volume fraction is reduced further to between 0.17 and 0.28. In the last structure, spheres that are arranged in a body centered cubic lattice can be observed at a volume fraction of less than 0.17. The schematic of the four phases: lamellae, gyroid, cylinders and spheres are shown in figure 3.10.

The phase behavior of coil-coil BCP has been extensively investigated using both theoretical and experimental methods [16, 17]. At the order disorder transition temperature the BCP phases undergo step like transitions to the disordered states. Matsen and researchers developed a comprehensive theoretical phase diagram using self consistent mean field approaches in the intermediate segregation limit with a slight refinement in computation [16, 17]. Their work resulted in a calculated theoretical phase diagram as shown in figure 2.2 [16, 17]. The phase diagram consists of the traditional lamellae, gyroid, cylinder, and sphere phases as a function of volume fraction. Experimental validation of the phase diagram using polystyrene-*b*-polyisoprene (PS-*b*-PI) BCP (Figure 2.2) was in good agreement with the calculated phase diagram [15]. The various ordered morphologies are now generally recognized features in BCP self-assembly. The diversity of BCP systems that produce the traditional morphologies indicates that the coil-coil phase behavior is generally applicable to the BCP system [18].

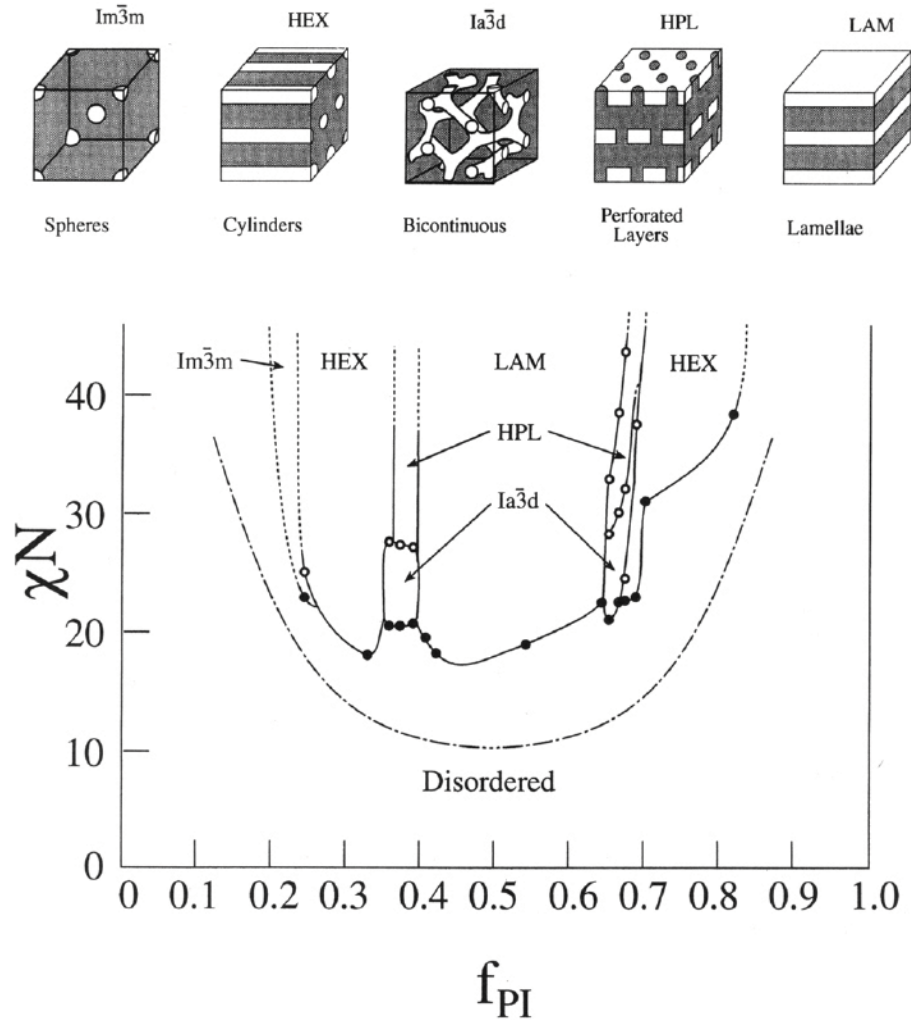


Figure 2.1: The experimentally determined phase diagram of a BCP [15].

### 2.2.2 Top-Down Techniques

Though the self-assembly process is efficient and can assemble a wide range of structures the inability to control self-assembly has limited its wide spread use in manufacturing. However, Top-down techniques for micro- and nano-fabrication have been widely employed to fabricate filters, computer chips, and optical elements through electrospinning, lithography and holography. The advantages of the top-down method are the ability to form continuous fibers, precisely control the placement of electronic

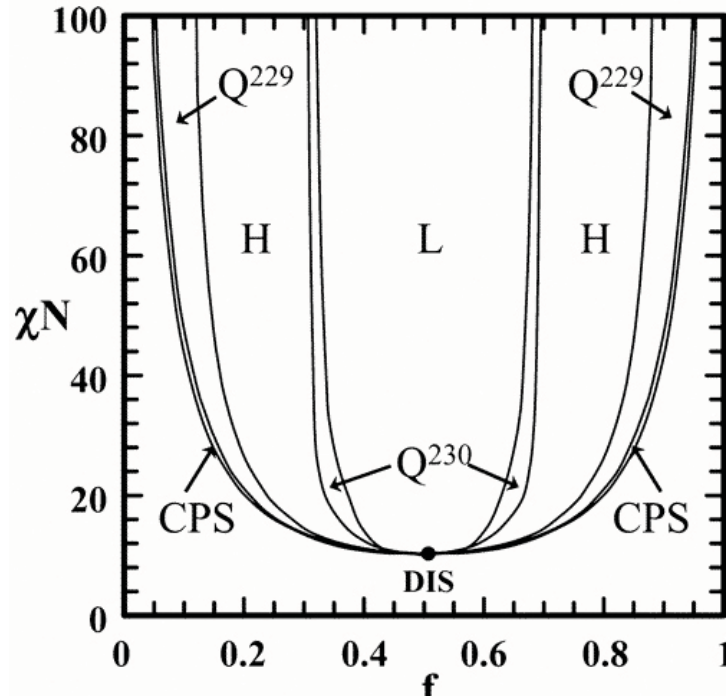


Figure 2.2: Theoretically determined phase diagram of a BCP with their corresponding morphologies [16, 17].

materials, produce defect-free, and controlled defect structures. Many techniques are currently available for microfabrication, lithography is one important technique in the fabrication of hierarchical nanostructures and for controlling self-assembly.

Lithographic techniques are ideal for patterning the surfaces of substrates, such as silicon wafers. Electron beam lithography has been the most widely employed method for patterning small structures with dimensions of 10 nm and above [19, 20]. Electron beam lithography, photolithography, and mask-less photolithography are a group of techniques that make-up noncontact lithography [20]. The other class of lithography is called soft or nonconventional lithography, which includes contact molding and microcontact printing [21]. Both techniques rely on a pattern transfer, yet conventional lithography transfers the pattern through electron beam or light exposure, while soft lithography requires a chemical or physically defined master

mold.

Conventional lithography including electron-beam, photolithography, and interference lithography are standard methods for creating templates that will have confining geometries [4]. Conventional photolithography is a three step process of exposure, pattern transfer, and removal of the resist layer. The arbitrary pattern with a pre-selected geometry and configuration is illuminated on the substrate surface resulting in a crosslinking reaction. The unreacted polymer is rinsed away and the substrate is preferentially etched by an electron beam source or chemical agent. The excess resist is then removed leaving the substrate with the surface features intact [20].

The alternative to photo-lithography are the soft lithographic techniques popularized by George Whitesides. Soft lithography can be used to make templates with sub-100 nm features using a stamp, mold or mask [21]. A mold can be fashioned from polydimethylsiloxane or UV-curable monomers that are typically made from a silicon master, which was written using conventional lithography [21]. The pattern transfer occurs by stamping the substrate that has a polymer above its glass transition. Then it is quickly cooled by infiltrating monomers that can be photocured. The mold or stamp is then removed from the substrate revealing the transferred pattern. Soft lithography can also add an additional level of control by introducing both physical confinement and chemical patterning. The facile nature of soft lithography and low capital cost makes it advantageous over the bulky, specialized, and costly machinery needed for photo-lithography [21].

### **2.2.3 Limitations and Opportunities**

Many nanomanufacturing techniques are being employed today to manufacture materials and components in our everyday lives. Top-down techniques are employed by computer chip manufacturing companies to fabricate microprocessors, while elec-

trospinning is used to fabricate microporous filters and surgical mats. Bottom-up strategies have found their way into tires and flooring through such products as DURADENE from Firestone, Inc. However, two problems exist in nanoscale fabrication using either top-down or bottom-up methods; defects will arise in self-assembled systems and the cost of making smaller feature sizes with lithography is growing exponentially.

Two examples of defects that arise in self-assembling structures are shown in figure 2.3. In figure 2.3a, a PS-b-polybutadiene (PS-b-PB) solution was cast onto a carbon substrate and the solvent evaporated to form a thin film [22]. The PS microdomains appear bright due to the selective  $\text{OsO}_4$  staining of the PB blocks. The unannealed sample contains many dislocation defects and the height variations in the sample enable changes in morphology. The microdomains themselves are composed of a group of different blocks with characteristic sizes that only extend several tens of nanometers due to random nucleation. In figure 2.3b the grain boundary contains areas where the hexagonal arrangement of domains is distorted to include five or seven nearest neighbors. The type of defects occurring in BCP is dictated by the symmetry of the particular BCP microdomain pattern [23]. The point, line, and surface defects occur just as in any other crystalline material. These defects prevent BCP technology from being implemented into main stream manufacturing because engineering applications demand control over the orientation, the position of the microdomains, and the film thickness. Some defects are welcome as long as they can be designed into the self-assembling structure in a controlled fashion [12].

Several techniques for controlling the ordering of self-assembling structures already exist by introducing an external field or surface pattern [7, 24–28]. The use of an external field or chemical pattern enables orientation on a substrate while reducing the rapid decay of global order. These methods resulted in the production of larger self-assembled single crystals. The development and controlling of microdomain

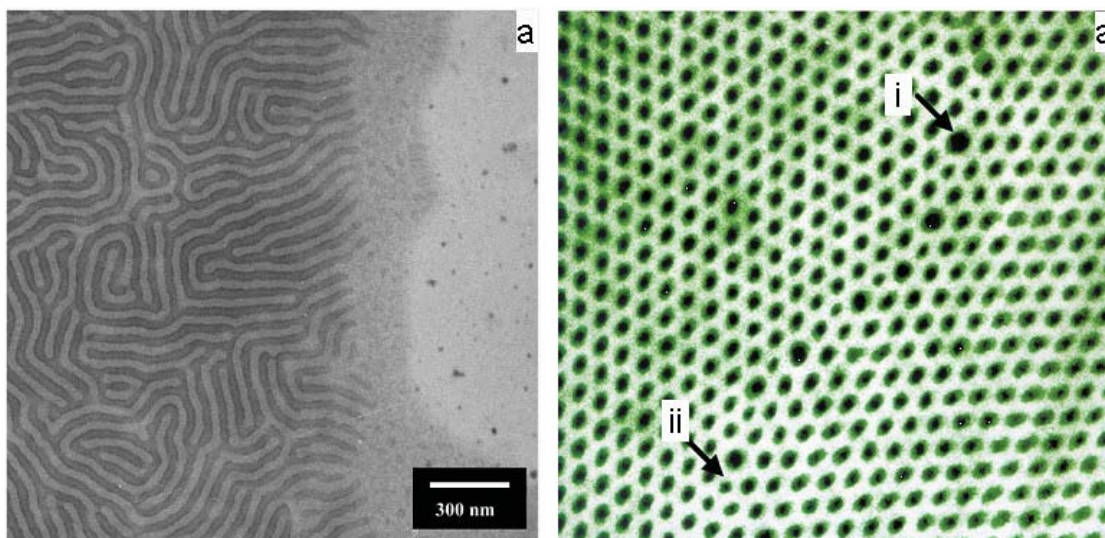


Figure 2.3: Examples of defects that arise in BCP systems [22, 23].

structures in self-assembling BCP is the cornerstone for enabling commercialization of passive nanoscale structures [29, 30]. Many techniques were developed including epitaxy and graphoepitaxy to align BCP microdomains. Yet, large single domains of self-assembled structures are not needed, instead control over the placement and confinement of the material is desired [5]. The many problems associated with an all self-assembled hard drive or medical instrument are being worked out, but in the mean time controlling the morphology and structure of microdomains in colloidal crystals and BCP can be addressed by confining the BCP to small domains.

In comparison lithographic techniques are currently transferring patterns down to 32 nm according to Intel, Inc. [31]. The drawback to microfabrication is that the process is becoming prohibitively expensive. As companies like Intel, Inc. and Advanced Micro Devices, Inc. compete to stay ahead of Moore's first law, which states that transistor density should double every eighteen months. The current trend in cost for constructing new manufacturing facilities is headed for the hundreds of billions of dollars as shown in figure 2.4. To give a perspective on the cost of

constructing a manufacturing facility, the gross domestic product of only fifty-seven countries in 2008 was larger than a hundred billion dollars. The high cost should then be considered a market driver for innovation.

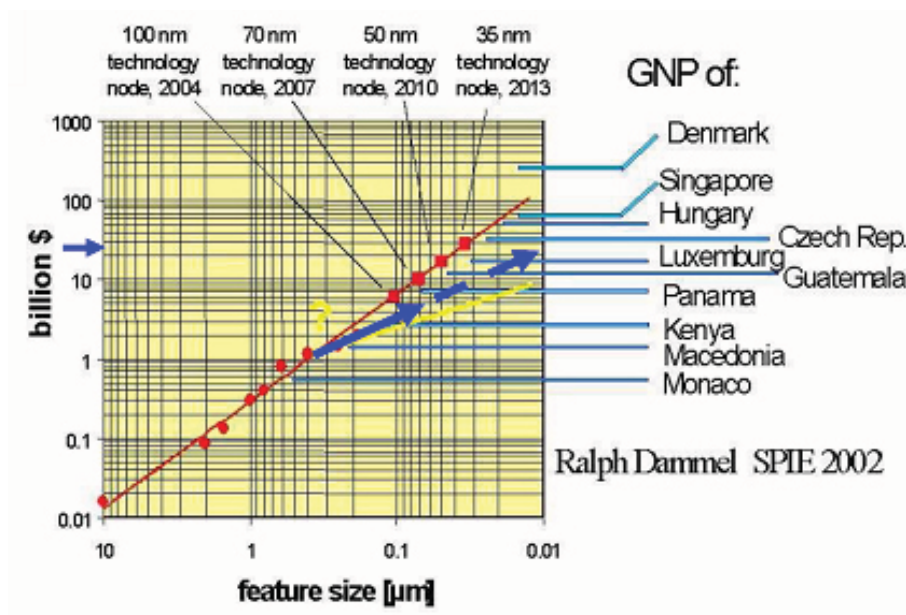


Figure 2.4: Moore's second law demonstrates that the cost of manufacturing is growing exponentially.

A strong interest in the development of hierarchical structures to fit within current manufacturing schemes requires either self-assembly or a combination of self-assembly and microfabrication. The liquid crystal BCP systems continue to produce hierarchical structures with much promise through self-assembling routes. Meanwhile, the convergence of top-down and bottom-up processes has great potential. Utilizing parallel processing to confine and control the placement of self-assembling materials, these applications desire ordered structures in specified areas. The combination of two or more different microfabrication techniques provide another route for fabricating hierarchical structures.

### 2.3 Self-Assembly Approaches to Obtain Hierarchical Structures

At the nanoscale, liquid crystalline BCP exhibit a hierarchical structure due to liquid crystal ordering on the 1 nm to 10 nm scale, combined with BCP phase separation on the 10 nm to 100 nm length scale. The phase behavior of the liquid crystalline BCP is influenced by two competing interactions, BCP microphase separation and liquid crystal ordering. The competition between the two forces can result in unique phase structures that could not be attained in either liquid crystalline or BCP systems. The dependence of the structure on the interactions can result in both liquid crystal dominated phases and BCP dominated phases. The interaction of the liquid crystal with the BCP backbone can be achieved by noncovalent and covalent methods [32–35]. Covalently bonded small molecules, called mesogens, can form a rigid backbone (Figure 2.5a). The rigidity imparted on one segment of the BCP backbone contributes to naming these BCP systems rod-coil, to emphasize the differences between the stiff liquid crystal block and the flexible coil block. A second class of BCP that self-assembles into hierarchical structures is the side chain liquid crystal BCP shown in figure 2.5b. This holds the mesogen in place and increases the rigidity of the backbone. The last method for forming self-assembled hierarchical structures is based on noncovalent bonding of the liquid crystal to the BCP. this is achieved by blending mesogens with a functionalized BCP. The interaction between the mesogen and the BCP using weak secondary forces such as hydrogen bonding, results in hierarchical structure formation (Figure 2.5c). These types of BCP are called comb-coil BCP. The BCP microphase structure is dictated by the Florry-Huggins interaction parameter, molecular weight, and volume fraction of one block. The three types of BCP in figure 2.5 often times diverges from the coil-coil BCP structures due to the extended polymer chain conformation. The novel self-assembling material results in complex phase structures and behavior due to the different length scales of ordering. This

is achieved by incorporating different functionalities along each block giving rise to hierarchical structures.

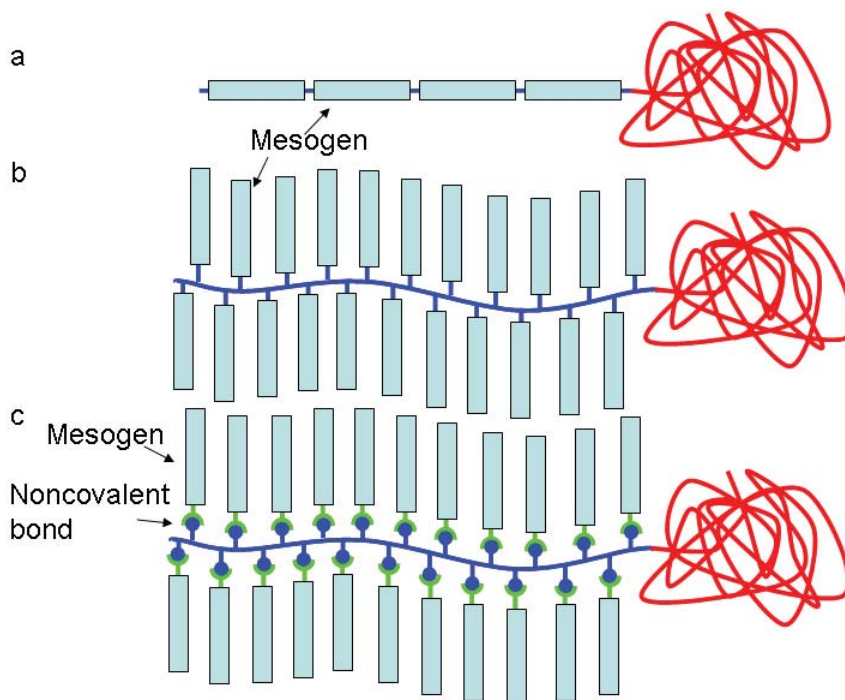


Figure 2.5: The molecular architecture of three types of BCP. In the BCP one part is a coil and the other block is composed of (a) a main chain liquid crystalline polymer, (b) a covalently bound side chain liquid crystalline BCP or (c) a noncovalently bound side chain liquid crystalline BCP.

The phase behavior of rod-coil BCP will be different from coil-coil BCP systems due to the liquid crystals' rigid and preferential orientation. Oligomeric rod-coil BCP display phase behavior similar to coil-coil BCP systems with morphologies such as spheres, cylinders, gyroid, and lamellae [36–41]. By increasing the molecular weight and rod length, the rod-rod interactions become stronger. This suppresses morphologies with curved interfaces such as spheres, cylinders, and gyroids while structures with flat surfaces dominate the phase diagram. Flat interface structures such as stripped, hockey-puck, zig-zag, arrow head, and lamellar shapes were calculated and found experimentally [42]. The liquid crystal behavior within these unique morpholo-

gies were theorized using free energy calculations in that the assumed strong segregation resulted in nematic, smectic, and bilayer ordering [43–48]. If weak segregation persists between BCP layers then the morphologies predicted based on samples with small rod lengths with respect to the size of the coil diameter resulted in microphase separated structures with isotropic behavior. At large rod lengths with respect to the coil diameter the liquid crystal could achieve a nematic phase [49]. The theoretical predictions were confirmed by experimental studies of the phase behavior [42].

Stiff main chain BCP systems that form rod-coil structures are synthesized by rigid small molecules linked together to form a main chain rigid block that is then connected to an amorphous block. The Ober and Thomas group demonstrated that stiff helical rods of poly(hexyl isocyanate) (PHIC) about 50 nm to 60 nm long and a PS coil at one end present very unique phase structures. Several samples with molecular weight varying from  $70 \frac{kg}{mol}$  to  $1800 \frac{kg}{mol}$  and a volume fraction of the rod varying between 0.42 and 0.98 were investigated. A variety of morphologies were observed: including a wavy lamellae at a volume fraction of PHIC at 0.42 (Figure 2.6a); zig-zag lamellae at a volume fraction of PHIC between 0.73 and 0.90 (Figure 2.6b); and an arrow head shaped domain at a volume fraction of PHIC around 0.98 (Figure 2.6c) [50,51]. The PHIC domains contained the rigid rod moieties arranged in a smectic phase with a slight tilt with respect to the lamellar like structure. The thickness of the lamellae were approximately 50 nm resulting in an interdigitated structure.

Low molecular weight rods made up of rigid moieties can also present interesting morphologies. Stupp’s group investigated the phase structure of an oligomer created by combining an azo dye molecule and biphenyl carboxylic acid to form a 6 nm rod attached to PI of  $3.2 \frac{kg}{mol}$  [52]. The short rod-coil structure allowed the researchers to explore the competition between microphase separation and liquid crystal ordering by controlling the molecular weight of PI [52–55]. At a rod volume fraction of 0.36, a

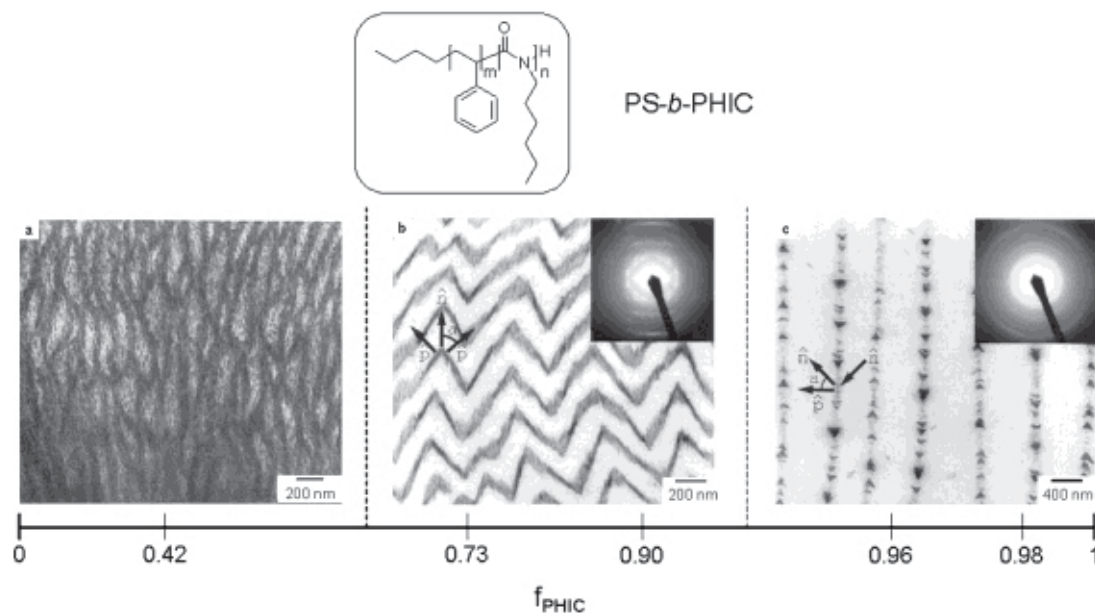


Figure 2.6: TEM micrographs of the three morphologies that are formed by PHIC-*b*-PS rod-coil diBCP at different rod-volume fractions [50, 51].

stripped pattern of rods could be observed inside a PI matrix. Inside the stiff mesogen region, the rods possess a hexagonal symmetry, though the orientation with respect to the PI matrix can not be confirmed. In comparison the coil-coil BCP system at this volume fraction also shows a phase morphology of cylinders. The strip-like patterns are similar to the broken lamellae phases reported by numerical calculation of Ganesan and researchers [42, 54, 55]. By decreasing the volume fraction of the rod to 0.25, the morphology changes from stripes to a super-lattice aggregate. The super-lattice aggregate contains pucks 7 nm in diameter that are oriented parallel to the substrate and arranged with a hexagonal in-plane symmetry in the PI matrix. The packing of the short mesogens suggest that the distribution of PI is not uniform around the mesogen. These distortions can manifest themselves as a unique mushroom shaped nanostructure as shown in figure 2.7. A mushroom morphology was assembled from a 100 units of a triblock BCP containing PS, PI, and three biphenyl units. The

number of rod molecules in the cluster is limited by the size of the PS/PI coils. The mushrooms stack to form a layered structure with the rods orienting normal to the substrate leading to self-organized films with a unique hierarchical structure.

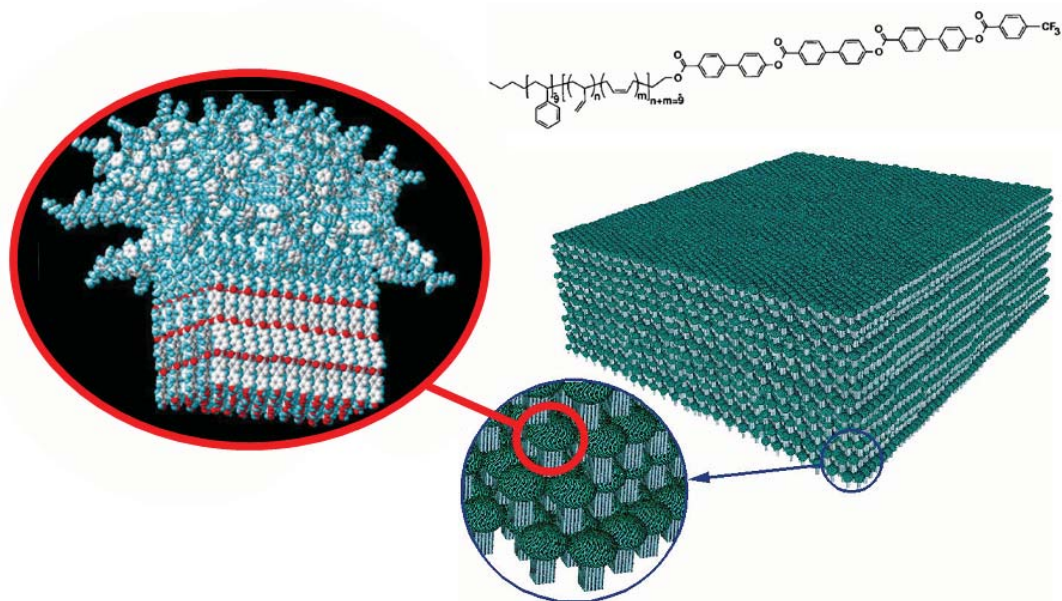


Figure 2.7: The hierarchical structure from a rod-coil BCP [55].

Side-chain liquid crystalline BCP is another class of rod-coil BCP that form a hierarchical structure. The side-chain liquid crystal BCP uses the bulkiness of the liquid crystal moieties to straighten the polymer backbone to form a rod-coil structure. In comparison to the main-chain liquid crystal rods, the decoupling of the strong interactions on the polymer backbone influences the phase behavior allowing conventional phase structures similar to the coil-coil systems. In addition, improvements in the liquid crystal ordering were observed. The side-chain liquid crystals BCP possess a certain degree of flexibility allowing the liquid crystals to adopt to the boundary of the microphase separated structures [33–35, 56]. The orientation of the liquid crystal relative to BCP phase separated block interface can be either perpendicular or parallel depending on the anchoring of the liquid crystal to the polymer backbone [57].

A diverse collection of chemistries was used to fabricate side-chain liquid crystal BCP with conventional coil-coil BCP phase behavior and either smectic or nematic liquid crystal ordering [33–35,56–67]. Theoretical analysis of the phase behavior using self-consistent field theory demonstrates that the segregation strength for microphase separation is smaller than the energy to go from isotropic to nematic liquid crystal phases. The results indicate that microphase separation structures are necessary for obtaining ordered liquid crystal phases [68]. Three phases were predicted from these calculations, as shown in figure 2.8. The first phase is a cylinder structure with the liquid crystal phase being continuous at low volume fraction of the coil block. In the second phase, a lamellar structure at equal volume fraction can be observed. The last phase is a cylinder structure composed of liquid crystals that occurs at high volume fractions of coil block, which forms the continuous phase. The mesogen at low and high volume fractions was oriented parallel to the cylinder axis to facilitate stretching of the polymer backbone. At almost equal volume fraction the mesogen is parallel to the lamellae. In this case, the liquid crystal structure was dictated by the BCP morphology resulting in the self-assembly of ordered small liquid crystal molecules and BCP on two length scales.

The Ober and Thomas groups experimentally confirmed the structures of side-chain liquid crystal BCP using PS-*b*-PI functionalized with an azobenzene based mesogen on the isoprene as a function of the volume fraction of the PI-liquid crystal [57, 62]. The PS volume fraction of fifty percent results in a lamellar structure, while at higher volume fractions a cylinder morphology was observed. In both cases the liquid crystal formed a smectic A phase. A cylinder structure formed during microphase separation when PS was the minor component. Using mechanical shear to align the BCP cylinders and liquid crystal, the authors observed a transformation of the orientation of the cylinders as a function of shearing temperature. If the BCP was sheared below the isotropic to smectic A transition, the cylinders oriented

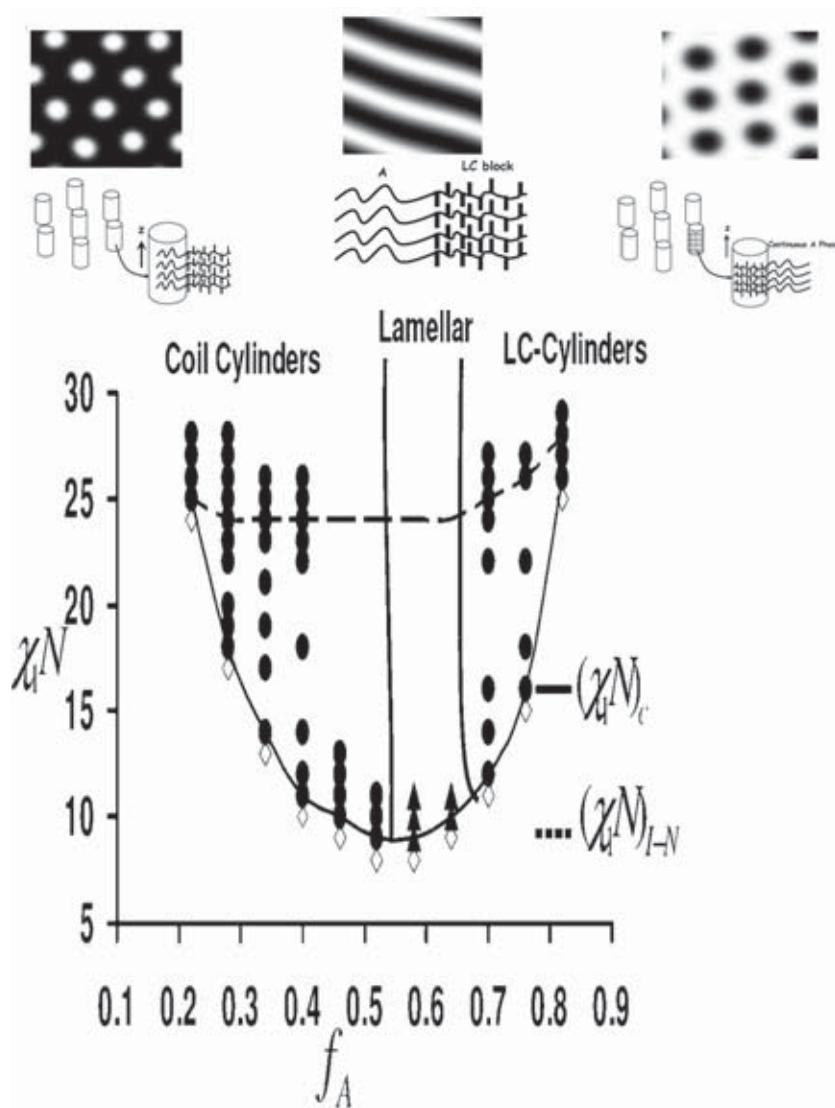


Figure 2.8: The phase diagram for a side-chain liquid crystal BCP predicted by self-consistent field theory [68].

themselves with the cylinder axis perpendicular to the shear direction and in the plane of the shear. This is known as the transverse orientation and the smectic A mesogens were parallel to the cylinder axis. If the BCP was mechanically sheared above the smectic to isotropic transition the cylinders would reorient to parallel to the shear direction. Four possible models are proposed for the side-chain liquid crystal BCP systems when the liquid crystal forms the matrix. In figure 2.9, the parallel-transverse, perpendicular-transverse, parallel-parallel, and transverse-perpendicular structures are possible. The nomenclature is based on the orientation of the cylinder axis with respect to the shear direction and the second word tells the direction of the smectic layers. Of these configurations the transverse-perpendicular orientation is the most favorable morphology. The morphology is a compromise between smectic ordering and BCP orientation. The transverse-perpendicular orientation does not strain the smectic layers or the BCP cylinders, while the liquid crystal mesogens can align parallel to the cylinder axis.

Switching from covalently bound liquid crystal mesogens to noncovalently bound small molecules blended with a polymers results in supramolecular structures. The noncovalent interactions such as ionic interactions, metal coordination, and hydrogen bonding between polymer and low molecular weight surfactants leads to 1 nm to 5 nm structures [11, 69–77]. In general, poly(acrylic acid) (PAA), poly(4-vinyl pyridine) (PVP), poly(vinyl phenol), poly(ethylene oxide) (PEO), and polysiloxanes (POS) form the backbone to which the small molecules can attach. Two factors that influence the formation of these mesomorphic structures are the strength of bonding between the polymer and small molecule, and the stronger polar-nonpolar interactions between the two small molecules [78]. The result is a hierarchical structure-in-structure morphology as shown in figure 2.10.

Determination of the comb-coil BCP phase behavior with respect to a small molecule, PS-b-PVP was blended with 3-pentadecyl phenol and methanesulfonic acid

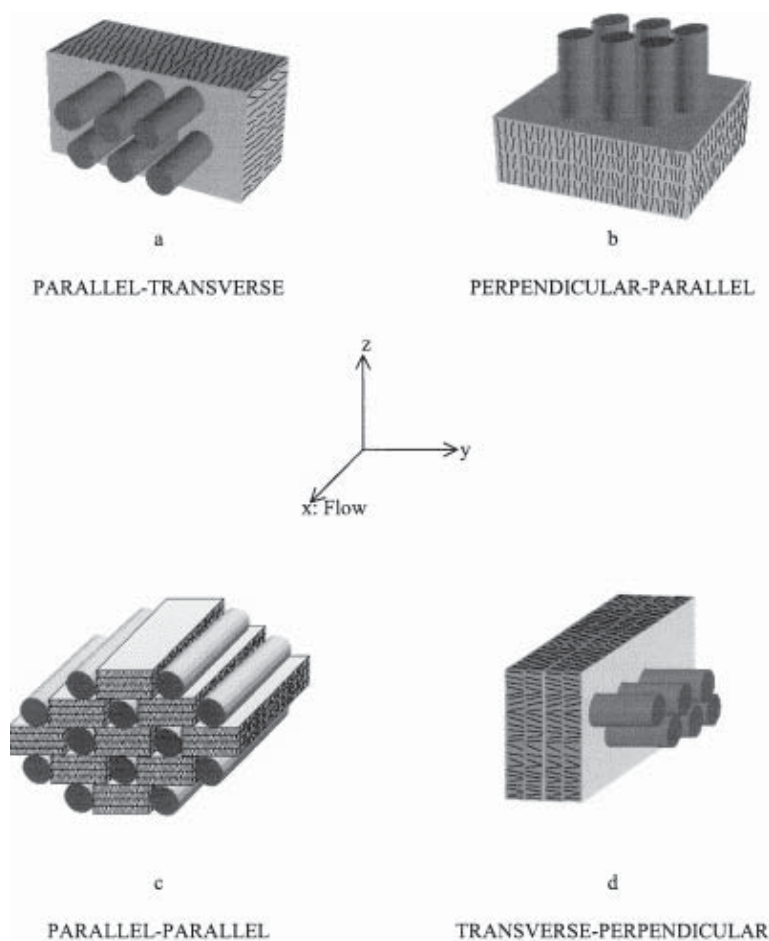


Figure 2.9: The four possible BCP and smectic layer orientations in a cylinder-forming side-chain liquid crystal BCP [57].

(MSA) [73–75, 80–82]. The structure of both systems was investigated as a function of the weight fraction of the small molecule and temperature. The different ordering length scales involved, resulted in unique hierarchical structures in every case. The BCP organized on the 10 nm to 100 nm length scale while the small molecule organized on the 1 nm to 5 nm length scale resulted in lamellae-in-lamellae, lamellae-in-cylinders, lamellae-in-hexagonally perforated layers, and lamellae-in-spheres. The first word refers to the morphology at the 1 nm to 5 nm scale while the second word refers to the morphology at the 10 nm to 100 nm scale. The authors observed

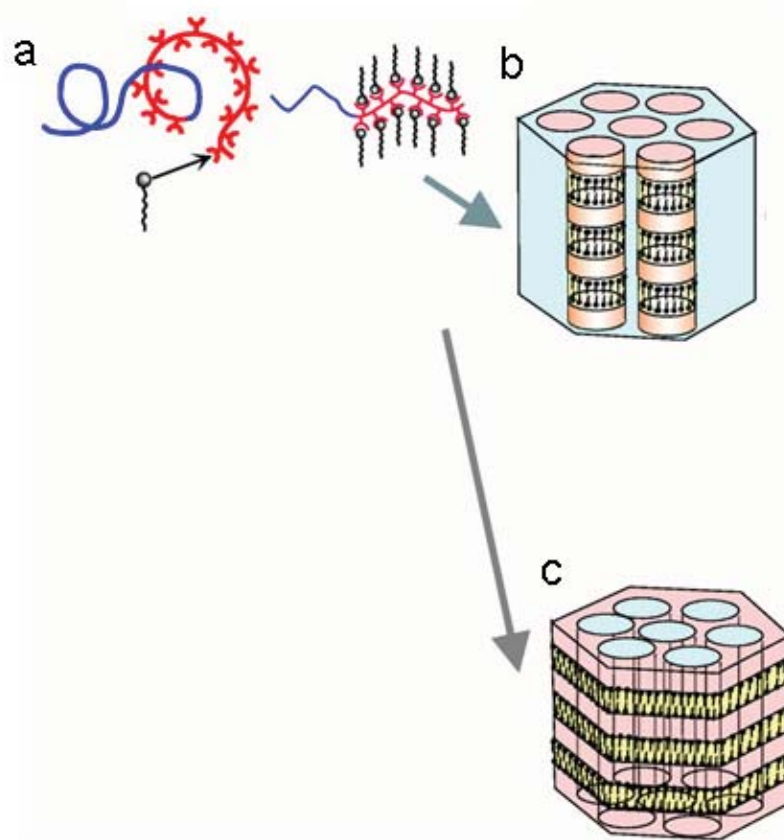


Figure 2.10: Comb-coil BCP and their hierarchical self-organization that results from self-assembly of small molecules and BCP (a) is an arbitrarily defined primary structure for the BCP. The resulting molecular recognition and microphase separation results in hierarchical structures (b and c) [79].

that multiple transitions took place when samples blended with 3-pentadecyl phenol were heated. At  $60^{\circ}\text{C}$  3-pentadecyl phenol disassociates from the BCP backbone resulting in an order-to-disorder transition for the small molecules while the BCP lamellar structure was maintained. When the temperature went above  $120^{\circ}\text{C}$  the 3-pentadecyl phenol becomes soluble in the PS layer thereby resulting in the BCP structure to change to a cylinder structure. Above  $175^{\circ}\text{C}$ , the 3-pentadecyl phenol becomes insoluble in PVP but not in PS resulting in a spherical morphology regardless of the net BCP architecture. The resulting order-to-order transitions diverge greatly from the coil-coil BCP systems.

The design of supramolecular materials for dynamic and functional response is a promising area of research because of the ease with which complex architectures can be formed and deformed. Photonic crystals fabricated using comb-coil BCP demonstrates the complex behavior of noncovalent interactions in BCP systems [81]. PS-*b*-PVP and MSA/3-pentadecyl phenol were blended to form a lamellae-in-lamellae structure of PVP/MSA and PS. The one-dimensional structure reflected/diffracted light at approximately 460 nm [81]. The overall size of the domain was greater than 100 nm and can be attributed to the chain stretching of PVP and PS. The authors further demonstrated the tunability of the lamellar BCP structure by heating and cooling the samples. At the temperature where 3-pentadecyl phenol becomes soluble in PS, a thermal switch to shorter wavelengths was observed due to the relaxation of the BCP chains. Thus a hierarchical self-assembled structure was fabricated with complex thermo-optical switching.

In summary of self-assembling hierarchical structures, the association of liquid crystals and BCP by either main-chain, side-chain covalently bound mesogens or side-chain noncovalently bound mesogens results in liquid crystal ordering occurs at the 1 nm to 10 nm length scale, while the dimension of the BCP microphase separation is on the order of 10 nm to 100 nm. The design criteria for constructing

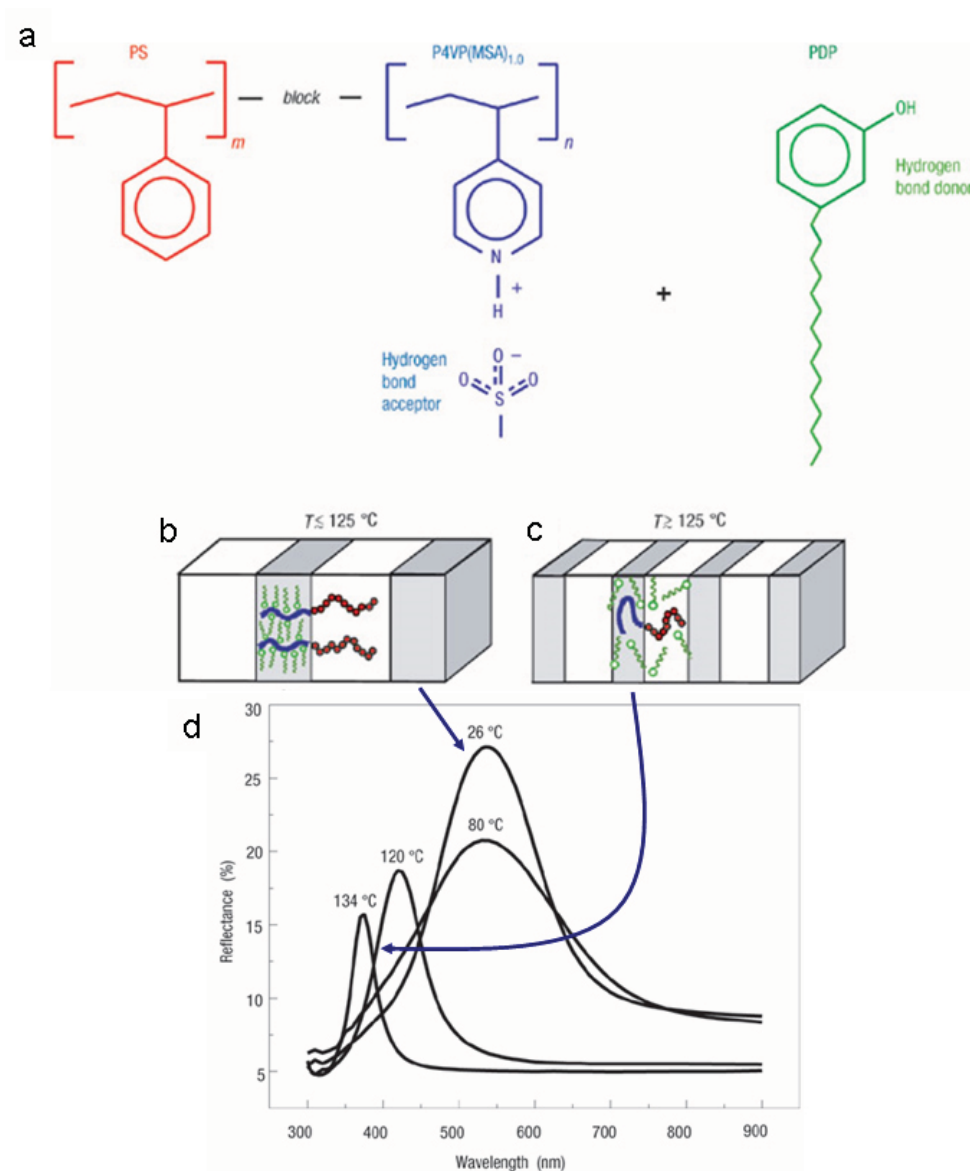


Figure 2.11: (a) A comb-coil BCP selected to induce structural hierarchy. (b) At room temperature the small molecules are confined to the PVP and the sample reflects green light. (c) When the sample is heated to above  $125^\circ\text{C}$  the grating wavelength blue-shifts and the intensity decrease because the small molecule dissociates and becomes a non-specific solvent for PS and P4VP/MSA [81].

hierarchical self-assembled structures is complicated by the competition between the ordering mechanisms at the two length scales. These complexities of behavior and structure are important in order to realize the potential of self-assembled hierarchical structures as advanced materials.

## 2.4 Top-Down and Bottom-Up Combined Nanoscale Fabrication

Hierarchical structures in synthetic systems are still not well understood. In contrast bone, butterfly wings, and diatoms are examples of biological systems that tend to possess a hierarchical structure that can lead to extraordinary mechanical, optical, and physical properties. Biological hierarchical structures are constructed through an all bottom-up approach. An example of self-assembling biological structures can be observed in the hard components of diatoms, as shown in figure 2.12. The control that diatoms demonstrate in the formation of their shell is desired in synthetic systems [83]. Though much work has been done on increasing our knowledge of self-assembling hierarchical structures, we are not at the point of completely fabricating by self-assembly [50]. The hierarchical structures reviewed before illustrates the need for precise molecular design of complex structures. There is also a need for hierarchical structures and fabrication routes that are nonspecific. This can be achieved by combining top-down techniques such as microcontact printing and holographic-patterning [84]. The complex morphology results in functional properties that diverge from conventional materials; for example the mechanical behavior of bone a hierarchical structure is superior to many conventional materials. The complex behavior in biological polymeric systems are the cumulative effect of the structures on different length scales [10]. These complexities are a result of fabrication techniques that combine structures over multiple length scales. The combination of fabrication techniques has resulted in a diverse number of structures that combine several different

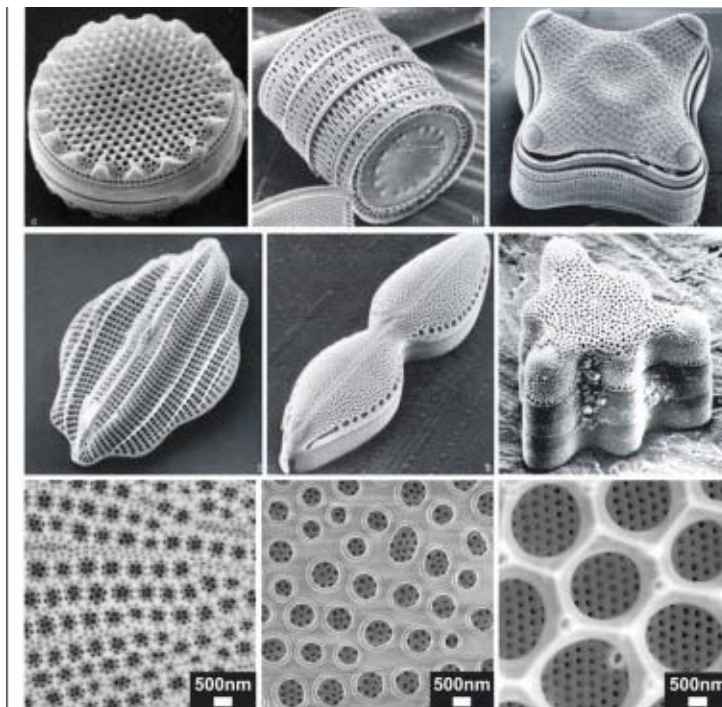


Figure 2.12: Examples of hierarchical structures in diatom cell walls as observed with scanning electron microscopy images of cell walls from different diatom species [85].

nanoscale processes. The physical and chemical interactions that aide in determining the structure and function of these hierarchical process are still being unraveled.

The numerous biological examples provide a starting point for developing synthetic hierarchical structures by combining nanoscale fabrication techniques. The goal of designing and developing hierarchical structures is to develop parallel and even novel materials. In the proceeding sections we will review the current literature on fabricating hierarchical structures from a combination of top-down and bottom-up methods. In the first section we will discuss the routes to forming hierarchical structures along with their advantages and disadvantages. In the second and third sections, the combination of nanofabrication techniques are described by the starting direction of the nanoscale fabrication technique. The first route to fabricating hierarchical structures starts with the top-down technique and then relies on sequestering

the BCP or colloidal crystal, known as external-in methods. The second strategy starts with the self-assembled layer and then uses a top-down technique to shape the hierarchical structure, this is called the internal-out method. The third strategy allows both fabrication techniques to be combined simultaneously and mutually exclusive.

#### **2.4.1 Fabricating Hierarchical Structures by Combining Nanofabrication Techniques**

The ability to construct a process flow scheme for fabricating hierarchical structures is an important part of building up from the nanoscale. If nanoscale fabrication processes are thought of as unit operations then the construction of hierarchical materials at the nanoscale requires a process flow chart for manufacturing. Two processes, BCP self-assembly and lithography were combined to demonstrate that integrated nanoscale devices can be manufactured [86]. Bal and researchers use a multistep lithographic fabrication process that incorporates the assembly of a diblock BCP during the assembly of a magnetoelectronic device [86]. A four-probe resistor was prepared using e-beam lithography on a poly(methyl methacrylate) (PMMA) resist, which was spin coated on top of a silicon substrate. The preformed pattern was then spin coated with a cylinder forming PS-b-PMMA as the template for growing nanowires. The films were annealed at an elevated temperature under an applied electric field to induce ordering of the BCP cylinders perpendicular to the substrate. The PMMA was then removed by selective etching and the PS was crosslinked using the e-beam. Cobalt was then electro-deposited to form nanowires. The close-packing of the cobalt nanowires formed from BCP templates were then probed for magnetoresistance. The nanoscale devices formed from the integrated nanoscale processes demonstrated that giant magnetic resistance can be achieved [86]. The ability to fabricate an electronically useful device using the combination of nanoscale methods is a powerful new approach to the design and implementation of self-assembly.

Nanoscale confined microdomains will have a significant impact on the BCP structure, orientation, number of periods, and placement accuracy. In order to achieve control over microdomain structure for design applications, a diverse number of nanoscale processes described in Table 2.1 can be combined. The combination of top-down and bottom-up techniques was demonstrated by three research groups in 2003 and early 2004 as a method to control self-assembly [7, 83, 87]. We can expect one of three possible outcomes when we combine two or more fabrication techniques. First, the two techniques are incompatible for forming hierarchical structures. In this case, no hierarchical structure was formed. Second, the two techniques can be combined and the hierarchical structure is the summation of the techniques. Pai used a combination of lithography and BCP self-assembly to fabricate mesoporous silicates with a hierarchical structure to mimic the organosilicate structures of diatoms. Pai presented a generic multistep technique for fabricating hierarchical structure by combining commercially available BCP surfactants with photolithography to form structured mesoporous silicate templates [83]. The BCP was first spin coated onto a silicon substrate then impregnated with silica precursor, which was then selectively condensed by UV lithography [83]. The sample was then reduced in the presence of super critical carbon dioxide [83]. The resulting silicate structure possessed hexagonally packed cylinders with long range ordering at the interface between exposed and unexposed regions [83]. Third, the combination of the two nanoscale fabrication techniques results in one technique influencing the morphology and structure of the other technique [7]. Kim and researchers demonstrated that molecular level epitaxy was effective on larger length scales. This was achieved by lithographically defining a substrate so that the BCP with a comensurate structure could self-assemble in a controlled fashion. A direct consequence of this scenario is that some hierarchical fabrication techniques are path dependent while others are path independent.

The early combination of top-down and bottom-up methods demonstrates that

both directions have their advantages and disadvantages. In the top-down method the confinement of the self-assembling material can be detrimental to the microdomains, while the microdomains in the bottom-up approach are conserved but registration and interface of the domains are sacrificed. Yuan and coworkers demonstrated the hierarchical structure when top-down and bottom-up were combined regardless of where they started [88]. In that work a hierarchical pattern of iron nanoparticles was achieved by combining BCP micelle self-assembly and microcontact lithography [88]. The authors compared micropatterning substrates versus the microcontact stamping using poly(dimethylsiloxane) (PDMS) as the resist and the stamp [88]. In the first method, a simple one-dimensional photoresist composed of PDMS on silicon was used as the stamp, shown in the schematic diagram of figure 2.13 (right side) [88]. Subsequently, PS-b-PVP micelles in toluene were loaded with iron (III) chloride and spin coated onto the stamp. The loaded substrate was then exposed to oxygen plasma to form iron nanoparticles on the silicon substrate [88]. In the second method, a simple one-dimensional PDMS stamp was fabricated and the PS-b-PVP loaded with iron (III) chloride was spin coated onto the stamp, shown in figure 2.13(left side) [88]. The stamp was then placed in contact with the silicon substrate [88]. The loaded substrate was then again exposed to oxygen plasma [88]. Both methods led to hierarchical structures with aperiodic assembly of nanoparticles inside domains with a periodicity of approximately two microns. However, similar defects arose at the interface even though different mechanisms to those imperfections were attributed to the problems. The results provide evidence that some nanoscale processes can be thought of as directionally independent. The microdomains and interface of both techniques were investigated and compared [88]. Yun and coworkers observed that micropatterning of micelles led to an accumulation of nanoparticles at the edge of the microdomains [88]. They attributed the variations to the thickness of the pattern and tried two different thickness, 1.4 microns and 200 nm. A more uniform dispersion of nanoparticles was

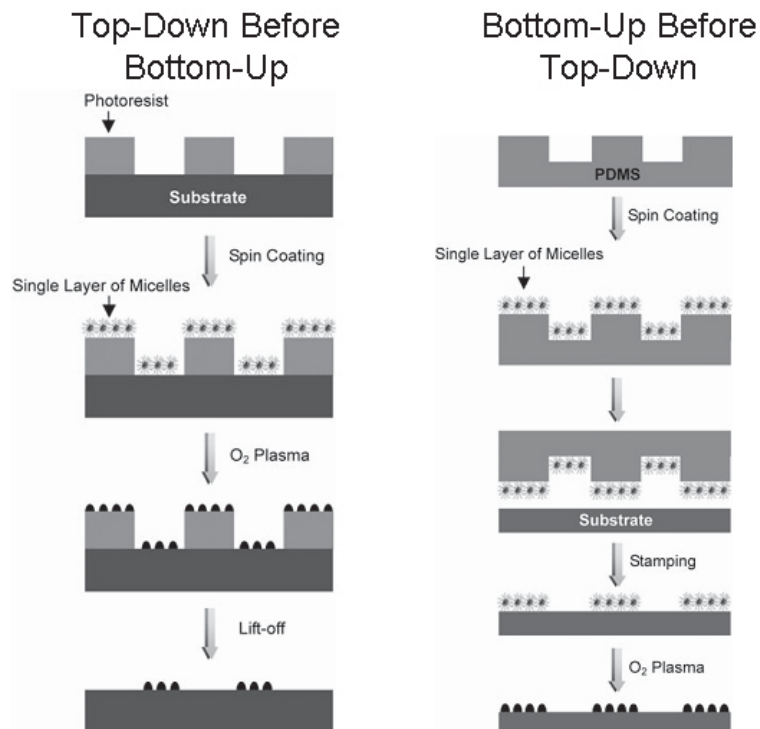


Figure 2.13: Schematic diagram comparing the procedure for a top-down method before bottom-up (left side) against a bottom-up method before top-down (right side) that was used to arrange nanoparticles from a combined lithography and thin layer of BCP micelles [88].

obtained with the reduction in thickness, but not eliminated. In the other case, the microcontact printing of iron precursor micelles, on a PDMS stamp with two micron thick parallel lines, results in a similar structure for the microdomains at the center and interface [88]. The discrepancies in the distribution of nanoparticles could be attributed to the small geometrical distortions in the stamp or pattern thickness at the edge and ridge [88]. These small geometric distortions reduced the quality of the hierarchical structure.

### 2.4.1.1 External-In Methods to Forming Hierarchical Structures

The ability to control the morphology by confining self-assembled colloidal crystals and BCP was shown in the previous section. This section investigates the confinement of self-assembling materials into microdomains by first applying the top-down technique before the bottom-up technique. Hierarchical structures fabricated by using top-down techniques to sequester and control the self-assembling material can be fabricated in both colloidal particles or BCP. Using the top-down before the bottom-up method provides control over microdomain registration and orientation (the external-in method), which is useful when spatially distributing self-assembling materials. As a result, the physically confined self-assembly is impacted by the confining walls chemical nature and geometry.

One example of an external-in method was demonstrated by combining polymer micelles and e-beam lithography. Spatz and researchers demonstrated that the combination of self-organized 7 nm gold nanoparticles micelles and e-beam lithography organized the nanoparticles inside 200 nm holes. The lithographically defined holes were spaced 2 microns apart, which resulted in the precise placement of nanoparticles [89]. The hierarchical structure was achieved by preparing metal nanoparticles of gold within the core of PS-*b*-PVP BCP micelles [90]. The amphiphilic BCP micelles containing the nanoparticles were then spin cast onto the pre-patterned silicon substrate. The loaded substrate was dipped in acetone to remove the resist and excess nanoparticles leaving only the nanoparticles that were in contact with the substrate [89]. Figure 2.14 shows a dark-field optical microscopic image that demonstrates the fabrication of a two-dimensional square array of micelles. It was observed that the loaded substrate trapped micelles in both grooved and dimpled geometries [89]. The micelles are pulled in and positioned in the pre-patterned geometries by capillary forces [91, 92]. The number of micelles trapped in each hole

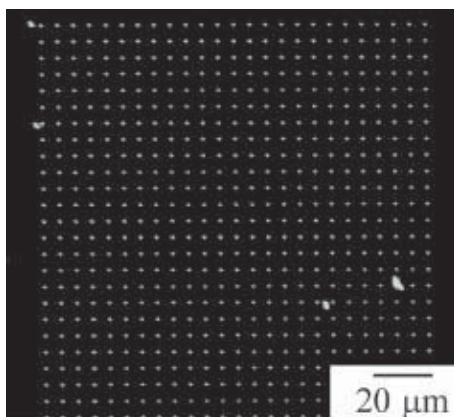


Figure 2.14: Optical dark-field microscopy image of a square array of BCP micelles on a lithographically defined substrate [89].

or line is dependent on the confining geometry as in the colloidal particle confinement work of Xia and coworkers [93]. The thickness of the resist and dimensions of the patterned features will determine the number of nanoparticles that are confined within a single microdomain. The accuracy of placing nanoparticles on substrate surfaces with combined top-down and bottom-up techniques was then investigated using atomic force microscopy (Figure 2.15) [89]. The AFM height profile in figure 2.15 shows that a single micelle loaded with gold nanoparticles was deposited in each hole of photo resist. The holes were arranged in a two-dimensional square geometry with 2 micron spacing [89]. The accuracy of nanoparticle placement was determined to be better than 10 nm over 2 microns. This indicated that control over the microdomain structure should be attributed to both self-assembly and microfabrication techniques.

In addition to the work of Spatz and collaborators, Park and researchers demonstrated that a hierarchical porous structure can be fabricated by applying a grating to confine droplets of water [94]. A hexagonal close-packed array of water droplets with uniform size was fabricated from a template and solution processing tech-

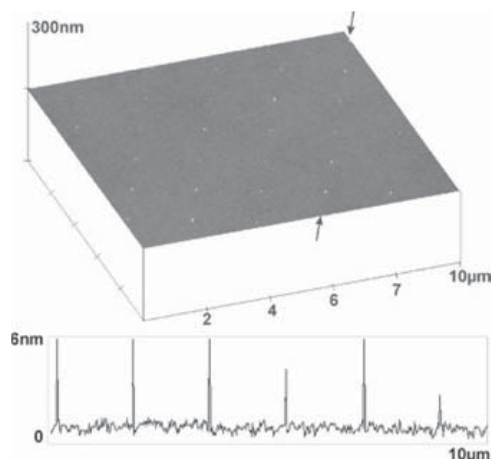


Figure 2.15: AFM image and height profile of a square array of BCP micelles on a lithographically defined substrate [89].

nique, known as breath figures [94]. Breath figures are facile method to fabricate two-dimensional porous polymer structures, where by the condensation of water or any other suitable solvent on a cold surface results in spotanious ordering of the droplets [95]. The typical morphology of polymers that have been patterned with the breath figure technique is shown in figure 2.16. The holes are due to the condensation of water on the surface of a benzene/PS solution. In figure 2.16 there are also two grain boundaries at the lower left and upper right hand corners. In order to control domain shape and limit defects for the breath figure technique, Park and colleagues were able to fabricate hierarchical structures by placing templates on top of a polymer solution, then exposed the solution to humid air [94]. The polymer solution contained PS ( $M_w$ :  $50 \frac{kg}{mol}$ ), benzene and varying amounts of the BCP PS-b-PEO. The humidity and flow rate was kept constant at 80% and 4 L/min at room temperature [94]. The condensation of water and evaporation of benzene resulted in two-dimensionally ordered hierarchical structures. The degree of ordering depended on the BCP concentration. The template was a crucial step in the formation of highly ordered porous structures [94]. If the solution was placed on top of the grating no

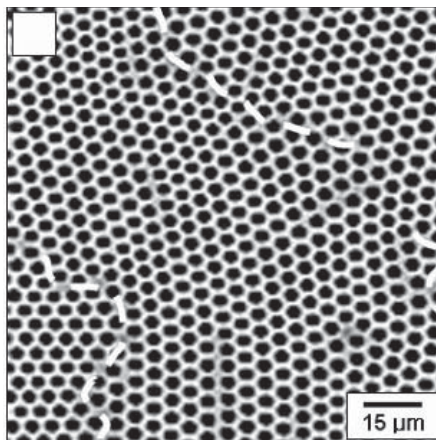


Figure 2.16: SEM micrograph of a polymer film that was patterned using the breath figure technique [94,95].

hierarchical structure would be observed indicating that the template was critical during the condensation stage of the droplet formation [94]. Floating the template on the polymer solution guided the aqueous droplets.

The closed-packed hexagonal array of aqueous droplets in the hierarchical structure was dependent on the concentration of the amphiphilic BCP [94]. Polymer solutions without amphiphilic BCP did not wet the template due to the hydrophobicity of the solution, which led to structures that were not well ordered [94]. The addition of a small amount of amphiphilic BCP decreased the contact angle between the template material and polymer solution indicating that the polymer solution was wetting the template [94]. The increased wetting decreases the convex meniscus that forms at the polymer solution air interface. The reduction in the meniscus limits the inhomogeneities during evaporation of solvent [96]. The surfactant also influences the size of the droplets and the number of grains in the porous membrane. The increase in BCP content results in a decrease in droplet size and an increase in grain boundaries [94]. The decrease in aqueous droplet size depends more on the BCP concentration than on the overall condensation rate as was first observed in BCP breath figures [97]. The

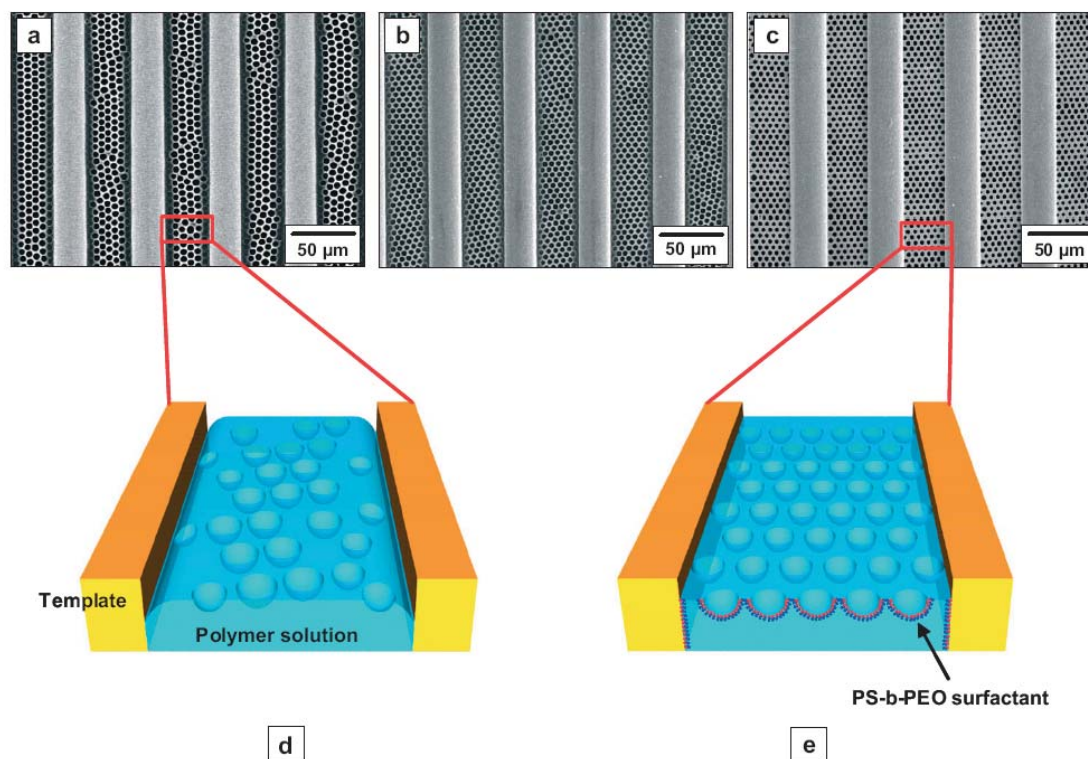


Figure 2.17: The effect of surfactant on the polymer solution to induce the highly ordered arrays of polymer holes confined between domain walls. The SEM images of the hierarchical structure formed by a) 4 wt% polymer solution without polymeric surfactant contains defects, b) 4 wt% polymer solution involving 0.4 wt% polymeric surfactant with less defects, and c) 4 wt% polymer solution and 0.8 wt% polymeric surfactant shows a defect free structure [94].

decrease in grain size in the bulk indicates that the increased ordering due to the BCP surfactant is due to the introduction of the template.

Park and coworkers also investigate the effect of microdomain geometry that is imposed on the self-assembling micelles [94]. Three different template geometries were used to investigate the effect that the microdomain geometry would have on the self-assembling material (shown in Figure 2.18). The self-assembly of micelles in hexagonal and linear microdomains showed good registration due to the micelles sharing one or more principle lattice directions [94]. When a square template was

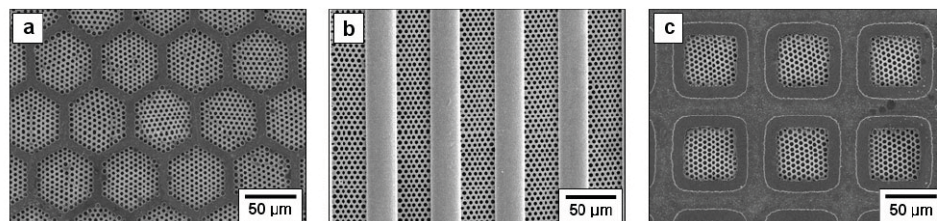


Figure 2.18: The SEM micrographs demonstrate the impact of confining geometry shape on the self-assembly of breath figures. a) Image of hierarchical structure fabricated using a hexagonal grating, b) a parallel grating and c) a square grating [94].

used, the registration was poor due to lattice mismatch between the template and micelles [94]. They concluded that the micelles were able to self-assemble with fewer defects when the colloidal crystal principle lattice directions matched with one or more of the confining directions [94].

Finally, the external-in technique fabricated hierarchical nanoscale structures form hexagonal arrangements of BCP droplets using controlled dewetting on prepatterned substrates [98]. A highly ordered nanostructure was fabricated by combining microcontact printing self-assembled monolayers on a substrate followed by spin coating a solution containing PS-*b*-PEO [98]. The BCP was spin coated onto the prepatterned substrate and subsequently annealed in a vapor of benzene and water [98]. Figure 2.19 shows an outline of the the procedure for hierarchical fabrication of hexagonally arranged BCP droplets by controlled dewetting. The final structure shows order over two length scales (Figure 2.19). The hexagonal distribution of convex BCP droplets regularly patterned over  $1 \text{ mm}^2$  are shown in figure 2.19. A single BCP droplet (Figure 2.19b) with a diameter of 4 microns contained a regular arrangement of the BCP domains (Figure 2.19c).

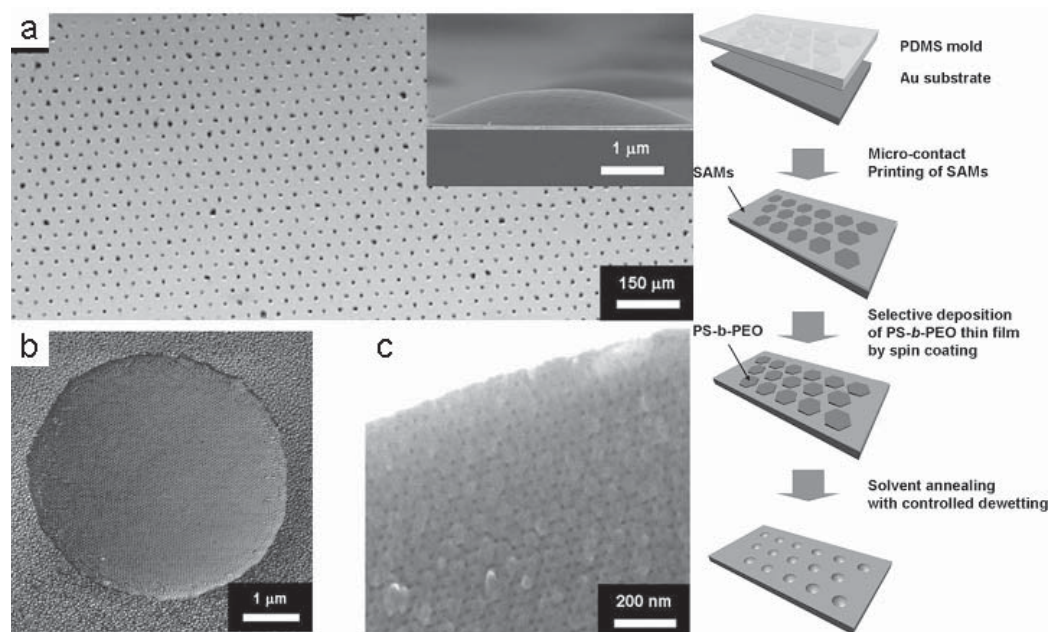


Figure 2.19: The procedure for hierarchical fabrication of hexagonally arranged BCP droplets by controlled dewetting of PS-*b*-PEO thin films upon solvent annealing by combining with microcontact printing lithography. The final structure showed order over two length scales, (a) the hexagonal distribution of BCP domains from controlled dewetting, (b) a single BCP domain showing a hexagonal arrangement of cylinders, and (c) a cross section of one of the BCP domains [98].

#### 2.4.1.2 Internal-Out Methods to Fabricating Hierarchical Structures

In contrast to the previous section, hierarchical structure can be fabricated by sculpting self-assembled layers. The bottom-up method before top-down can prevent unwanted or unnecessary confinement effects as well as enable layer-by-layer sculpting of single colloidal crystals. A hierarchical array of nanopores was fabricated from the assembly of a monolayer colloidal crystal and used in combination with photolithography [99]. The colloidal particles were composed of poly(styrene-co-glycidyl methacrylate), which can be crosslinked under UV-radiation. These particles self-assembled into a monolayer on a silicon substrate [99]. The monolayer of the colloidal crystal was then photo-patterned resulting in some particles being crosslinked [99]. The substrate

is then baked to deform the unpolymerized colloidal particles while the polymerized particles retained their shape [99]. The patterned colloidal particle array was used as a mask for reactive ion etching of the silicon substrate to transfer the hierarchical pattern from the template to the substrate [99]. The result was a hexagonal arrangement of holes in silicon with a microdomain period of 10 microns [99].

Another hierarchical structure was fabricated from a combination of bottom-up combined with top-down using micelles and e-beam lithography. Monomicellar films were prepared by dipping a silicon wafer into a solution containing PS-b-PVP BCP solution [100]. The self-assembled monolayer inter-particle domain spacing was controlled by using different molecular weight BCP [100]. The thin films were then washed with a solution containing  $\text{HAuCl}_4$  [100]. The micelles arranged themselves in a hexagonal structure. The quality of the self-assembled monolayer of micelles reduced with increasing the overall molecular weight. Meanwhile, the quality of the structure increased after hydrogen plasma treatment removed the polymer and deposited the nanoparticles on the silicon substrate [100]. Nanoparticles of 2, 5, 6 or 8 nm were fabricated in this way as observed in the SEM micrographs, figure 2.20. In order to pattern the assembled monolayer of micelles, a focused e-beam in an SEM was used to crosslink the PS on the substrate with squares, circles, and ring geometries. The unexposed regions are removed and the patterned substrate is exposed to hydrogen plasma to form gold nanoparticles [100]. The subsequent hierarchical structure should then have microdomains that are not influenced by the confining geometry of the domain walls as was the case in the external-out method [94]. The interface of the microdomain geometries was also investigated in these hierarchical structure. The micelles at the boundary of the e-beam exposed areas seemed to contain smaller or no nanoparticles at all, figure 2.20 [100]. The partial crosslinking of the PS-region of the BCP domains at the boundary of the e-beam lithographically defined regions, resulted in a washout of the gold chloride [100]. This washout reduced the quality of

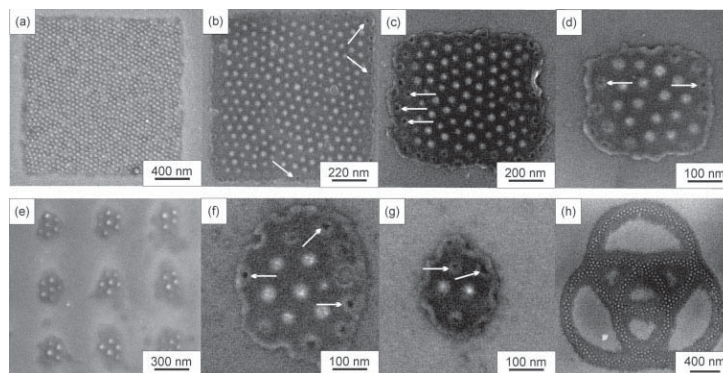


Figure 2.20: SEM micrographs of a variety of lithographically patterned regions containing gold nanoparticles [100].

the lithographically defined domains and became more of a problem as the ratio of perimeter length to surface area increased. These effects resulted in discrepancies in the size of the nano particles at the interface and interior, which detracts from the overall performance that is gained from using the internal-out method [100].

The internal-out technique was extended further to quasi three-dimensional hierarchical structures by removing self-assembled colloidal particles using a layer-by-layer microcontact printing technique [101]. The technique uses soft lithography to pattern colloidal crystal microdomains by selective removal of particles one layer at a time [101]. The self-assembled colloidal crystal contained silica microspheres ranging in size from 231 nm to 321 nm on a silicon substrate [101]. In order to pattern the colloidal crystal, a PDMS stamp with a prescribed pattern was brought into contact with colloidal crystal at  $100^{\circ}\text{C}$  [101]. The lift-up technique was applied several times until the desired geometry could be obtained [101]. The combination demonstrates that self-assembling colloidal particles before microcontact printing results in a hierarchical structure [101]. The layer-by-layer control over the microstructure of the colloidal crystal was realized by selective transfer of a single layer of close-packed microspheres from the crystal film to the PDMS stamp surface [101]. Figure 2.21

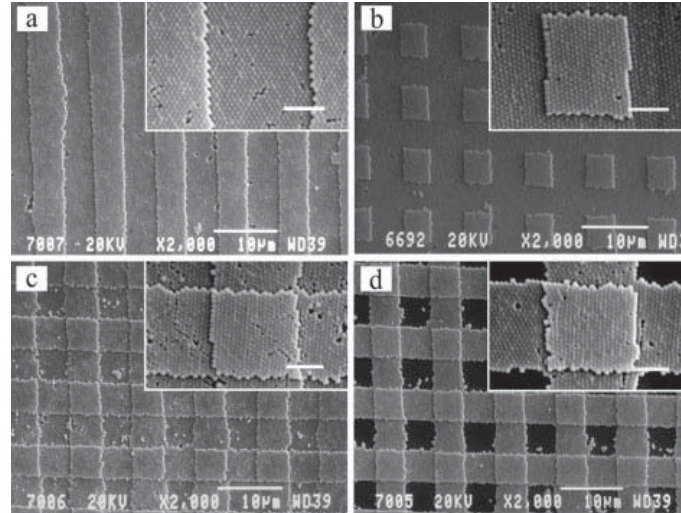


Figure 2.21: The sculpting of a colloidal crystal by lift-off microcontact printing. (a) a one-dimensional structure stamped into the colloidal crystal. (b) a two-dimensional structure by rotation of the PDMS stamp in a two step microcontact printing process. (c) and (d) a quasi three-dimensional basket weave pattern obtained by multistep microcontact printing [101].

demonstrates the quasi three-dimensional pattern by multiple microcontact printing steps. The flexibility of the PDMS stamp was used to demonstrate that the microstructure could be controlled using a two-step removal of the particles by the contact printing method [101]. The first step removed the top layer of colloidal crystals to form a trench in the crystal [101]. In the second step, the PDMS stamp was rotated  $90^\circ$  and brought in contact with the colloidal crystal with a pressure of  $0.2 \times 10^5$  Pa [101]. At this pressure only the top layer of particles were removed to form a two-dimensional square array of close-packed colloidal crystals (Figure 2.21) [101]. A weaved pattern was obtained when the pressure was increased to  $1 \times 10^5$  Pa (Figure 2.21) because the PDMS stamp conforms to the height differences of the colloidal crystal during the stamping process [101]. Using microcontact printing the topological features of hierarchical structures can be controlled by changing the orientation and pressure applied to the self-assembled colloidal crystal.

### 2.4.1.3 Parallel Fabrication of Hierarchical Structures

In earlier sections the external-in and internal-out methods for obtaining hierarchical structures resulted in one nanoscale ordering process influencing the other regardless of the direction of nanoscale fabrication. Yet, as we discussed earlier top-down and bottom-up can be combined in such away that the two techniques do not interfere with one another. The Liebler group demonstrated that this combination of top-down and bottom-up nanomanufacturing could be achieved using soft lithography and self-assembly of nanowires. Orientational order was induced using surface compression of surfactant stabilized nanowires that were dispersed in a Langmuir-Blodgett trough [87]. The aligned nanotubes where then transfered to a patterned substrate with a square array of square hydrophobic domains [87]. The nanowires are collected on the surface then sonicated to remove nanotubes that were not in contact with the hydrophobic regions [87]. The combination of top-down and bottom-up techniques used in parallel demonstrates the advantage of both techniques to orient and control the spatial arrangement of nanowires.

Another example of combining nanostructures in parallel resulted in a hierarchical plasmonic mask. The researchers combined interference lithography and BCP self-assembly with nanoparticles to fabricate two-dimensional in two-dimensional hierarchical structures [102]. The plasmonic mask was then used to fabricate a hierarchical two-dimensional in two-dimensional photoresist [102]. The fabrication of the plasmonic mask was accomplished using a multistep fabrication technique that included interference lithography and BCP micelles of PS-b-PVP shown in figure 2.22 [102]. A hexagonal surface relief pattern was fabricated by using a periodic one-dimensional standing wave interference pattern that occurred perpendicular to the substrate surface [102]. Three exposures were used with a  $60^\circ$  rotation between each exposure to fabricate the hexagonal structure. BCP spherical micelles were then solution cast

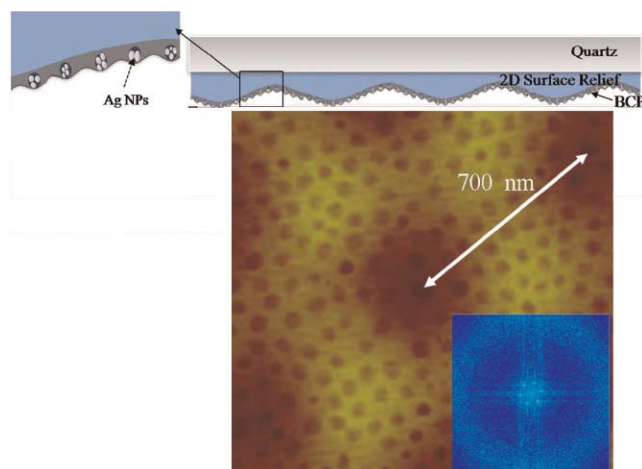


Figure 2.22: At the top of the figure is an illustration of a two-dimensional surface relief grating covered by a thin film of BCP. Bottom of the figure is an atomic force micrograph and fast fourier transform of a hierarchical two-dimensional in two-dimensional structure in photoresist that resulted from the parallel assembly of nanoscale fabrication techniques.

onto the exposed substrate and soaked in a silver nitrate solution. The solution and substrate were reduced with sodium borohydrate and washed [102]. The clusters of silver particles were confined to the PVP domains and the BCP displayed a hexagonal morphology [102]. The two-dimensional hexagonal array of the interference pattern combined with the two-dimensional array of BCP micelles results in a hierarchical structure, figure 2.22 [102]. The fabrication route to form the hierarchical structure can be considered to occur in parallel, since the two steps do not influence one another.

## 2.5 Confinement of Self-Assembling Nanostructures

The microdomains in the fabrication of hierarchical structures is a major concern to the overall quality. This is due to the intrinsic problem of self-assembly, namely its inability to form long range ordered structures due to thermal fluctuations and polydispersity [14]. To overcome these limitations top-down was used to help bottom-

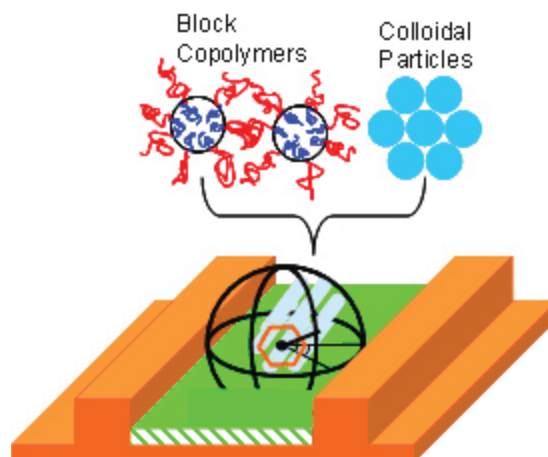


Figure 2.23: BCP and colloidal nanoparticles self-assembling inside narrow substrates. [4].

up [4]. The confinement of self-assembly to areas or small regions using top-down techniques is also important to the fabrication of hierarchical structures. Figure 2.23 depicts the general features of templated self-assembly. In the rest of this section the confinement of BCP are discussed.

The ability for BCP and colloidal particles to self-assemble in confined spaces between 5 nm to 5000 nm presents many advantages over conventional nanofabrication including smaller feature sizes. This has led researchers to identify several design considerations that are needed to control the structure, orientation, ordering, persistence length, epitaxy, and registration [4, 5]. The interplay of these variables within the confining geometry will dictate the use of the self-assembling systems in the manufacturing of devices.

### 2.5.1 Structure

The confinement of BCP and Nanoparticles between hard domain walls become more important as the width of the domain shrinks. The packing of colloidal crystals was studied extensively by Xia [93]. The morphologies that were observed were dependent

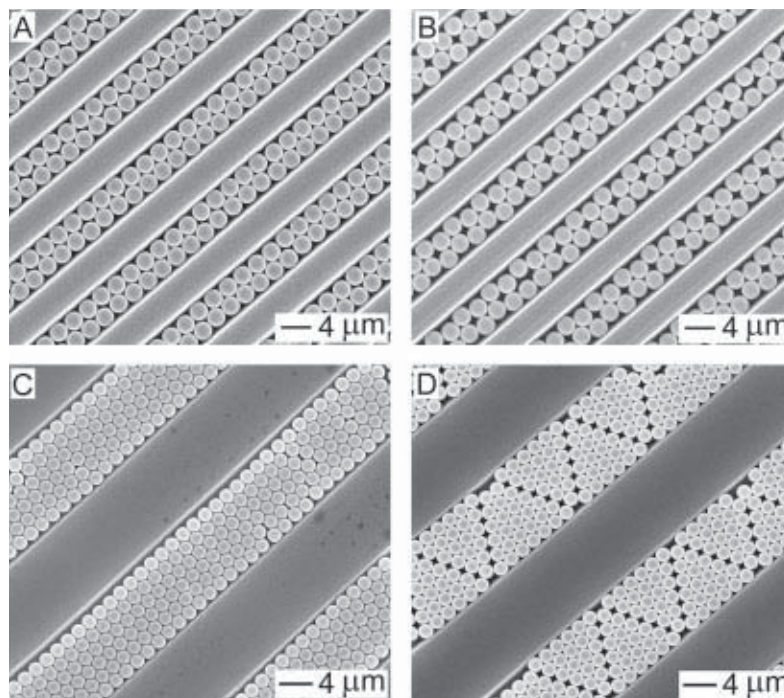


Figure 2.24: SEM images of a single layer of colloidal particles in a lithographically defined substrate. (A) and (C) are the images of a colloidal crystal when the confining geometry is commensurate. (B) and (D) are the images when the size of the well is not commensurate with the dimensions of the colloidal crystals. [93].

on the size of the colloidal particles in relation to the confining geometry, shown in figure 2.24. In figure 2.24, the size of the confinement directly influences the number of particles and as a result the assembly of the colloidal particles. The parameters that influence the morphology in these cases include, interactions between the components, the rigidity of the self-assembling material, the surface energies of the components, and the interactions with the substrate [103]. The hard sphere morphology of colloidal particles results in ordered structures with interesting morphologies. Similar interactions occur when BCP are confined.

The behavior of a BCP is similar to the colloidal crystals in confined geometries. The confinement of a BCP between two parallel plates was studied in depth by researchers in the late nineties [104–107]. Each lamellar layer is composed of two

linear copolymer chains and any number of layers was confined between two flat surfaces. The orientation of the lamellar BCP and BCP period was influenced when the width of the domain was below a threshold confinement length [106]. Later work extended this idea to include spherical and cylindrical domains [6, 108]. The configurations with a half-odd-integer number of layers occurred when the difference between the two polymer surface tensions are small and only below some critical plate separation thickness [6]. Below the threshold length, confinement of the colloidal particles and BCP were observed as integer multiples of their periods as shown in figure 2.25 A [6]. The step-wise function of the number of periods is dependent on the strain and potential energy associated with the confining walls shown in figure 2.25 B [6]. If only a small number of periods are confined, the energy penalty for inserting or deleting a row is large, as seen in figure 2.25 C [6]. However, as the width of the domain increases the energy penalty decreases and coexistence of plus or minus one row can exist. Coexistence is also the result of imperfections in the size and shapes of the domains and the surface ruffness [108].

On most surfaces BCP will tend to prefer one block to interact with the substrate due to the lower surface energy of one component, which imbibes a segregation of one block to the substrate or surface [109]. The interactions between the BCP and domain wall can be tuned by copolymerizing the same chemical constituents on the substrate surface [110]. A random copolymer mixture of the BCP components can then be used to control the interaction of the BCP with the domain walls. The surface modified with a random copolymer then results in a mutually weak interaction between both of the blocks in the BCP and the domain walls. The orientation of BCP then depends on film thickness and both perpendicular and parallel orientation with respect to the domain walls can be observed [110–113]. The dependence of thickness on the orientation is due to the configurational restrictions that force the BCP to orient perpendicular to non-preferential interfaces [111]. However, strong interactions with

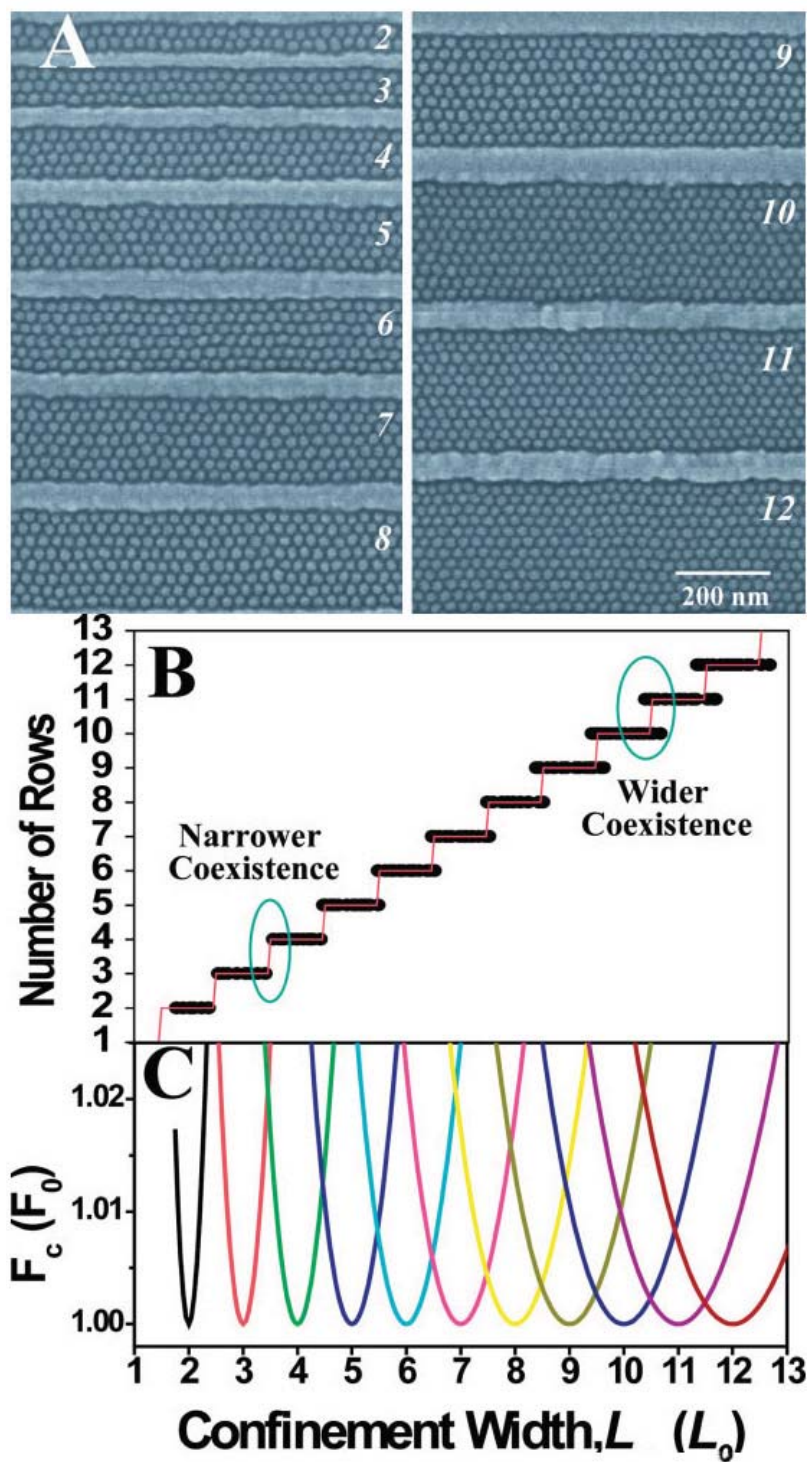


Figure 2.25: The confinement of PS-b-polyferrocenyldimethylsilane in A) templates of various widths, B) a plot of the number of rows versus the confinement width of the channel in A, and C) the free energy per polymer chain of the confined array of spheres with respect to the confinement width of the channel [6].

one block will favor the BCP domains to orient themselves parallel to the domain walls [114]. This dependence of the BCP morphologies on the surface properties can result in a wide range of morphologies depending on the curvature of the confining surface [115–117].

The confinement of self-assembling BCP in curved geometries becomes more extraordinary due to the additional compensatory elements needed to account for curvature constraints. The interaction of a BCP in a nonplanar surfaces, such as a cylinder can have an impact on the periodicity, morphology, and symmetry of the BCP. Cylindrical confinement of lamellar BCP results in a coaxial arrangement of lamellae at large values for the diameter of the confining geometry (Figure 2.26) [115, 116, 118]. As the diameter decreases incommensurability and strong curvature imposed on the BCP causes the morphology to change from curved lamellae to toroidal-type structures [119]. The morphology of cylinder-forming BCP confined within cylinders results in toroidal and helical features [120]. At large diameters the BCP cylinders align parallel to the tube axis; as the diameter shrinks stacked donuts and helical morphologies were observed [120]. In spherical confinement, the volume fraction of the block plays an important role in the morphology as the BCP is confined. A BCP that forms a gyroid or cylinder phase in bulk can become disordered or forms complex structures when the diameter of the confining wall is small [121, 122].

### 2.5.2 Placement Accuracy and Registration

Cheng and researchers addressed the accuracy of self-assembled BCP under confinement [123]. The correlation of spherical BCP domains cast into a thin film will decay exponentially, which is a characteristic of soft matter. Figure 2.27 A is a graph of the pair distribution fluctuations, which is the correlation of two particles some distance apart. The decay of the peaks in the graph is due to the random fluctu-

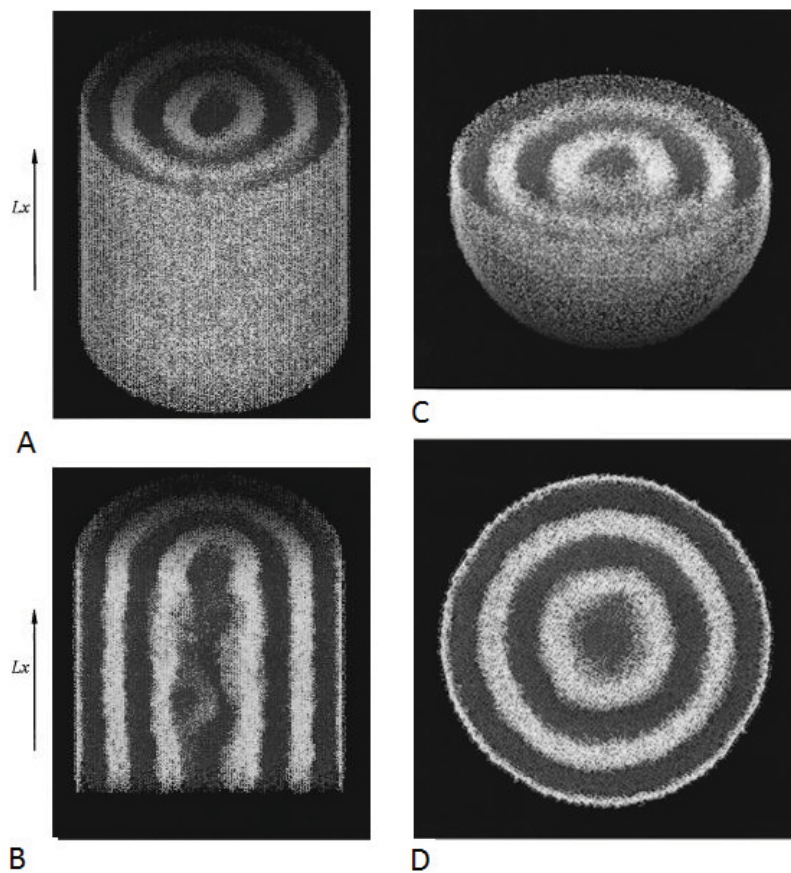


Figure 2.26: Morphological pattern of a lamellar forming BCP under (A) cylindrical confinement and (B) its cross sectional structure. The morphology of a lamellar BCP under (C) spherical confinement and (D) its cross sectional structure [115].

ations of PS-*b*-polyferrocenyldimethylsilane spherical domains. The same BCP in a one-dimensional well self-assembled with a domain position relative to the wall that exceeded 35 periods with a standard deviation of approximately a tenth of the period length, which can be observed in figure 2.27B. This indicates that soft matter can be defect free in confined spaces [123]. Errors in confinement of colloidal crystals and BCP originate from the confining boundaries surface roughness and spacing variations of the microdomains [123]. These two sources of errors ensure that a defect will be propagated into the self-assembling domain, but the small domain-domain potential energy absorbs the additional interfacial energy that has been created dampening the

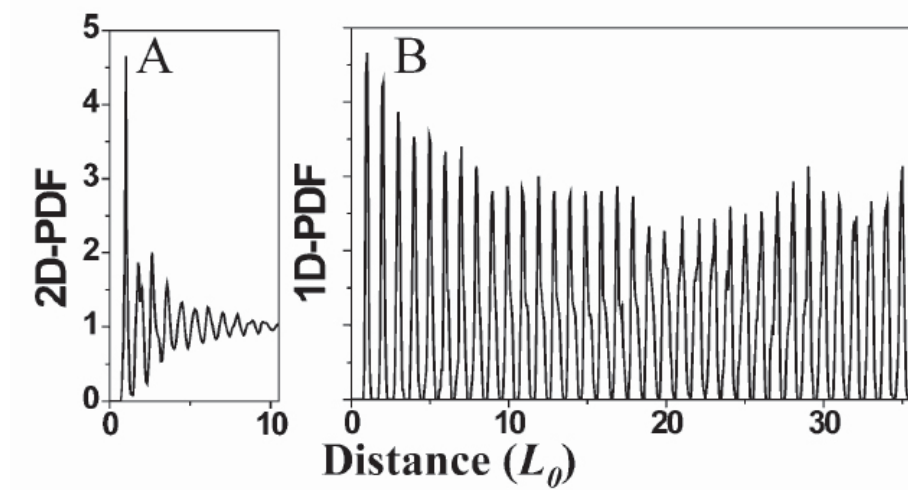


Figure 2.27: A comparison of the pair distribution fluctuations (PDF) for a thin film of a spherical forming BCP (A) on a flat two-dimensional surface and (B) in a shallow small well [6, 123].

propagation of the defect with increasing distance. This results in an arbitrary area or volume some distance away that should not be affected by a defect, due to the intrinsic fluctuations of phase separation thermodynamics and polydispersity. These interactions makes it possible for the confined soft matter to absorb small errors and dampen error propagation.

### 2.5.3 Summary of Hierarchical Structures Formed at the Nanoscale

The aforementioned results highlight the uniqueness and complexity of combining nanoscale fabrication techniques. The design of self-assembling supramolecular materials and their interactions between length scales is essential to realizing them as advanced materials. The combination of top-down and bottom-up nanomanufacturing avoids some of the design problems associated with self-assembling hierarchical structures. The developments in these areas are just starting and the experimental results and theoretical calculations for the diverse number of methods that can be

used to fabricate hierarchical structures is limited. Thus, much more work is needed to build up from the nanoscale using hierarchical structures by combining top-down and bottom-up.

## 2.6 Objectives of this Dissertation

The vast number of nanoscale fabrication techniques that potentially can be combined to form hierarchical nanostructures offers tremendous variety and flexibility in processing of advanced materials. However, from the review of literature on hierarchical nanoscale structures, there is a need to extend these ideas forward. Two gaps were evident from the literature. First, the fabrication of hierarchical nanostructures from a combination of nanoscale fabrication techniques has been limited to fibers and substrate surfaces [7, 124]. However, these systems do not offer the ease and flexibility to pattern hierarchical structures in a volume of material. Second, although dynamic tuning of hierarchical structures by applying heat has shown promise, the systems studied thus far have been self-assembled liquid crystalline BCP [81, 125]. The difficulty in using hierarchical self-assembled BCP as photonic materials is that the chemical interactions between the polymer and small molecules need to be taken into account limiting the number of BCP that can be used for photonic applications. In addition, the self-assembly process is prone to defects which degrades the optical performance of the material. In an attempt to address these issues this dissertation will fabricate a hierarchical nanoscale structure in a volume of material based on combining principles of top-down and bottom-up nanomanufacturing. HP and BCP self-assembly were chosen such that the techniques could be employed to pattern a volume of material. Previously, HP was used on small molecules to pattern periodically nanoscale liquid crystal droplets [126]. In addition to patterning liquid crystals, Vaia et al. recently applied this technique to pattern a variety of nanosized objects

including gold nanoparticles (5 nm in diameter), PS, latex spheres (260 nm diameter), and silicate nanoplates [127]. The patterning of various sized nanoparticles indicates that HP could pattern polymers since the radius of gyration of a  $10 \frac{kg}{mol}$  random coil chain in a good solvent is on the order of 10 nm in size.

The first part of this research focused on the characterization of homopolymers that were HP. Poly(ethylene glycol) (PEG), poly( $\epsilon$ -caprolactone) (PCL), and poly(L-lactide) (PLLA) were blended into a prepolymer mixture and exposed using a simple one-dimensional interference pattern to fabricate a volume grating. PEG was then thermally tuned to investigate the effect of semicrystalline polymers on the grating. The thermal switching was observed to coincide with polymer crystallization and melting. The temperature of the phase transition could be tuned by using different molecular weight PEG samples. Details of the investigation are provided in chapter 4.

After establishing the morphology and behavior of the semicrystalline homopolymers in a volume grating, the second part of this dissertation focused on incorporating a BCP into the prepolymer mixture that would result in the formation of a hierarchical structure. PEO-b-PCL was patterned into a volume grating and the morphology and structure was investigated. Chapter 5 presents details of these observations.

The confinement of the BCP in the hierarchical structure was then studied by thermally tuning the volume grating. A unique thermal switching occurred when the PEO-b-PCL melted and crystallized. The soft confinement of the PEO-b-PCL was attributed to the thermo-optic effect. The whole process is reversible and independent of writing and thermal history; Chapter 6 provides details of that investigation.

In chapter 7, the two-dimensional HP of PEG is explored. The structure of the photonic crystal was investigated using TEM and thermally switching was demonstrated. The PEG inside the two-dimensional photonic structure was not confined as evidenced by the optical micrographs and the thermal switching.

## **Chapter 3. Materials and Methods to Fabricating Hierarchical Volume Gratings**

### **3.1 An Introduction to Polymer Based Photonic Crystals**

In the last chapter, certain self-assembled hierarchical structures were able to reflect or diffract light because one of the length scales resulted in a periodic modulation in refractive index. This is due to microphase separation on the order of the wavelength of visible light. In general, polymer based photonic crystals can be achieved using either bottom-up techniques such as self-assembly and colloidal crystals or top-down techniques like photolithography and microcontact printing [128]. The periodic spatial modulation in refractive index leads to inhibition of some light frequencies while others pass through without interaction. In addition, many of the polymer properties that are advantageous such as biocompatibility and flexibility can be exploited in polymer based photonic crystals for use as mirrors, switches, filters, sensors, and resonators. In this section we review HP as a method for fabricating photonic crystals, the spatial control that this method provides over small molecules, and nanoparticles and the dynamic tuning of holographic polymer dispersed liquid crystals. From this technique it may be possible to pattern semicrystalline polymers and BCP.

#### **3.1.1 Coherent Light Scattering from Periodic Media**

Photonic crystals are a class of materials that inhibit some frequencies of light based on their structure. Figure 3.1 are illustrations of the periodic structures of one-, two-, and three-dimensional photonic crystals. These structures become important in producing a complete bandgap that will reflect or inhibit certain frequencies of light [129, 130]. Yet, differences in refractive indexes of polymers are often very low; fluorinated polymers have a refractive index of 1.3 while polystyrene has a refractive

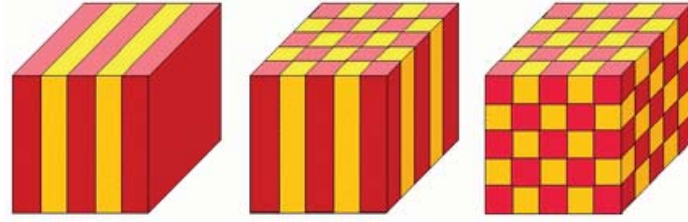


Figure 3.1: An illustration of photonic crystals with ordered structures in one-, two-, and three-dimensions.

index of 1.6, making the difference in refractive index between most polymers only about 0.5. The small difference in refractive index makes it difficult to achieve complete photonic bandgaps. However, many metal/ceramic air photonic structures have a refractive index modulation of three or higher making complete photonic bandgaps easily accessible. Polymer photonic crystals still display the same characteristics as full bandgap materials including guiding and molding the flow of light [128].

The refractive index profile also provides sufficient information for determining the propagation of light through the periodic structure. The interaction of propagating waves through the material can then be solved using Maxwell's equations. The interaction of light with a photonic crystal is then described in terms of group velocities. For polymeric systems, the group velocity of light near the edge of the stopband decreases because of an increased density of states [131, 132]. The frequencies inhibited due to a decrease in the group velocity results in a bandgap. The photonic crystal is then used to enhance or suppress spontaneous emission at the edge of the bandgap. In the polymeric materials, modulations in refractive index of lamellar structures results in a small number of electromagnetic wave frequencies matching the period. Analytical methods are available for the one-dimensional photonic crystal; the alternating layers of materials with a period on the order of the wavelength of light results in diffractive effects as first described by Lord Rayleigh [133]. A profile of the refrac-

tive index can be mathematically constructed using a step function to describe the periodicity normal to a crystallographic plane, such as equation 3.1.

$$n = n_0 + \frac{2}{\pi} \sum n_s \frac{1}{s} \sin\left(\frac{2s\pi x}{\Lambda}\right); s = 1, 2, 3, \dots \quad (3.1)$$

The periodic nature of the refractive index in one-dimensional structures results in diffraction/reflection gratings that produce coherent scattering. The refractive index modulation of the periodic materials is described by the average refractive index,  $n_0$ , refractive index contrast,  $n_1$ , and the pitch of the grating,  $\Lambda$ , parallel to the layer normal as observed in the x direction. In the weak segregation limit of a polymer blend, it is sufficient to truncate the refractive index profile after the first term in order to extract a sinusoidal function of the refractive index through the material. Using Bragg's Law (Equation 3.2), the wavelength,  $\lambda$ , of the scattered light can be calculated using the average refractive index, the pitch of the grating, and the angle of incident light  $\Theta$ .

$$\lambda = 2n_0\Lambda \sin(\Theta) \quad (3.2)$$

The periodic structure results in the reflection of a characteristic wavelength, which can be described by equation 3.2. This gives a method to probe the grating structure as a function of wavelength. The intensity of these reflections or decrease in transmitted light at a certain wavelength was described by Kogelnik in 1969 using the coupled wave theory for thick optical gratings (Equation 3.3) [134].

$$\eta = \tanh^2\left(\frac{n_1}{n_0}N\right) \quad (3.3)$$

In the above equation,  $\eta$  is the diffraction efficiency and  $N$  is the number of alternating layers in the grating. We can see from equation 3.3 that the diffraction efficiency depends on changes in the average refractive index and the index modulation. Any

changes in these two parameters will result in a change in the diffraction efficiency. The structure from HP of polymers will result in a characteristic wavelength of light being partially reflected, while the intensity of the light is indicative of the underlying material morphology.

### 3.1.2 Dynamic Polymer Photonic Crystals

The attractiveness of polymer photonic crystals in applications makes use of coherent scattering from the periodic structure in response to a stimulus. Several different stimuli have been shown to induce a change in the photonic crystal structure and/or refractive index of one or all of the components in the polymer photonic crystal. The changes in spectral positions and intensity in response to electric fields, magnetic fields, heat, electro-magnetic radiation, binding affinity of chemical species, and mechanical forces have been observed. In the rest of this section we describe how dynamic tuning arises in response to each of the previously mentioned stimuli.

Electric fields can be used to tune both the structure and the refractive index in polymer photonic crystals of one-, two-, and three- dimensions [126, 128, 135–137]. Electro-optical tuning of the photonic crystal normally includes liquid crystals such as 4-cyano-4-pentylbiphenyl, which can be induced to align itself in an electric field. The liquid crystal has two refractive indices depending on the alignment direction below the nematic to isotropic transition temperature, shown in figure 3.2a. In a normal mode holographic polymer dispersed liquid crystal diffraction grating, light is diffracted due to a mismatch in refractive index (Figure 3.2b). The application of an electric field to a randomly oriented dispersion of liquid crystals in crosslinked polymer composites with a periodic structure, results in a reorientation and change in the apparent refractive index of the liquid crystal. The switching manifests itself as a change in the diffraction or reflection intensity (Figure 3.2b). In addition to using

electric fields to tune the refractive index of one component, the application of electric fields have also been shown to reduce the spacing of colloidal crystals [138, 139]. In this case, a hydrogel of poly(2-methoxyethyl acrylate) loaded with silver nanoparticles would contract perpendicular to the plane of two parallel plates when an electric field of as little as 5 volts/micron is applied. The contraction manifested itself as a blue-shift in the reflection spectrum. The field induced changes in the spectrum were ascribed to the strain that developed due to the reorientation of the polar phase (otherwise known as the electrostrictive effect). In addition, contraction occurs due to the stress that arises on the two plates from coulombic interactions. The speed and ease of using electric fields to induce a physical change in the polymer based photonic crystal has been sought after for several devices [140–145].

Magnetic field induced control of photonic crystals is another convenient and precise method for tuning the properties of photonic crystals. Asher and researchers first approached this method for dynamic tuning of photonic crystals by fabricating a self-assembled colloidal crystal using highly charged polystyrene microspheres, which contained superparamagnetic nanoparticles [147]. In this case, the magnetic forces exerted on the colloids were weak relative to interparticle electrostatic forces. This was due to the low loading of the magnetic materials, which led to a small tuning range and long response time. In order to increase response time and tuning range, polyacrylate-capped superparamagnetic magnetite colloidal nanocrystal clusters with tunable sizes from 30 nm to 180 nm were assembled into photonic crystals [148, 149]. The photonic crystal of polymer coated superparamagnetic clusters was then tuned by applying a magnetic field that covered the entire visible range. The driving force for the high degree of tunability was due to charged polyacrylate-capped surfaces and the strong interaction of the magnetite with a magnetic field.

An all optical response in polymer photonic crystals of one-dimension were fabricated using HP to demonstrate another method for dynamic tuning. The alternating

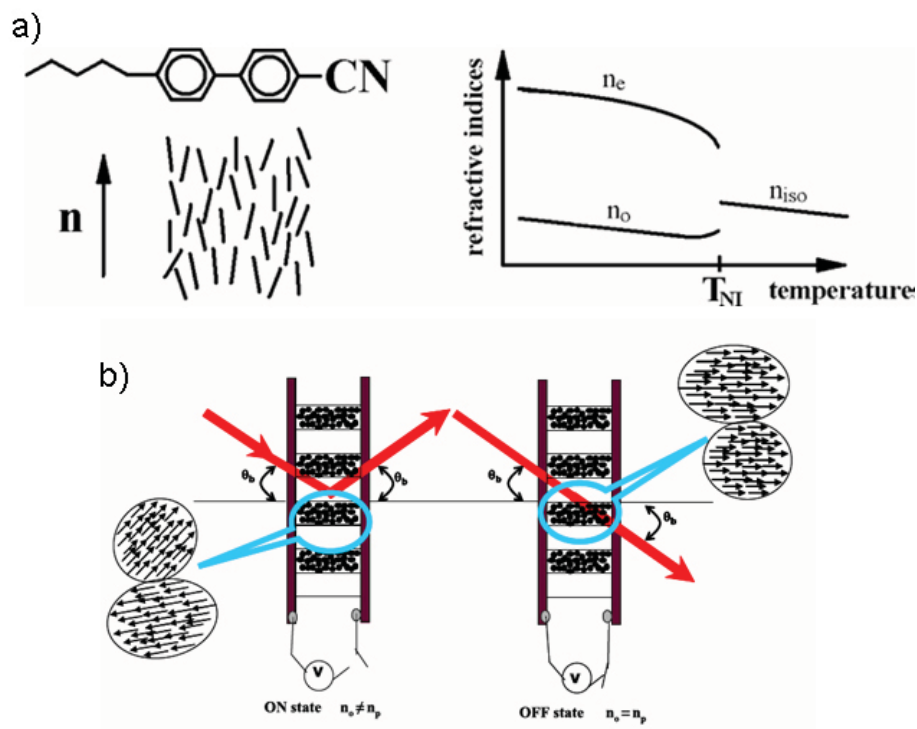


Figure 3.2: Nematic liquid crystals such as 4-cyano-4-pentylbiphenyl tend to align in a direction parallel to  $\mathbf{n}$ . The refractive index parallel and perpendicular to the director are different below the nematic to isotropic transition temperature (a). The electro-optical switching of (b) a holographic polymer dispersed liquid crystal diffraction grating [126, 135, 146].

layers contained a crosslinked polymer and a mixture of nematic and azo-liquid crystal, shown in figure 3.3 [150]. When the sample was illuminated with UV light, a change in the transmitted light intensity was observed at the Bragg wavelength. Inside the sample the azo-liquid crystal undergoes cis-trans photoisomerization when exposed to UV light, inducing a nematic to isotropic transition. The all optical response is a technological advancement for polymer based photonic crystals.

In addition to optical response, thermal switching of polymer based photonic crystals was observed in colloidal crystals, BCP, and HP photonic crystals [81, 125, 151, 152]. Heating and cooling mesoscopically periodic self-assembled poly(N-isopropylacrylamide) colloidal array resulted in a volume change, which demonstrated the tuning of the

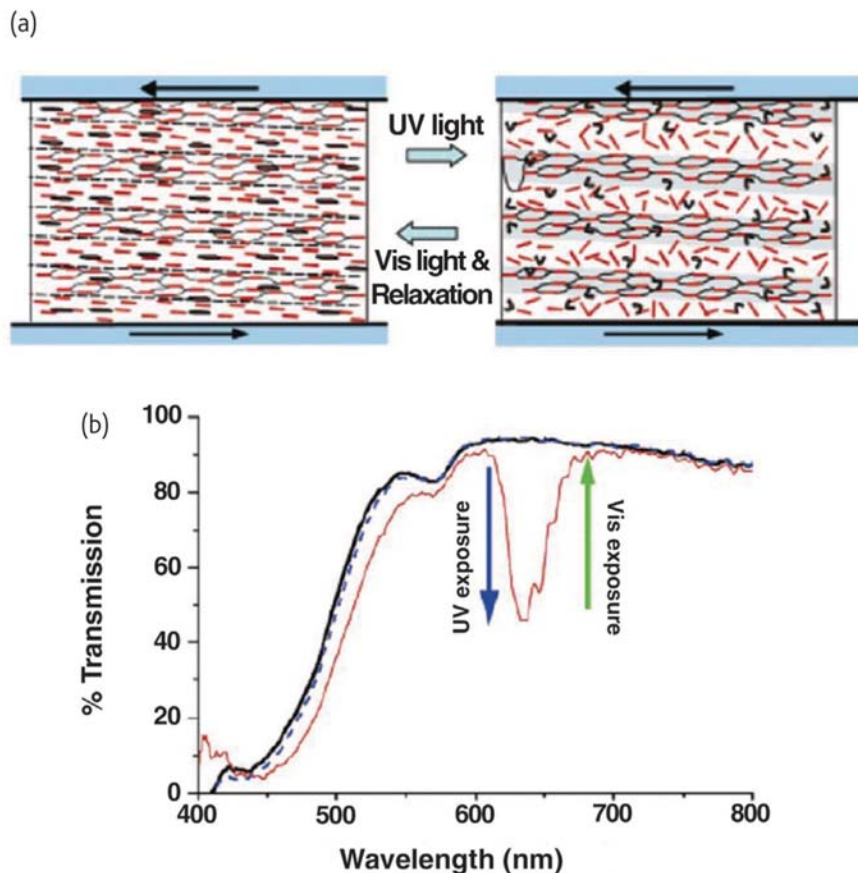


Figure 3.3: Diagram of several layers of a HP, polymer stabilized, liquid crystal structure and the optical response of the same material when exposed to UV and visible light [150].

photonic properties [151]. Figure 3.4a illustrates that the diameter of a poly(N-isopropylacrylamide) particle shrinks in water and increases in turbidity when heated. This indicates that the polymer has undergone a temperature induced volume contraction at around  $35^{\circ}\text{C}$ . The reflection from a body-centered-cubic colloidal crystal of hydrated poly(N-isopropylacrylamide) particles swollen in water were tuned through the infrared, visible, and ultraviolet light when the temperature was changed, shown in figure 3.4b. Raising the temperature above  $35^{\circ}\text{C}$ , resulted in a blue-shift in the reflected wavelength due to the temperature induced volume phase transition as-

sociated with poly(N-isopropylacrylamide) (Figure 3.4b). Hydrogen bonded liquid crystal BCP also results in a photonic crystal that can be thermally tuned. Osuji and Valkama discussed the interaction between BCP and hydrogen bonded liquid crystal when heated, which resulted in a large reversible change in the reflected light [81,125]. The thermal switching was a result of either hydrophilic/hydrophobic changes or hydrogen bonded liquid crystal dissociation/reassociation. In all the aforementioned cases, thermal stimulation was observed in bottom-up self-assembled photonic crystals and relied on the chemical binding affinity of the polymers. Thermal tuning has also been observed in holographic polymer dispersed liquid crystals, where a large change in the diffraction intensity occurred at around  $58^{\circ}\text{C}$  [153]. The observed transition can be associated with the nematic to isotropic transition, which is recognized in bulk samples as  $61^{\circ}\text{C}$ . At the nematic to isotropic transition for the aligned liquid crystals between crosslinked layers of polymer, a transition from anisotropic to isotropic medium results in a change in the refractive index, as shown in figure 3.2a. This change in refractive index resulted in a change in diffraction efficiency and wavelength shift in the holographic polymer dispersed liquid crystal system [153].

Other dynamic responses include analyte detection and strain induced changes in the structure of the photonic crystal. The introduction of analytes produces chemically active photonic crystals that can change their structure and refractive index [154–157]. The ability of polymers to bind selectively with metal ions and small molecules was used in each case to change the film thickness, refractive index, and reflectivity in response to the chemical species. In addition to using chemical methods for tuning photonic structures, mechanical stress/strain can be applied to tune polymer photonic crystals [158–160]. The diversity of dynamic responses mentioned in this section can be attributed to the versatility of polymers.

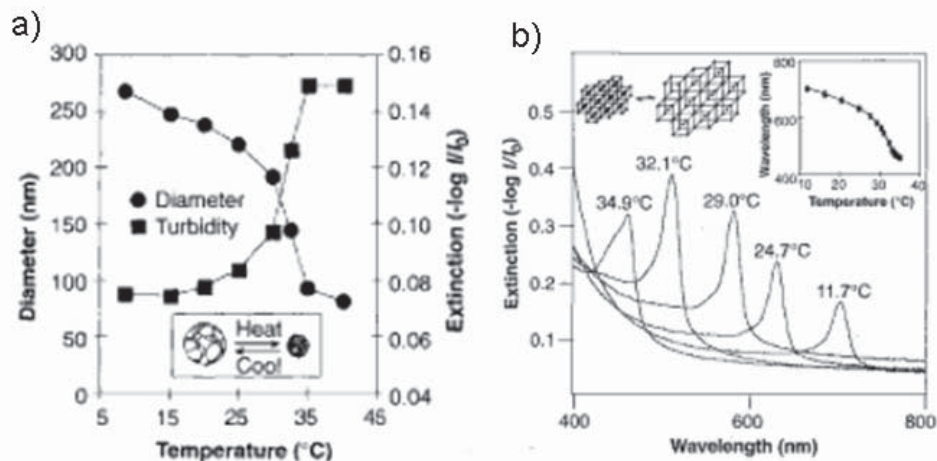


Figure 3.4: (a) A graph of the diameter and turbidity as a function of temperature for a colloidal crystalline array of poly(N-isopropylacrylamide) (b) the diffraction of the colloidal crystalline array of poly(N-isopropylacrylamide) as a function of temperature [151].

### 3.1.3 Holographic-Lithography as a Method for Patterning Photonic Crystals

A number of different methods, including colloid crystal assembly, lithography, extrusion, and BCP self-assembly, have been used to fabricate wavelength scale photonic structures in order to mold the flow of light [103,161–164]. Recently, holography has been proven to be a simple, fast and attractive means to fabricate complex photonic structures in a volume of material at a relatively large scale [162]. Holography is a process of capturing the interference pattern between two or more mutually coherent electric fields on a surface or in a volume of material. The recorded object can then be reconstructed by illuminating the interference pattern in the medium. The three-dimensional appearance of the recorded hologram arises because coherent recording traps the phase information along with amplitude of the electro-magnetic waves, unlike photography which only records the amplitude of light. Nobel Laureate Dennis Gabor was the first to describe the principles of holography [165]. Much of modern

day holography can be attributed to the invention of the laser. Without the coherent source of light many advances would not be possible [166,167]. Using lasers to record the hologram, a typical setup requires three elements: the object beam, reference beam, and recording medium. If the number of simple waves created from using a laser or group of lasers is small, than the recording process is termed holographic-lithography. The small number of unique light waves passing through the sample enables the design of a pattern that can be transfered by holographic-lithography to the medium, in the same way that lithography transfers a pattern from a mask to a substrate.

The design of photonic crystals using holographic-lithography requires that the pattern be transfered from an intensity profile of  $N$  coherent beams with respect to polarization, phase, propagation, and irradiance [168]. The total irradiance,  $I(\bar{r})$ , within a material is equal to the time average square of the magnitude of the electric field, shown in equation 3.4 [169]. For completeness,  $\nu$  is the speed of light within the medium and  $c$  is the speed of light in a vacuum.

$$I(\bar{r}) = \epsilon\nu \left\langle \overline{E_{Total}^2}(\bar{r}, t) \right\rangle \quad (3.4)$$

The total electric field can then be related to the sum of the electric field component of  $N$  plane waves, where  $A_m$  is the complex amplitude-polarization vector, shown in equation 3.5.

$$\overline{E_{Total}} = \sum_{m=1}^N \overline{A_m} e^{ik \cdot \bar{r}} \quad (3.5)$$

The sinusoidal nature of equation 3.5 reduces the time average of the electric field to  $\left\langle \overline{E_{Total}^2}(\bar{r}, t) \right\rangle = \frac{1}{2} \overline{E_{Total}} \overline{E_{Total}^*}$ . Inserting equation 3.5 into equation 3.4 the

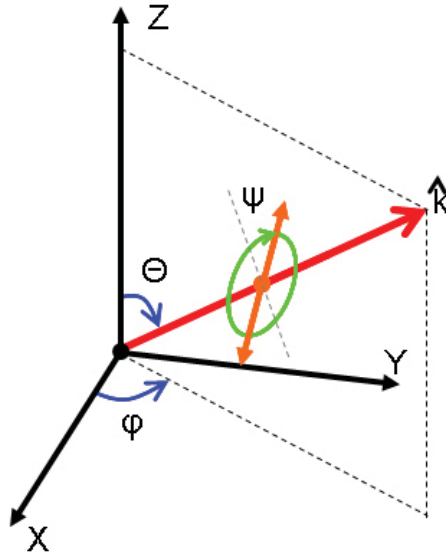


Figure 3.5: A diagram illustrating the vector representation of a plane wave traveling in a direction defined by  $\bar{k}_m$  and amplitude  $\bar{A}_m$ .  $\psi$  is the polarization angle,  $\theta$  is the angle between the Z-axis and the vector  $\bar{k}_m$  and  $\varphi$  is the angle between the projection of  $\bar{k}_m$  onto the XY-plane and the X-axis

irradiance can be rewritten as shown in equation 3.6 [169–171].

$$I(\bar{r}) = \frac{n}{2\sqrt{\mu_0/\epsilon_0}} \sum_{l=1}^N \sum_{m=1}^N \overline{A_l A_m} e^{i(\bar{k}_l - \bar{k}_m) \cdot \bar{r}} \quad (3.6)$$

The irradiance within a volume of material can now be determined if the wave vectors, polarizations, and phase relationship for each laser beam is assigned. The inputs for equation 3.6 are listed in the table below for a cartesian coordinate system for  $\bar{k}_m$  and  $\bar{A}_m$ . The magnitude of  $\bar{A}_m$  is proportional to the square root of the intensity and  $\delta_m$  is the phase. Figure 3.5 illustrates the components of  $\bar{k}_m$ . The magnitude of  $\bar{k}_m$  is  $k_m = 2n_0\pi/\lambda_0$ , the azimuthal angle of  $\bar{k}_m$  is  $\varphi_m$  and the polar angle of  $\bar{k}_m$  is  $\theta_m$ .

The spatial variations in intensity given by equation 3.6 leads to fluctuations in the intensity of light in a volume of space. This in turn results in locally faster regions of

$\bar{k}_m$	$\begin{pmatrix} \bar{k}_x \\ \bar{k}_y \\ \bar{k}_z \end{pmatrix} = k_m \begin{pmatrix} \cos\varphi_m \sin\theta_m \\ \sin\varphi_m \sin\theta_m \\ \cos\theta_m \end{pmatrix}$
$\bar{A}_m$	$\begin{pmatrix} \bar{A}_x \\ \bar{A}_y \\ \bar{A}_z \end{pmatrix} = A_m e^{i\delta_m} \begin{pmatrix} \sin\varphi_m \sin\psi_m - \cos\varphi_m \cos\theta_m \cos\psi_m \\ -\cos\varphi_m \sin\psi_m - \sin\varphi_m \cos\theta_m \cos\psi_m \\ \cos\theta_m \cos\psi_m \end{pmatrix}$

Table 3.1: The vectorial description of a monochromatic plane wave propagation and electric field vectors.

reactivity when a suitable photosensitive medium is exposed. Photosensitive materials can include emulsions, positive, and negative resist materials. The curing of the photosensitive material captures the spatial interference pattern, which can later be probed by illuminating the captured pattern.

### 3.1.4 HP of Liquid Crystals and Nanoparticles

The power of holographic-lithography is the spatial control that can be exerted in three-dimensions on mixtures of photocrosslinkable polymers and inert materials. The spatial patterning of these materials is termed HP. Holographic polymer dispersed liquid crystals were first realized by trying to control the spatial distribution of liquid crystals in reactive polymer blends. Several groups demonstrated switchable diffraction gratings formed from the interference of light [172–175]. In 1991, researchers at Polaroid also demonstrated that holographic polymer dispersed liquid crystals could be formed by backfilling porous holographic structures with liquid crystals [176]. Advances in refractive index modulation using HP subsequently formed the basis for DuPont’s holographic component product line [177]. Materials developments in the early-nineties enable visible light exposure and refinement of the electro-optical switching due to the holographic polymer dispersed structures [174, 178]. The results of these works and others led researchers to envision electro-optical switching in de-

vices. Researchers in Japan proposed using reflective Bragg gratings as a material for full-color reflective displays [179]. In other applications, optical media storage, optical lenses, freespace-fiber couplers, variable attenuators, and time-delay units have been proposed and/or demonstrated [140–145].

Before HP exposure, the typical mixture is composed of crosslinkable monomers, photoinitiator, and liquid crystals in an optically transparent thin cell. The exposure of the cell to two or more coherent light beams with an irradiance profile described in the section above, induces polymerization of the monomers in areas of higher intensity light. The polymerization process results in high molecular weight crosslinked networks that gel and indefinitely record the intensity profile. The exposure or writing process consumes the monomers locally resulting in a concentration gradient. The result of the concentration gradient is a net movement of monomers towards the illuminated reaction sites and liquid crystal moving to areas vacated by the monomers [180, 181]. The end result is a spatial distribution of liquid crystals and crosslinked polymer networks in a one-dimensional photonic crystal, as shown in figure 3.6 [126, 182]. In the same manner two- and three-dimensional photonic crystals were fabricated [136, 137].

HP was also used to demonstrate that sub-micrometer particles over large areas could be arranged spatially [127]. The permanent distribution of particles was recorded in a matter of seconds. The Bragg gratings exhibited appreciable diffraction efficiencies indicating that the distribution of nanoparticles did occur. Figure 3.7 a-c shows a cross-sectional fracture surface of a transmission grating formed using clay powder, polystyrene spheres and gold nanoparticles. Figure 3.7d is a TEM micrograph of a cross-section of grating containing gold nanoparticles. The mechanism for patterning the nanoparticles is shown in figure 3.7e. Polymerization is first induced by interference of two coherent beams. Before exposure, the particles reside in a homogeneous reactive fluid. Upon illumination, a dense crosslinked polymer is

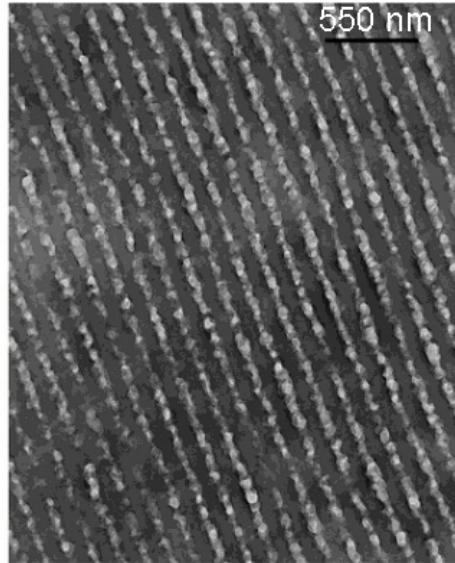


Figure 3.6: A cross section of a holographic polymer dispersed liquid crystal one-dimensional photonic crystal fabricated from HP [182]

formed in the high intensity regions, which results in an impenetrable wall. As time progresses, polymerization increases the wall thickness until particle motion ceases. The large size of the particles that were HP demonstrates that diffusion is important during the formation of the grating, but not a limiting factor in recording photonic crystals with holographic-lithography.

### 3.1.5 Summary of Polymer Based Photonic Crystals

The body of work mentioned in this section highlights the strong push to develop photonic crystals into a mature field. Many factors play into the design, fabrication, and properties of photonic crystals. Understanding the interplay between material and function is important to realize HP photonic crystals as advanced materials. The numerous experimental results and theoretical calculations offer advice and guidance in the design of more complex photonic structures.

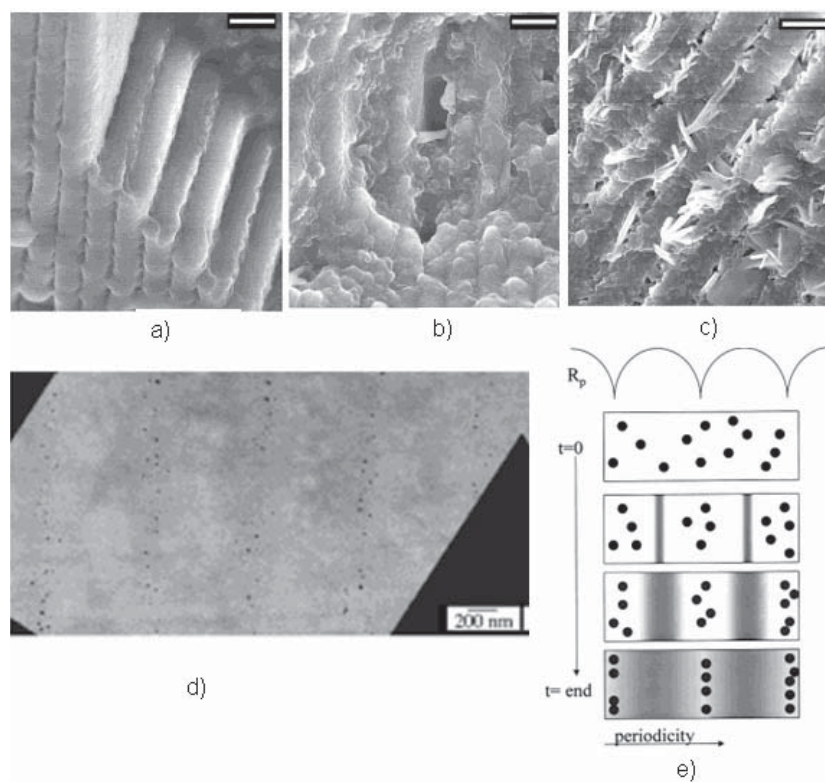


Figure 3.7: SEM images of cross-sectional fracture surfaces of transmission gratings demonstrating that nanoparticles can be sequestered by HP. gold nanoparticles (a), PS spheres (b) and clay powder (c) were all patterned. (d) is a TEM micrograph of the gold nanoparticles patterned using HP. (e) is the evolution of structure shown for two periods. Scale bars correspond to 1.5 micron (a), 1.5 micron (b) and 600 nm (c). [127]

## 3.2 Materials

### 3.2.1 Photopolymerizable Monomers and Initiators

The three major components that constitute a prepolymer syrup are crosslinkable monomers, photoinitiators, and inert polymers. The crosslinkable monomers and photoinitiators are commercially available. The mixture of crosslinkable monomers, NOA 65 from Norland Products is a trade secret. However, the components are believed to be 55 mole percent isophorone diisocyanate (Figure 3.8a) and trimethylolpropane diallyl ether (Figure 3.8b) in stoichiometric relation to one another [183].

Those components are mixed with approximately 41 mole percent trimethylolpropane tris(3-mercaptopropionate) (Figure 3.8c), and approximately 4 mole percent of the photoinitiator benzophenone (Figure 3.8d). A small amount of the photoinitiator Darocure 4265 from CIBA-Geigy Inc. is added to make NOA 65 more UV sensitive. The initiator 2,4,6-trimethylbenzoyl-diphenyl-phosphineoxide (Figure 3.8e) and coinitiator 2-hydroxy-2-methyl-1-phenyl-propan-1-one (Figure 3.8f) are mixed in equal parts. The refractive index of NOA 65 and Darocure 4265 are 1.52 and 1.58, respectively. Table 3.2 summarizes the photocrosslinkable monomer information and refractive index data.

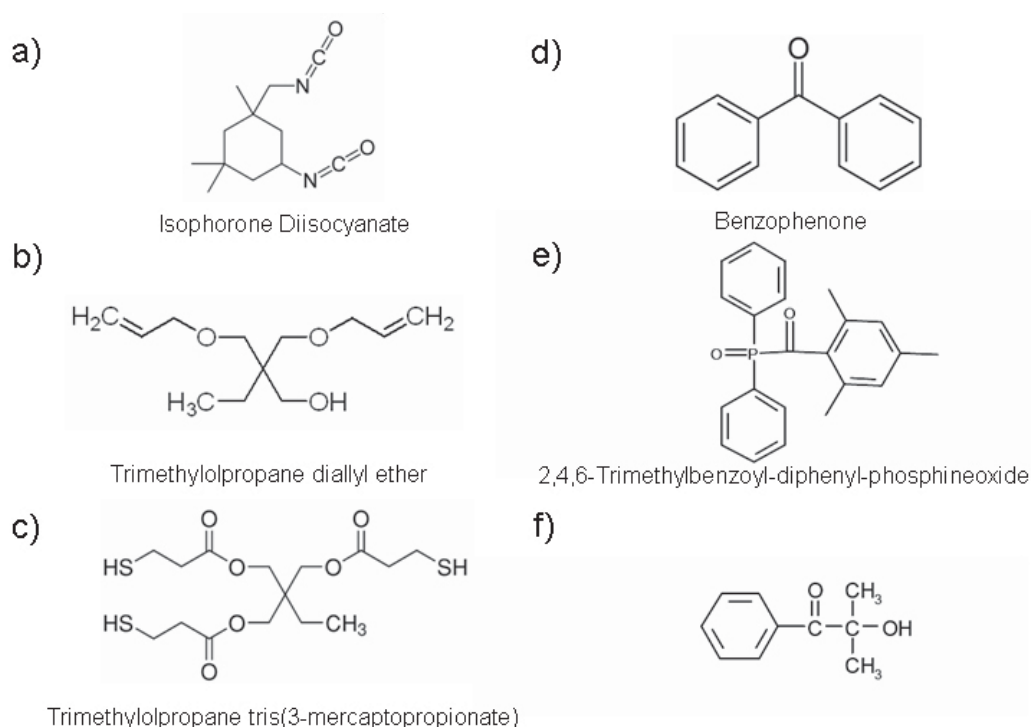


Figure 3.8: The chemical structure of the components that make-up Norland optical adhesive NOA 65 (a-d) and CIBA-Geigy Inc., Darocure 4265 (e-f).

Category	Name	Vendor	Refractive Index
Crosslinkable Polymer	NOA 65	Norland Products, Inc.	1.52
Photo Initiator	Darocure 4265	Ciba-Geigy, Inc.	1.58

Table 3.2: The components of the prepolymer syrup used in the holographic patterning of polymers and BCP.

### 3.2.2 Homopolymers

The homopolymer PEG (Figure 3.9a) of molecular weight  $600 \frac{g}{mol}$ ,  $1000 \frac{g}{mol}$ ,  $4600 \frac{g}{mol}$ , and  $8000 \frac{g}{mol}$  and PCL (Figure 3.9b) of molecular weight  $10,000 \frac{g}{mol}$  were purchased from Sigma-Aldrich, Inc. and used as received. In addition, PLLA (Figure 3.9c) with a molecular weight of  $2,000 \frac{g}{mol}$  was purchased from Polymer Source, Inc. and used as received.

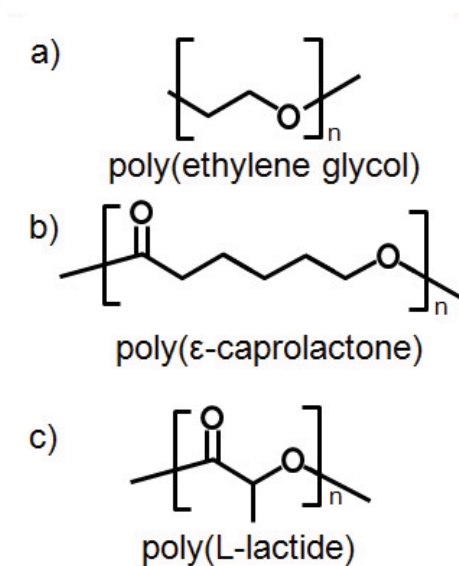


Figure 3.9: The chemical structure of the inert homopolymers used in this dissertation: (a) PEG, (b) PCL and (c) PLLA.

### 3.2.3 Block Copolymers

Two BCP were purchased from Polymer Source, Inc. and used in this study. Those BCP were poly(ethylene oxide)-b-poly( $\epsilon$ -caprolactone) (PEO-b-PCL) with a molecular weight of 5k-b-5k  $\frac{g}{mol}$  (Figure 3.10a) and poly(ethylene oxide)-b-poly(D,L-lactide) (PEO-b-PDLA) with a molecular weight of 5k-b-6.7k  $\frac{g}{mol}$  (Figure 3.10b). Poly(ethylene oxide)-b-poly(ethylene) (PEO-b-PE) was purchased under the commercial trade name of Brij 700 from Sigma-Aldrich, Inc. and used as received.

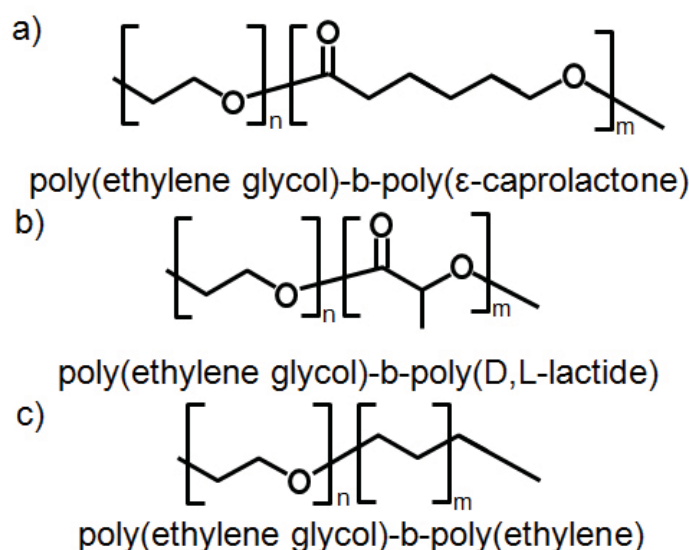


Figure 3.10: The chemical structure of the BCP used in this dissertation: (a) PEO-b-PCL, (b) PEO-b-PDLA and (c) PEO-b-PE.

In addition to the purchased BCP, PEO-b-PCL of varying molecular weights and architecture were graciously provided by researchers at Zhejiang University, China. The samples are listed in table 3.3.

The formulation of a typical prepolymer syrup consisted of 15 wt% to 30 wt% inert homopolymer or BCP, 65 wt% to 80 wt% crosslinkable monomers, and 3 wt% to 5 wt% photoinitiators. The polymer solution was heated, vortexed and a small amount of 4 to 30 micron spacers were added to control the thickness of the volume

Name	Molecular Weight	Polydispersity	Unit Architecture	Volume Fraction of PEG
PCL34-PEO44	7,104 $\frac{g}{mol}$	1.04	34/44	0.27
PCL56-PEO44	10,903 $\frac{g}{mol}$	1.05	56/44	0.18
PCL70-PEO44	13,832 $\frac{g}{mol}$	1.07	70/44	0.14
PCL90-PEO44	17,756 $\frac{g}{mol}$	1.10	98/44	0.11
PCL112-PEO44	18,126 $\frac{g}{mol}$	1.10	112/44	0.11

Table 3.3: The different PEO-b-PCL BCP volume fractions that were used in this work.

grating. The mixture was then placed between two pieces of glass and clamped to spread the solution. The polymer solution between the two pieces of glass constituted a cell.

### 3.3 Method for Fabricating Homopolymer and Block Copolymer Volume Gratings

HP was used to pattern polymer volume gratings. The fabrication process of reflection gratings was achieved using a Coherent Ar ion laser (Model 308c) with a laser wavelength of 363.8 nm and an output power of 100 mW. A single laser beam configuration was used to pattern reflection and transmission gratings as shown respectively in figure 3.11a and figure 3.11b.

Reflection and transmission gratings patterned with the single beam and prism technique start with a cell containing the prepolymer mixture. The cell is placed in optical contact with the hypotenuse of the prism as shown in figure 3.11. Optical contact with the prism is made by adding a drop of Cargille index matching fluid that was selected for fused silica at 75°C. A one-dimensional reflection grating can be patterned using HP; the diagram in figure 3.11a shows the experimental setup.

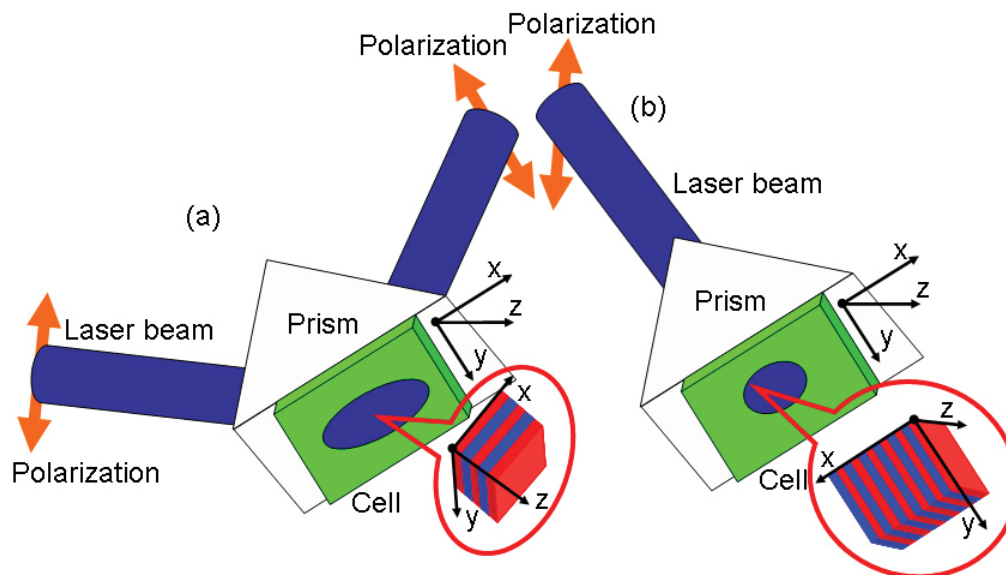


Figure 3.11: Experimental set up for fabricating a (a) reflection grating and (b) a transmission grating using a single prism.

The incoming beam is s-polarized meaning the direction of the electric field is perpendicular to the angle of the incident beam. The angle of incidence for the beam on the side of the prism, known as the prism angle, can be defined as the angle between the surface normal of the prism face and the incident beam. The prism angle will dictate the width of the interference pattern and grating spacing. As the beam passes the air/prism interface it is refracted slightly. The beam then passes from the prism to the cell containing the prepolymer syrup. After the beam travels through the cell, it reflects off of the cell/air interface at the hypotenuse of the prism and passes back through the cell containing the prepolymer syrup. The overlap of the beams passing through the cell before and after being reflected results in an interference pattern. Figure 3.12 shows the interference pattern intensity profile inside the cell for the YZ plane. The resulting intensity profile is a one-dimensional layered structure. The bright and dark regions have a periodicity of approximately 210 nm and are approximately parallel to the surface of the cell glass surface. The interference pattern that

arises initiates polymerization in the bright regions. The bright regions develop areas of crosslinked polymer as the polymerization process progresses. The spatial distribution of crosslinked polymer sets the structure, which results in a one-dimensional photonic structure known as a volume grating.

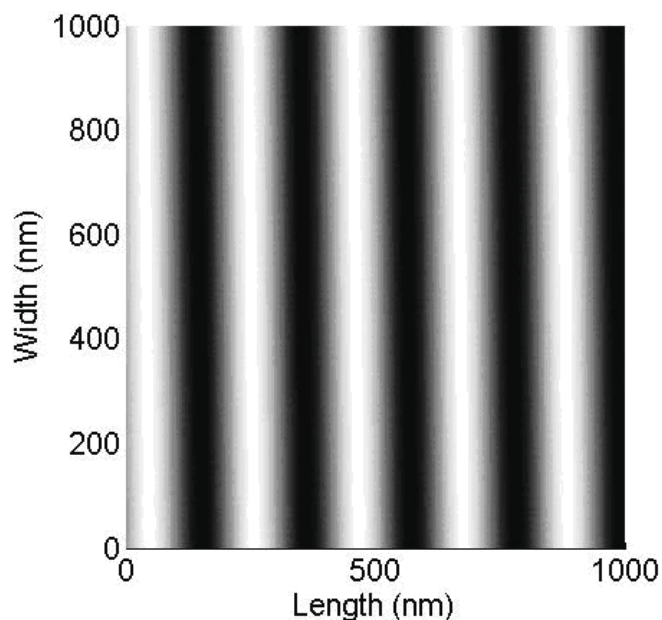


Figure 3.12: The intensity profile for a reflection grating with a prism angle of  $18^\circ$ .

The typical exposure time of HP was between 30 to 120 seconds. In order to control the period of the grating, the prism and the cell assembly were placed on a rotation stage. The prism technique can be used to pattern a variety of different volume grating pitches, known as the period of the grating (Figure 3.12). Figure 3.12 demonstrates that by changing the prism angle the volume grating pitch can be tuned from 400 nm to 100 nm. However, the amplitude of the interference pattern or the difference between bright and dark regions of the writing pattern will decrease sharply when the prism angle is above  $50^\circ$  and below  $-10^\circ$ . A hotstage was mounted between the rotation stage and the prism in order to control the temperature of the cell. The

typical temperature for HP writing was  $75^{\circ}\text{C}$ . After 10 minutes, the difference in temperature between the top and bottom of the prism was  $3^{\circ}\text{C}$  when the prism was held at  $75^{\circ}\text{C}$ . The temperature was chosen to ensure that PEO and PCL were in the molten state [184]. In addition to reflection gratings, transmission gratings can also be obtained. The laser set-up for the transmission grating writing is shown in figure 3.11b. The prism split the UV laser beam into two beams. The beams converge on the cell and form an interference pattern that is perpendicular to the plane of the glass in the cell (The interference is periodic in the X direction). The polymerization process is the same as in the reflection case.

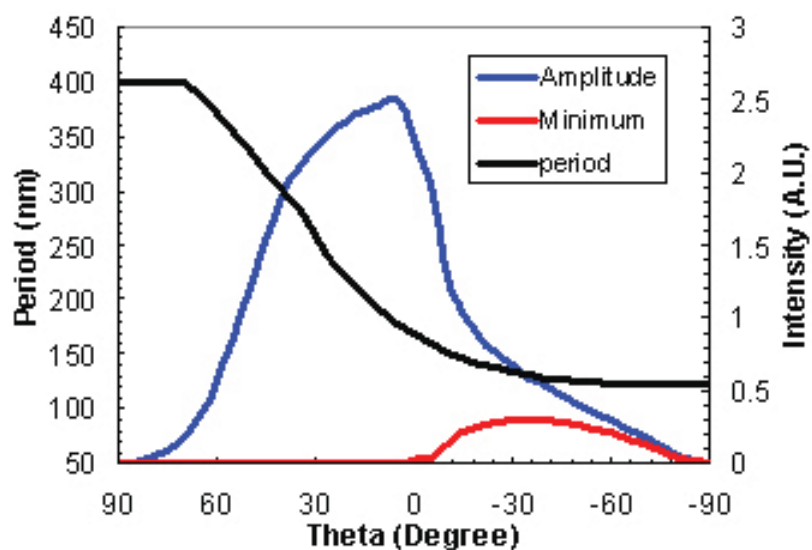


Figure 3.13: A chart displaying the intensity of the interference pattern in the sample (Blue line) and the period of the interference pattern (Black line) dependent on the incident angle of the laser beam relative to the surface normal that are possible for HP in the current setup.

### 3.4 Characterization

Visualizing nanoscale structures over several lengths scales requires a series of complimentary techniques. The shortfalls of any one technique was complimented with another technique. An example of such complimentary techniques is demonstrated by combining TEM with X-ray diffraction and UV-Vis transmission spectroscopy. The images gained from TEM inspects a small sample volume, but the information is complimented by X-ray diffraction and UV-Vis transmission spectroscopy to provide structural information throughout the sample. The rest of this section describes the methods used during the study of this project. These techniques include microscopy, X-ray scattering, and spectroscopy.

#### 3.4.1 Optical Microscopy

Microscopy in material science provides a real space image of a small area or cross section of sample. The real space image and observation of defects makes microscopy an indispensable tool. Light microscopy is a common yet powerful tool in polymer characterization. Polarized light microscopy in particular is especially useful in the study of polymer crystals. Polymer crystals possess a dielectric anisotropy due to unequal distribution of electron density along different axes of the crystal. The electric portion of the electromagnetic wave interacts with matter, which causes the electric wave to become retarded in certain directions leading to birefringence [185]. The rotation of polarized light can be observed when a sample of material is placed in the beam's path. An analyzer removes any waves of light that were not rotated by the sample. The net result is an image of a sample that elucidates the areas where the polymer crystallized. In this work, an Olympus BX51 polarized optical microscope attached with an Insight digital camera was used to study crystallization of polymers in the HP structure. The sample was encapsulated between two glass slides and

a Mettler hotstage FP 82 HT with FP-90 central processor was used to study the morphology at room and high temperature.

### 3.4.2 Electron Microscopy

TEM is a sophisticated and elegant tool employed in the study of mesoscopic and microscopic structures of matter at very high resolution [186]. Although the premise of TEM is similar to optical microscopy, the wave like properties of electrons instead of photons is exploited. In a TEM with an accelerating voltage of 100 KeV the wavelength of the electron emitted from a gun is 0.004 nm and ideally the resolution is on the same order of magnitude. The theoretically high resolution allows for atomic resolution of a sample. A typical TEM is built with a vertical ray path. The source of electrons is at the top of the machine and the viewing screen or camera is at the bottom, see figure 3.14. In order to reach very high resolution the column maintains a vacuum of  $10^{-4}$  mbar to  $10^{-13}$  mbar. The beam path is controlled by a series of coils that produces a strong magnetic field. The fields bend and shape the electron beam similar to optical components and are called electromagnetic lenses. The focal length is varied by changing the current to the electromagnetic coils, this facilitates the final image formation. A double condenser lens system uniformly illuminates the sample by bringing the electron beam into focus upon the specimen and removing stray electrons. The focused beam interacts with the sample, which is approximately 10 nm to 100 nm thick.

The ray path for electrons traveling through a TEM is shown in figure 3.14. The ray path can then be followed through the TEM to describe image formation. The transmitted electrons are focused to a point called the back focal point, located below the objective lens. The objective lens inverts and magnifies the image. The objective aperture is used to eliminate scattered electrons, this gives rise to two techniques.

When the aperture is placed in the transmitted beam path all incoherently and coherently scattered electrons are removed resulting in the technique of bright field imaging. If the objective aperture is placed around a diffracted beam the transmitted and incoherent electrons are blocked, giving rise to dark field imaging. The final image is projected onto a phosphorescent screen that emits visible light when the electron beam strikes the surface. The image can also be captured using CCD camera or a photographic plate.

In this work a JEOL 2000FX TEM with an accelerating voltage of 120kV and  $LaB_6$  tip was used in bright field mode to image thin cross sections of sample. A Gatan low dose CCD camera and software was used to collect images. A typical sample was prepared using the steps listed in the section below.

### 3.4.3 Transmission Electron Microscopy Sample Preparation

Thin sections of the volume grating were prepared for TEM using ultramicrotomy. A free standing film was obtained by opening the glass cell with a razor blade. The film was embedded into a two part Epofix cold hardening epoxy mixed in 8:1 weight ratio of resin and hardener. The resin was mixed and allowed to stand for 1 hour to thicken. A drop of resin was added to each well of a shallow silicon mold. The sample was cut into thin 0.5 mm or less strips and placed in the shallow silicon mold. More resin was poured over the thin films to fill the mold. The resin and sample would stand in the mold for two days at room temperature. Approximately 50 nm thin sections were prepared by ultramicrotomy of the resin encapsulated film. Excess resin was initially removed using a razor blade and the embedded sample was mounted and sectioned using a Leica UC6 ultramicrotome. The sections were collected at room temperature from the reservoir of a Diatome diamond knife that was filled with water. The collected samples were then dried on filter paper. The samples were stained using

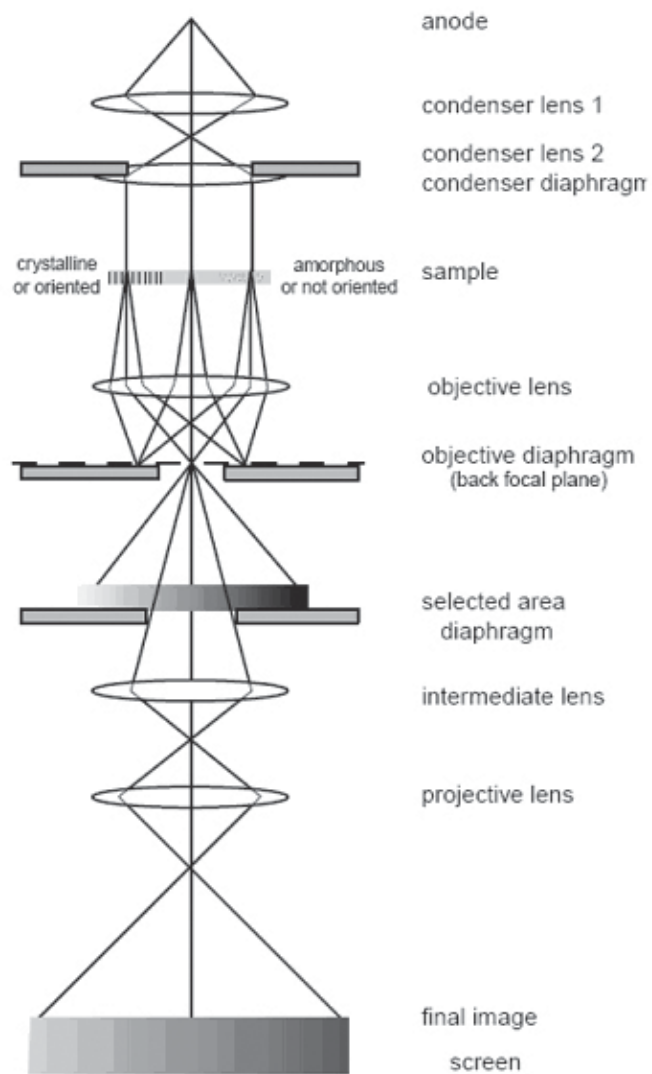


Figure 3.14: Schematic of electron beam through TEM for image formation [186].



Figure 3.15: An image of a JEOL 2000-fx TEM [187].

the heavy element compound  $\text{RuO}_4$  in order to enhance the contrast by preferentially staining aromatic or oxygen rich regions [188]. The TEM sections were subjected to  $\text{RuO}_4$  vapors for approximately 45 minutes in a sealed atmosphere.

#### 3.4.4 X-ray Diffraction and Scattering

X-rays are a large class of electromagnetic radiation ranging in wavelength from 10 pm to 10 nm and interact only slightly with matter. These two properties make them ideal for use in material science. X-rays are used to probe features that are 100 nm and smaller and provide information about the whole sample [189]. The local information during analysis is lost but average information over large areas, 1 mm to 3 mm, can be elucidated for a more global view of the sample.

X-ray diffraction and scattering provide crucial information about the crystal structure as well as periodic morphology on larger length scales. A sample containing a periodic pattern will produce coherent scattering; while a sample without

periodic density fluctuations will only produce diffuse scattering. The intensity of the scattering depends on the electron density and angle of the scattered photon. Collecting the scattered photons at very acute angles (less than  $2^\circ$ ) with respect to the incident beam provides information about the larger periodic features in the sample. The collection of scattered photons in this region is known as SAXS. In our case the structure of the homopolymer lamellae and BCP period is approximately 10 nm to 100 nm. The X-ray scattering experiments will provide information about the orientation and structure. If the X-ray scattering is at very large angles with respect to the incident beam, then the ordered structures are 0.1 nm to 10 nm in size. When X-ray studies are done at large angles with respect to the incident beam, it is called WAXD and it can be used to investigate polymer crystal structure and orientation.

In this dissertation, two-dimensional SAXS and WAXD experiments were carried out at the synchrotron X-ray beamline X-27C with a wavelength of 0.1371 nm at the National Synchrotron Light Source in Brookhaven National Laboratory [190]. Figure 3.16 is a schematic representation of the simultaneous SAXS and WAXD setup. The synchrotron beam passes through the monochromator assembly and the pinhole collimation assembly. The monochromatic symmetric beam then interacts with the sample. The two-dimensional area detector is a fluorescent image plate that can be placed approximately 18 cm to 205 cm from the sample so that both the WAXD and SAXS regions can be observed. The zero pixel of the two-dimensional SAXS pattern was calibrated using silver behenate with the first-order scattering vector  $q$  being  $1.076 \text{ nm}^{-1}$ . The two-dimensional WAXD patterns were calibrated with aluminum oxide with the first order scattering vector being  $18.03 \text{ nm}^{-1}$ . The air scattering was subtracted from the WAXD images. The X-ray beam spot was 0.1 mm in diameter. The X-ray beam was aligned parallel (the Y-direction in Figure 3.11a) and normal (the Z-direction in Figure 3.11a) to the surface of the sample. The simultaneous recording of the SAXS and WAXD data allows structural information

to be recorded without altering the sample, thus providing information on the relative orientation of polymer chains and BCP domains.

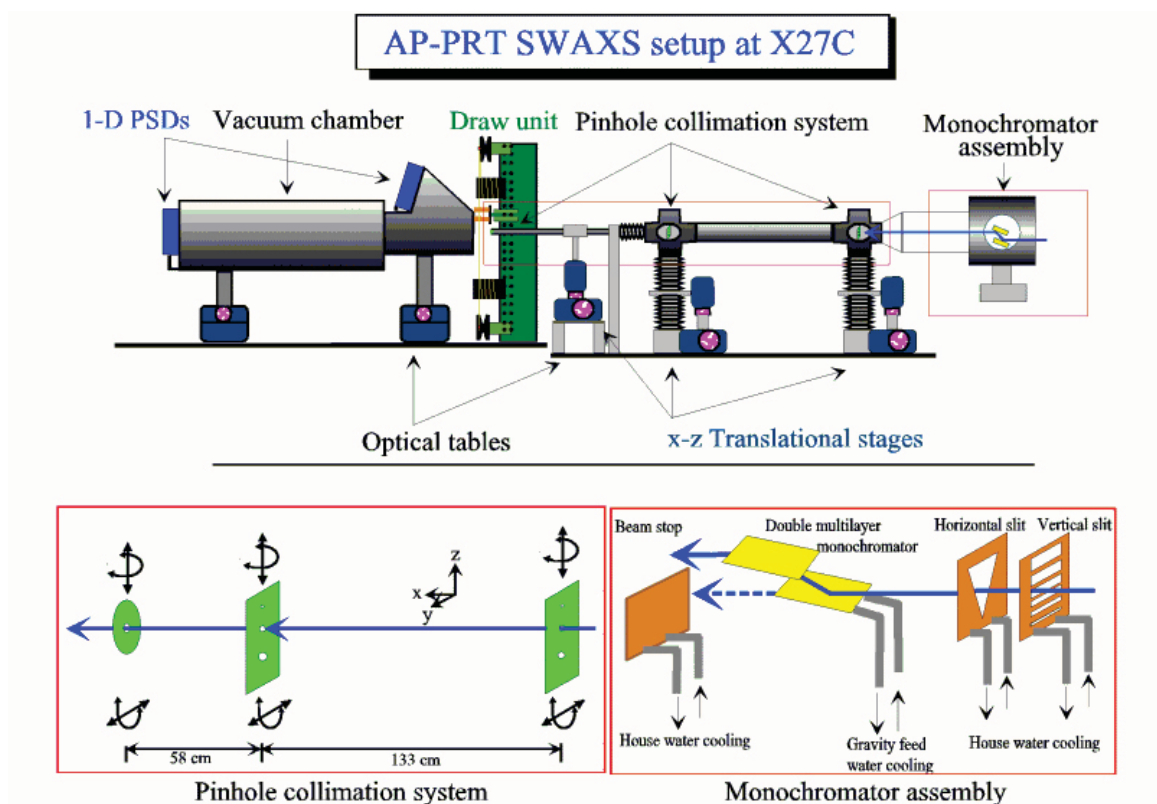


Figure 3.16: Schematic representation of simultaneous SAXS and WAXD setup at beamline X-27C, NSLS, Brookhaven National Laboratory [190].

### 3.4.5 UV-Visible Transmission Spectroscopy

Visible light is unique in that it is the only part of the electromagnetic spectrum that can be detected by the human eye. This provides an instant detector for observing the properties of materials. As light passes through a material it can be transmitted, reflected/refracted or absorbed. The interactions of the transmitted beam depend directly on the materials' properties. In this case we are interested in the transmission of light through the samples we fabricated using the HP technique.

As visible light passes through a sample, the difference in refractive index results in a decrease in intensity due to some of the light being reflected by specular or diffuse reflection. In the case of a multilayered stack, light of a certain wavelength is reflected by a culmination of reflections. The wavelength that is reflected is based on Bragg's Law modified to account for the refractive index of a sample (Equation 3.2). It is often easier to measure intensity over a range of wavelengths for visible light than to change the angle of the probe and detector. Thus we set  $\Theta$  to  $90^\circ$  making  $\sin\Theta$  equal to one. This reduces equation 3.2 to equation 3.7.

$$\lambda_o = 2n\Lambda \quad (3.7)$$

In this work, the optical characterization of the reflection gratings was carried out using an Ocean Optics fiber spectrometer. A white light source coupled to a fiber-optic delivery system was used as the light source. A decrease in transmitted intensity was due to a periodic modulation of refractive index that results from HP. In addition, polarizers and a hotstage could be incorporated into the setup with some modifications in order to study polymer chain orientation and response due to thermal stimulation.

#### **3.4.6 Thermal Analysis**

DSC was used to study the thermal phase transition temperature of semicrystalline polymers, BCP, and blends. The DSC measures heat flow to and from a sample in comparison with a reference sample. A furnace is used to control the temperature in which the sample and empty pans are placed. The pans are connected to heating elements and thermocouples in a feedback loop that maintains both pans at the same temperature. The excess energy absorbed or released by the sample during a thermal transition is shown as a step or peak when the differential heat flow is plotted as a

function of temperature. The typical sample size for DSC is approximately 2 mg to 5 mg. The sample is encapsulated in an Al pan before performing the experiment. DSC is also performed on an In standard using the same heating/cooling conditions. In has a melting peak at  $156.6^{\circ}\text{C}$  and the corresponding heat of fusion is 28.45 J/g. The sample data is calibrated for temperature and heat flow using the data for In standard. In this research, samples of the volume grating were removed from the glass cell and placed in an Al pan. The samples were then heated and cooled to determine melting and crystallization transitions in the volume gratings using the Perkin Elmer DSC7 and Mettler Toledo DSC822e.

### 3.4.7 Infrared Spectroscopy

Infrared spectroscopy is an analytical technique that measures the transmitted infrared intensity over a range of wavenumbers. Information about the stretching, contracting and bending of chemical bonds is imparted on the transmitted infrared beam as it passes through a material. As a result, a chemical functional group tends to absorb infrared radiation in a specific wavenumber range regardless of the structure of the rest of the molecule. Infrared spectroscopy detects the vibrations of chemical functional groups, which can be used to identify a functional group in a sample. The wavenumber positions where functional groups absorb are consistent, despite the effect of temperature, pressure, sampling, or change in the molecule structure in other parts of the compound. Yet, the intensity for some wavenumbers can be influenced by these stimuli and forms the basis of dynamic fast Fourier infrared spectroscopy. Thus the presence of specific functional groups can be monitored by these types of infrared bands, which are called group wavenumbers. The infrared bands of PEO-b-PCL in the melt can be observed as the volume grating was heated and cooled. The Nicolet Nexus 870, a transmission fast Fourier transform infrared spectroscope was coupled

with an Instec hotstage and liquid nitrogen intracooler in these experiments.

## Chapter 4. Volume Gratings by Combining Holographic Patterning and Semicrystalline Homopolymers

### 4.1 Introduction

HP is a useful technique for spatially controlling the distribution of high molecular weight crosslinked networks for photonic devices [162]. Spatial control of polymer dispersed liquid crystals have been used successfully to fabricate dynamic holographic optical elements [126]. In addition to patterning liquid crystals, a variety of nano-sized objects have also been patterned into ordered photonic structures [127]. These investigations provide evidence that HP is not diffusion limited and that a wide range of nanoscale materials can be patterned. This chapter discusses the patterning of semicrystalline polymers. A semicrystalline polymer is patterned and the morphology and structure of is discussed. In addition to fabricating volume gratings, the semicrystalline polymer system can be thermally tuned to produce a thermal switch. This is due to the volume and refractive index changes associated with crystallization and melting. The thermal switching was then tuned using a series of different molecular weight PEG samples. These experiments determined that the PEG was confined between layers of crosslinked resin. A blend of two homopolymers was also HP and the results are discussed at the end of this chapter.

### 4.2 Experimental

Reflection gratings were fabricated using a single beam configuration described in chapter 3. A Coherent Ar-ion laser (Model Sabre Innova 10R/2) with a laser wavelength of 363.8 nm and an output power of 300 mW patterned PEG, PCL, and PLLA. The homopolymers were blended into a mixture of photocrosslinkable monomers containing approximately 90% NOA 65 from Norland Products, Inc. and approximately

10% Darocure 4265 photoinitiator from CIBA-Geigy Inc. The mixture of homopolymer and photocrosslinkable monomers was normally mixed at a ratio of 1:2 by weight.

Characterization of the homopolymer volume gratings employed several techniques. TEM was used to investigate the morphology. PLM of the isothermal characterization was carried out by preheating gratings on a hotplate at  $90^{\circ}\text{C}$  then transferred to a Mettler-Toledo hot stage for observation. Optical characterization of the reflection gratings was performed using an Ocean Optics fiber spectrometer. Two-dimensional SAXS and WAXD experiments were done at the synchrotron X-ray beamline X-27C at the National Synchrotron Light Source in Brookhaven National Laboratory.

### 4.3 The Structure and Morphology of PEG Volume Gratings

A mixture containing PEG and photocrosslinkable monomers was placed between two glass slides and exposed to UV light during HP. A simple one-dimensional interference pattern oriented parallel to the glass substrate was used in HP PEG. When observed outside after exposure the sample reflected a characteristic wavelength of light (Figure 4.1).

The green color in the center of figure 4.1 is the area that was patterned using HP. The green color can be attributed to the periodic interference pattern that was captured in the mixture of homopolymer and crosslinked polymer. At the periphery of figure 4.1 the cell looks hazy, this area was not patterned but was exposed to diffuse UV light. The haze is attributed to random scattering in the unpatterned region. HP therefore has a significant impact on the optical properties of the mixture containing the semicrystalline homopolymer PEG.

UV-Vis spectra were collected to quantify the light being reflected by the patterned mixture of semicrystalline homopolymer PEG and crosslinked polymer. Figure 4.2a

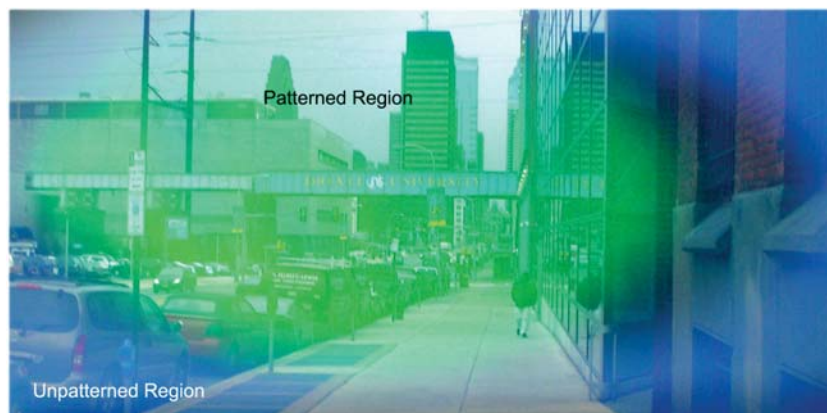


Figure 4.1: A sample cell containing a mixture of PEG and photocrosslinkable monomers after HP.

shows the transmission spectra of NOA 65 adhesive with 27% PEG. Four different molecular weights of PEG were used, namely,  $600 \frac{g}{mol}$ ,  $1,000 \frac{g}{mol}$ ,  $4,600 \frac{g}{mol}$ , and  $8,000 \frac{g}{mol}$ .

Sharp notches are evident for all the PEG volume gratings tested as shown in figure 4.2. The diffraction efficiency of PEG  $600 \frac{g}{mol}$  and PEG  $1,000 \frac{g}{mol}$  samples are approximately 40% to 50%, while those of the PEG  $4,600 \frac{g}{mol}$  and  $8,000 \frac{g}{mol}$  systems are 20% to 40%. The sharp notches in the transmission spectra of these PEG volume gratings suggest that an appreciable refractive index modulation was achieved. Morphology of a NOA 65 and PEG  $M_w 4,600 \frac{g}{mol}$  reflection grating was studied using TEM. Approximately 60 nm thick sections of the reflection grating were obtained by ultramicrotoming the sample in the X-direction. Figure 4.2b shows a TEM micrograph of a thin section of the NOA 65 and PEG  $M_w 4,600 \frac{g}{mol}$  reflection grating. The TEM micrograph in figure 4.2b corresponds to the YZ-plane with respect to the glass slide cell (See chapter 3). It is evident that a long-range, uniform layered structure with alternating dark and light regions has been achieved. The alternating layers of dark and light regions of the YZ-plane is similar to the predicted morphology

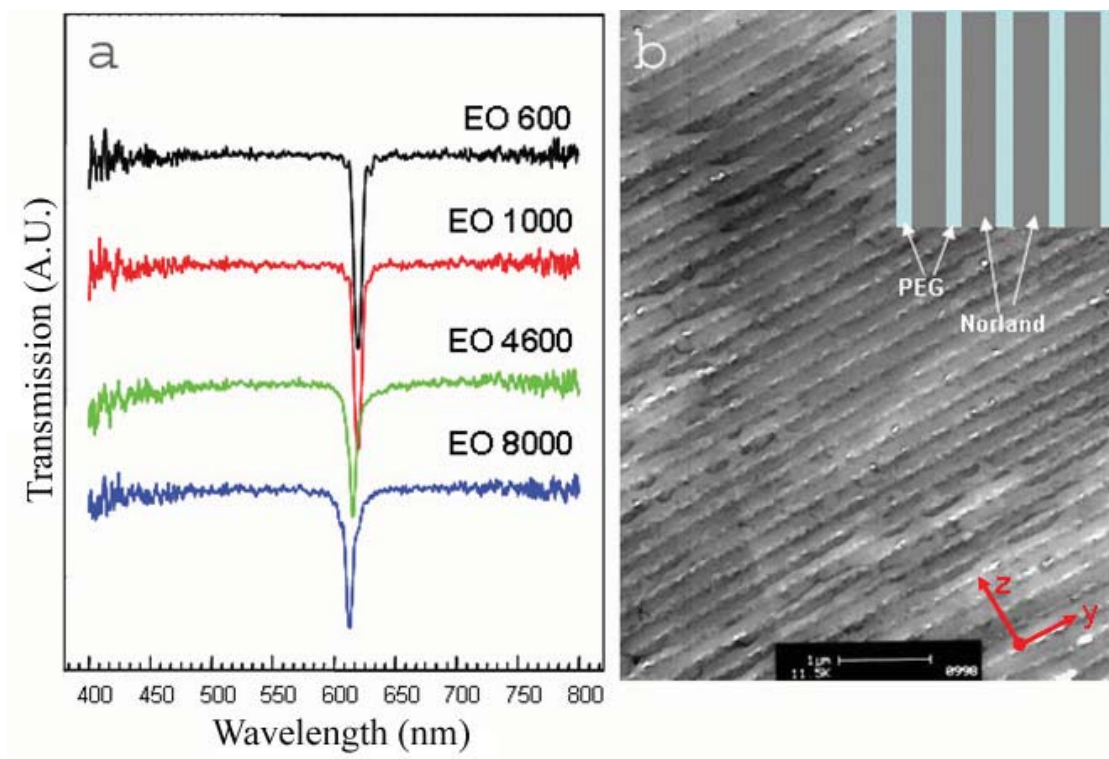


Figure 4.2: Transmission spectra and TEM image of volume gratings containing PEG formed by HP.

for the interference pattern when a single prism technique is used (See chapter 3). The dark regions represent NOA 65 resin while the light regions represent PEG. This assignment can be confirmed by the appearance of the holes in the PEG region, which results from the dissolution of PEG by water during the sample preparation process. The refractive index of the polymerized NOA 65 and PEG are 1.52 and 1.4563 (Or higher), respectively [184,191]. The alternating PEG and crosslinked layers on the submicron level leads to the observation of coherent reflection as observed in figure 4.2a. Unlike the 100 nm to 200 nm LC droplets observed in the holographic polymer dispersed liquid crystal systems, the PEG forms a semi-continuous layered structure. All the spectra in figure 4.2a show nearly 100% transmission over the entire wavelength range (400 nm to 800 nm). This is consistent with the absence of

the nanodroplets and formation of a uniform layered system as observed in the TEM experiment.

Using figure 4.2b, the grating d-spacing was measured to be 220 nm. The grating pitch was calculated using the optical properties of the patterned films and equation  $\lambda_0 = 2n_0\Lambda$ . The wavelength,  $\lambda_0$ , is the minima in the transmission spectra and the average refractive index can be approximated by  $n_0 = 0.7n_{NOA65} + 0.3n_{PEG}$ , for the thiol-ene polymer and PEG mixture. Based on the notch position of figure 4.2 and the average refractive index of NOA 65 and PEG, the resulting grating pitch can be calculated to be 208 nm, which is consistent with the TEM results.

Since the volume gratings containing PEG are confined between crosslinked NOA 65 resin layers, it is of interest to determine the structure of the PEG under physical confinement using synchrotron X-ray diffraction and polarized light microscopy experiments. Thin free-standing films (thickness approximately 10  $\mu\text{m}$ ) were obtained from the cell containing the PEG volume gratings. This film was subjected to two-dimensional X-ray diffraction studies. Figure 4.3 shows the X-ray diffraction pattern of PEG volume gratings with X-ray aligning parallel (Figure 4.3a, c, e, and g), and perpendicular (Figure 4.3b, d, f, and h) to the grating surface. Figure 4.3a and b show the schematic representations of the experimental set-up. In figure 4.3c, e, and g the X-ray diffraction patterns show clear orientation while in figure 4.3d, f, and h only ring patterns were obtained. A detailed investigation showed that the inner diffraction arcs can be assigned as the (120) with a d-spacing of 0.493 nm, while the outer diffraction can be assigned as the overlap of (-132), (032), (112), (-212), (124), (-204), and (004) reflections with a d-spacing of approximately 0.396 nm. In figure 4.3c, e, and g it is clear that the (120) diffractions are located on the meridian direction, while the outer (-132), (032), (112), (-212), (124), (-204), and (004) reflections are located in the quadrants, as shown in the azimuthal scan (Figure 4.4). Note that in the parallel alignment the volume grating film is parallel to the X-ray and the

meridian direction. This indicates that all the (120) are parallel to the equator of the X-ray diffraction pattern in the parallel set-up. Unoriented diffraction patterns in the perpendicular set-up indicate that the PEG crystals do not have any in-plane orientation. One can conclude from X-ray diffraction that the patterned regions of the PEG volume grating form lamellar crystals and the PEG chains are perpendicular to the grating layers.

PLM observations for the mixture of PEG and crosslinked NOA 65 resin inside (Figure 4.5a) and outside (Figure 4.5b) the patterned region displayed different morphologies after recrystallization. Since all the polymers were dissolved in the monomer syrup before writing (In the case of PEG  $M_w$  8,000  $\frac{g}{mol}$ , heating was applied to ensure the homogeneous syrup), solidification/crystallization occurred after polymerization. Initially, the morphology observed for the as-written samples in the patterned and unpatterned regions (Figure 4.1) show a grainy texture, although the grating region has much lower birefringence. After melting and recrystallization two-dimensional spherulite growth can be obtained in both regions and the inner region still possesses a lower birefringence. The appearance of spherulites in the outer region is consistent with the light scattering observed in the unpatterned region of figure 4.5. Inside the grating region, multilayer growth can be observed when crystallizing the grating at  $25^\circ C$ . The result of the isothermal crystallization at  $25^\circ C$  is shown in figure 4.5a. This may be due to the crystal growing in different layers of the grating, which is consistent with continuous layers of alternating PEG and crosslinked resin. The relatively weak birefringence in the pattern region suggests that polymer chains are parallel to the film normal. The PLM observation is thus consistent with the X-ray diffraction results.

Figure 4.6 shows the schematic representation of the hierarchical structures of the PEG volume grating. On the approximately 200 nm level, lamellar layered structures were formed. PEG molecules are confined between two crosslinked NOA 65

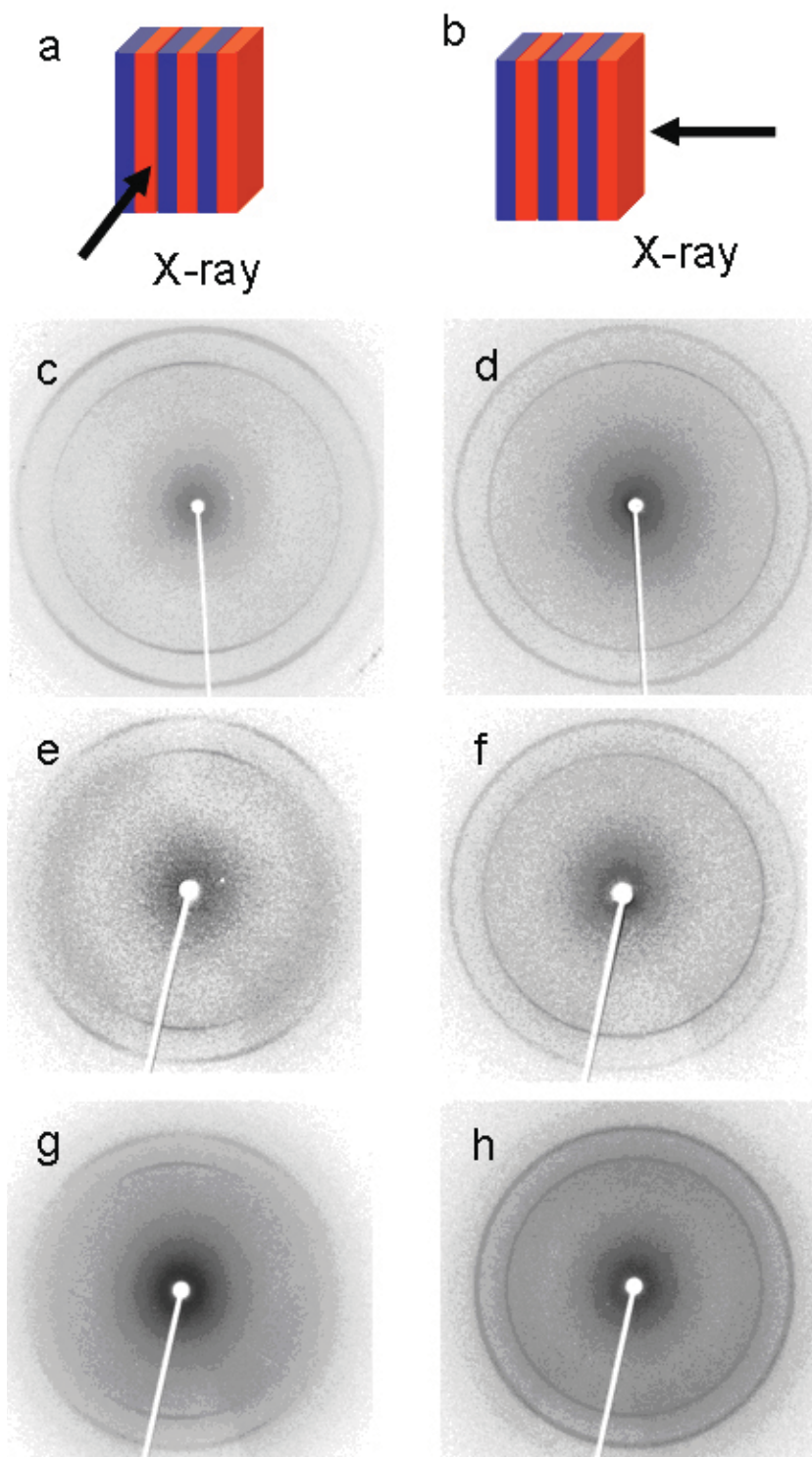


Figure 4.3: Two-dimensional X-ray pattern of PEG volume gratings. (a) X-ray geometry for parallel setting, (b) X-ray geometry for perpendicular setting, (c) two-dimensional X-ray pattern for parallel setting PEG  $M_w 2,000 \frac{g}{mol}$ , (d) two-dimensional X-ray pattern for perpendicular setting PEG  $M_w 2,000 \frac{g}{mol}$ , (e) two-dimensional X-ray pattern for parallel setting PEG  $M_w 4,600 \frac{g}{mol}$ , (f) two-dimensional X-ray pattern for perpendicular setting PEG  $M_w 4,600 \frac{g}{mol}$ , (g) two-dimensional X-ray pattern for parallel setting PEG  $M_w 8,000 \frac{g}{mol}$ , and (h) two-dimensional X-ray pattern for perpendicular setting PEG  $M_w 8,000 \frac{g}{mol}$ .

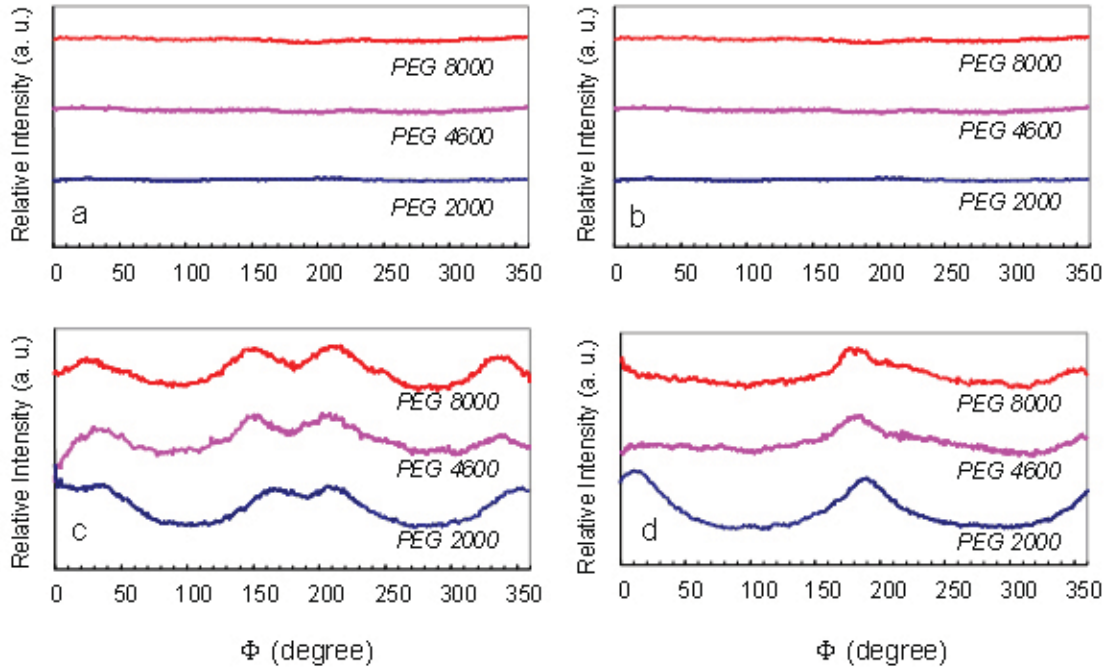


Figure 4.4: Azimuthal scans of the two-dimensional X-ray diffraction patterns in figure 4.3. (a) perpendicular setting of PEG volume grating, outer ring d-spacing = 0.398 nm, (b) perpendicular setting of PEG volume grating, inner ring d-spacing = 0.494 nm, (c) parallel setting of PEG volume grating, outer ring d-spacing = 0.398 nm, and (d) parallel setting of PEG volume grating, inner ring d-spacing = 0.494 nm.

layers. Upon crystallization PEG chains are parallel to the layer normal and the (120) planes are perpendicular to the layer surface. Confinement growth of polymer single crystal has been extensively studied in BCP systems. Crystal orientation depends on the crystallization conditions in PEO-b-PS samples (Molecular weight of PEO was approximately  $8,700 \frac{g}{mol}$  and the molecular weight of polystyrene was approximately  $9,200 \frac{g}{mol}$ ). The parallel crystal orientation was observed at temperatures higher than  $35^{\circ}C$  [192]. The lamellar periodicity is approximately 18.7 nm. In the present case, the structure formed from HP possesses a much larger scale compared to the previous BCP systems. This indicates that the nanoconfinement effect can also be observed at the 60 nm scale. Furthermore, the PEG molecules are not tethered

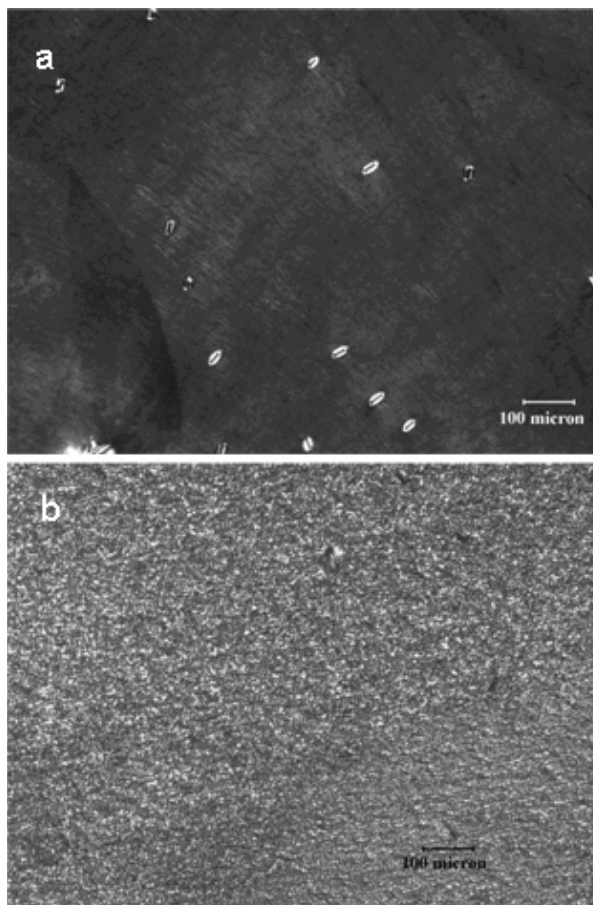


Figure 4.5: PLM image of volume gratings containing PEG.

with the crosslinked matrix, which negates the argument that a near perpendicular orientation to the inter-material dividing surface is due to the tethered junctions. The perpendicular chain orientation of the PEG crystal appears to be a thermodynamically more stable state. The in-plane orientation of the PEG lamellae leads to a larger crystal and allows the  $\langle 120 \rangle$  direction to be parallel with the grating layers. A tilted or parallel chain orientation with respect to the grating layers would result in the  $\langle 120 \rangle$  direction of the crystal being oblique or perpendicular to the crosslinked volume grating layers. The crystal would then quickly meet the solid confinement of the crosslinked resin prohibiting large size crystals, which in turn, reduces their

overall stability.

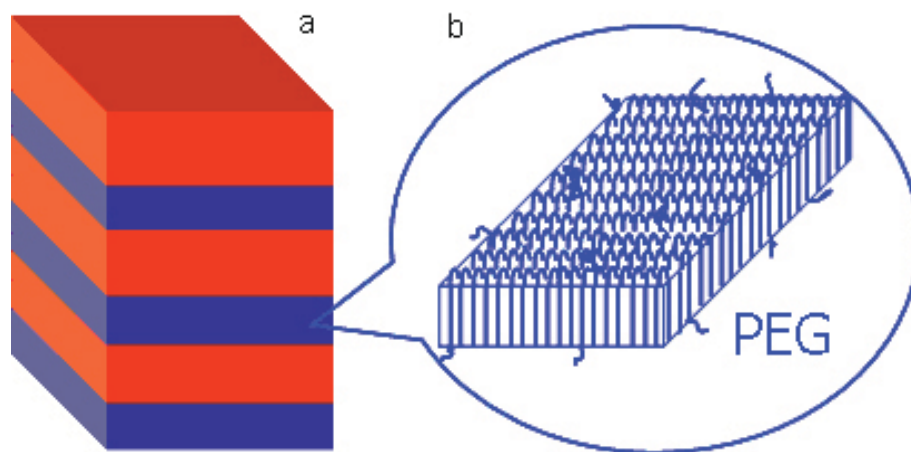


Figure 4.6: Schematic representation of the hierarchical structure of the PEG volume grating. (a) lamellar structures are formed with a periodicity of approximately 200 nm, (b) within the PEG layers, PEG crystals are formed and the lamellar crystals are parallel to the volume grating surface and the PEG chains are parallel to the grating pitch.

#### 4.4 Thermal Tuning of PEG Volume Gratings

##### 4.4.1 Crystallization as a Method for Switching Volume Gratings

The fabricated PEG volume grating resulted in a confined semicrystalline polymer between layers of crosslinked resin. The confined PEG when heated should result in a density and refractive index change [184,191]. The impact that these changes have on the volume grating would result in a shift in the reflected wavelength and diffraction efficiency. In order to demonstrate the response of the grating to temperature, PEG with a molecular weight of  $4,600 \frac{g}{mol}$  in a volume grating was heated from  $25^{\circ}C$  to  $70^{\circ}C$  at  $10 \frac{^{\circ}C}{min}$  followed by cooling to  $25^{\circ}C$  at the same rate. Figure 4.7 shows the in-situ transmission spectra of a PEG volume grating at different temperatures. Figure 4.8 shows the plots of the diffraction efficiency and notch positions of figure 4.7 with respect to temperature. Upon heating the volume grating, the notch position red-

shifts from 586 nm to 604 nm and the diffraction efficiency increases with temperature from 20% to 60%. Upon cooling the volume grating the notch shifts back to its original position at 586 nm and the diffraction efficiency reverts back to 20%. In figure 4.8, there is a rapid change of diffraction efficiency and notch position at  $50^{\circ}\text{C}$  for heating and at  $30^{\circ}\text{C}$  for cooling. For both heating and cooling curves, the changes of diffraction efficiency and notch position are synchronized. A temperature tunable volume grating therefore has been achieved.

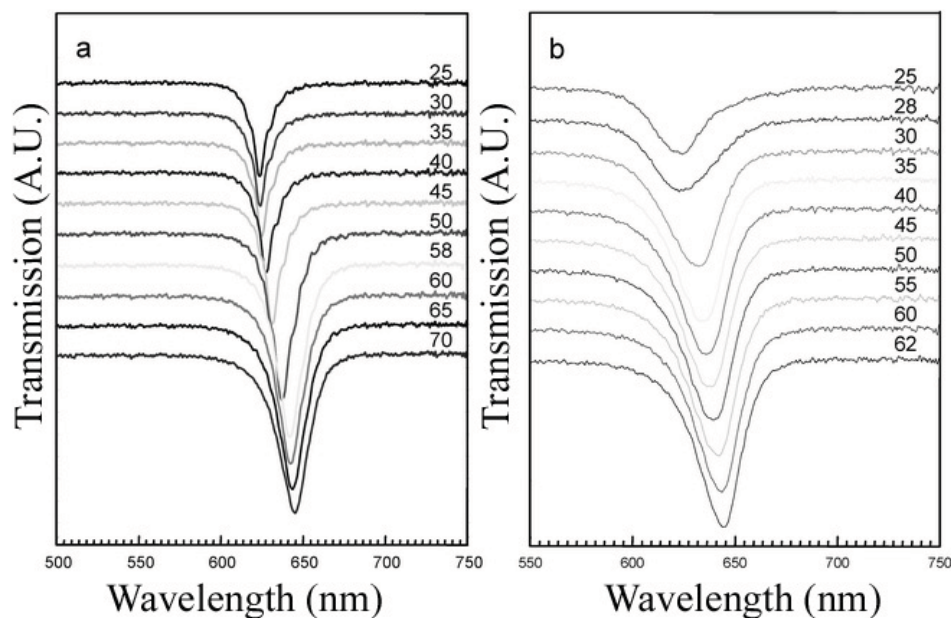


Figure 4.7: Heating (a) and cooling (b) transmission spectra of a PEG volume grating. The numbers on the right side of both (a) and (b) correspond to the temperatures in Celsius at which the spectra were taken.

This unique temperature induced notch wavelength and diffraction efficiency change can be attributed to the phase transition of PEG from crystalline to molten state. PEG is a semicrystalline polymer with a crystal melting point ranging from  $5^{\circ}\text{C}$  to  $68^{\circ}\text{C}$ , depending upon the molecular weight [193, 194]. DSC thermograms of pure PEG and its volume grating reveal melting temperatures of  $62^{\circ}\text{C}$  and  $50^{\circ}\text{C}$  and crystallization temperatures of  $38^{\circ}\text{C}$  and  $32^{\circ}\text{C}$ , respectively, as shown in figure 4.9. The

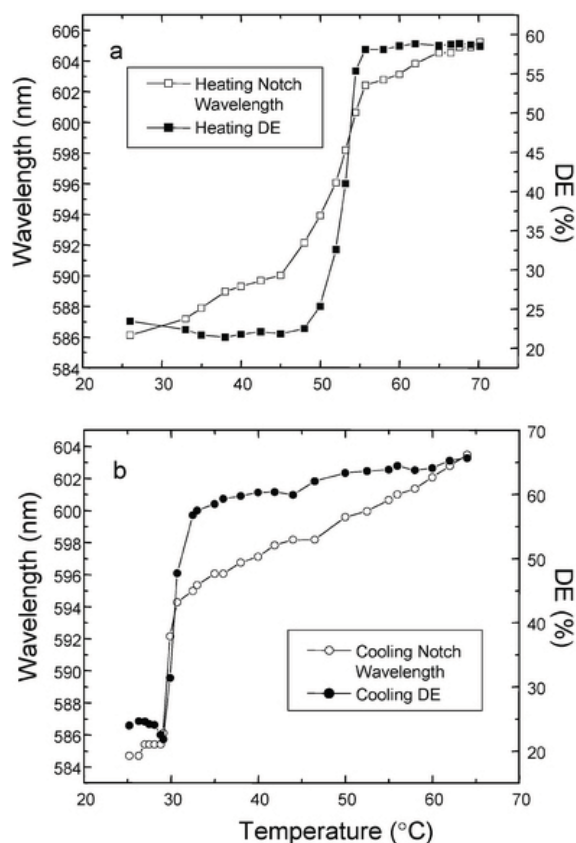


Figure 4.8: Notch position and diffraction efficiency change with respect to temperature for figure 4.7. (a) represents heating and (b) represents cooling.

observation of the melting point/crystallization temperature depression in the PEG volume grating supports the previous work on confined polymer crystallization. This suggests that the melting point/crystallization temperature of polymer crystals decrease in the confined state [195, 196]. In this case the melting and crystallization temperatures of PEG grating match with the rapid changes of diffraction efficiency and notch position in figure 4.8. The observed change in transmission spectra and the DSC thermograms indicate that the dynamic behavior of the PEG reflection grating is due to crystallization/melting.

It has been recognized that both density,  $\rho$ , and refractive index,  $n_0$ , of amorphous and crystalline PEG are different. The PEG crystalline density,  $\rho_c$ , is  $1.227 \frac{g}{cm^3}$  while

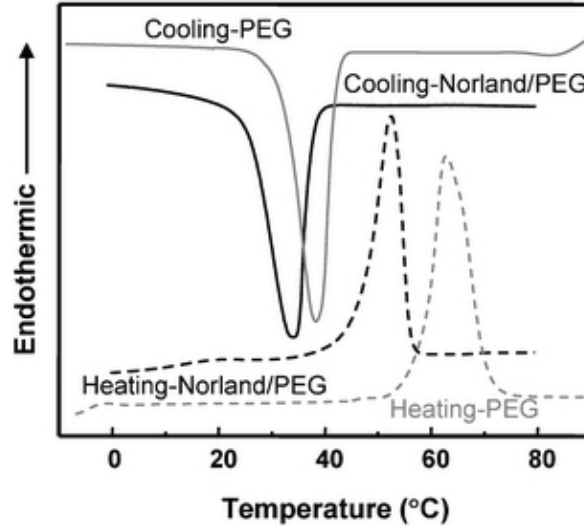


Figure 4.9: DSC thermograms of pure PEG and PEG volume gratings. The cooling and heating rates were controlled to be  $10 \frac{^{\circ}C}{min}$ .

the amorphous PEG density is dependent upon the temperature (Equation 4.1).

$$\rho_a = 1.1422 - 0.0008T \quad (4.1)$$

In the equation above,  $T$  is defined as the temperature. The  $\rho_a$  values of PEG at  $30^{\circ}C$  and  $60^{\circ}C$  can therefore be estimated as  $1.1182 \frac{g}{cm^3}$  and  $1.0942 \frac{g}{cm^3}$ , respectively [184]. PEG possesses a refractive index of 1.4563 (or higher at  $30^{\circ}C$ ) [191]. The large volume expansion as the refractive index decreases when the PEG crystals melt ( $1.4535$  at  $75^{\circ}C$ ). The change in refractive index then leads to an increase in the refractive index contrast between the PEG and crosslinked layers. This may be the main reason for the diffraction efficiency increase or decrease during melting or crystallization. Since the refractive index of PEG decreases upon melting, it should lead to a blue-shift of the notch position according to equation 4.2.

$$\frac{\Delta\lambda}{\lambda_a} = \frac{\Delta n_0}{n_{0_a}} + \frac{\Delta\Lambda}{\Lambda_a} \quad (4.2)$$

The wavelength shift given by  $\frac{\Delta\lambda}{\lambda_a}$  is approximately 2.98%. The approximate average refractive index shift for the crystalline and melt PEG volume gratings would result in  $\frac{\Delta n_0}{n_{0a}}$  contributing to a blue-shift in the volume grating of approximately 0.06%. The change in average refractive index is two orders of magnitude smaller than the wavelength shift. The observed red-shift must then be induced by an expansion of the grating. The red-shift in the grating spacing,  $\frac{\Delta\Lambda}{\Lambda_a}$  is approximately 3.04%, translating into a 6 nm change in volume when PEG goes from crystalline to melt. According to the densities of pure crystalline and amorphous PEG, 12% volume expansion may occur upon melting. However, in the volume grating not all the PEG is crystalline at room temperature. The PEG crystallinity in the grating can be calculated from the DSC results shown in figure 4.9. 100% crystalline PEG gives rise to a heat of fusion of  $8.66 \frac{kJ}{mol}$  [193], whereas the heat of fusion for the PEG grating at  $50^\circ C$  is  $6.93 \frac{kJ}{mol}$ . Crystallinity of PEG confined between crosslinked layers can therefore be calculated to be approximately 80%, which leads to an 11% volume expansion of the PEG layer in the reflection grating. Assuming that the surface area of each layer of PEG remains the same upon melting, the volume increase should only be caused by the grating spacing expansion. Since PEG occupies 30% of the film, the spacing of the grating should increase 3.3% upon heating. This result matches remarkably well with the calculated grating expansion (3%) from the red-shift of the spectra according to equation 4.2. Therefore, the main reason for the diffraction efficiency and notch position changes of the PEG volume grating is the volume change, which is driven by melting and crystallization.

#### 4.4.2 Tuning of the Switching Temperature

A one-dimensional volume grating was patterned using the same HP configuration previously discussed with three different molecular weight PEG samples (the molecu-

lar weight of the samples were  $2,000 \frac{g}{mol}$ ,  $4,600 \frac{g}{mol}$ , and  $8,000 \frac{g}{mol}$ ). The three semicrystalline polymers will have different melting/crystallization temperatures [193,194]. In this section, the PEG volume gratings with different molecular weights will be used to demonstrate the tuning of the switching temperature. Figure 4.10 shows the transmission spectra of PEG volume gratings with different molecular weights; transmission notches with modest diffraction efficiency can be seen. The notch position is approximately 600 nm to 610 nm. The appreciable diffraction efficiency indicates a refractive index modulation in the volume grating due to the spatial distribution of crosslinked resin and PEG. Figure 4.10b shows a TEM micrograph of a thin section of the grating of NOA 65 and PEG with a molecular weight of  $2,000 \frac{g}{mol}$ . The morphology observed in figure 4.10b is similar to the volume gratings containing PEG  $M_w$  of  $4,600 \frac{g}{mol}$ . A long range uniform layered structure with alternating dark and light regions is evident from the micrograph. The PEG layers therefore form a continuous layered structure with a lamellar spacing of approximately 200 nm.

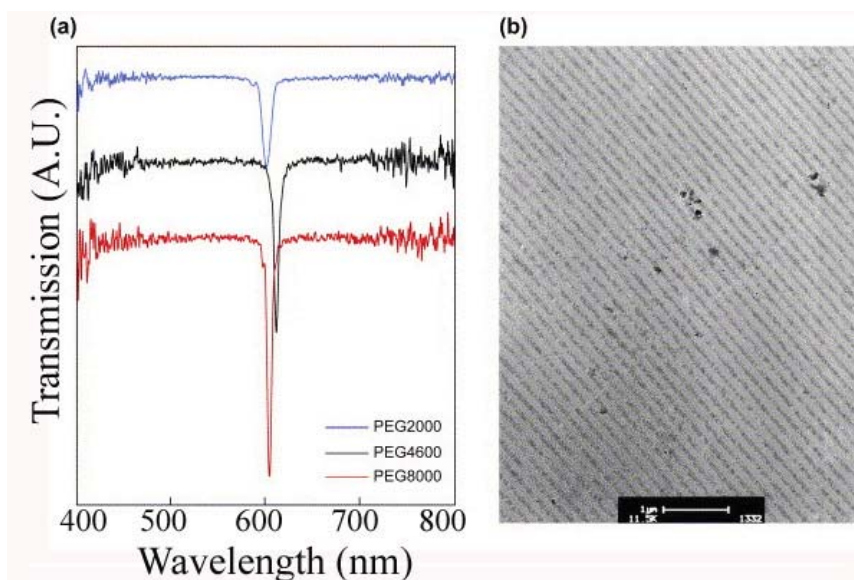


Figure 4.10: (a) Transmission spectra of the reflection gratings of PEG and crosslinked resin. The baselines have been offset for clarity in display of the spectra. (b) TEM micrograph of a thin section of a PEG with a  $M_w$   $2,000 \frac{g}{mol}$  and crosslinked resin.

In the previous study the notch position as well as the diffraction efficiency of these volume gratings could be modulated by varying the temperature. As the temperature increases, both the notch position and the diffraction efficiency increase and the reverse occurs upon cooling. This is due to PEG going through a crystal/melt transition, the volume increases and the grating expands, which in turn leads to a red-shift of the notch as observed in the transmission spectra. Furthermore, the refractive index of PEG is smaller in the amorphous state. The refractive index of the crosslinked resin is higher than that of PEG. A decrease in PEG refractive index leads to an increase in the refractive index contrast between the crosslinked resin and the PEG. This dramatically increased the diffraction efficiency of the volume grating. The melting points of the PEG crystal depends on polymer molecular structures such as molecular weight. The different molecular weight PEG volume gratings may have different thermoswitching temperatures.

In order to confirm this hypothesis, three different molecular weight PEG samples were used in the thermal switching experiments. Figure 4.11 shows the notch position and diffraction efficiency with respect to temperature plots for PEG 2,000  $\frac{g}{mol}$ , PEG 4,600  $\frac{g}{mol}$ , and PEG 8,000  $\frac{g}{mol}$  volume gratings. Figure 4.11a, c, and e exhibit the characteristic red-shift and increase in diffraction efficiency during the heating cycle while figure 4.11b, d, and f show the reverse effects of the cooling process. The transition temperatures for PEG 2,000  $\frac{g}{mol}$ , PEG 4,600  $\frac{g}{mol}$ , and PEG 8,000  $\frac{g}{mol}$  volume gratings were identified as 46°C, 50°C, and 57°C. Upon cooling, PEG 4,600  $\frac{g}{mol}$  and PEG 8,000  $\frac{g}{mol}$  volume gratings showed 30°C and 35°C transitions, respectively. The various switching temperatures can be attributed to the different melting points of the PEG volume gratings. The PEG 2,000  $\frac{g}{mol}$  volume grating cooling curve shows that the notch position and diffraction efficiency do not have a sharp change, but there is a gradual decrease in both. This is attributed to the slow crystallization kinetics of the PEG 2,000  $\frac{g}{mol}$  confined between layers of crosslinked resin at room temperature.

Therefore, a thermosensitive volume grating with the switching temperatures ranging from  $30^{\circ}\text{C}$  to  $57^{\circ}\text{C}$  can be readily obtained.

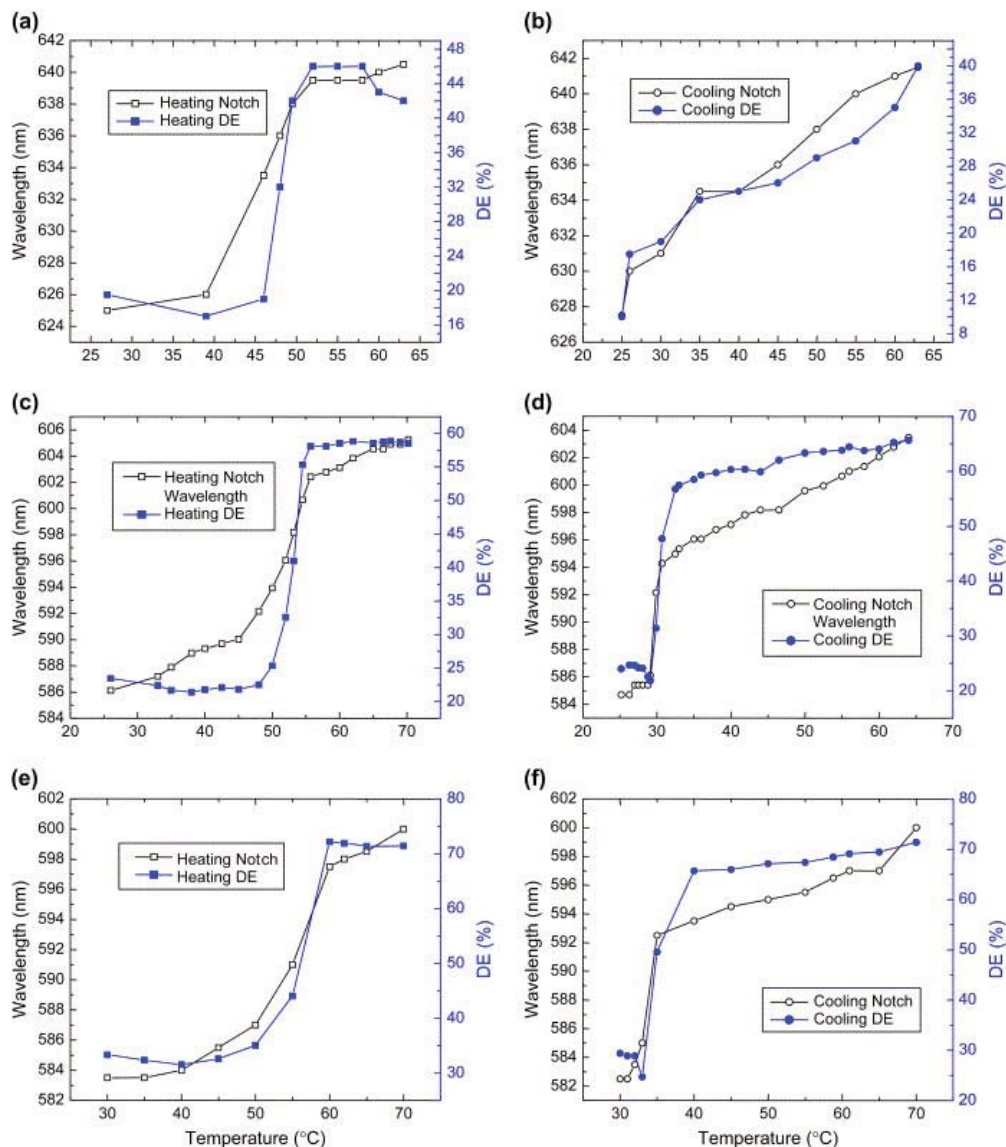


Figure 4.11: Plots of the notch position and diffraction efficiency with respect to temperature in transmission spectra of the PEG volume gratings. (a) PEG 2,000  $\frac{g}{mol}$  on heating, (b) PEG 2,000  $\frac{g}{mol}$  on cooling, (c) PEG 4,600  $\frac{g}{mol}$  on heating, (d) PEG 4,600  $\frac{g}{mol}$  on cooling, (e) PEG 8,000  $\frac{g}{mol}$  on heating, and (f) PEG 8,000  $\frac{g}{mol}$  on cooling.

#### 4.5 The morphology of PCL and PLLA Volume Gratings

In order to investigate whether the PEG volume grating morphology is universal to all semicrystalline homopolymers, HP was applied to mixtures of photocrosslinkable monomers combined with PCL  $M_w$  10,000  $\frac{g}{mol}$  or PLLA  $M_w$  2,000  $\frac{g}{mol}$ . The one-dimensional interference pattern using the same single beam configuration as the PEG case was employed to write the two homopolymers. Figure 4.12 shows the different transmission spectra for PCL (top) and PLLA (bottom). The background transmission in the sample containing PCL is 98% at 500 nm. However, the sample containing PLLA shows random scattering occurring across the visible spectrum and reduces the background transmission at 500 nm to 77%. In addition to the background scattering, the transmission notch is quite different. A sharp notch at 592 nm in the transmission spectrum with modest diffraction efficiency (40%) was observed for the sample containing PCL. While only a small diffraction efficiency (14%) and broad notch at 602 nm was observed in the sample cell containing PLLA. The differences in the transmission spectra between the two homopolymers indicates that the underlying morphology of the patterned homopolymer samples differ from one another. The transmission spectra of PLLA is reminiscent of the scattering observed in holographic polymer dispersed liquid crystals. In the holographic polymer dispersed liquid crystals case, HP of a solution containing liquid crystals results in the formation of periodic droplet layers [126]. In the case of PCL, the absence of scattering indicates that a morphology similar to the PEG volume gratings was patterned.

To confirm these morphologies, the polymer gratings were microtomed along the film normal direction at room temperature similar to the PEG volume gratings. The morphologies of PCL and PLLA observed from TEM, as shown in figure 4.13, are remarkably different. The TEM micrographs of the sample that contained PCL (Figure 4.13a) confirms that alternating layers of homopolymer and crosslinked resin were

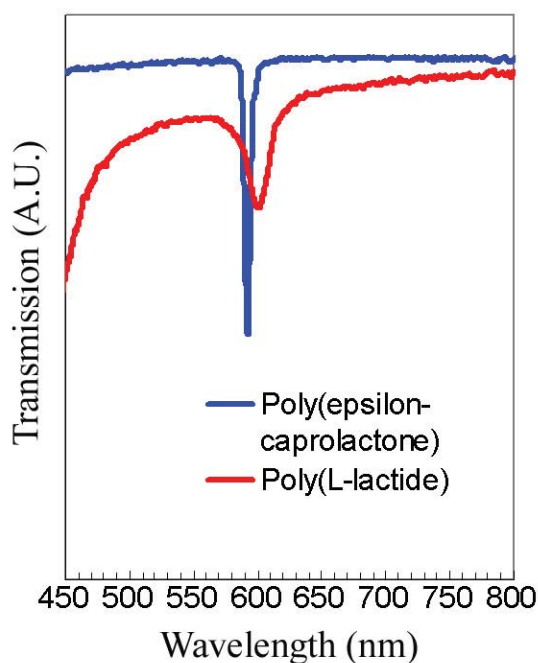


Figure 4.12: Transmission spectra in the visible spectrum for mixtures of photocrosslinkable monomers combined with PCL (top) and PLLA (bottom) that were patterned using HP.

patterned with a period of 190 nm. The darker regions can be attributed to the preferential staining of PCL over NOA 65 (confirmed by staining NOA 65 and PCL for the same length of time and measuring the absorbance of visible light). This is similar to PEG in NOA 65 sample, which showed a long range uniform layered structure. However, the PCL in figure 4.14 shows that the patterning still produced protrusions of the homopolymer into the crosslinked region. In addition, a closer inspection of the PCL region in figure 4.14 reveals dark and light regions. This may be due to preferential staining of amorphous over crystalline polymer segments that formed when the sample was cooled to room temperature. The appearance of PCL in the crosslinked region is intriguing since no scattering was observed in the transmission spectra for this sample.

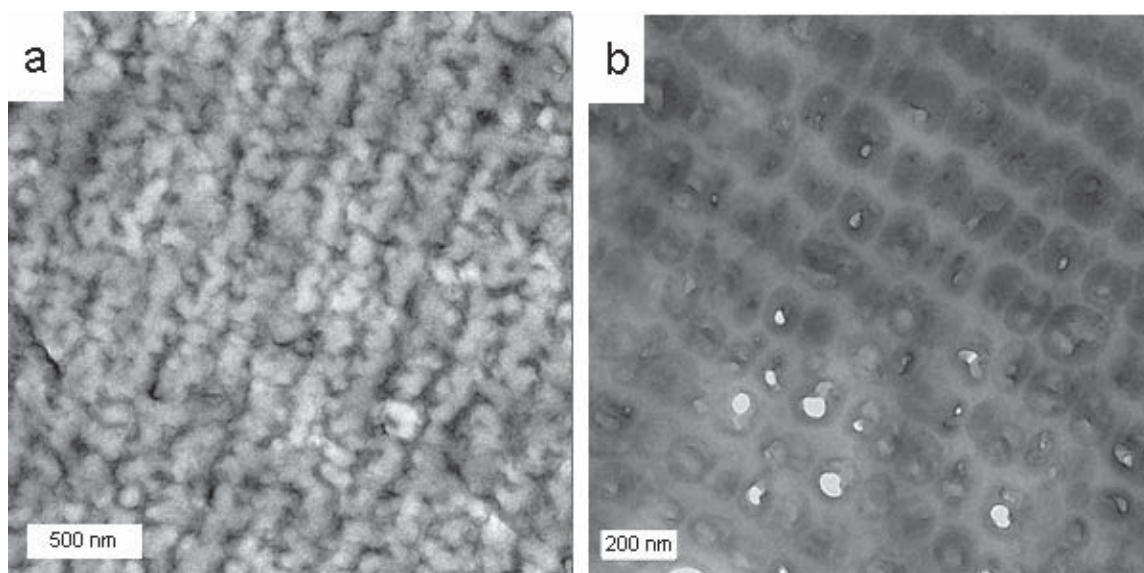


Figure 4.13: TEM of thin cross section of (a) PCL and (b) PLLA confined between layers of crosslinked NOA 65 resin.

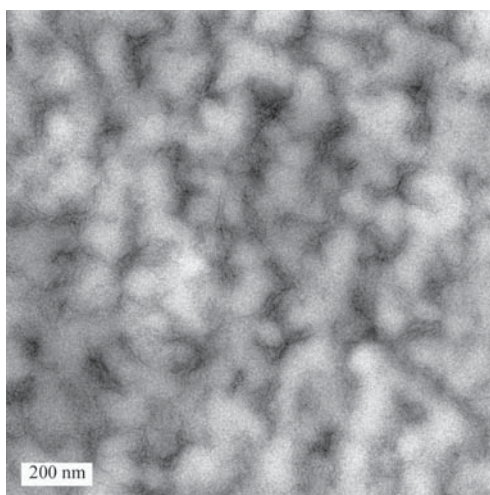


Figure 4.14: A magnified view of the TEM of a thin cross section of a volume grating containing PCL in a mixture with photocrosslinked polymers.

In comparison to PCL and PEG, the sample containing PLLA displays a periodic distribution of droplets with a period of approximately 200 nm in the TEM micrograph of volume grating cross sections (Figure 4.13b). This is consistent with the transmission spectra. The darker regions can be attributed to the preferential staining of PLLA over NOA 65 (confirmed by staining NOA 65 and PLLA for the same length of time and measuring the absorbance of visible light). The periodic distribution of droplets is consistent with the decrease in transmission due to random scattering. HP therefore was successful at patterning both PCL and PLLA indicating that the current method is generic and could potentially pattern a wide range of homopolymers.

#### 4.5.1 A Volume Grating Confining a Blend of PCL and PLLA

The thermal switching in the homopolymer volume gratings initially motivated us to investigate the possibility of multiple thermal switching using a blend of two homopolymers. This was not realized due to the slow crystallization kinetics of PLLA, but the discrepancy between PLLA and PCL volume grating morphology was overcome by blending the two homopolymers together. Patterned volume gratings using HP resulted in a continuous layered structure that was observed in the PEG case. A 50:50 weight ratio of PCL and PLLA was blended in a 1:2 weight ratio with the photocrosslinkable monomers. The prepolymer syrup was then exposed using the simple reflection mode HP setup mentioned in the experimental section. The transmission spectra in figure 4.15 (middle) indicates that the blending of PCL and PLLA resulted in an appreciable improvement in the background transmission over the PLLA case. Background transmission at 450 nm improved to 98% and the notch depth was approximately 40%, as shown figure 4.15 (middle). In comparison to PCL and PLLA the transmission spectra looks similar to the PCL indicating that the polymer blend

can improve the optical properties of one component.

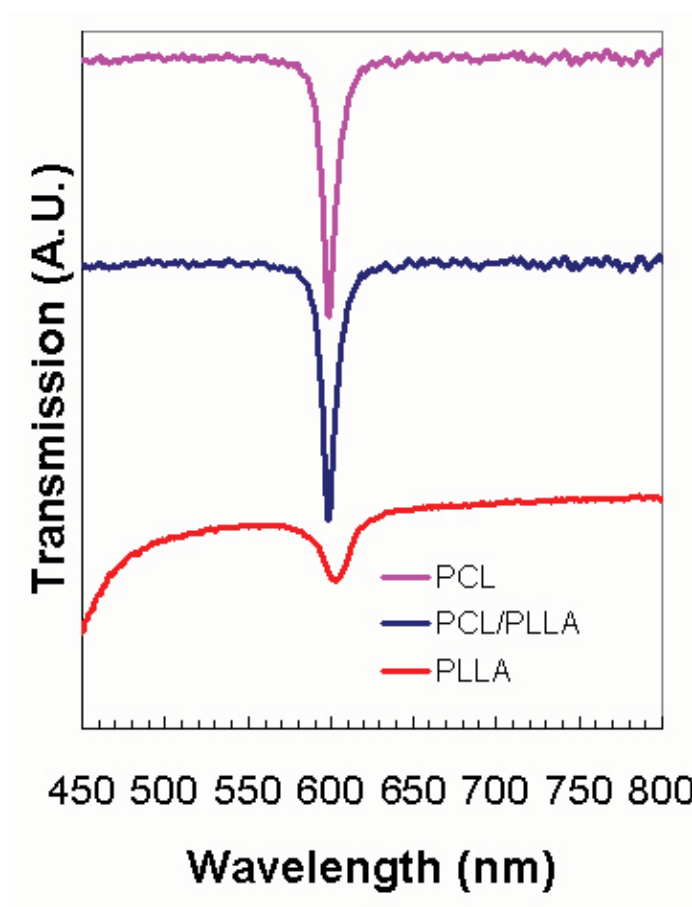


Figure 4.15: Visible light transmission spectra comparing a volume grating containing a 50:50 weight fraction blend of PCL and PLLA in a mixture with 70% photocrosslinked polymers with the homopolymer spectra of the individual components.

The transmission spectra of the polymer blend shows only one notch. Two notches would be expected if the PCL and PLLA had macrophase separated within a single layer containing the two homopolymers over an area larger than a few hundred nanometers. The slight difference in refractive index of PCL and PLLA indicates that they have not macrophase separated even though in bulk the two polymers are immiscible [184, 197]. In order to further understand what is happening the

blended samples were prepared for TEM by sectioning and staining. The periodic one-dimensional structure fabricated by HP is shown in figure 4.16. The 200 nm period measured from the TEM micrograph is consistent with the transmission spectra based on an average refractive index of approximately 1.5 for the polymer solution. The dark region can be assigned to the polymer blend while the crosslinked polymer is in the lighter region. PLLA is preferentially stained over PCL [188]. A closer look at figure 4.16 indicates that there are darker and brighter regions in the polymer blend, which are confined between crosslinked layers of resin. The integrated intensity of the grating profile was performed parallel and perpendicular to the grating, shown in figure 4.17. In the parallel direction randomly spaced regions of the two polymers are observed (Figure 4.17 blue or bottom profile). The brighter regions in figure 4.16 will have higher intensity counts. In contrast, the integrated intensity profile perpendicular to the grating displays a periodic fluctuation with a period of approximately 200 nm (Figure 4.17 red or top profile). The polymer blend resides at the minima of the profile in figure 4.17 (red or top profile). The small notch at 119 nm, 325 nm, and 706 nm in the trough can be attributed to PLLA, which is preferentially stained in this case. A notch is not present at 506 nm due to the large amount of PLLA in this layer. PCL in the present case appears to be between the PLLA and the crosslinked resin. The confinement of the homopolymer PLLA droplets, combined with the continuous layered morphology from blending PCL into the mixture improved the background transmission of the PLLA volume grating.

## 4.6 Summary

Three unique morphologies were discussed in detail in this chapter. In the PEG case, the semicrystalline polymer is confined between crosslinked layers of resin and the polymer lamellae tend to orient themselves parallel to the grating. Thermal switch-

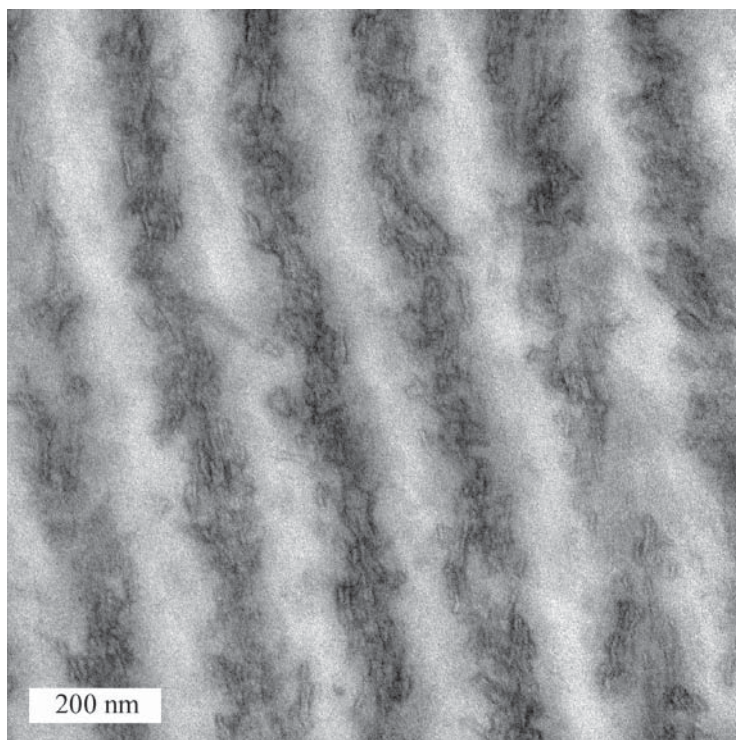


Figure 4.16: A TEM micrograph of a thin cross section of volume grating containing a 50:50 weight fraction blend of PCL and PLLA in a mixture with 70% photocrosslinked polymers.

ing suggests that no interboundary mixing occurs upon melting. In the PCL case, a uniform continuous layered structure was formed. Yet, the boundary contained many polymer protrusions indicating that PCL and crosslinked resin were compatible. In the PLLA case, the formation of droplets indicates that phase separation occurred during the writing process. The three homopolymer morphologies observed display three possible confined structures. If phase separation dominates the morphology than a droplet formation is observed as in the PLLA volume grating case. If crystallization is dominate (as in the PCL case) than a distribution of semicrystalline polymer through a spatially distributed crosslinked polymer network can be observed. In the third case, the phase separation process and crystallization work synergistically to form a semicontinuous layered structure with the homopolymer confined to the dark

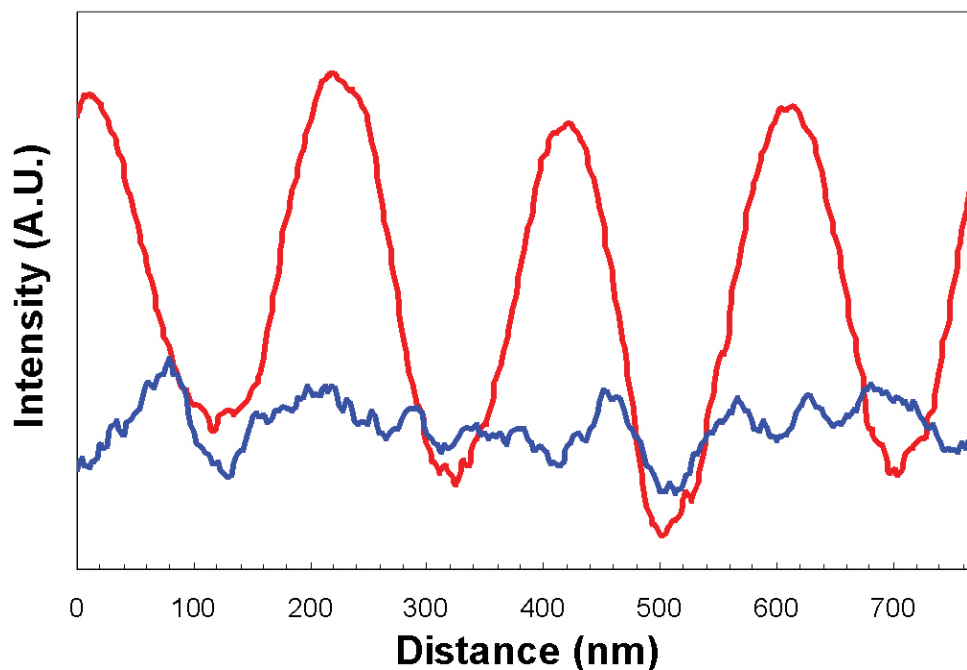


Figure 4.17: The integrated intensity profile parallel (blue-bottom) and perpendicular (red-top) to the patterned layers for a volume grating containing a 50:50 weight fraction blend of PCL and PLLA in a mixture with 70% photocrosslinked polymers.

regions. This was observed in the PEG volume grating case. These results then stimulated an investigation into how two polymers that result in different morphologies would behave when combined together. PLLA and PCL were blended together and patterned using HP. The resulting morphology is unique in that the PLLA is located in the center of the volume grating while the PCL is located at the periphery. HP can therefore pattern polymer blends and improve random scattering properties of volume grating.

## Chapter 5. Hierarchical Volume Gratings from Combined Nanoscale Fabrication Techniques

### 5.1 Introduction

In structures patterned by HP, the feature size is greater than the 100 nm length scale. In contrast, BCP are known to self-assemble into a variety of ordered structures (lamellae, cylinder, gyroid, body centered cubic etc.) on the order of 5 nm to 50 nm. Thus, there is enough room in the HP structure for BCP self-assembly. By combining these two techniques into one system, BCP may be confined in a sub 100 nm nanoenvironment (or scaffold) created by HP fabrication. Further self-assembly of BCP could lead to hierarchical nano and microstructures. Figure 5.1 shows the schematic representation of this hierarchical fabrication process. The hierarchical nanostructures may be fabricated within a few seconds, confining the BCP between layers of crosslinked resin.

### 5.2 Experimental

The double crystalline BCP PEO-b-PCL (5k-b-5k  $\frac{g}{mol}$  molecular weight and a polydispersity of 1.06) combined with photocrosslinkable monomers to make a homogeneous mixture. Reflection gratings containing PEO-b-PCL and crosslinked thiol-ene monomers were fabricated at 80°C using a single beam method. This was done in order to make a one-dimensional periodic structure from a syrup containing 55 wt% NOA 65, 40 wt% PEO-b-PCL, and 5 wt% photoinitiator. Experimental details can be found in the chapter 3. The hierarchical structure and morphology was confirmed using synchrotron SAXS, WAXD, and TEM techniques.

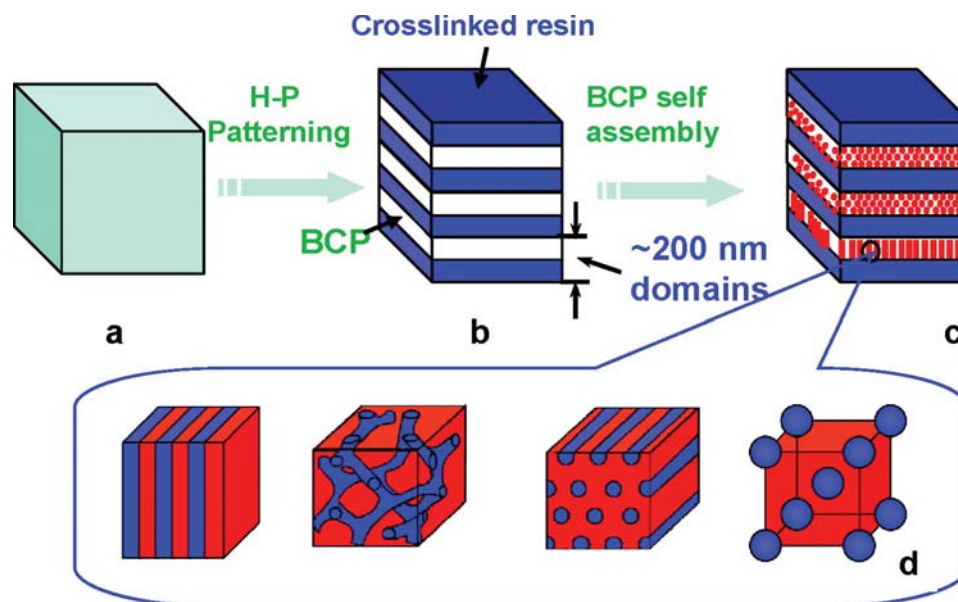


Figure 5.1: Schematic representation of hierarchical nanomanufacturing by combining HP and BCP self-assembly. (a) syrup containing photopolymerizable monomers, BCP, and photoinitiator, (b) HP formed ordered structures on a 200 nm scale, (c) BCP self-assembles in nanodomains created by HP structures, and (d) a variety of different BCP structures could be confined in the HP layers.

### 5.3 The Structure of a PEO-b-PCL Volume Grating

The mixture of photocrosslinkable monomers and PEO-b-PCL exposed to UV light produced appeared to reflect red light. Figure 5.2 shows a sharp notch in the transmission spectrum of a PEO-b-PCL volume grating around 610 nm. The diffraction efficiency of the BCP sample is approximately 48%. The sharp notch in the transmission spectrum suggests that an appreciable refractive index modulation was achieved from the separation of BCP and NOA 65. To confirm this the morphology of the volume grating was studied using TEM. Thin sections (approximately 50 nm thick) of the reflection gratings were obtained by microtoming sample films along the film normal direction. Figure 5.3 shows a TEM micrograph of a thin section of the PEO-b-PCL volume grating.  $\text{RuO}_4$  was used to stain the sample. The TEM micrograph of the

volume grating displays a long range uniform layered structure with alternating dark and light regions. This morphology is similar to the PEG volume gratings discussed in chapter 4, which also had a long range uniform layered structure. In the present case, the BCP formed continuous layers segregated by the crosslinked resin. This might be due to better compatibility between PEO-b-PCL and the crosslinked resin, which led to slower phase separation kinetics. Therefore, phase separation occurred in the later stages of the polymerization at which point uniform layered structures were formed. The interface between the resin and the BCP is vague and it is clear that some of the BCP are trapped in the resin, confirming the incomplete phase separation. This morphology is consistent with the transmission spectrum results. In figure 5.2, nearly 100% background transmission was observed for the PEO-b-PCL volume gratings, which is again similar to the background transmission observed in PEG volume gratings. The lack of random scattering in the PEG volume grating case was attributed to a continuous layered structure. In the PEO-b-PCL volume gratings, BCP and crosslinked resin were separated into a continuous layer-by-layer structure resulting in no significant light scattering, which in turn led to the nearly 100% baseline transmission.

The alternating layers of NOA 65 and BCP at the submicron level leads to the observation of volume gratings as seen in figure 5.2. Since the refractive index of NOA 65 is approximately 1.52 and PEO-b-PCL is approximately 1.46, the grating d-spacing can be obtained using equation  $\lambda = 2n_0\Lambda$ . The position of the notch in figure 5.2 and the average refractive index of the thiol-ene polymer and PEO-b-PCL were used to calculate the resulting grating period, which is approximately 204 nm. The grating period that was calculated matches with the observed layer spacing of the grating from the TEM results.

Upon phase separation between NOA 65 and PEO-b-PCL, the PEO-b-PCL was confined into 80 nm to 100 nm thick layers. Within these layers the BCP has room

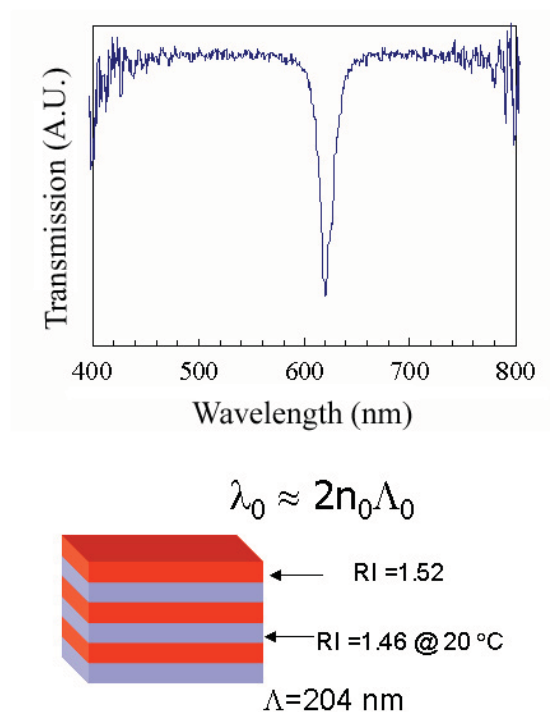


Figure 5.2: Transmission spectrum of a mixture of NOA 65 and PEO-b-PCL patterned using HP.

to microphase separate and form ordered structures on a smaller length scale. Figure 5.4 shows the enlarged TEM images of figure 5.3. Inside the BCP layer alternating dark and light lines can be seen. The lines are relatively parallel to the grating layer. There are approximately six dark lines within each BCP layer and the period is 17 nm to 20 nm. These dark and light lines represent PCL and PEO regions and the contrast arises from the  $\text{RuO}_4$  staining. The alternating lines indicate that PEO and PCL are phase separated within each BCP layer. Since both PEO and PCL are crystalline polymers, crystallization occurred as the grating was cooled from the writing temperature (approximately  $80^\circ\text{C}$ ) to room temperature. This was confirmed by DSC experiments, which are discussed later in this chapter. In this particular case the PEO and PCL lamellar crystals were formed and aligned parallel to the HP layers upon crystallization. Therefore, a layer-in-layer hierarchical nanostructure was

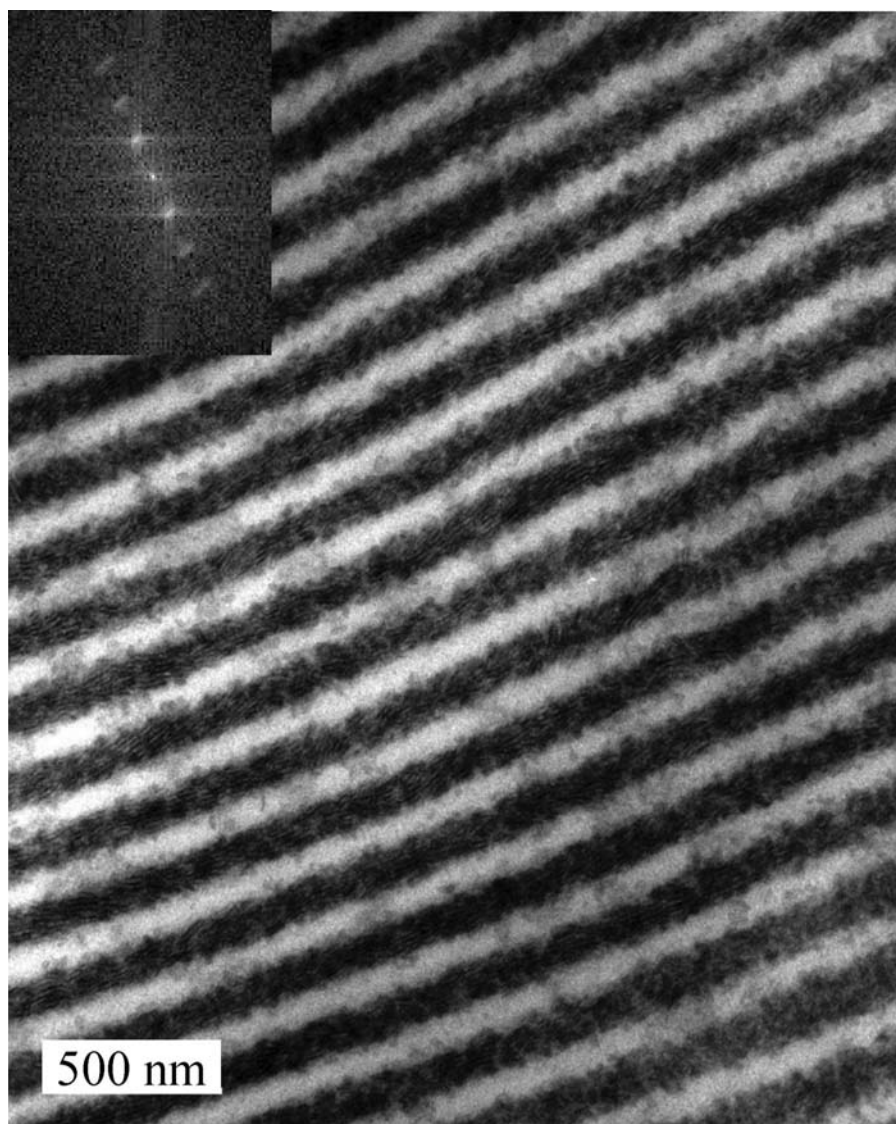


Figure 5.3: TEM image of the crosssection of a PEO-b-PCL volume grating.

successfully achieved based on top-down and bottom-up fabrication techniques. The ordered scales are approximately 200 nm and 20 nm, respectively.

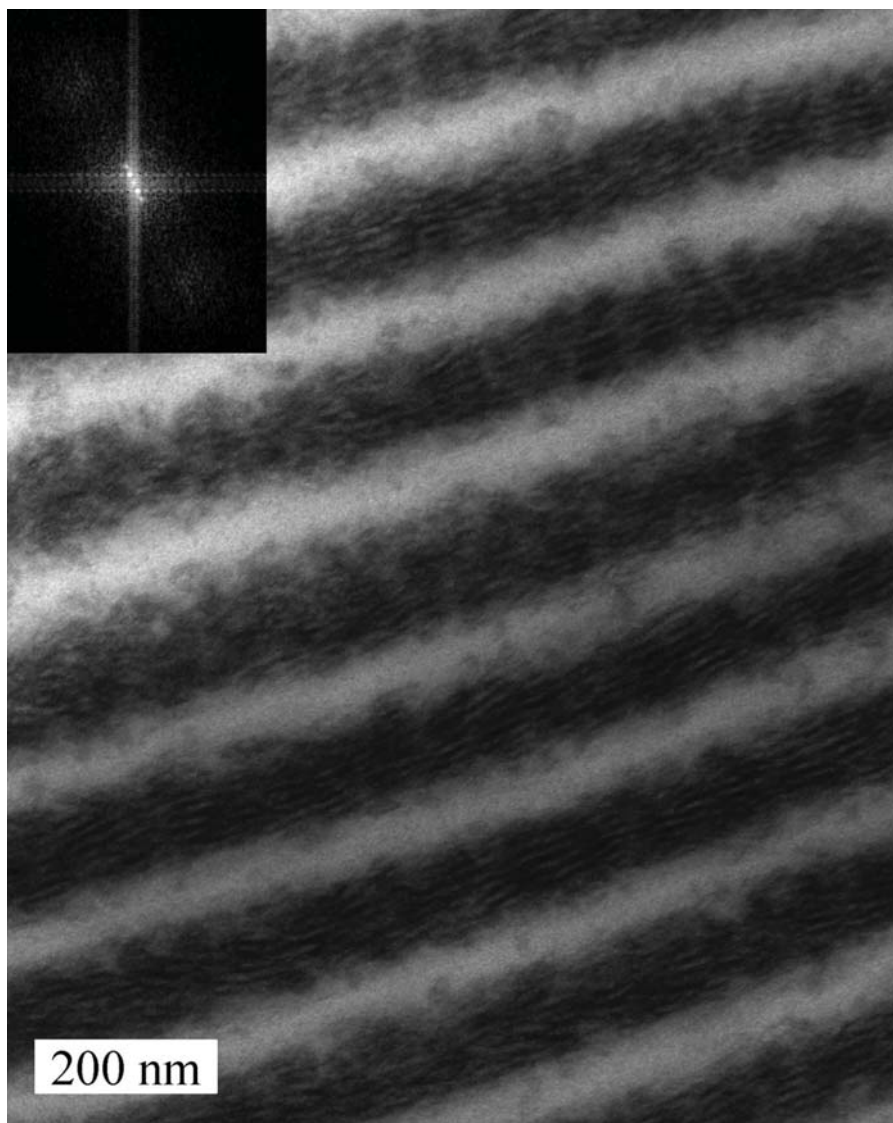


Figure 5.4: A closer look at the TEM image of the cross section of a PEO-b-PCL volume grating.

To further confirm the BCP structure and the orientation of the macromolecular chain, SAXS and WAXD experiments were conducted. Thin, free-standing films approximately 15  $\mu\text{m}$  thick were obtained from the PEO-b-PCL volume grating cell.

Two-dimensional SAXS experiments were carried out with the film being parallel and perpendicular to the X-ray beam and the results are shown in figure 5.5a and b. The inset of figure 5.5a shows an integration of the two-dimensional pattern. The first and second order reflections in the PEO-b-PCL volume grating corresponds to  $q$  approximately  $0.293 \text{ nm}^{-1}$  and  $0.583 \text{ nm}^{-1}$  with a d-spacing of approximately 21 nm for the first order reflection. This indicates a lamellar structure of the BCP with a period of 21 nm, which is consistent with the TEM observations. The control experiment was performed on pure PEO-b-PCL sample and a similar lamellar structure was observed, as shown in figure 5.6. While the X-ray beam was perpendicular to the grating, no small-angle scattering was observed (Figure 5.5b), indicating that the BCP lamellar normal is perpendicular to the grating layers.

WAXD and DSC experiments were employed to study the crystallization behavior of the free-standing PEO-b-PCL volume grating. Figures 5.5c and d show the two-dimensional WAXD patterns with the X-ray beam aligning parallel (Figure 5.5c) and perpendicular (Figure 5.5d) to the grating surface. In figure 5.5c, orientated diffraction arcs were observed in the WAXD pattern, while in figure 5.5d only a ring pattern was obtained. A detailed investigation determined that the inner diffraction arcs can be assigned as PEO (120) with a d-spacing of 0.494 nm [192]. The outer diffraction can be assigned as the overlap of PEO (-132), (032), (112), (-212), (124), (-204), and (004) reflections with a d-spacing of approximately 0.398 nm [192]. The central diffraction arc located on the meridian with a d-spacing of 0.412 nm can be attributed to the (110) PCL diffraction [198]. Thus, both PEO and PCL are crystalline in the confined nanoenvironments. This can also be confirmed with the DSC experiments as shown in figure 5.7. Both pure PEO-b-PCL and the volume gratings were subjected to DSC cooling and heating experiments. For pure BCP two exothermic peaks can be observed at  $26^{\circ}\text{C}$  and  $33^{\circ}\text{C}$  during cooling, corresponding to PEO and PCL crystallization, respectively. Upon heating, both PEO and PCL

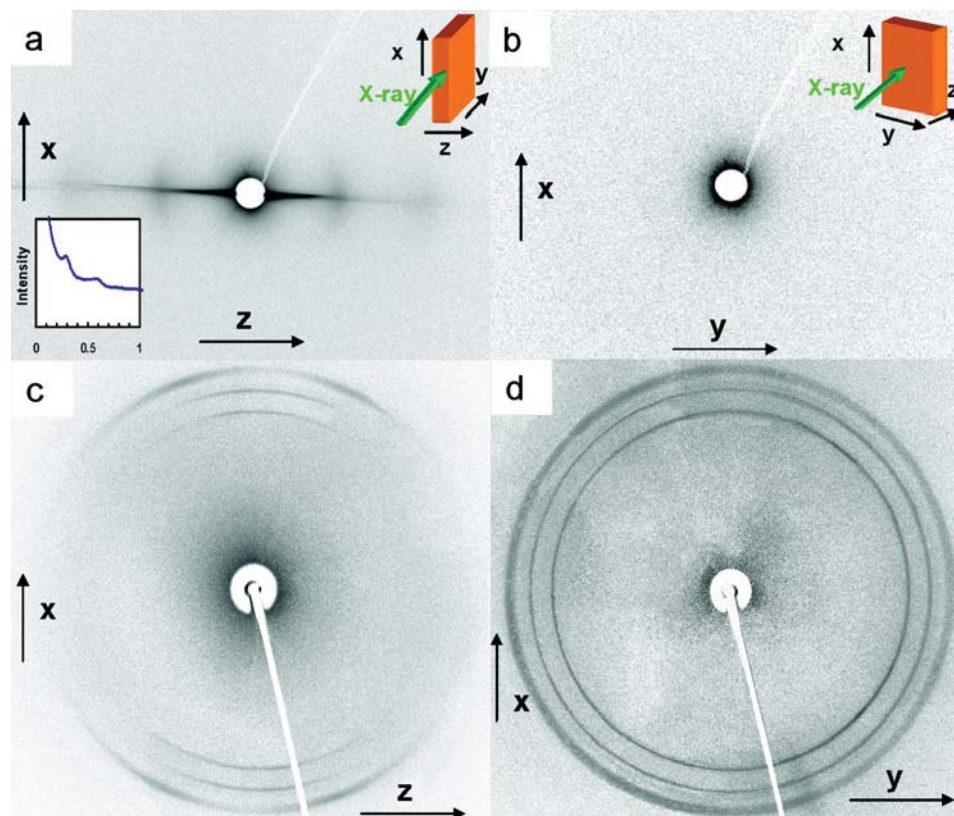


Figure 5.5: Two-dimensional SAXS (a and b) and two-dimensional WAXD (c and d) of a PEO-b-PCL volume grating. The X-ray beam was parallel (a,c) and perpendicular (b,d) to the grating film, as indicated in the top-right insets of (a) and (b).

melt at a similar temperature,  $59^{\circ}\text{C}$ . For the grating sample, much weaker and broader crystallization was observed at  $4^{\circ}\text{C}$  and  $22^{\circ}\text{C}$ . The melting temperature of PEO-b-PCL was  $38^{\circ}\text{C}$ , which occurs  $21^{\circ}\text{C}$  lower than the pure PEO-b-PCL. The lower melting and crystallization temperatures of PEO and PCL can be attributed to the confinement effect of the NOA 65 matrix. This effect is similar to the previous chapter's results in the case of semicrystalline polymers. Furthermore, according to our previous studies on the PEG volume grating structure, the location of the PEO (120) diffraction on the meridian in the edge-on diffraction pattern suggests that the PEO chains are parallel to the lamellar normal. The edge-on and flat-on patterns

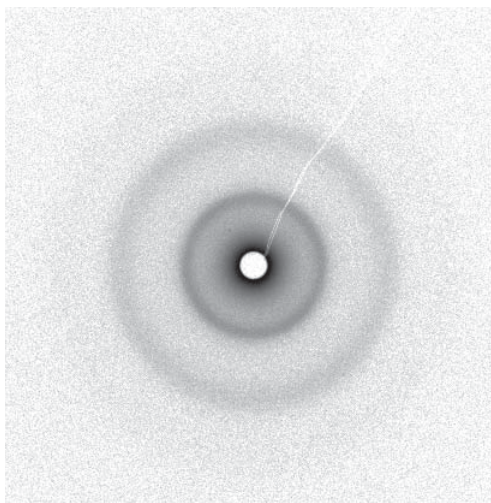


Figure 5.6: The two-dimensional SAXS of a bulk sample of PEO-b-PCL.

of the PCL (110) peak suggest that the PCL chains are also parallel to the PEO chains and perpendicular to the BCP lamellae and HP layers. The chain orientation is similar to the confined crystallization of PEO and PCL in the PEO-b-PS and PCL-b-PS case [192,199]. The perpendicular chain orientation of the PEG and PCL crystal appears to be in a thermodynamically more stable state at the present crystallization condition. The hierarchical nanostructure of the HP BCP can be summarized in figure 5.8. On the 200 nm level, lamellar layered structures are formed due to HP, and the BCP are confined between the crosslinked resin. Upon cooling, PEO and PCL undergo phase separation/crystallization resulting in a structure with a period of approximately 20 nm and both chains are parallel to the layer normal.

HP and BCP self-assembly were combined into one system (PEO-b-PCL volume grating) to manufacture layer-in-layer hierarchical nanostructures. Large uniform lamellar structures between the crosslinked NOA 65 resin and PEO-b-PCL were formed with a period of approximately 200 nm from the HP technique. The refractive index modulation between NOA 65 resin and the BCP led to the observation of a reflection notch in the transmission spectrum with a diffraction efficiency of approxi-

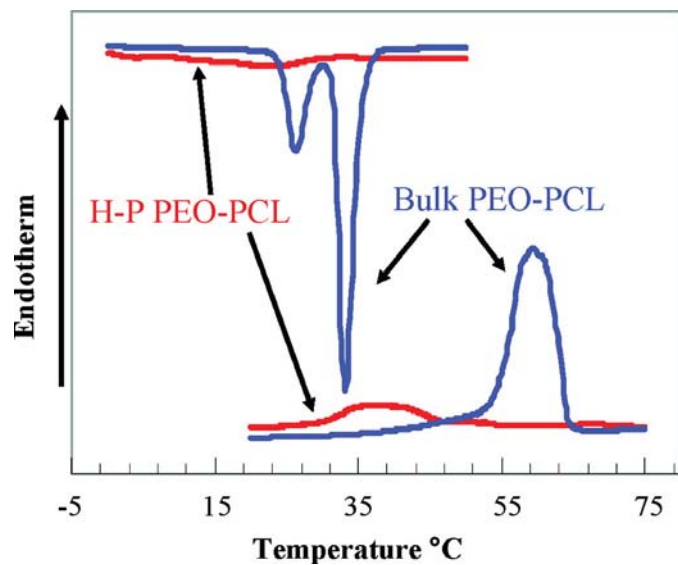


Figure 5.7: DSC thermograms of PEO-b-PCL in bulk and in a volume grating.

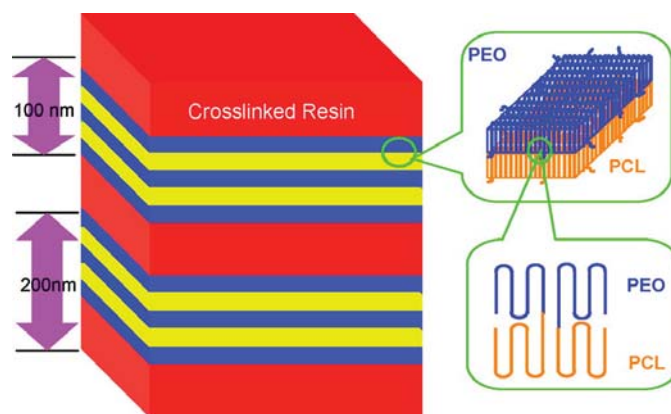


Figure 5.8: Schematic representation of the hierarchical nanostructures formed by combining HP and BCP self-assembly.

mately 48%. This indicates phase separation of BCP and NOA 65 resin. The nearly 100% background transmission between 400 nm and 800 nm was attributed to the continuous layer-by-layer structure in the present system. The PEO-b-PCL confined between the NOA 65 resin, phase separated into a lamellar structure with a period of approximately 21 nm, as determined by the SAXS. DSC results suggested that the crystallization of PEO and PCL confined within the crosslinked matrix showed lower melting and crystallization temperatures than the bulk samples. Synchrotron WAXD experiments showed that PEO and PCL chain axes were parallel to the grating normal.

#### 5.4 Summary

HP and BCP self-assembly were combined in one system to manufacture layer-in-layer hierarchical nanostructures. Large size, uniform lamellar structures between the crosslinked NOA 65 resin and PEO-b-PCL were formed with a period of approximately 200 nm from the HP technique. The refractive index modulation between NOA 65 resin and the BCP led to the observation of a reflection notch in the transmission spectra with a diffraction efficiency of approximately 48%, indicating phase separation of BCP and crosslinked resin. The nearly 100% background transmission between 400 nm and 800 nm was attributed to the continuous layer-by-layer structure in the present system. The PEO-b-PCL was confined in the NOA 65 resin, and within each BCP region, PEO-b-PCL phase separated into a lamellar structure with a period of 21 nm as determined by the synchrotron SAXS experiments. DSC results suggested that the crystallization of PEO and PCL confined within the NOA 65 matrix showed a decrease in the melting and crystallization temperatures. Synchrotron WAXD showed that PEG and PCL chain axes were parallel to the grating normal. These experiments indicate that HP of the prepolymer solution resulted in

confinement of the PEO-b-PCL.

## Chapter 6. Thermally Switching Hierarchical Volume Gratings

### 6.1 Introduction

The thermal switching of hierarchical structures was observed in BCP systems [81, 125]. In those cases a large reversible change in the optical properties led to an observable change in wavelength and diffraction efficiency. The unique properties of hierarchical photonic structures is promising for device applications. However, the high specificity in design criteria for hierarchical self-assembling BCP limits the number of materials that can be used. In order to overcome the limitations of self-assembly, two nanoscale fabrication techniques, BCP microphase separation and HP, can be combined. We attempt to produce a temperature sensitive hierarchical photonic structure based on the combination of nanoscale fabrication techniques. In the previous chapters, the morphology and structure of polymer and BCP were discussed. In addition, the PEO volume gratings underwent volumetric changes when heated and cooled due to crystallization and melting. These observations indicate that a hierarchical volume grating composed of the BCP PEO-b-PCL would also undergo thermal switching. Heating and cooling the PEO-b-PCL volume grating results in a switching of the reflected wavelength and the diffraction efficiency due to crystallization and melting. A closer inspection of the diffraction efficiency reveals that a dip occurs during the thermal switching. The origin of the dip and subsequent morphological changes associated with the dip are discussed in the proceeding sections.

### 6.2 Materials and Methods

Reflection gratings were fabricated using a single laser beam and prism configuration described in chapter 3. PEO-b-PCL, molecular weight 10,000  $\frac{g}{mol}$  was combined

with NOA 65 and Darocure 4265. The typical mixture contained 65% crosslinkable monomers, 30% BCP, and 5% initiator. This mixture was combined with 4 to 10 micron spacers and placed between two glass slides. In some studies the fraction of BCP was varied, in those cases the ratio of NOA 65 to initiator was held constant.

Characterization of the BCP volume gratings employed several techniques including TEM to investigate the morphology. Optical characterization of the reflection gratings was carried out using an Ocean Optics fiber spectrometer coupled with an Instec hotstage. In addition, FT-IR and DSC were also employed to determine the crystallization and melting behavior as a function of the grating's temperature. A more detailed explanation can be found in chapter 3.

### 6.3 Thermal Tuning of a PEO-b-PCL Volume Grating

HP of a prepolymer mixture containing PEO-b-PCL and crosslinked thiol-ene monomers were fabricated at  $75^{\circ}\text{C}$ . Transmission spectra and TEM confirm that a hierarchical volume grating was fabricated, as seen in figure 6.1. (The TEM micrograph was taken of a PEO-b-PCL volume grating that had been written at  $75^{\circ}\text{C}$  for 2 minutes then quenched to room temperature and ultramicrotomed.) The sharp notch in the transmission spectrum indicates that an appreciable refractive index modulation was achieved from the separation of BCP and NOA 65. The PEO-b-PCL region occupied approximately 85 nm, while the crosslinked region occupied 129 nm. The reflecting wavelength notch position was 608 nm which is consistent with the overall pitch of the grating measured from TEM as 214 nm. In figure 6.1, alternating dark and light lines are observed. The BCP region appears darker than the crosslinked region due to the contrast that arises from the  $\text{RuO}_4$  staining. Inside the darker region black and gray lines are apparent and correspond to PCL and PEO, respectively. Since both PEO and PCL are crystalline polymers, crystallization occurred as the grating

was cooled from the writing temperature ( $75^{\circ}\text{C}$ ) to room temperature. The PEO and PCL lamellar crystals formed and aligned parallel to the HP layers upon crystallization. This indicates that a hierarchical nanostructure based on the top-down and bottom-up fabrication techniques with ordered scales of 200 nm and 20 nm was fabricated similar to the preceding chapter.

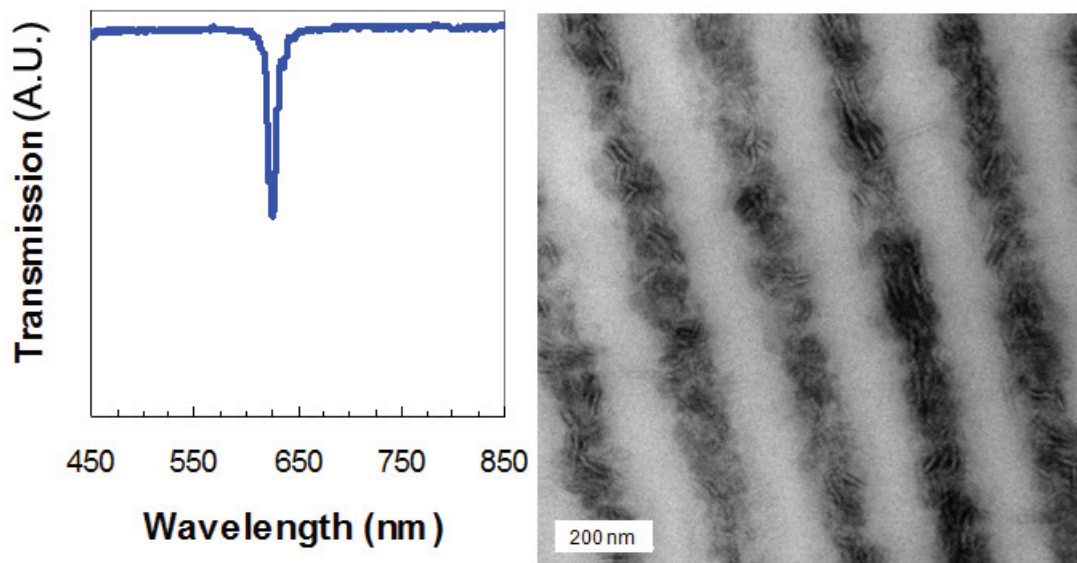


Figure 6.1: The transmission spectra and TEM of PEO-b-PCL patterned using HP.

The PEO-b-PCL volume grating described above was heated from  $25^{\circ}\text{C}$  to  $75^{\circ}\text{C}$  at  $1\frac{^{\circ}\text{C}}{\text{min}}$  then cooled to  $0^{\circ}\text{C}$  at the same rate. The progression of the transmission notch wavelength position and diffraction efficiency from figure 6.1 was followed with a photodetector and white light source (Figure 6.2). A dynamic behavior with respect to temperature occurs when the PEO-b-PCL volume grating was heated and cooled. The diffraction efficiency and notch position over the scanning temperatures increased during heating and decreased when cooled. Upon heating, the notch position redshifts from 608 nm to 622 nm, and the diffraction efficiency changes with temperature from 65% to 67%. In figure 6.2, there is a change in the notch position and a dip in the

diffraction efficiency starting at around  $33^{\circ}\text{C}$  (region b of Figure 6.2) and ending at  $50^{\circ}\text{C}$  with a minimum at  $47^{\circ}\text{C}$  in the heating curve. Upon cooling, the notch position shifts back to the original 608 nm position and the diffraction efficiency changes back to 63%. A blue-shift in the notch position occurred when the volume grating cooled from  $37^{\circ}\text{C}$  to  $27^{\circ}\text{C}$  (region d of Figure 6.2). Over the same temperature range the diffraction efficiency goes through a minimum at  $34^{\circ}\text{C}$  (region d of Figure 6.2). The heating and cooling curves show that changes in diffraction and notch position are synchronized.

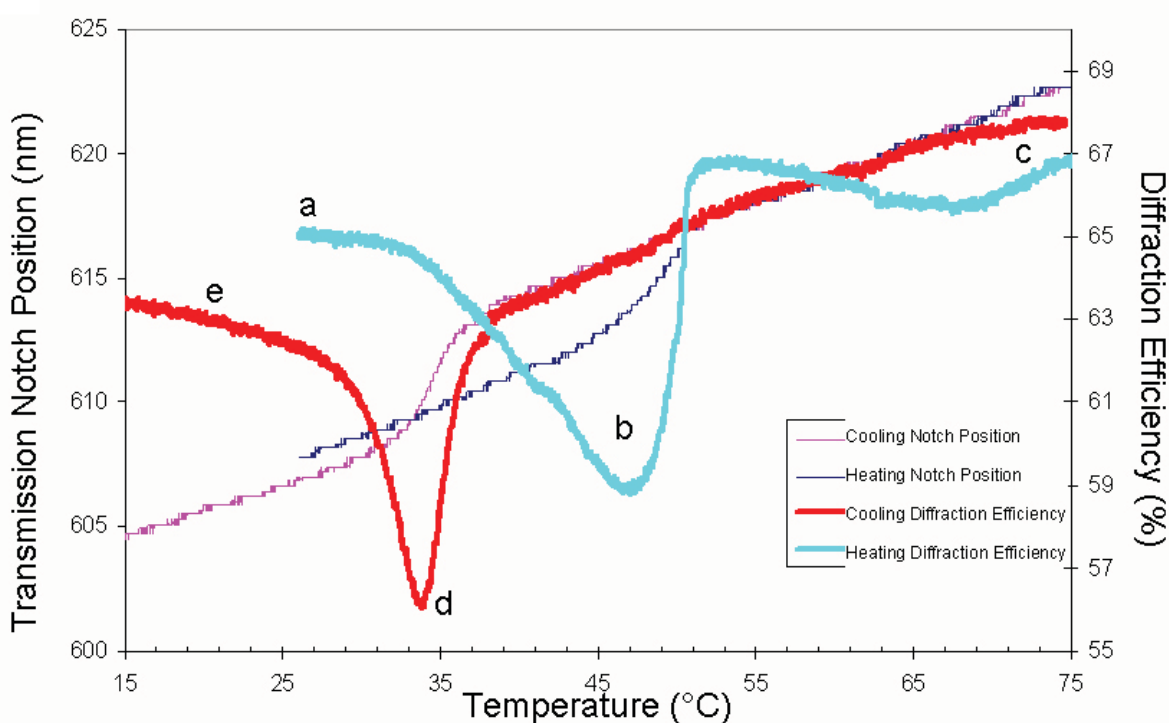


Figure 6.2: The transmission notch position wavelength and diffraction efficiency of PEO-b-PCL hierarchical grating being heated from  $25^{\circ}\text{C}$  to  $75^{\circ}\text{C}$  then cooled down to  $0^{\circ}\text{C}$  at  $1\frac{^{\circ}\text{C}}{\text{min}}$ .

This temperature induced notch wavelength and unique diffraction efficiency change is attributed to the phase transition of PEO-b-PCL from a crystalline to molten state. DSC thermograms of PEO-b-PCL volume gratings reveal that the melting/crystal-

lization temperatures for the BCP are lower than the bulk samples when they were heated and cooled at  $10 \frac{^{\circ}\text{C}}{\text{min}}$ . For the pure BCP, two exothermic peaks can be observed at  $26^{\circ}\text{C}$  and  $33^{\circ}\text{C}$  during cooling, which correspond to PEO and PCL crystallization, respectively. Both PEO and PCL melt at  $59^{\circ}\text{C}$  when heated. The melting and crystallization temperatures of the PEO-b-PCL volume gratings match those temperatures, which correspond to rapid changes in diffraction efficiency and notch position as indicated in figure 6.3. This suggests that the dynamic behavior of the PEO-b-PCL volume grating is due to the crystallization/melting of PEO-b-PCL crystals.

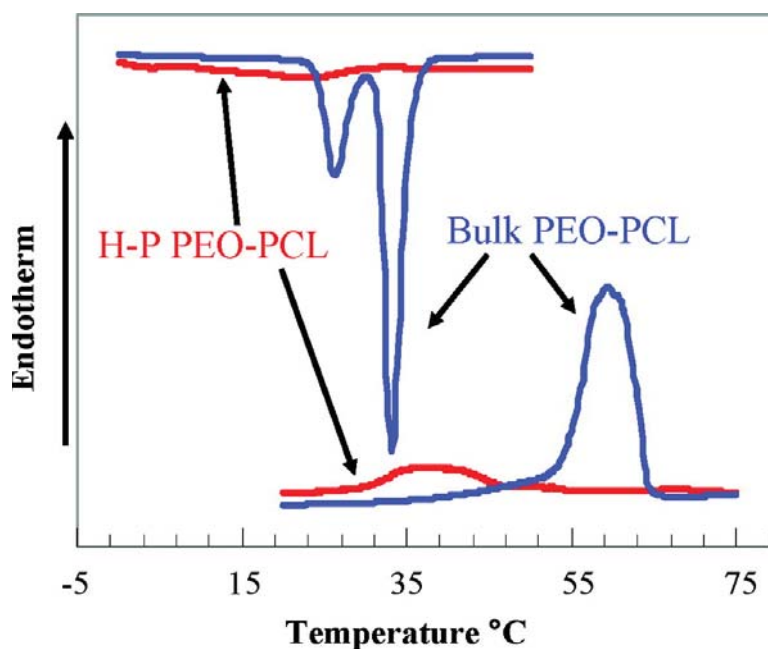


Figure 6.3: DSC thermograms of PEO-b-PCL in bulk and in volume gratings. The cooling and heating rate was  $10 \frac{^{\circ}\text{C}}{\text{min}}$ .

The temperature induced switching of the hierarchical volume gratings can be attributed to both PEO and PCL inside the volume grating. FTIR was performed to confirm the crystallization behavior of PEO and PCL. FTIR spectra of free standing volume gratings were recorded isothermally at different temperatures starting from room temperature. Figure 6.4a is the FTIR spectra for PEO-b-PCL volume grating

at room temperature. In order to evaluate the PEO and PCL melting behavior, the vibrational bands at  $843\frac{1}{cm}$  and  $731\frac{1}{cm}$  were chosen for their characteristic absorption dependence on crystalline PEO and PCL, respectively [200]. A decrease in intensity for both PEO and PCL from room temperature to  $75^{\circ}C$  was observed in figure 6.4b. The onset, peak, and end of PEO melting measured from the intensity change at  $843\frac{1}{cm}$  occurred at  $33^{\circ}C$ ,  $40^{\circ}C$ , and  $50^{\circ}C$ , whereas the onset, peak, and end of PCL melting occurred at  $41^{\circ}C$ ,  $46^{\circ}C$ , and  $50^{\circ}C$ , respectively. The melting of PEO and the onset of the dip at  $33^{\circ}C$  match, indicating that the onset of the decrease in diffraction efficiency can be attributed to PEO melting. From  $41^{\circ}C$  to  $47^{\circ}C$  both PEO and PCL are melting according to figure 6.4b, which corresponds to a continued decrease in the diffraction efficiency. The subsequent increase and end of the diffraction efficiency switching can be attributed to the completion of PEO and PCL melting. The fact that both PEO and PCL melting contributes to the dip in diffraction efficiency provides evidence that the dip is due to molten PEO-b-PCL and not recrystallization of either PEO or PCL.

#### 6.4 Thermal Tuning and the Morphology of the Volume Grating

In order to understand the optical behavior for the PEO-b-PCL hierarchical volume gratings, samples were patterned at  $75^{\circ}C$ , then quenched to room temperature. The samples were then heated and cooled at  $1\frac{^{\circ}C}{min}$  to a predetermined temperature and then quenched in liquid nitrogen and investigated using TEM. Little change in the wavelength position and diffraction efficiency is detected in region a,  $25^{\circ}C$  to  $32^{\circ}C$  in figure 6.1. The observation is consistent with the DSC data that suggests no melting is occurring. The corresponding TEM micrograph in figure 6.1 shows the hierarchical structure at room temperature and indicates good separation between the BCP region and the crosslinked region. The BCP region was measured to occupy approximately

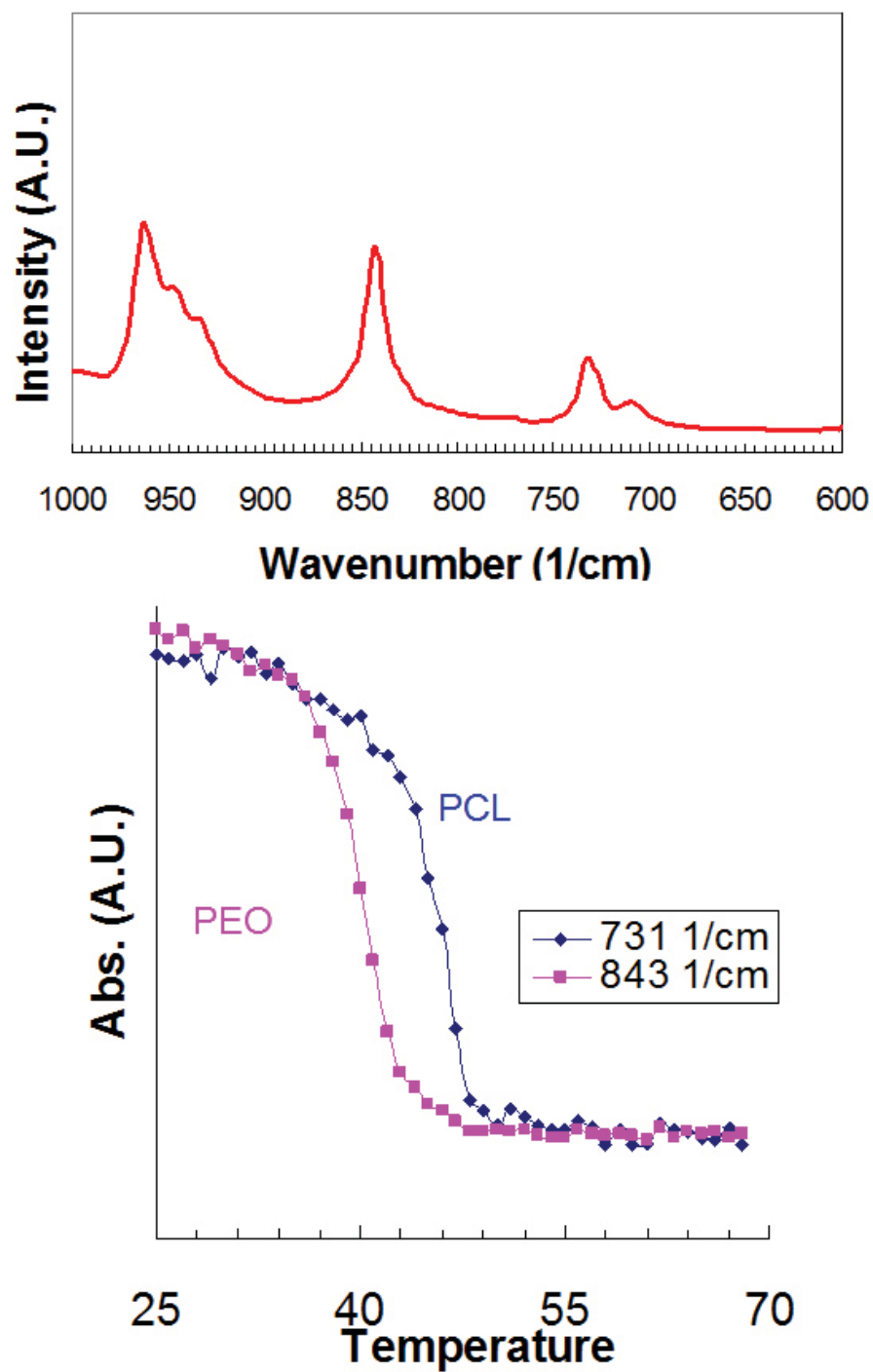


Figure 6.4: (a) FT-IR at room temperature of a PEO-b-PCL volume grating containing. The change in intensity at  $843 \frac{1}{cm}$  and  $731 \frac{1}{cm}$  going from room temperature to  $75^{\circ}C$ .

85 nm while the crosslinked region occupied 129 nm. The reflecting wavelength notch position was 608 nm which is consistent with the overall pitch of the grating measured from TEM as 214 nm. The BCP region, which is stained darker than the Norland region in figure 6.1 (this was confirmed in chapter 5) contains alternating dark and light lines. These lines correspond to PCL and PEO, respectively. At room temperature the BCP is in the crystalline state as evidenced by DSC and does not appear to melt until  $32^{\circ}\text{C}$ .

A noticeable change in diffraction efficiency starting at  $32^{\circ}\text{C}$  and continuing to  $47^{\circ}\text{C}$  appears simultaneously as the grating wavelength begins to red-shift. Figure 6.5 shows two TEM micrographs of a sample that had been heated at  $1\frac{\circ\text{C}}{\text{min}}$  to  $47^{\circ}\text{C}$  and then quenched in liquid nitrogen. The morphology of the grating is noticeably different as the boundary between crosslinked resin and BCP has smeared and dark protrusions can be seen in the crosslinked region, figure 6.5a. The corresponding diffraction efficiency at  $47^{\circ}\text{C}$  has decreased to a minimum, approximately 59%, while the wavelength begins to red-shift from  $32^{\circ}\text{C}$  to  $47^{\circ}\text{C}$ . The reflecting wavelength notch position, 613 nm, was used to calculate a grating pitch of 208 nm which is consistent with the overall pitch of the grating measured from TEM as 211 nm. The change in diffraction efficiency can be ascribed to changes in the refractive index contrast, average refractive index, and the number of layers in the grating. The BCP begins to melt when the volume grating was heated through region b. At higher magnification, figure 6.5b shows that in this region lamellae like protrusions of the BCP move into the crosslinked resin region. The alternating dark-light-dark morphology of the protrusions is indicative of either cylinder or lamellae with the PEO portion surrounded by PCL. The phase separation between resin and BCP can be seen and the BCP confined between the crosslinked resin has a period of approximately 22 nm measured from the TEM micrograph.

When the PEO-PCL is heated from  $47^{\circ}\text{C}$  to  $50^{\circ}\text{C}$  the diffraction efficiency and

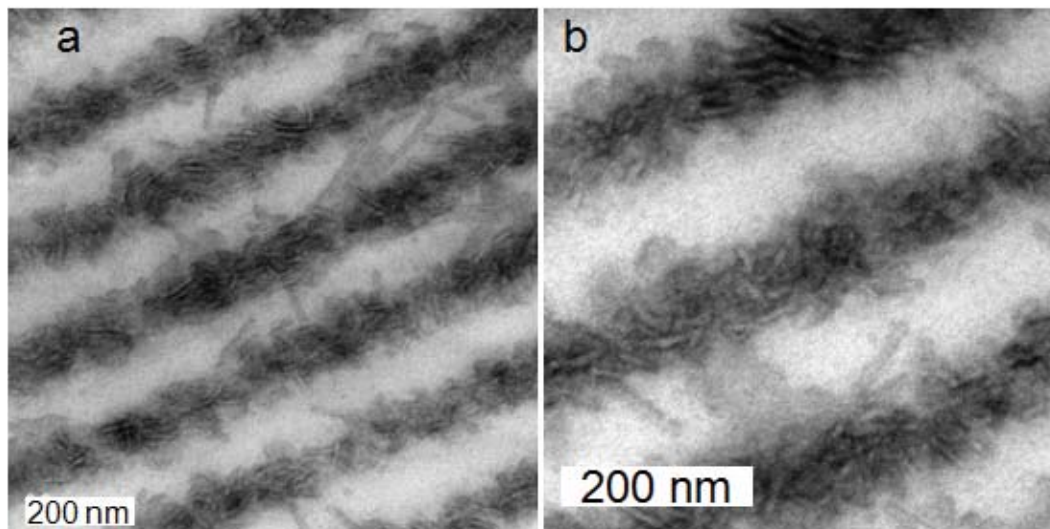


Figure 6.5: TEM micrographs of (a) PEO-b-PCL grating quenched from  $47^{\circ}\text{C}$  and (b) a magnified image of the volume grating.

the wavelength of the transmission notch increases and continues to red-shift (corresponding to region c of Figure 6.2). The red-shift in the notch position of the wavelength can be attributed to the continued melting of approximately 90% of the BCP, which contributes to an increase in the grating period. This is due to volume expansion and the continued decrease in the average refractive index. From  $50^{\circ}\text{C}$  to  $75^{\circ}\text{C}$  we see a small monotonic shift in the wavelength and a small increase in the diffraction efficiency. At the end of heating, the notch position has shifted to 624 nm from 617 nm while the diffraction efficiency has not changed significantly, less than 1%. In figure 6.6 the cross section of the grating shows that the BCP occupies 105 nm of the grating period, while the crosslinked resin occupies 113 nm. The overall size of the grating is 218 nm. The change in the fractional width of the area occupied by the BCP indicates that an increase in diffraction efficiency is expected. This is due to the increase in refractive index contrast as the PEO-b-PCL goes from crystalline to melt and the increase in the fractional width of the BCP region. The observation that

the diffraction efficiency does not change significantly is then counter to what would be expected. This suggests that the movement of PEO-b-PCL into the crosslinked region, observed in figure 6.6, significantly impacted the change in the diffraction efficiency from room temperature to  $75^{\circ}\text{C}$  upon heating.

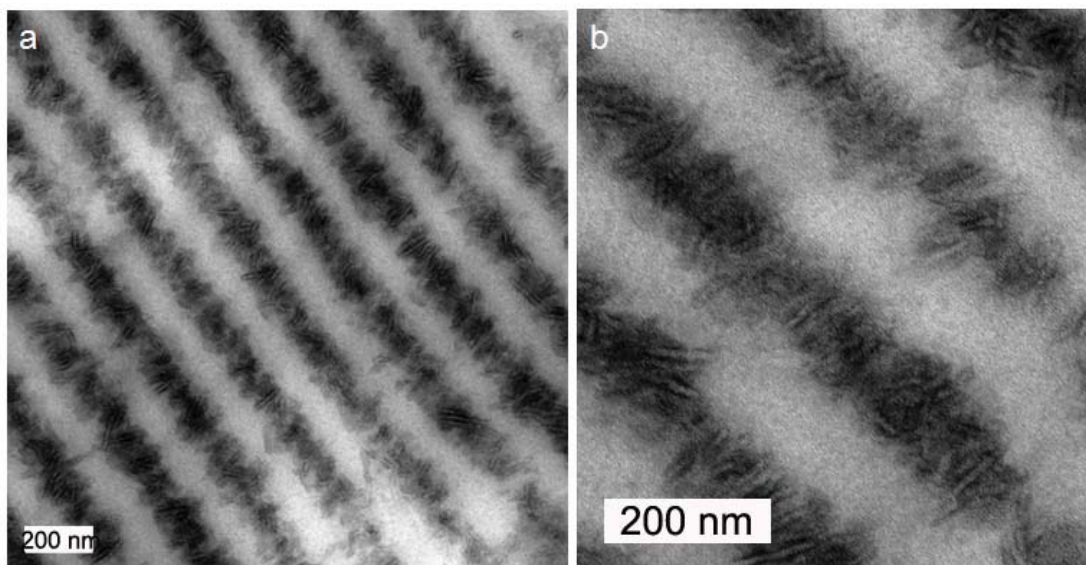


Figure 6.6: TEM micrographs of (a) PEO-b-PCL grating quenched from  $75^{\circ}\text{C}$  and (b) a magnified image of the volume grating.

Upon cooling the sample from  $75^{\circ}\text{C}$  we see the reverse phenomenon occurring, with a decrease in diffraction efficiency and a blue-shifting of the wavelength to  $40^{\circ}\text{C}$ . The change in diffraction efficiency and reflecting wavelength can be attributed to a small linear volume change. The change in refractive index contributes to the diffraction efficiency decrease, while the wavelength begins to blue-shift.

After  $40^{\circ}\text{C}$  the diffraction efficiency decreases sharply to around 56% from 63% at  $34^{\circ}\text{C}$ , while the wavelength of the transmission notch blue-shifts from 613 nm to 608 nm. The diffraction efficiency reaches a minimum while the wavelength continues to blue-shift. Corresponding to the sharp decrease in diffraction efficiency, a sample that was slowly cooled to  $34^{\circ}\text{C}$  and then quenched was cross-sectioned and viewed

under TEM. The same protrusions in figure 6.7 were also observed in figure 6.5b. The crystallization of the BCP decreases the fractional width of the BCP layer in the grating period and decreases the refractive index contrast between Norland and PEO-b-PCL. This contributes to the sharp decrease in the diffraction efficiency. The observation of polymer protrusions in the crosslinked resin when heated and cooled, link this phenomenon to both the crystallization and melting of the BCP volume grating.

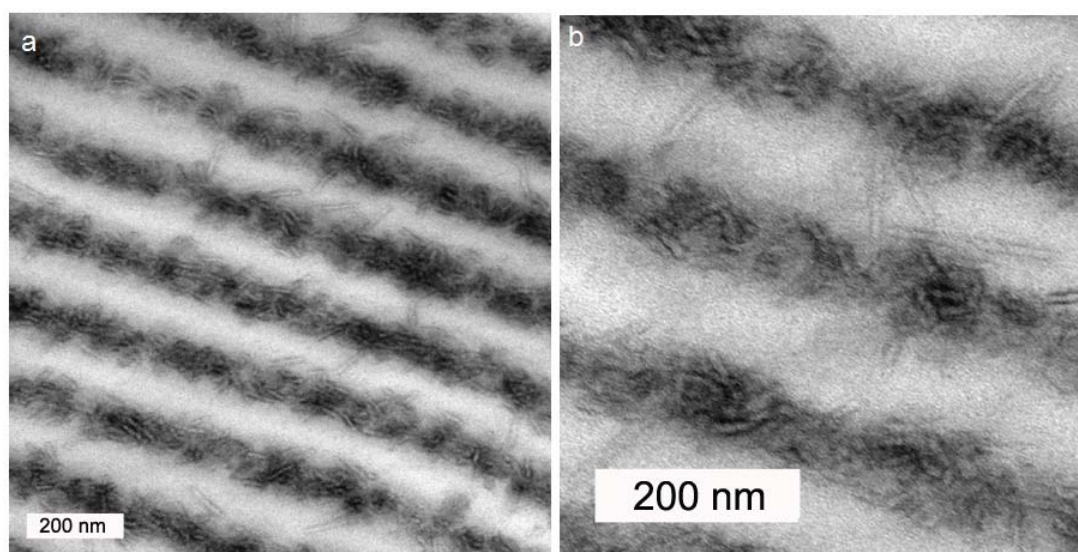


Figure 6.7: TEM micrographs of (a) PEO-b-PCL grating quenched from  $34^{\circ}\text{C}$  and (b) a magnified image of the volume grating.

Cooling the grating further from  $34^{\circ}\text{C}$  to  $0^{\circ}\text{C}$  results in an increase in the diffraction efficiency until reaching  $27^{\circ}\text{C}$ . At that temperature the diffraction efficiency stops increasing and the wavelength stops blue-shifting. Figure 6.8b shows a TEM image of the grating after it was cooled to  $0^{\circ}\text{C}$  and brought back to room temperature for TEM. The polymer protrusions that were present at the dip in the diffraction efficiency have disappeared and the width of the BCP layer has decreased from 90 nm to 85 nm. Figure 6.8b is similar in morphology to figure 6.1 in that we observe the

original hierarchical structure. The similarity in the images also provides evidence that the whole process is reversible.

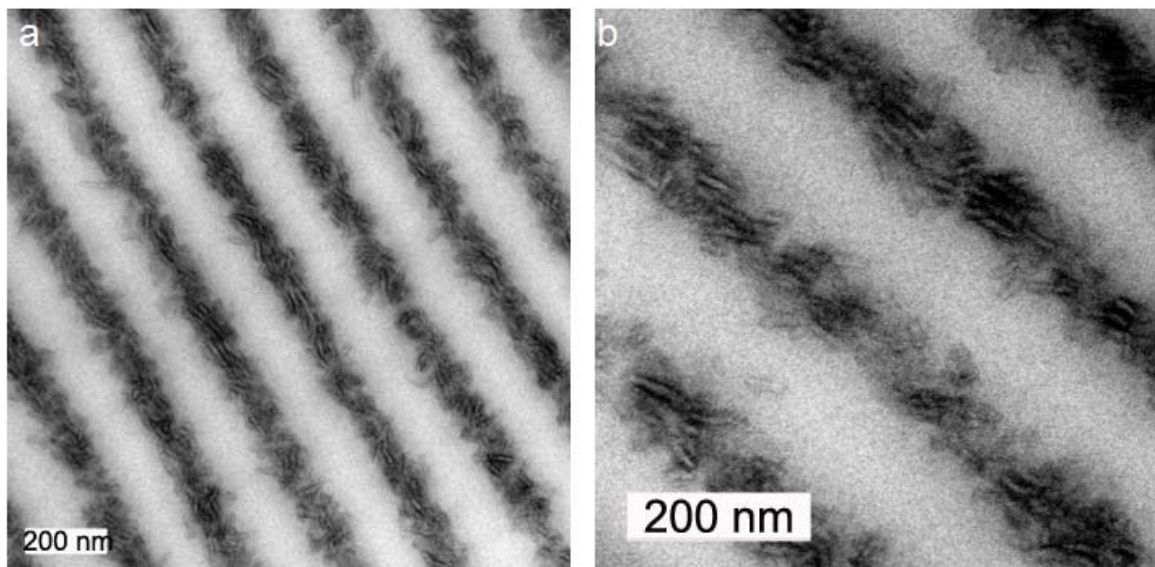


Figure 6.8: TEM micrographs of (a) PEO-b-PCL grating after heating and cooling and (b) a magnified image of the volume grating.

The PEO-b-PCL volume grating goes through a temperature induced change in diffraction efficiency and reflected wavelength. This provides a decrease in the diffraction efficiency and a red-shift in the wavelength notch position. The observations suggests a reduction in the refractive index modulation and increase in volume of the grating. The FTIR supports that melting occurred when the volume grating was heated. At  $831 \frac{1}{cm}$  and  $743 \frac{1}{cm}$  the increase in intensity is indicative of PEO and PCL melting. The increase in diffraction efficiency occurs during the later part of the BCP melting. The refractive index modulation is at a maximum when the BCP is in the molten state at  $75^{\circ}C$ . This dip can be attributed to melting of PEO-b-PCL near the boundary between the BCP and the crosslinked resin. The molten BCP subsequently moves into the crosslinked region. Upon cooling the grating the BCP crystallizes at the center of the BCP region in the grating, resulting in a decrease

in the diffraction efficiency. As the crystallization draws to a close the diffraction efficiency begins to increase as the BCP is moves out of the crosslinked region. The morphology of BCP in lamellar geometries has been extensively studied in top-down helps bottom-up techniques [4,5]. The confinement of the BCP in those cases depends on an impermeable or a hard boundary at the interface [104–107]. The width of the confining geometry dictates the number of periods and the interaction will dictate the orientation [104–107]. In the present case, the boundary between BCP and the confining geometry is permeable or soft, allowing BCP to move in and out of the crosslinked region as the temperature varies. Yet, the confinement effect on the BCP is still present indicating that the prerequisite for hard confinement is not necessary and a hierarchical structure appears even with a weak confinement of the BCP.

#### 6.4.1 Thermal Tuning of PCL Volume Gratings

The appearance of polymer protrusions in the crosslinked resin may be attributed to the movement of PEO-b-PCL. In addition, the protrusions appeared to have a dark-light-dark morphology indicating that the PCL was more compatible with the crosslinked resin than PEO. In order to confirm this, PCL was heated and cooled similar to the PEG melting/crystallization studies performed in an earlier chapter. The PCL volume grating morphology discussed in chapter 4 demonstrated that a periodic structure was fabricated using HP. The HP process produced crosslinked layers that confined the PCL. When PCL is heated, it should result in a density and refractive index change [184]. The impact that these changes have on the volume grating would result in a shift in the reflected wavelength and diffraction efficiency.

PCL with a molecular weight of  $10,000 \frac{g}{mol}$  in a volume grating was heated from  $25^{\circ}C$  to  $70^{\circ}C$  at  $1 \frac{^{\circ}C}{min}$  and cooled to  $10^{\circ}C$  at the same rate in order to demonstrate the response of the grating to temperature. Figure 6.9 shows the plots of the diffrac-

tion efficiency and notch positions with respect to temperature. Upon heating, the notch position red-shifts from 597 nm to 604 nm between 44°C and 54°C, and the diffraction efficiency increases with temperature from 55% to 62%. When the volume grating was cooled to -20°C and then brought to room temperature, the notch position shifts from 66% to 63% and returns to its original position at 590 nm. In figure 6.9 there is an initial decrease in the diffraction efficiency followed by a subsequent increase, referred to as the dip; at the same time the wavelength is red-shifting. The opposite occurs when the sample was cooled. (The difference in diffraction efficiency is due to a relaxation of the grating that occurred at 75°C after heating.) For both heating and cooling curves, the changes of diffraction efficiency and notch position are synchronized.

This unique temperature induced notch wavelength and diffraction efficiency change can be attributed to the phase transition of PCL from crystalline to molten state. PCL is a semicrystalline polymer with a crystal melting point at approximately 64°C depending on the molecular weight [193,194]. DSC thermograms of the PCL volume grating reveal melting from 35°C to 57°C and crystallization temperatures of PCL from 35°C to 24°C, respectively, as shown in figure 6.10. The melting and crystallization temperatures of PCL grating match the rapid changes of diffraction efficiency and notch position in figure 6.9. This suggests that the dynamic behavior of the PCL reflection grating is due to PCL crystallization/melting.

In the PEG case it was recognized that density,  $\rho$ , had a greater impact on the change in wavelength than refractive index during crystallization and melting. We therefore can simplify our analysis to only changes in volume. The PCL crystalline density,  $\rho_c$ , is  $1.195 \frac{g}{cm^3}$  while the amorphous PCL density depends on the temperature (Equation 6.1) where  $T$  is the temperature [193,194].

$$\frac{1}{\rho_a} = 0.899 + 0.00067T \quad (6.1)$$

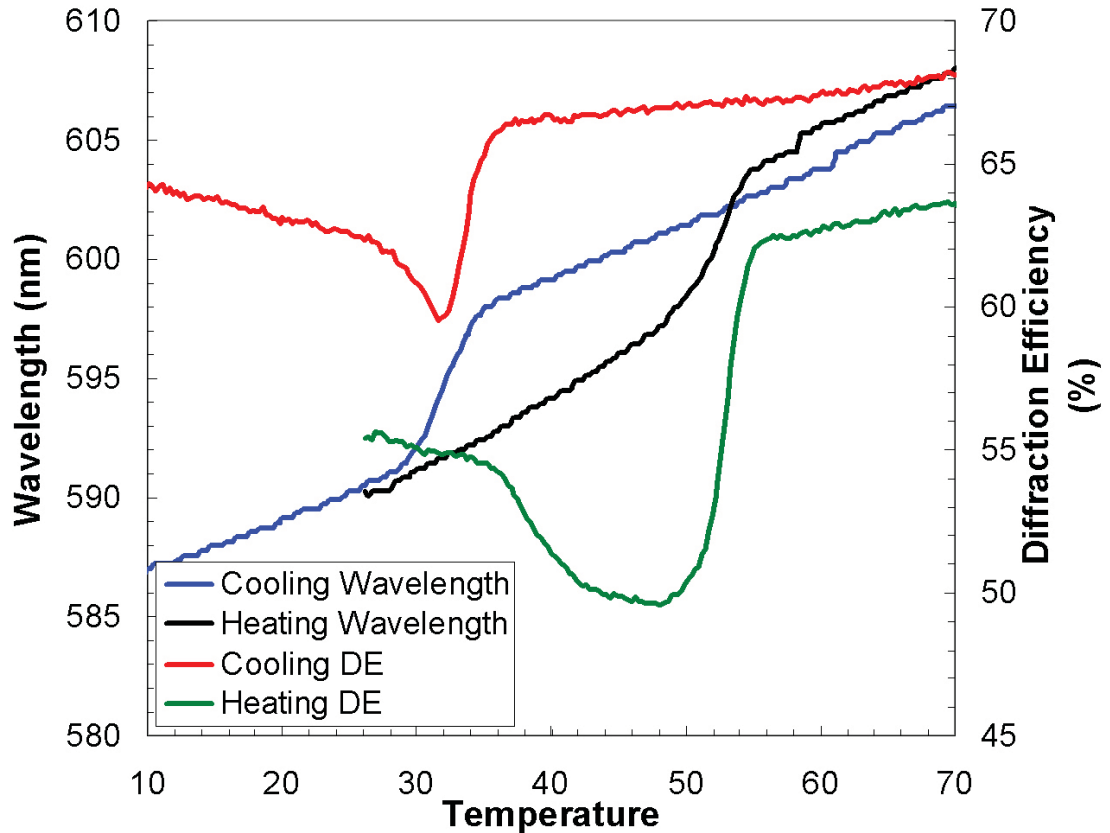


Figure 6.9: The notch position and diffraction efficiency as a function of temperature. When the PCL volume grating was heated and cooled.

The  $\rho_a$  values of PCL at  $30^\circ\text{C}$  and  $60^\circ\text{C}$  can be estimated as  $1.08802 \frac{g}{\text{cm}^3}$  and  $1.0647 \frac{g}{\text{cm}^3}$ , respectively [184]. We can ignore the contribution of refractive index to thermal switching and reduce equation 4.2 to equation 6.2. The volume expansion during melting of the PCL crystals then leads to a red-shift of the notch position according to equation 6.2.

$$\frac{\Delta\lambda}{\lambda_a} \approx \frac{\Delta\Lambda}{\Lambda_a} \quad (6.2)$$

The wavelength shift given by  $\frac{\Delta\lambda}{\lambda_a}$  is approximately 1.1%. The red-shift then equals a change in the grating spacing,  $\frac{\Delta\Lambda}{\Lambda_a}$ , which should be about 1.1%. This translates into a 7 nm change in volume for PCL going from crystal to melt. According to the

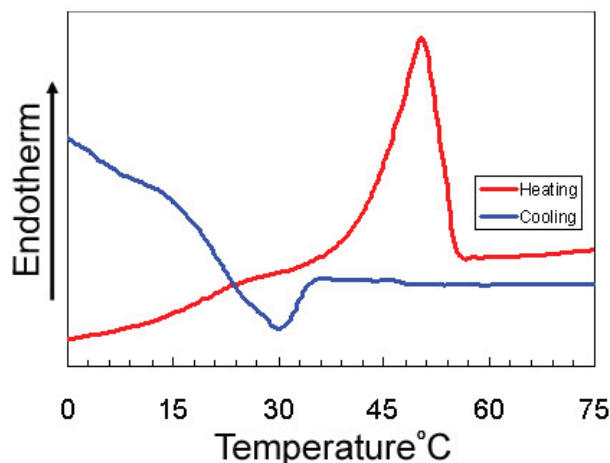


Figure 6.10: DSC thermograms of PCL volume gratings with a  $10 \frac{^{\circ}\text{C}}{\text{min}}$  heating and cooling rate.

densities of pure crystalline and amorphous PCL, 11% volume expansion should occur upon PCL melting. However, in the PCL volume grating, not all the PCL molecules are in the crystalline form at room temperature. Crystallinity of the PCL in the grating can be calculated from the DSC results shown in figure 6.10. 100% crystalline PCL gives rise to a heat of fusion of  $75.6 \frac{\text{kJ}}{\text{g}}$  [193], whereas a heat of fusion for the PCL grating at  $50^{\circ}\text{C}$  was  $60.2 \frac{\text{kJ}}{\text{g}}$ . Crystallinity of PCL confined within crosslinked layers can therefore be calculated to be approximately 79%, which leads to 8.7% volume expansion of the PCL layer of the reflection grating. If the surface area of each PCL layer is assumed to remain the same upon melting, then the volume increase should solely be caused by the grating spacing expansion. Since PCL occupies 30% of the film, the spacing of the grating should increase 2.2% upon heating. This does not match the wavelength shift that resulted in a 1.1% volume change. In this case the size of the volume expansion is reduced by more than half. The difference in the two observations is in the assumption that all of the volume expansion is contributing to the change in wavelength. If some of the melt polymer is mixing with the crosslinked

resin when melting occurs, then the apparent change in volume from the transmission spectrum would be reduced.

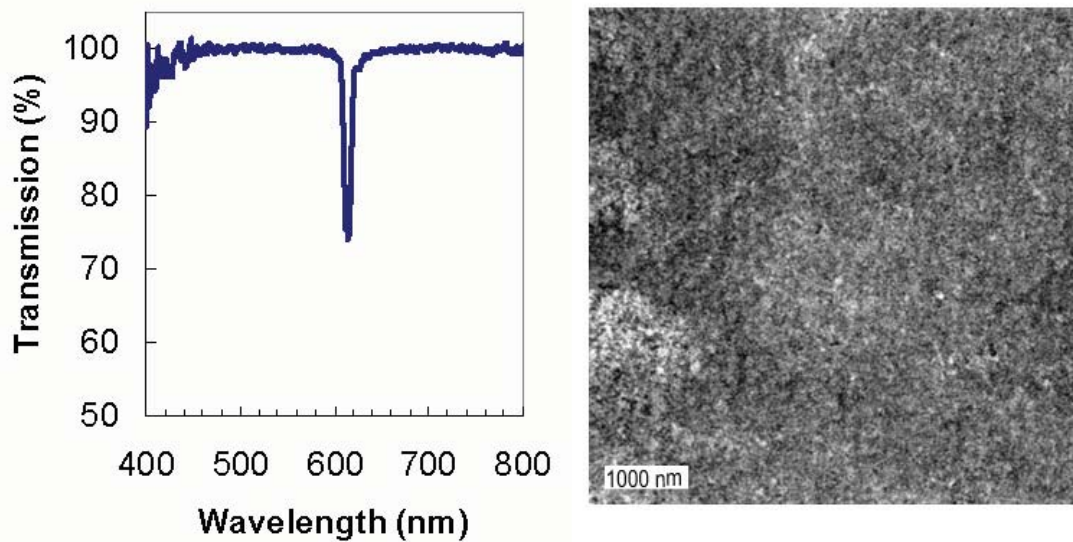


Figure 6.11: Transmission optical spectra (left) and TEM micrograph (right) of a cross section of a PCL volume grating after being quenched in liquid nitrogen from  $75^{\circ}\text{C}$ .

In order to confirm that PCL is mixing with the crosslinked resin a PCL volume grating was held at  $75^{\circ}\text{C}$  for two hours and then quenched. The sample was then sectioned and observed under TEM (Figure 6.11). The quenched sample shows a barely discernible grating (Figure 6.11 right). A notch in the transmission spectra (Figure 6.11 left) of approximately 20% indicates that a modulation in refractive index is present due to the distribution of crosslinked resin. Figure 4.13a compared to figure 6.11 illustrates that PCL moves into the crosslinked resin region at an elevated temperature. This confirms that PCL mixes with the crosslinked resin when heated. This contributes to the reduction in the wavelength shift due to volume expansion.

The transmission spectra and DSC results suggest that PCL mixes to some degree with the crosslinked resin. Mixing was not observed in the PEG case, since the

total volume change from crystallization and melting contributed to the wavelength shift in the transmission spectra. This indicates that the BCP composed of PEG and PCL interact with the crosslinked resin, preferentially. PCL then should preferentially interact with the crosslinked region over PEO. This is consistent with the dark-light-dark morphology observed in the TEM micrographs at  $47^{\circ}\text{C}$  and  $34^{\circ}\text{C}$ . Thus, the morphology of the polymer protrusions is PCL surrounding a PEG core in the crosslinked region.

### **6.5 On the Structure of the Polymer Protrusions Contained within the PEO-b-PCL**

Polymer protrusions that coincided with the dip in diffraction efficiency were observed during the morphology studies. The TEM micrographs of the crosslinked region appear to contain a lamellar or cylinder structures. To confirm the morphology of the protrusion, a volume grating was cooled at  $1\frac{\circ\text{C}}{\text{min}}$  from  $75^{\circ}\text{C}$  and quenched at  $34^{\circ}\text{C}$ . The sample was then cross sectioned, stained, and observed under TEM. Figure 6.12 shows the TEM micrographs of a sample that was untilted and tilted through  $45^{\circ}$  with the arrows indicating tilt direction. One of the circled regions highlights a polymer protrusion that is aligned parallel with the tilt direction. Based on the geometry at  $0^{\circ}$  tilt, either a cross section of a cylinder or a lamellar BCP micelle structure is possible. The tilting of the sample stage  $45^{\circ}$  reveals no change in morphology. This indicates that the protrusion perpendicular to the grating possesses a lamellar structure. To reaffirm the lamellar structure, several smaller protrusions that are oblique and perpendicular to the grating can also be observed when the sample is tilted to  $45^{\circ}$ . In these cases tilting the grating brings some of the lamellar structures into view, since the lamellae are angled to the viewing plane. Thus, tilting thin cross sections of the PEO-b-PCL volume grating confirms that the protrusions are lamellar in nature.

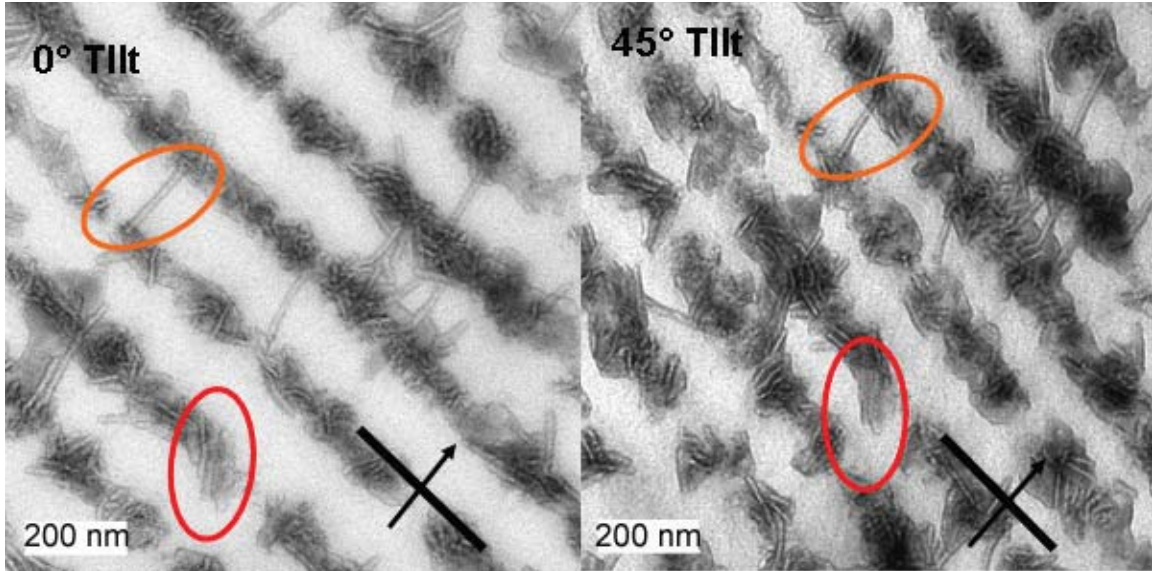


Figure 6.12: The TEM micrograph of a PEO-b-PCL grating (a) at  $0^\circ$  tilt and (b) at  $45^\circ$  tilt.

## 6.6 The Impact of the Polymer Protrusions on the Diffraction Efficiency

In an earlier section, the appearance of PEO-b-PCL in the crosslinked region was associated with a decrease in diffraction efficiency. Melting and crystallization are linked to the dip in the diffraction efficiency. The evolution of the dip in the diffraction efficiency depends on the average refractive index and the refractive index modulation for an ideal reflection grating given by equation 3.3. We discussed that average refractive index changes are not substantial. The refractive index modulation should be the major factor in the diffraction efficiency change based on the observed grating morphologies between room temperature and  $75^\circ\text{C}$ . The refractive index modulation can be approximated by equation 6.3 [134].

$$n_1 = \frac{2\phi_c}{\pi} (n_{\text{crosslinked resin}} - n_{\text{homopolymer}}) \sin(\alpha\pi) \quad (6.3)$$

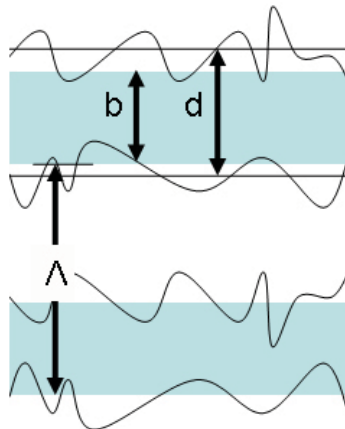


Figure 6.13: A schematic representation of PEO-b-PCL in a volume grating.

The refractive index modulation,  $n_1$ , can be attributed to the volume grating dimensions and the difference between the refractive index of the layers. The variables that effect  $n_1$  can be broken down into refractive index dependent components and grating dimensional components shown in figure 6.13. The first variable in equation 6.3 is the fraction of PEO-b-PCL inside the homopolymer region defined by  $\phi_c = \frac{b}{d}$ . The second variable in equation 6.3,  $(n_{crosslinked\ resin} - n_{homopolymer})$ , is the difference in refractive index between crosslinked resin (the high refractive index layer) and PEO-b-PCL (the low refractive index layer) of the volume grating. The last variable in the equation,  $\alpha$ , is the fraction of the grating occupied by the PEO-b-PCL region  $\alpha = \frac{d}{\Lambda}$ . In this case the difference in refractive index and  $\alpha$  should increase when PEO-b-PCL melts. The only parameter that may decrease is  $\phi_c$ . In order for  $\phi_c$  to decrease some of the BCP would need to move into the crosslinked region. The TEM confirms the mixing of the two regions at the beginning of melting or end of crystallization. This suggests that a fraction of the BCP contributes to the decrease or increase in diffraction efficiency. The decrease is due to  $\phi_c$ , since the BCP moves out of the low index region. The subsequent increase in diffraction efficiency can be attributed to the increase in refractive index contrast when the rest of the BCP melts. The reverse

should occur when the grating is cooled, resulting in the polymer moving out of the crosslinked region. As crystallization begins the diffraction efficiency decreases due to a lower refractive index contrast. The increase in the diffraction efficiency can then be ascribed to the movement of the PEO-b-PCL out of the crosslinked region as crystallization nears completion.

The above mentioned dip in the diffraction efficiency can be attributed to a layer between the low and high index region that develops during crystallization and melting. The dip is due to BCP mixing with crosslinked resin in this layer. The layer defined as b-d (Figure 6.13) contains BCP in crosslinked resin. When melting begins, the molten BCP mixes with the crosslinked resin at the interface between the low and high index region. This contributes to the decrease in diffraction efficiency since b-d is increasing, in turn reducing  $\phi_c$ . As melting continues, the BCP in the low index region melts, increasing the refractive index contrast and contributing to the increase in the diffraction efficiency. At the end of melting some BCP remains in the crosslinked region layer, which was confirmed by TEM. When volume grating is cooled, the BCP begins to crystallize in the low index region decreasing the refractive index contrast, which reduces the diffraction efficiency. This is consistent with the movement of the PEO-b-PCL out of the grating, since crystallization at the interface would trap the polymer or BCP in the crosslinked region.

## 6.7 The Isothermal Crystallization of PEO-b-PCL Volume Gratings

The layer between the high and low refractive index regions that were described in the earlier section should be affected by the crystallization temperature. If crystallization occurs quickly, then the BCP would be trapped in this region. However, when crystallization is slow the BCP should have time to move out of the crosslinked resin and form a layer-in-layer hierarchical structure. In order to investigate this compe-

tition, PEO-b-PCL volume gratings were held at  $75^{\circ}\text{C}$  for two hours, then cooled to  $45^{\circ}\text{C}$ ,  $35^{\circ}\text{C}$ ,  $25^{\circ}\text{C}$ , and liquid nitrogen quenched (Figure 6.14 shows the transmission spectrum of the hierarchical volume gratings). A notch at approximately 610 nm is observed for each sample. The diffraction efficiency for the isothermally crystallized samples ranged from approximately 40% for the isothermally crystallized sample at  $45^{\circ}\text{C}$  to 10% for the sample quenched in liquid nitrogen. The two samples isothermally crystallized at  $35^{\circ}\text{C}$  and  $25^{\circ}\text{C}$  had a diffraction efficiency of approximately 35% and 25%, respectively. The differences in the diffraction efficiency discussed earlier are attributed to layer thickness variations in the BCP region of the volume grating. The lack of scattering near the UV region of the transmission spectrum suggests that continuous layered structures were maintained. To investigate the morphology further, the samples were annealed at  $75^{\circ}\text{C}$  for 2 hours, quenched to their respective temperatures, quenched in liquid nitrogen, brought back to room temperature, and observed under TEM.

The TEM images for the four samples are shown in figure 6.15. Each sample displays the characteristic alternating dark and light regions from the spatial distribution of crosslinked polymer. The average refractive index of the gratings is approximately 1.54 for each sample. The grating layer thickness calculated from the notch position was approximately 194 nm and this was consistent with the TEM observations for each sample.

In the TEM micrographs of figure 6.15, the distribution of BCP inside the volume gratings are different depending on the crystallization temperature. In figure 6.15c, the volume grating was quenched from  $75^{\circ}\text{C}$  in liquid nitrogen, trapping a large fraction of BCP inside the crosslinked resin. This indicates that at  $75^{\circ}\text{C}$  the molten BCP is dispersed throughout the grating. In contrast, figure 6.15a shows most of the BCP is confined between the crosslinked layers of resin with a few BCP protrusions. Figures 6.15b and d have some BCP confined between the crosslinked layers while some

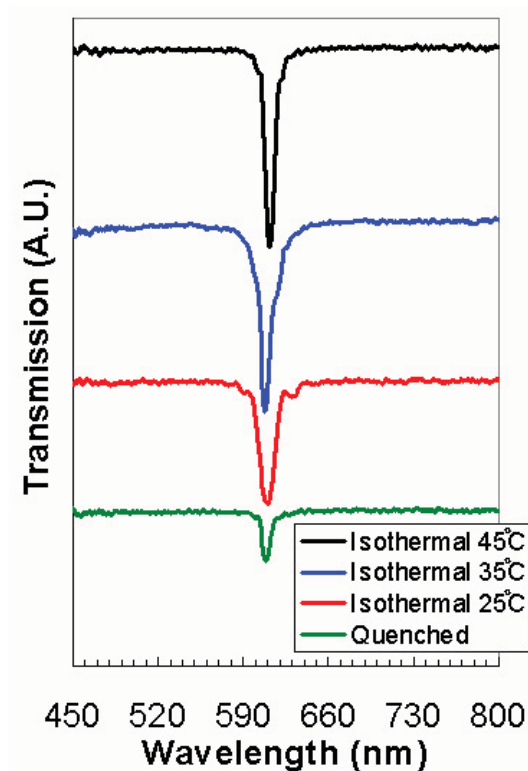


Figure 6.14: The visible light transmission spectrums for isothermal crystallization.

of the BCP is trapped in the crosslinked resin. The wavelength of the notch position in the transmission spectra changes very little for all of the samples. This implies that the thickness of the grating layer and the average refractive index did not change even though the two properties depend on the crystallinity. The observation indicates that in the present case, notch position can be considered morphology independent. However, the refractive index modulation depends on the morphology of the volume grating. The change in diffraction efficiency as the crystallization temperature decreases is consistent with a decrease in the refractive index modulation. A decrease in the amount of BCP in the low index region increases the PEO-b-PCL trapped in the crosslinked region, which reduces the refractive index modulation. Thus, the movement of PEO-b-PCL in the crosslinked region during BCP crystallization is the

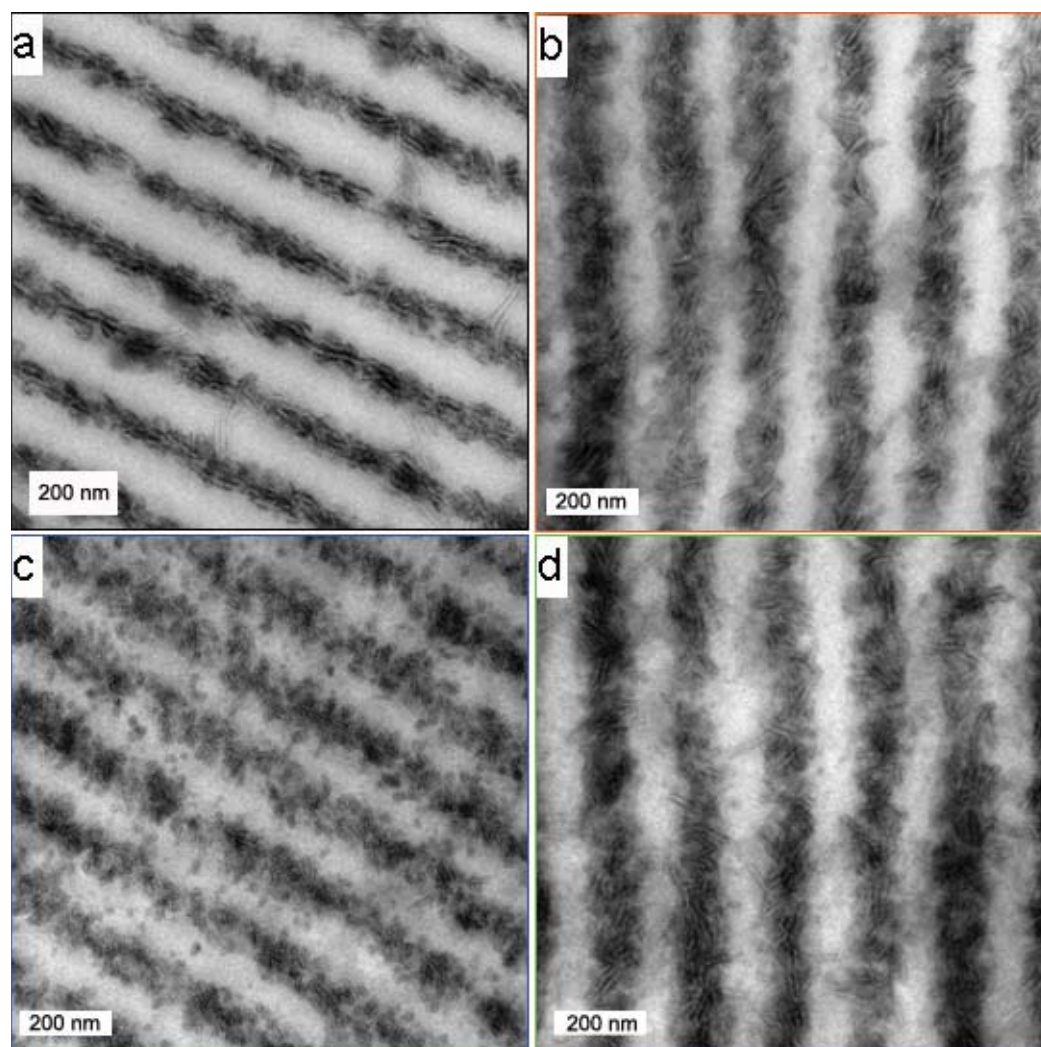


Figure 6.15: The TEM images of isothermally crystallized hierarchical volume gratings at, (a)  $45^{\circ}\text{C}$ , (b)  $35^{\circ}\text{C}$ , (c) quenched in liquid nitrogen, and (d)  $25^{\circ}\text{C}$ .

major influence on the diffraction efficiency.

To demonstrate that the isothermal crystallization process is reversible, a volume grating was subjected to a temperature profile shown in figure 6.16d. Figure 6.16a is the initial volume grating isothermally crystallized at  $35^{\circ}\text{C}$ . The volume grating was then heated to  $75^{\circ}\text{C}$  for 2 hours then quenched in liquid nitrogen, shown in figure 6.16b. Subsequently, the grating was brought back to  $75^{\circ}\text{C}$  for 2 hours and then allowed to isothermally crystallize at  $35^{\circ}\text{C}$ , figure 6.16c. The morphology observed in figure 6.16a and c look similar. Figure 6.17 shows that two transmission spectra overlap when the volume gratings were isothermally crystallized at  $35^{\circ}\text{C}$ , confirming the volume grating structures are similar. However, the transmission spectra for figures 6.16a and b do not overlap and the diffraction efficiency for the liquid nitrogen quenched sample was low in comparison to the other spectra. The process of quenching, subsequent remelting at  $75^{\circ}\text{C}$ , and isothermal crystallization at  $35^{\circ}\text{C}$  of the PEO-b-PCL volume grating indicates that the morphology is driven by crystallization and phase separation and not fabrication. The reversibility of the morphology confirms that the crosslinked region appears to be porous. The porous interface would indicate that the boundary between crosslinked resin and BCP possesses many protrusions or defects. The previous argument that the presence of defects reduces the confinement effect can be disregarded in the PEO-b-PCL volume grating case [4], since PEO-b-PCL movement in and out of the grating appears to be reversible.

## 6.8 Conclusion

The nonisothermal and isothermal crystallization of PEO-b-PCL were investigated in this chapter. A unique thermo-optic effect was observed and described in terms of a boundary layer that included molten BCP and crosslinked resin. The morphology and structure were investigated using TEM and transmission optical spectra. The

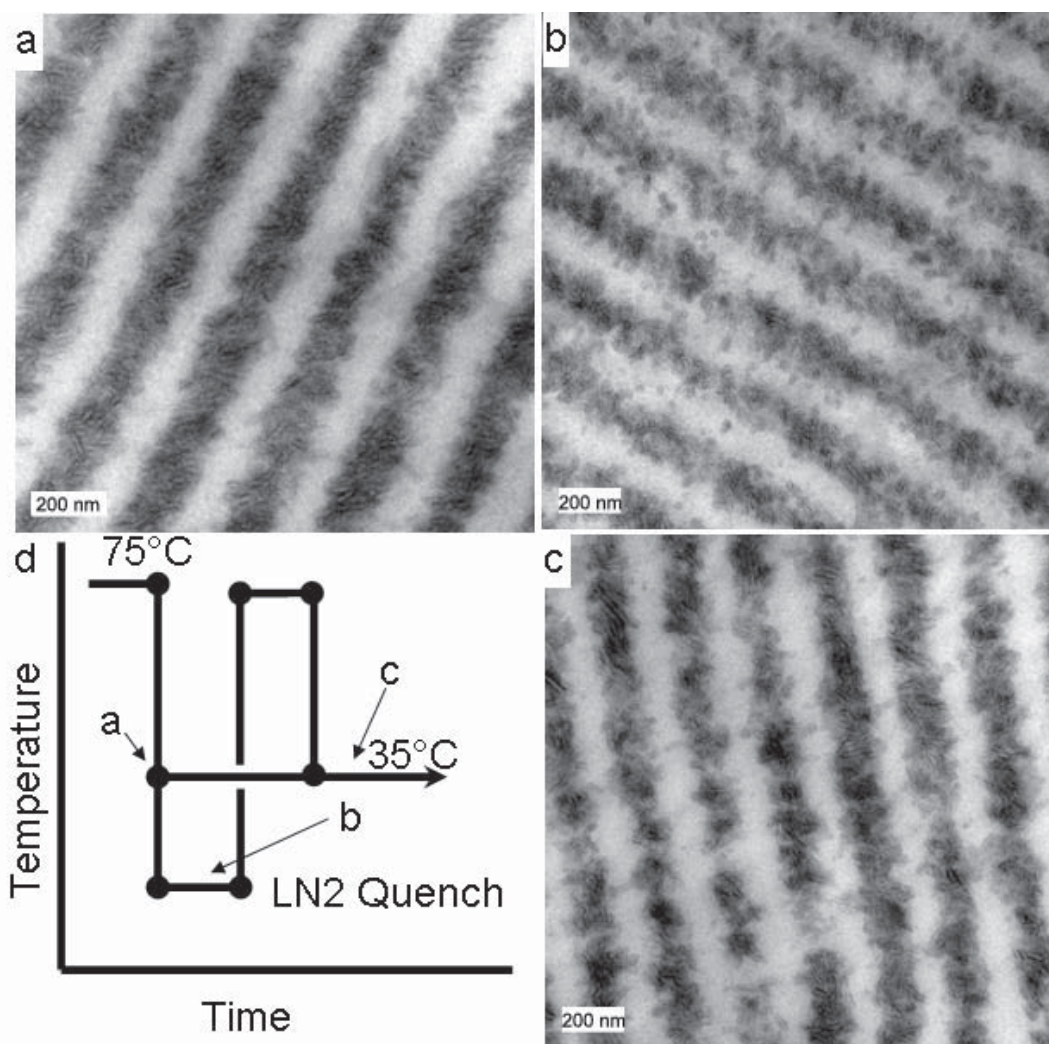


Figure 6.16: The TEM images of hierarchical volume gratings that were isothermally crystallized at (a)  $35^{\circ}\text{C}$ , (b) then quenched in liquid nitrogen, (c) followed by annealing at  $75^{\circ}\text{C}$  then crystallized at  $35^{\circ}\text{C}$ .

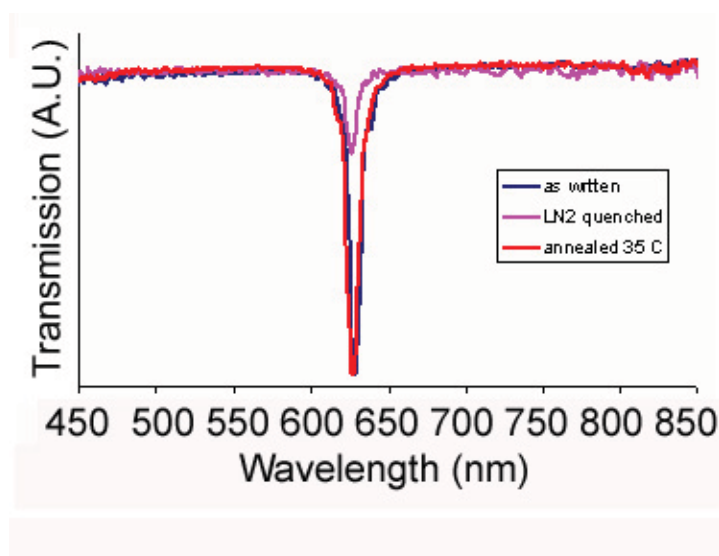


Figure 6.17: The transmission spectra of hierarchical volume gratings that were isothermally crystallized at (a)  $35^{\circ}\text{C}$ , (b) then quenched in liquid nitrogen, (c) followed by annealing at  $75^{\circ}\text{C}$  then crystallized at  $35^{\circ}\text{C}$ .

crystallization of the PEO-b-PCL in the volume grating at  $45^{\circ}\text{C}$  resulted in a hierarchical morphology, where the grating formed a periodic structure of 194 nm and the BCP phase separated and crystallized in a region approximately 50 nm wide. This led to the observation of two to three BCP periods with a thickness of approximately 20 nm oriented parallel to the grating surface. The boundary between BCP and the confining geometry is permeable or soft, allowing BCP to move in and out of the crosslinked region as the temperature varies. This is novel compared to previous observations on the hard confinement of BCP. The confinement effect on the BCP is still present indicating that the prerequisite for hard confinement is not necessary. The parallel orientation of the BCP to the grating layers can be attributed to both preferential compatibility of PCL to the crosslinked resin and the preferential crystal orientation of PEO and PCL to the confining surface. The layer-in-layer hierarchical structure appears even with a weak confinement of the BCP.

## Chapter 7. Two-dimensional HP of PEG Photonic Crystals

### 7.1 Introduction

In this chapter, we report the fabrication and thermal tuning of the stimulated emission from a two-dimensional photonic structure consisting of PEG, Pyrromethene 597 (PM597), and the thiol-ene based polymer NOA 65. We fabricated pillars of thiol-ene crosslinked polymers surrounded by PEG. When the two-dimensional PEG photonic structure was stimulated with 532 nm radiation a characteristic wavelength was emitted. Upon heating, PEG melts resulting in a change in the refractive index and density. The change in the refractive index manifests itself as a shift and increase in the intensity of light emitted when stimulated. The PEG crystallizes upon cooling and the intensity and wavelength shifts back.

### 7.2 Experimental

The HP of a two-dimensional photonic crystal started from a prepolymer syrup containing PEG  $M_w$  4,600  $\frac{g}{mol}$ , PM597 (purchased from Exciton, Inc.), NOA 65, and Darocure 4265. The photonic structure was written using the same technique employed for fabricating holographic polymer dispersed liquid crystals in two-dimensional photonic crystals [201]. The grating was written using a Coherent Ar-ion laser (model Sabre Innova 10R/2) with a laser wavelength of 363.8 nm and an output power of 200 mW to 300 mW. A four laser beam setup was used with two pairs of perpendicularly polarized beams creating an interference pattern within the prepolymer syrup. The writing setup and pattern are shown in figure 7.1. The interference pattern shown is for the XY-plane with respect to the surface of the glass; this corresponds to an intensity profile parallel to the cell surface. The periodic regions of high and low

intensity were spatially distributed in a square lattice. The high intensity regions induced polymerization, which results in the solidification of the system. The cell was positioned at the intersection of the four beams.

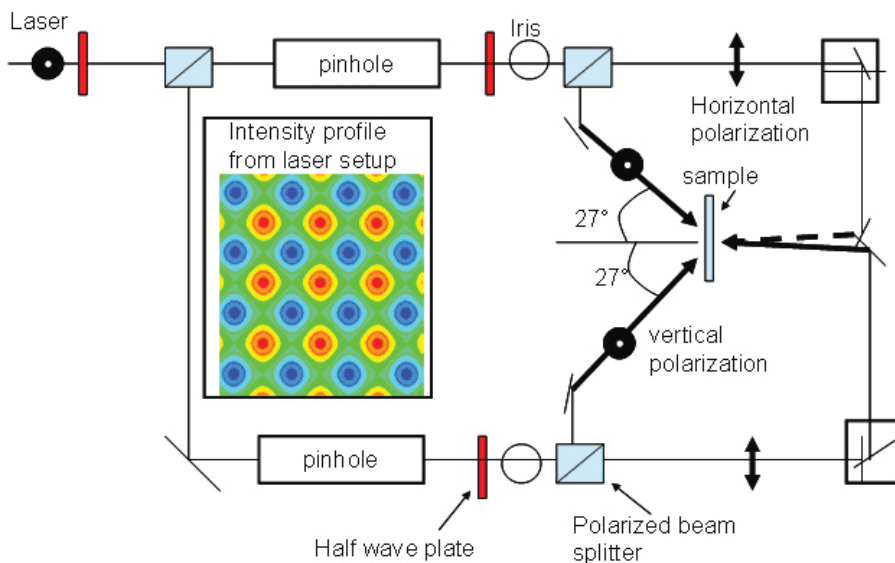


Figure 7.1: The schematic of a two-dimensional HP setup and laser intensity profile parallel to the sample cell surface.

### 7.3 The Morphology of a Two-Dimensional PEG Volume Grating

The morphology of PEG and PM597 in two-dimensional structures by HP was investigated using TEM. Thin sections of the grating were obtained by ultramicrotoming sample films along the film normal direction of the  $45^\circ$ -plane, YZ-plane, and XZ-plane (Figure 7.2 schematic shows the cutting planes). Figure 7.2 shows the TEM micrographs of thin sections of PEG. In each image, a uniform continuous structure was patterned with alternating dark and light regions. The dark regions can be assigned to NOA 65 while the light region represents PEG; inside the lighter regions there are dark specks. This can be attributed to the PM597 in the the PEG region. The assignment of the PEG region can be confirmed by the appearance of holes in

the lighter region (not shown), which resulted from the dissolution of PEG by water during the sample preparation process. The d-spacing from the TEM micrographs, figure 7.2b and c, are 392 nm for the XZ-plane and YZ-plane and 554 nm for the 45° plane, figure 7.2a. The ratio of the d-spacing for the 45° plane and the XZ-plane or YZ-plane was 1.41. The periodicity of the XZ- and YZ-plane suggests that the PEG photonic crystal is two-dimensional. The cross section of the 45° plane indicates that the periodicity of the XZ- and YZ- planes are square. The observed morphology is consistent with the writing geometry.

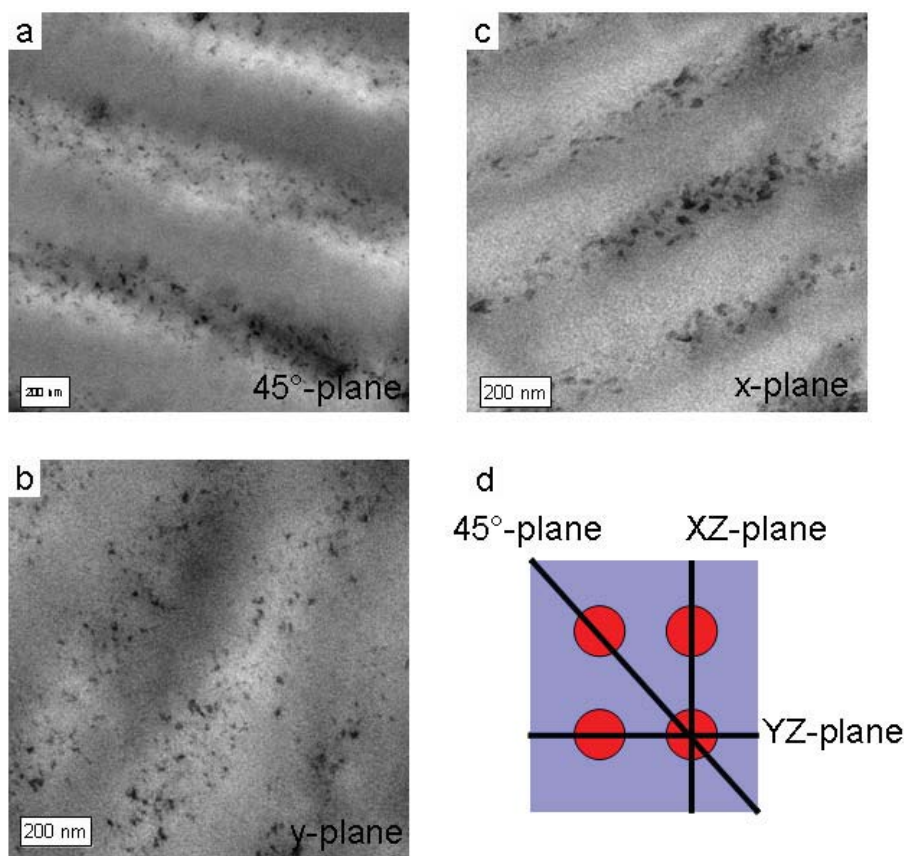


Figure 7.2: The TEM micrographs of cross sections of the grating formed from HP PEG and NOA 65 in the (a) 45° plane, (b) YZ-plane, and (c) XZ-plane. The schematic of the cutting planes are shown in (d).

To confirm the structure, the diffraction angle and efficiency was measured with a

He-Ne laser at 632 nm. The alternating PEG and NOA 65 regions on the submicron level led to the observation of diffraction arcs located along the equator and meridian. The measured diffraction angle was  $54^\circ$  with a diffraction efficiency of 32%. The refractive index of the polymerized NOA 65 and PEG are approximately 1.52 and 1.46 (or higher), respectively [184, 191]. The grating d-spacing was calculated to be 392 nm using the diffraction angle. The appearance of the reflection arcs on the meridian and equator with the same angle and diffraction efficiency confirms a square lattice perpendicular to the glass cell. This is consistent with the TEM micrographs and laser geometry used during HP. This is one example of a non-reactive linear polymer that was patterned into a two-dimensional geometry using the HP technique.

The PEG based gratings are quenched to room temperature after HP at an elevated temperature. After HP the sample was quenched from an elevated temperature, preventing PEG from crystallizing into a hierarchical structure. The PLM image in figure 7.3 shows the sample after being quenched. However, if the sample is kept at  $75^\circ\text{C}$  for 2 hours then cooled at  $2\frac{^\circ\text{C}}{\text{min}}$ , a large spherulite can be seen as shown in figure 7.3b. The large spherulite inside the patterned region suggests that crystallization of the PEG is continuous over long ranges. The appearance of the PEG spherulite in the PLM image indicates that crystallization is not confined, which is different than our previous observation in the one-dimensional reflection grating. Lasing can still be observed at room temperature indicating that although the PEG crystallizes, the periodic structure from HP is maintained. This may open an avenue for HP to be combined with other self-assembly techniques to fabricate hierarchical structures.

The small amount of PM597 added to the prepolymer solution was observed in the PEG domains from the TEM images. When the sample was exposed to green light at 532 nm from the doubled output of a Nd:YAG laser that had a repetition rate of 10 Hz and a pulse duration of 5 ns to 8 ns, the HP PEG Norland sample emitted a strong orange/red color light. The peak lasing was approximately 602 nm (Figure 7.4), which

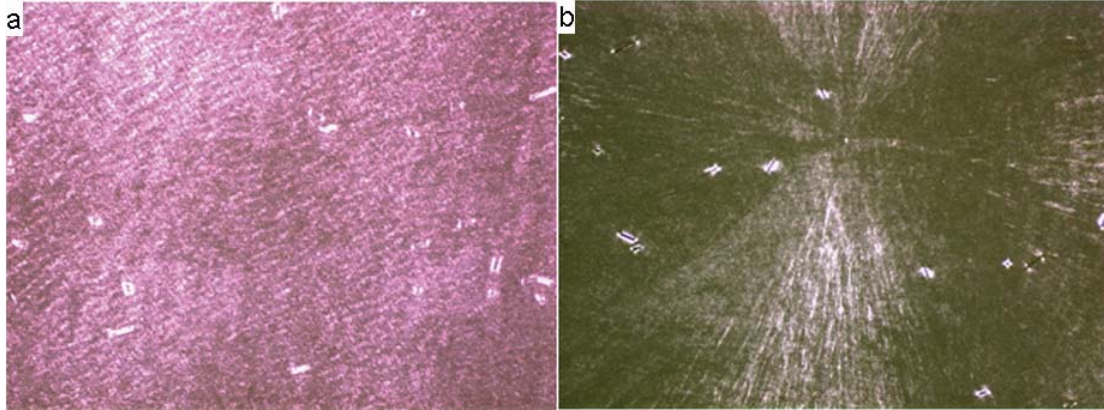


Figure 7.3: The PLM images of the two-dimensional PEG photonic crystal (a) before and (b) after recrystallization.

was detected by an ocean optics fiber spectrometer setup orthogonal to the beam. The strong narrow peak may be due to the group velocity of the photons approaching zero as the band flattens, which was described by Sakoda [131]. The sample was then heated to  $75^{\circ}\text{C}$  resulting in the peak blue-shifting 8 nm and increasing in intensity (Figure 7.4). The peak red-shifts back to the original position when cooled. The shift may be due to the increase in refractive index contrast between PEG and NOA 65 that occurs when PEG is heated to  $75^{\circ}\text{C}$ . The change in PEG refractive index from room temperature to  $75^{\circ}\text{C}$  is .003 [184, 191], which contributes to the blue-shift in the stimulated emission wavelength and the increase in the lasing intensity. The change in density of PEG upon heating would contribute to an increase in the cylinder spacing. Yet, we observed earlier that crystallization is continuous indicating that the PEG is not confined. The lack of confinement may then also allow the PEG to expand and contract without changing the lattice dimensions and the peak lasing wavelength. This confirms that PEG is not confined in the present system. The present system demonstrates that PEG was not confined to a region of the photonic crystal fabricated from HP. It is envisioned that by varying the PEG weight fraction, PEG crystals may be confined in two-dimensional morphologies.

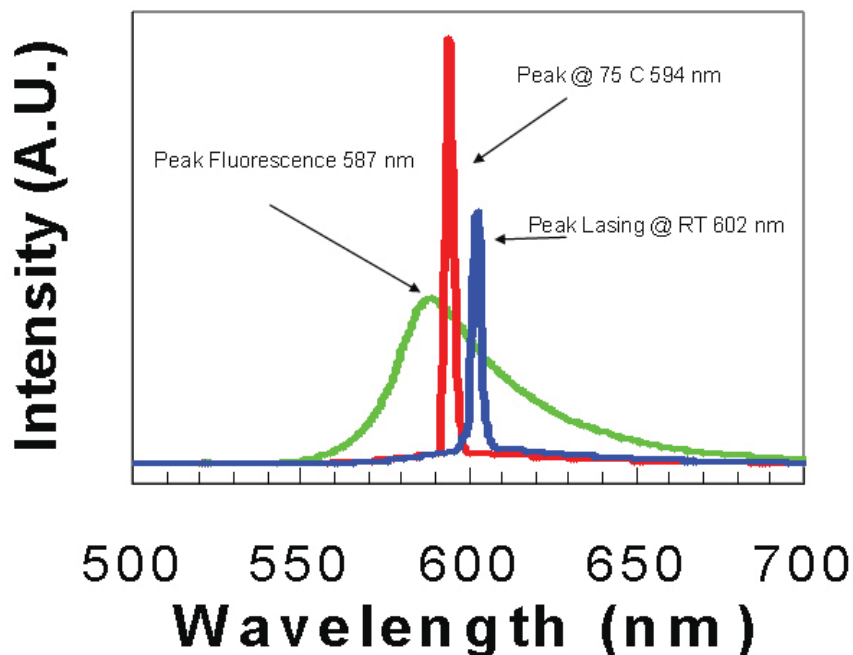


Figure 7.4: Light scattering results with narrow peaks of scattered light from a sample of HP PEG in NOA 65 at room temperature and  $75^{\circ}\text{C}$ .

#### 7.4 Summary

In summary, PEG and NOA 65 were patterned into two-dimensional sub-micron structures using HP. Reflection arcs on the equator and meridian indicate a finite refractive index modulation present in the sample, which is due to spatial segregation of PEG and crosslinked resin into a square lattice. Stimulated emission characteristic of the holographic patterned PEG was observed when exposed to green light. When the sample was heated to  $75^{\circ}\text{C}$ , the peak lasing intensity blue-shifted and increased in intensity due to the change in refractive index of PEG. Cooling the sample to room temperature returned the lasing intensity and peak wavelength to their original values. The present case demonstrates that a square lattice of a polymer based photonic crystal was fabricated using HP and crystallization of PEG was not confined.

## Chapter 8. Conclusion and Outlook

### 8.1 Concluding Remarks

- Three unique semicrystalline volume grating morphologies were described in detail.
- In the PEG case, the semicrystalline polymer was confined between crosslinked layers of resin and the polymer lamellae oriented itself parallel to the grating.
- Thermal switching was realized and no interboundary mixing occurred when PEG melted, indicating that hard confinement was achieved.
- In the PCL case, the thermal switching determined that PCL mixed with the crosslinked resin when the polymer was molten, indicating that the confining geometry was permeable.
- The three homopolymers displayed three different volume grating morphologies that highlighted the possible homopolymer gratings that can be formed. If phase separation dominates the morphology then droplets are observed. If crystallization dominates than a distribution of semicrystalline polymer through a spatially distributed crosslinked polymer network can be observed. In the third case, the phase separation process and crystallization work synergistically to form a semicontinuous layered structure with the homopolymer confined to the dark regions.
- To improve the optical performance of PLLA volume gratings, PCL was blended into the prepolymer mixture. The resulting morphology is unique in that the PLLA is located in the center of the volume grating while the PCL is located

at the periphery. HP can therefore pattern a blend of PLLA and PCL and improve the optical properties.

- A hierarchical volume grating was fabricated based on combining top-down and bottom-up principles. The layer-in-layer hierarchical structure possessed ordered length scales of 200 nm and 20 nm.
- The hierarchical grating was thermally tuned to demonstrate a unique thermo-optical transition.
- The changes in the optical properties of the volume grating are the result of the BCP moving into the crosslinked region.
- The structure of the BCP polymer protrusions were later found to be discotic in nature.
- The movement of the BCP in and out of the crosslinked region while still resulting in a confined layer-in-layer morphology, indicates that the hard confinement of BCP is not necessary in this case.
- The reversibility of the hierarchical morphology indicated that the boundary formed during fabrication does not play a significant role in the formation of the hierarchical structure. Instead crystallization competing with the movement of BCP in and out of the crosslinked region has a larger impact on volume grating morphology.

## 8.2 Suggestions for the Future of Hierarchical Volume Gratings

- How do BCP and HP combine to form a hierarchical structure? During the presentation of this thesis the formation dynamics involved were neatly ignored by stating that diffusion and phase separation of the BCP during HP was not

significant compared to crystallization. Yet, the two Flory-Huggins interaction parameters for the BCP and the one for the crosslinkable resin are not trivial. Three scenarios can be envisioned in one hierarchical system. First, the BCP phase separates into an ordered structure before patterning. Second, HP will occur before BCP phase separation. Lastly, the two nanoscale assemblies will compete to form ordered structures, which may or may not be ideal.

- The advantage of the current system may have more impact in improving and developing mechano-optical hierarchical materials. The present system that was discussed incorporated structural elements, crystallization, interfacial energy, microphase separation, entanglement, and the spatial distribution of crosslinked polymer. It should then be possible through thermal-treatments to tune the mechanical properties of the hierarchical volume grating. In addition, the power of HP BCP to produce arbitrary structures quickly and efficiently may result in hierarchical, mechano-optical, quasi-crystalline nanostructures.
- The space provided by HP that allowed the BCP to self-assemble is intriguing. A ship in a bottle technique may be envisioned for assembling hierarchical volume gratings by incorporating hydrogen bonded side chain liquid crystalline BCP into the prepolymer mixture. The advantage to this technique is that more complex and sophisticated functionalities will be accommodated by higher molecular weights. Oneway of circumventing these problems could be to use specific interactions of small molecules or DNA to arrange into more complicated structures.

## Bibliography

---

- [1] K. Jensen, Ç. Girit, W. Mickelson, and A. Zettl, “Tunable nanoresonators constructed from telescoping nanotubes,” *Physical Review Letters*, vol. 96, no. 21, p. 215503, 2006. [Online]. Available: <http://link.aps.org/abstract/PRL/v96/e215503>
- [2] E. W. H. Jager, E. Smela, and O. Inganäs, “Microfabricating conjugated polymer actuators,” *Science*, vol. 290, no. 5496, pp. 1540–1545, 2000. [Online]. Available: <http://www.sciencemag.org/cgi/content/abstract/290/5496/1540>
- [3] [Online]. Available: <http://www.foresight.org/about/index.html>
- [4] J. Cheng, F. Zhang, H. Smith, G. Vancso, and C. Ross, “Pattern registration between spherical block-copolymer domains and topographical templates,” *Adv. Mater.*, vol. 18, pp. 597–601, 2006.
- [5] C. J. Hawker and Thomas P. Russell, “Block copolymer lithography: Merging ”bottom-up” with ”top-down” processes,” *MRS Bulletin*, vol. 30, no. 12, pp. 952 – 966, 2005, block copolymer; Interfacial properties; Microfabrication processes; Nanoscale;.
- [6] J. Y. Cheng, A. M. Mayes, and C. A. Ross, “Nanostructure engineering by templated self-assembly of block copolymers,” *Nature materials*, vol. 3, pp. 823–828, 2004.
- [7] S. O. Kim, H. H. Solak, M. P. Stoykovich, N. J. Ferrier, J. J. D. Pablo, and P. F. Nealey, “Epitaxial self assembly of block copolymers on lithographically defined nanopatterned substrates,” *Nature*, vol. 424, p. 411, 2003.
- [8] A. Blaaderen, R. Ruel, and P. Wiltzius, *Nature*, vol. 385, p. 321, 1997.
- [9] G. M. Whitesides and B. Grzybowski, “Self-assembly at all scales,” *Science*, vol. 295, pp. 2418–2421, 2002.
- [10] E. Baer, A. Hiltner, and H. D. Keith, “Hierarchical structure in polymeric materials,” *Science*, vol. 235, no. 4792, pp. 1015–1022, 1987. [Online]. Available: <http://www.sciencemag.org/cgi/content/abstract/235/4792/1015>
- [11] J. Ruokolainen, “Switching supramolecular polymeric materials with multiple length scales,” *Science*, vol. 280, pp. 557–560, 1998.

- [12] C. M. Garner, D. Herr, and C. Krautschik, "Directed self assembly requirements for sub 20nm lithography," ITRS International Technology Roadmap for Semiconductors, Tech. Rep., 2006.
- [13] D. Xia, T. C. Gamble, E. A. Mendoza, S. J. Koch, X. He, G. P. Lopez, and S. Brueck, "Dna transport in hierarchically-structured colloidal nanoparticle porous wall nanochannels," *Nano Lett.*, vol. 8, pp. 1610–1618, 2008.
- [14] I. W. Hamley, *Introduction to Soft Matter*. Jon Wiley and Sons, LTD, 2000.
- [15] A. K. Khandpur, S. Foerster, F. S. Bates, I. W. Hamley, A. J. Ryan, W. Bras, K. Almdal, and K. Mortensen, "Polyisoprene-polystyrene diblock copolymer phase diagram near the order-disorder transition," *Macromolecules*, vol. 28, no. 26, pp. 8796–8806, 1995. [Online]. Available: <http://pubs.acs.org/doi/abs/10.1021/ma00130a012>
- [16] M. Matsen and F. Bates, "Unifying weak and strong segregation block copolymer theories," *Macromolecules*, vol. 29, pp. 1091–1098, 1996.
- [17] E. W. Cochran, C. J. Garcia-Cervera, and G. H. Fredrickson, "Stability of the gyroid phase in diblock copolymers at strong segregation," *Macromolecules*, vol. 39, pp. 2449–2451, 2006.
- [18] I. W. Hamley, Ed., *Developments in block copolymer science and technology*. Wiley-VCH, 2003.
- [19] M. McCord and M. Rooks, *Handbook of Microlithography, Micromachining and Microfabrication*, P. Choudhury, Ed. SPIE, 1997, vol. 1.
- [20] R. C. Jaeger, *Introduction to Microelectronic Fabrication*, G. W. Neudeck and R. F. Pierret, Eds. Prentice Hall, 2002, vol. 5.
- [21] Y. Xia and G. M. Whitesides, "Soft lithography," *Annu. Rev. Mater. Sci.*, vol. 28, pp. 153–184, 1998.
- [22] S. Henkee, E. Thomas, and L. Fetters, *J Mater Sci*, vol. 23, p. 1685, 1988.
- [23] D. C. Martin and E. L. Thomas, "Grain boundaries in extended-chain polymers: Theory and experiment," *Philosophical Magazine A*, vol. 64, p. 903–922, 1991.
- [24] R. J. Albalak and E. L. Thomas, *J. Polym. Sci., Polym. Phys. Ed.*, vol. 31, p. 37, 1993.
- [25] T. Thurn-Albrecht, J. Schotter, G. A. Kastle, N. Emley, T. Shibauchi, L. Krusin-Elbaum, K. Guarini, C. T. Black, M. T. Tuominen, and T. P. Russell, "Ultrahigh-density nanowire arrays grown in self-assembled diblock copolymer templates," *Science*, vol. 290, no. 5499, pp. 2126–2129, 2000. [Online]. Available: <http://www.sciencemag.org/cgi/content/abstract/290/5499/2126>

- [26] A. Keller, E. Pedemonte, and F. M. Willmouth, *Nature (London)*, vol. 225, p. 538, 1970.
- [27] Z.-R. Chen, J. A. Kornfield, S. D. Smith, J. T. Grothaus, and M. M. Satkowski, *Science*, vol. 277, p. 1248, 1997.
- [28] U. Wiesner, *Macromol. Chem. Phys.*, vol. 198, p. 3319, 1997.
- [29] C. Park, J. Yoon, and E. L. Thomas, “Enabling nanotechnology with self assembled block copolymer patterns,” *Polymer*, vol. 44, no. 22, pp. 6725 – 6760, 2003. [Online]. Available: <http://www.sciencedirect.com/science/article/B6TXW-49J8W07-1/2/3e2c6a1048c2dc205e4e83b2a56b6cf1>
- [30] C. Tang, E. M. Lennon, G. H. Fredrickson, E. J. Kramer, and C. J. Hawker, “Evolution of block copolymer lithography to highly ordered square arrays,” *Science*, vol. 322, no. 5900, pp. 429–432, 2008. [Online]. Available: <http://www.sciencemag.org/cgi/content/abstract/322/5900/429>
- [31] [Online]. Available: [http://www.intel.com/pressroom/archive/releases/20070918corp\\_a.htm?iid=tech\\_arch\\_32nm+body\\_pressrelease](http://www.intel.com/pressroom/archive/releases/20070918corp_a.htm?iid=tech_arch_32nm+body_pressrelease)
- [32] G. Mao, *Handbook of Liquid Crystals*, C. Ober, Ed. Wiley-VCH, 1998, vol. 3.
- [33] M. Walther and H. Finkelman, “Structure formation of liquid crystalline block copolymers,” *Prog. Polym. Sci.*, vol. 21, p. 951, 1996.
- [34] H. Fischer and S. Poser, “Liquid crystalline block and graft copolymers,” *Acta Polym.*, vol. 47, pp. 413–428, 1996.
- [35] H. Fischer, “On the influence of the morphological structure on the liquid crystalline behavior of liquid crystalline side chain block copolymers,” *Macromolecules*, vol. 27, pp. 7133–7138, 1994.
- [36] M. Lee, “Supramolecular structures from rod coil block copolymers,” *Chem. Rev.*, vol. 101, pp. 3869–3892, 2001.
- [37] M. Lee and B. Cho, “Linear rod coil multiblock oligomers with a repeating unit dependent supramolecular organization,” *Macromolecules*, vol. 34, pp. 1987–1995, 2001.
- [38] M. Lee, “Spontaneous organization of supramolecular rod bundles into a body centered tetragonal assembly in coil rod coil molecules,” *J. Am. Chem. Soc.*, vol. 122, pp. 7449–7455, 2000.
- [39] M. Lee, C.-J. Jang, and J.-H. Ryu, “Supramolecular reactor from self assembly of rod coil molecules in aqueous environment,” *J. Am. Chem. Soc.*, vol. 126, pp. 8082–8083, 2004.

- [40] M. Lee and H. Oh, "Liquid crystalline rod coil polymers based on poly(ethylene oxide)s and the influence of the complexation of  $\text{LiCF}_3\text{SO}_3$  on the liquid crystalline assembly." *J. Mater. Chem.*, vol. 6, pp. 1079–1086, 1996.
- [41] M. Lee and Y. Yoo, "Supramolecular organization of block oligomers based on rod shaped mesogen into liquid crystalline assembly," *J. Mater. Chem.*, vol. 12, pp. 2161–68, 2002.
- [42] V. Pryamitsyn and V. Ganesan, "Self-assembly of rod coil block copolymers," *J. Chem. Phys.*, vol. 120, pp. 5824–5838, 2004.
- [43] A. Semenov, "Contribution to the theory of microphase layering in block copolymer melts," *Sov. Phys. JETP*, vol. 61, pp. 733–742, 1985.
- [44] J. Chen, "Zig zag morphology of a poly(styrene block hexyl isocyanate) rod coil block copolymer," *Macromolecules*, vol. 28, pp. 1688–1697, 1995.
- [45] J. Chen, E. Thomas, C. Ober, and G. Mao, "Self-assembled smectic phases in rod coil block copolymers," *Science*, vol. 273, pp. 343–346, 1996.
- [46] A. Semenov, "Theory of nematic smectic a transition in a melt of macromolecules consisting of rigid and flexible blocks," *Sov. Phys. JETP*, vol. 90, pp. 124–140, 1986.
- [47] E. Thomas, "Influence of a liquid crystalline block on microdomain structure," *Macro. Symp.*, vol. 117, pp. 241–256, 1997.
- [48] D. Williams and G. Fredrickson, "Cylindrical micelles in rigid-flexible diblock copolymers," *Macromolecules*, vol. 25, pp. 3561–3568, 1992.
- [49] R. Holyst and M. Shchick, "Correlations in a rigid flexible diblock copolymer system," *J. Chem. Phys.*, vol. 96, pp. 730–739, 1992.
- [50] M. Muthukumar, C. Ober, and E. Thomas, "Competing interactions and levels of ordering in self-organizing polymeric materials," *Science*, vol. 277, no. 5330, pp. 1225–1232, 1997. [Online]. Available: <http://www.sciencemag.org/cgi/content/abstract/277/5330/1225>
- [51] H. Klok and S. Lecommandoux, "Supramolecular materials via block copolymer self-assembly," *Advanced Materials*, vol. 13, pp. 1217–1229, 2001.
- [52] L. Radzilowski, "Three dimensional self assembly of rod coil copolymer nanostructures," *Macromolecules*, vol. 30, pp. 2110–2119, 1997.
- [53] L. Radzilowski and S. Stupp, "Nanophase separation in monodisperse rod coil diblock copolymers," *Macromolecules*, vol. 27, pp. 7747–7753, 1994.
- [54] S. Stupp, "Self-assembly of rod coil molecules," *Curr. Opin. Coll. Int. Sci.*, vol. 3, pp. 20–26, 1998.

- [55] S. I. Stupp, V. LeBonheur, K. Walker, L. S. Li, K. E. Huggins, M. Keser, and A. Amstutz, "Supramolecular materials: Self organized nanostructures," *Science*, vol. 276, pp. 384–389, 1997.
- [56] B. Gallot, "Comb like and block liquid crystalline polymers for biological applications," *Prog. Polym. Sci.*, vol. 21, pp. 1035–1088, 1996.
- [57] C. O. Osuji, J. T. Chen, G. Mao, C. K. Ober, and E. L. Thomas, "Understanding and controlling the morphology of styrene isoprene side group liquid crystalline block copolymers," *Polymer*, vol. 41, pp. 8897–8907, 2000.
- [58] M. Anthamatten, "A morphological study of well defined smectic side chain lc block copolymers," *Macromolecules*, vol. 32, pp. 4838–4848, 1999.
- [59] G. Mao, "Molecular design, synthesis, and characterization of liquid crystal coil diblock copolymers with azobenzene side groups," *Macromolecules*, vol. 30, pp. 2556–2567, 1997.
- [60] S. Poser, "Liquid crystal side group block and graft copolymers synthesis and structure/property relationships," *Prog. Polym. Sci.*, vol. 23, p. 1337, 1998.
- [61] M. Anthamatten and P. Hammond, "A saxs study of microstructure ordering transitions in liquid crystalline side-chain diblock copolymers," *Macromolecules*, vol. 32, pp. 8066–8076, 1999.
- [62] C. Osuji, "Transverse cylindrical microdomain orientation in an lc diblock copolymer under oscillatory shear," *Macromolecules*, vol. 32, pp. 7703–7706, 1999.
- [63] I. Hamley, "Interplay between smectic ordering and microphase separation in a series of side group liquid crystal block copolymers," *Macromolecules*, vol. 37, pp. 4798–4807, 2004.
- [64] E. Verploegen, "Observation of transverse cylinder morphology in side chain liquid crystalline block copolymers," *Macromolecules*, vol. 40, pp. 777–780, 2007.
- [65] M. Al-Hussein, "Nanoordering of fluorinated side chain liquid crystalline/amorphous diblock copolymers," *Macromolecules*, vol. 38, pp. 9610–9616, 2005.
- [66] I. Anasari, "Hierarchical order in a side group liquid crystalline block copolymer," *Macromolecules*, vol. 36, pp. 8898–8901, 2003.
- [67] I. Hamley, "Ordering on multiple length scales in a series of side group liquid crystal block copolymers containing a cholesteryl based mesogen," *Soft Matter*, vol. 1, pp. 355–363, 2005.
- [68] M. Shah, V. Pryamitsyn, and V. Ganesan, "A model for self-assembly in side chain liquid crystalline block copolymers," *Macromolecules*, vol. 41, pp. 218–229, 2008.

- [69] F. Brandys and C. Bazuin, "Mixtures of an acid functionalized mesogen with poly(4-pyridine)," *Chem. Mater.*, vol. 8, pp. 83–92, 1996.
- [70] O. Ikkala, "Mesomorphic state of poly(vinylpyridine)-dodecylbenzenesulfonic acid complexes in bulk and in xylene solution," *Macromolecules*, vol. 28, pp. 7088–7094, 1995.
- [71] B. Nandan, "Molecular architecture effect on the microphase separation in supramolecular comb coil complexes of polystyrene block poly(2-vinylpyridine) with dodecylbenzenesulfonic acid:  $(ab_n)a_n$  block arm star copolymer," *Macromolecules*, vol. 38, pp. 10 117–10 126, 2005.
- [72] J. Ruokolainen, "Poly(4-vinylpyridine)/zinc dodecylbenzenesulfonate mesomorphic state due to coordination complexation," *Macromolecules*, vol. 28, pp. 7779–7784, 1995.
- [73] S. Valkama, "Multicomb polymeric supramolecules and their self organization: Combination of coordination and ionic interactions," *Macro. Rapid Comm.*, vol. 24, pp. 556–560, 2003.
- [74] S. Valkama, T. Ruotsalainen, H. Kosonen, J. Ruokolainen, M. Torkkeli, R. Serimaa, G. ten Brinke, and O. Ikkala, "Amphiles coordinated to block copolymers as a template for mesoporous materials," *Macromolecules*, vol. 36, pp. 3986–3991, 2003.
- [75] O. Ikkala and G. Brinke, "Hierarchical self assembly in polymeric complexes: Towards functional materials." *Chem. Comm.*, vol. 19, pp. 2131–2137, 2004.
- [76] J. Ruokolainen, G. ten Brinke, and O. Ikkala, "Supramolecular polymeric materials with hierarchical structure within structure morphologies," *Adv. Mater.*, vol. 11, pp. 777–780, 1999.
- [77] A. Fahmi, "Fabrication of metallized nanowires from self assembled diblock copolymer templates," *Adv. Mater.*, vol. 15, pp. 1201–1204, 2003.
- [78] J. Ruokolainen, "Critical interaction strength for surfactant induced mesomorphic structures in polymer surfactant systems," *Macromolecules*, vol. 29, pp. 6621–6628, 1996.
- [79] O. Ikkala and G. ten Brinke, "Functional Materials Based on Self-Assembly of Polymeric Supramolecules," *Science*, vol. 295, no. 5564, pp. 2407–2409, 2002. [Online]. Available: <http://www.sciencemag.org/cgi/content/abstract/295/5564/2407>
- [80] S. Valkama, "Self-assembled structures in diblock copolymers with hydrogen bonded amphiphilic plasticizing compounds." *Macromolecules*, vol. 39, pp. 9327–9336, 2006.

- [81] S. Valkama, H. Kosonen, J. Ruokolainen, T. Haatainen, M. Torkkeli, R. Serimaa, G. ten Brinke, and O. Ikkala, "Self-assembled polymeric solid films with temperature induced large and reversible photonic bandgap switching," *Nat Mater*, vol. 3, no. 12, pp. 872–876, 2004, 10.1038/nmat1254.
- [82] S. Valkama, R. M. Ontto, M. Stamm, G. ten Brinke, and O. Ikkala, "Mesoporous polymeric materials based on comb-coil supramolecules," *Stud. Surf. Sci. Catal.*, vol. 141, pp. 371–378, 2002.
- [83] R. A. Pai, R. Humayun, M. T. Schulberg, A. Sengupta, J.-N. Sun, and J. J. Watkins, "Mesoporous silicates prepared using preorganized templates in supercritical fluids," *Science*, vol. 303, p. 507, 2004.
- [84] J. Moon, A. Small, G.-R. Yi, S.-K. Lee, W.-S. Chang, D. Pine, and S.-M. Yang, "Patterned polymer photonic crystals using soft lithography and holographic lithography," *Synthetic Metals*, vol. 148, pp. 99–102, 2005.
- [85] N. Krger, "Prescribing diatom morphology: toward genetic engineering of biological nanomaterials," *Current Opinion in Chemical Biology*, vol. 11, no. 6, pp. 662 – 669, 2007, model systems/Biopolymers. [Online]. Available: <http://www.sciencedirect.com/science/article/B6VRX-4R718PX-1/2/e269713f8bf7d176bf81a26d50943fce>
- [86] M. Bal, A. Ursache, M. T. Tuominen, J. T. Goldbach, and T. P. Russell, "Nanofabrication of integrated magnetoelectronic devices using patterned self-assembled copolymer templates," *Appl. Phys. Lett.*, vol. 81, p. 3479, 2002.
- [87] D. Whang, S. Jin, and C. Lieber, "Nanolithography using hierarchically assembled nanowire masks," *Nano Lett.*, vol. 3, pp. 951–954, 2003.
- [88] S.-H. Yun, B.-H. Sohn, J. C. Jung, W.-C. Zin, M. Ree, and J. W. Park, "Micropatterning of a single layer of nanoparticles by lithographical methods with diblock copolymer micelles," *Nanotechnology*, vol. 17, p. 450, 2006.
- [89] J. P. Spatz, V. Z.-H. Chan, S. Mossmer, F.-M. Kamm, A. Plettl, P. Ziemann, and M. Moller, "A combined top-down/bottom-up approach to the microscopic localization of metallic nanodots," *Adv. Mater.*, vol. 14, p. 1827, 2002.
- [90] M. Moller, J. P. Spatz, and A. Roescher, "Gold nanoparticles in micellar poly(styrene)-b-poly(ethylene oxide) films-size and interparticle distance control in monoparticulate films," *Adv. Mater.*, vol. 8, pp. 337–340, 1996.
- [91] J. Aizenberg, P. V. Braun, and P. Wiltzius, "Patterned colloidal deposition controlled by electrostatic and capillary forces," *Phys. Rev. Lett.*, vol. 84, no. 13, pp. 2997–3000, Mar 2000.

- [92] D. Qin, Y. Xia, B. Xu, H. Yang, C. Zhu, and G. M. Whitesides, "Fabrication of ordered two-dimensional arrays of micro- and nanoparticles using patterned self-assembled monolayers as templates," *Adv. Mater.*, vol. 11, pp. 1433–1437, 1999.
- [93] Y. Xia, Y. Yin, Y. Lu, and J. McLellan, "Template-assisted self-assembly of spherical colloids into complex and controllable structures," *Advanced Functional Materials*, vol. 13, pp. 907–918, 2003.
- [94] J. Park, S. Lee, T. Han, and S. Kim, "Hierarchically ordered polymer films by templated organization of aqueous droplets," *Adv. Func. Mater.*, vol. 17, pp. 2315–2320, 2007.
- [95] T. J. Baker, "Breath figures," *Philos. Mag.*, vol. 44, p. 752, 1922.
- [96] H. Yabu, M. Tanaka, K. Ijio, and M. Shimomura, "Preparation of honeycomb-patterned polyimide films by self-organization," *Langmuir*, vol. 19, pp. 6297–6300, 2003.
- [97] A. E. Saunders, J. L. Dickson, P. S. Shah, M. Y. Lee, K. T. Lim, K. P. Johnston, and B. A. Korgel, "Breath figure templated self-assembly of porous diblock copolymer films," *Physical Review E (Statistical, Nonlinear, and Soft Matter Physics)*, vol. 73, no. 3, p. 031608, 2006. [Online]. Available: <http://link.aps.org/abstract/PRE/v73/e031608>
- [98] T. Kim, J. Hwang, W. Hwang, J. Huh, H.-C. Kim, S. Kim, J. Hong, E. Thomas, and C. Park, "Hierarchical ordering of block copolymer nanostructures by solvent annealing combined with controlled dewetting," *Adv. mater.*, vol. 20, pp. 522–527, 2008.
- [99] J. H. Moon, W. S. Kim, J.-W. Ha, S. G. Jang, S.-M. Yang, and J.-K. Park, *Chem. Commun.*, p. 4107, 2005.
- [100] R. Glass, M. Arnold, J. Blummel, A. Kuller, M. Moller, and J. P. Spatz, "Micro nanostructured interfaces fabricated by the use of inorganic block copolymer micellar monolayers as negative resist for electron beam lithography," *Adv. Funct. Mater.*, vol. 13, p. 569, 2003.
- [101] J. Yao, X. Yan, G. Lu, K. Zhang, X. Chen, L. Jiang, and B. Yang, *Adv. Mater.*, vol. 16, p. 81, 2004.
- [102] W. Kim, L. Jia, and E. Thomas, "Hierarchically ordered topographic patterns via plasmonic mask photolithography," *Adv. Mater.*, vol. 21, pp. 1–6, 2009.
- [103] Y. Xia, B. Gates, Y. Yin, and Y. Lu, "Monodispersed colloidal spheres: Old materials with new applications," *Advanced Materials*, vol. 12, no. 10, pp. 693–713, 2000.

- [104] P. Lambooy, T. P. Russell, G. J. Kellogg, A. M. Mayes, P. D. Gallagher, and S. K. Satija, *Phys. Rev. Lett.*, vol. 72, p. 2899, 1994.
- [105] N. Koneripalli, N. Singh, R. Levicky, F. S. Bates, P. D. Gallagher, and S. K. Satija, *Macromolecules*, vol. 28, p. 2897, 1995.
- [106] M. S. Turner, "Equilibrium properties of a diblock copolymer lamellar phase confined between flat plates," *Physical Review Letters*, vol. 69, p. 1788, 1992.
- [107] G. J. Kellogg, D. G. Walton, A. M. Mayes, P. Lambooy, P. D. Gallagher, and S. K. Satija, *Phys. Rev. Lett.*, vol. 76, p. 2503, 1996.
- [108] T. Deng, Y. Ha, J. Cheng, C. A. Ross, and E. Thomas, *Langmuir*, vol. 18, p. 6719, 2002.
- [109] D. Walton, G. Kellogg, A. Mayes, P. Lambooy, and T. Russell, "A free energy model for confined diblock copolymers," *Macromolecules*, vol. 27, no. 21, pp. 6225–6228, 1994. [Online]. Available: <http://pubs.acs.org/doi/abs/10.1021/ma00099a045>
- [110] P. Mansky, Y. Liu, E. Huang, T. Russell, and C. Hawker, *Science*, vol. 275, p. 1458, 1997.
- [111] G. Pickett, T. Witten, and S. Nagel, *Macromolecules*, vol. 26, p. 1994, 1993.
- [112] M. Kikuchi and K. binder, *J. Chem. Phys.*, vol. 101, p. 3367, 1994.
- [113] M. Matsen, "Thin films of block copolymer," *J. Chem. Phys.*, vol. 106, p. 7781, 1997.
- [114] S. Anastasiadis, T. Russell, S. Satija, and C. Majkrzak, *Phys. Rev. Lett.*, vol. 62, p. 1852, 1989.
- [115] X. He, M. Song, H. J. Liang, and C. Y. Pan, *J. Chem. Phys.*, vol. 114, p. 10510, 2001.
- [116] G. J. A. Sevink, A. V. Zvelindovsky, J. G. E. M. Fraaije, and H. P. Huinink, "Morphology of symmetric block copolymer in a cylindrical pore," *J. Chem. Phys.*, vol. 115, p. 8226, 2001.
- [117] H. Xiang, K. Shin, T. Kim, S. Moon, T. McCarthy, and T. Russell, "The influence of confinement and curvature on the morphology of block copolymers," *Journal of Polymer Science, Part B: Polymer Physics*, vol. 43, no. 23, pp. 3377 – 3383, 2005, cubic arrays; Interfacial interactions; Packed cylinders; Pore walls; [Online]. Available: <http://dx.doi.org/10.1002/polb.20641>
- [118] H. Xiang, K. Shin, T. Kim, S. I. Moon, T. J. McCarthy, and T. P. Russell, "From cylinders to helices upon confinement," *Macromolecules*, vol. 37, p. 5660, 2004.

- [119] K. Shin, H. Xiang, S. I. Moon, T. Kim, T. J. McCarthy, and T. P. Russell, "Curving and frustrating flatland," *Science*, vol. 306, p. 76, 2004.
- [120] Y. Wu, G. Cheng, K. Katsov, S. W. Sides, J. Wang, J. Tang, G. H. Fredrickson, and G. D. Stucky, *Nat. Mater.*, vol. 3, p. 816, 2004.
- [121] A. C. Aresenault, D. A. Rider, J. I. Chen, N. Coombs, G. A. Ozin, and I. Manners, *J. Am. Chem. Soc.*, vol. 127, p. 9954, 2005.
- [122] Y. Y. Wu, T. Livneh, Y. X. Zhang, G. S. Cheng, J. Wang, J. Tang, M. Moskovits, and G. D. Stucky, *Nano Lett.*, vol. 4, p. 2337, 2004.
- [123] J. Cheng, F. Zhang, H. Smith, G. Vancso, and C. Ross, "Pattern registration between spherical block-copolymer domains and topographical templates," *Advanced Materials*, vol. 18, pp. 597–601, 2006. [Online]. Available: [US:http://dx.doi.org/10.1002/adma.200501936](http://dx.doi.org/10.1002/adma.200501936)
- [124] M. Ma, V. Krikorian, J. H. Yu, E. L. Thomas, and G. C. Rutledge, "Electrospun polymer nanofibers with internal periodic structure obtained by microphase separation of cylindrically confined block copolymers," *Nano Letters*, vol. 6, no. 12, pp. 2969–2972, 2006. [Online]. Available: <http://pubs.acs.org/doi/abs/10.1021/nl062311z>
- [125] C. Osuji, C. Y. Chao, I. Bitá, C. Ober, and E. Thomas, "Temperature-dependent photonic bandgap in a self-assembled hydrogen-bonded liquid-crystalline diblock copolymer," *Advanced Functional Materials*, vol. 12, pp. 753–758, 2002.
- [126] T. J. Bunning, L. V. Natarajan, V. P. Tondiglia, and R. L. Sutherland, "Holographic polymer dispersed liquid crystals," *Annu. Rev. Mater. Sci.*, vol. 30, p. 83, 2000.
- [127] R. A. Vaia, C. L. Dennis, L. V. Natarajan, V. P. Tondiglia, D. W. Tomlin, and T. J. Bunning, "One-step, micrometer-scale organization of nano- and mesoparticles using holographic photopolymerization: A generic technique so: *Advanced materials* vl: 13 no: 20 pg: 1570-1574 yr: 2001 cp: 2001 wiley-vch verlag gmbh, weinheim, fed. rep. of germany on: 1521-4095 pn: 0935-9648 ad: Air force research laboratory, materials and manufacturing directorate, aflr/mlpj, 3005 p. st., ste. 1, wpafb, oh 45433 (usa); science applications international corporation, 4031 colonel glenn highway, dayton, oh 45431 (usa); technical management concepts, inc., beavercreek, oh 45432 (usa) doi: 10.1002/1521-4095(200110)13:20;1570::aid-adma1570;3.0.co;2-x us: [http://dx.doi.org/10.1002/1521-4095\(200110\)13:20;1570::aid-adma1570;3.0.co;2-x](http://dx.doi.org/10.1002/1521-4095(200110)13:20;1570::aid-adma1570;3.0.co;2-x)," *Advanced Materials*, vol. 13, pp. 1570–1574, 2001.
- [128] C. Paquet and E. Kumacheva, "Nanostructured polymers for photonics," *Materials Today*, vol. 11, pp. 48–56, 2008.

- [129] E. Yablonovitch, “Strong localization of photons in certain disordered dielectric superlattices,” *Phys. Rev. Lett.*, vol. 58, pp. 2059–2062, 1987.
- [130] S. John, “Strong localization of photons in certain disordered dielectric superlattices,” *Phys. Rev. Lett.*, vol. 58, pp. 2486–2489, 1987.
- [131] K. Sakoda, “Enhanced light amplification due to group-velocity anomaly peculiar to two- and three-dimensional photonic crystal,” *Optics Exp.*, vol. 4, pp. 167–176, 1999.
- [132] J. P. Dowling, M. Scalora, M. J. Bloemer, and C. M. Bowden, “The photonic band edge laser: A new approach to gain enhancement,” *Journal of Applied Physics*, vol. 75, no. 4, pp. 1896–1899, 1994. [Online]. Available: <http://link.aip.org/link/?JAP/75/1896/1>
- [133] L. Rayleigh, “On the reflection of light from a regularly stratified medium,” *Proc. R. Soc. Ser. A*, vol. 93, p. 565, 1917.
- [134] H. Kogelnik, “Coupled wave theory for thick hologram gratings,” *The Bell System Technical Journal*, vol. 48, no. 9, pp. 2909–2947, 1969.
- [135] H.-S. Kitzerow and A. Lorenz, “Tuneable photonic crystals obtained by liquid crystal infiltration,” *physica status solidi (a)*, vol. 204, pp. 3754–3767, 2007.
- [136] M. J. Escuti, J. Qi, and G. P. Crawford, “Two-dimensional tunable photonic crystal formed in a liquid-crystal/polymer composite: Threshold behavior and morphology,” *Applied Physics Letters*, vol. 83, no. 7, pp. 1331–1333, 2003. [Online]. Available: <http://link.aip.org/link/?APL/83/1331/1>
- [137] V. P. Tondiglia, L. V. Natarajan, R. L. Sutherland, D. Tomlin, and T. J. Bunning, “Holographic formation of electro-optical polymer liquid crystal photonic crystals,” *Adv. Mater.*, vol. 14, pp. 187–191, 2002.
- [138] J. Xia, Y. Ying, and S. Foulger, “Electric-field-induced rejection-wavelength tuning of photonic-bandgap composites,” *Adv. Mater.*, vol. 17, pp. 2463–2467, 2005.
- [139] P. Mach, P. Wiltzius, M. Megens, D. A. Weitz, K. hui Lin, T. C. Lubensky, , and A. G. Yodh, “Electro-optic response and switchable bragg diffraction for liquid crystals in colloid templated materials,” *Phys. Rev. E*, vol. 65, p. 031720, 2002.
- [140] V. Tondiglia, L. Natarajan, R. Sutherland, T. Bunning, and W. Adams, “Volume holographic image storage and electro-optical readout in a polymer dispersed liquid crystal film,” *Opt. Lett.*, vol. 20, p. 1325, 1995.
- [141] L. Natarajan, R. Sutherland, V. Tondiglia, T. Bunning, and W. Adams, “Electro-optical switching characteristics of volume holograms in polymer dispersed liquid crystals,” *J. nonlinear Opt. Phys. Mater.*, vol. 5, pp. 89–98, 1996.

- [142] L. Domash, Y. Chen, B. Gomatam, C. Gozewski, R. Sutherland, L. Natarajan, V. Tondiglia, and T. Bunning, "Switchable-focus lenses in holographic polymer dispersed liquid crystal," *Proc. SPIE*, vol. 2689, pp. 188–194, 1996.
- [143] L. Domash, "Switchable optical components structures and methods for the fabrication thereof," US Patent 5 937 115, 1999.
- [144] T. Stone and M. Macult, "Optical time shifter and routing system," US Patent 5 982 515, 1999.
- [145] T. Stone, "Optical switching, routing, and time delay systems using switched mirrors," US Patent 6 072 923, 2000.
- [146] K. Pavani, I. Naydenova, J. Raghavendra, S. Martin, and V. Toal, "Electro-optical switching of the holographic polymer-dispersed liquid crystal diffraction gratings," *J. Opt. A: Pure Appl. Opt.*, vol. 11, p. 024023, 2009.
- [147] X. Xu, G. Friedman, K. D. Humfeld, S. A. Majetich, and S. A. Asher, "Superparamagnetic photonic crystals," *Advanced Materials*, vol. 13, pp. 1681–1684, 2001.
- [148] J. Ge, Y. Hu, M. Biasini, W. Beyermann, and Y. Yin, "Superparamagnetic magnetite colloidal nanocrystal clusters," *Angewandte Chemie International Edition*, vol. 46, pp. 4342–4345, 2007.
- [149] J. Ge, Y. Hu, and Y. Yin, "Highly tunable superparamagnetic colloidal photonic crystals," *Angewandte Chemie International Edition*, vol. 46, p. 7428, 2007.
- [150] A. Urbas, V. Tondiglia, L. Natarajan, R. Sutherland, H. Yu, J.-H. Li, and T. Bunning, "Optically switchable liquid crystal photonic structures," *Journal of the American Chemical Society* 2004 126 (42), 13580-13581, vol. 126, pp. 13 580–13 581, 2004.
- [151] J. M. Weissman, H. B. Sunkara, A. S. Tse, and S. A. Asher, "Thermally switchable periodicities and diffraction from mesoscopically ordered materials," *Science*, vol. 274, no. 5289, pp. 959–963, 1996. [Online]. Available: <http://www.sciencemag.org/cgi/content/abstract/274/5289/959>
- [152] I. Drevenšek Olenik, M. Jazbinšek, M. E. Sousa, A. K. Fontecchio, G. P. Crawford, and M. Čopič, "Structural transitions in holographic polymer-dispersed liquid crystals," *Phys. Rev. E*, vol. 69, no. 5, p. 051703, May 2004.
- [153] R. Caputo, L. D. Sio, A. Veltri, C. P. Umenton, and A. V. Sukhov, "Polycrystalline switchable holographic gratings: A promising grating electro-optical pixel for high resolution display applications," *Journal of Display Technology*, vol. 2, pp. 38–51, 2006.

- [154] J. H. Holtz and S. A. Asher, "Polymerized colloidal crystal hydrogel films as intelligent chemical sensing materials," *Nature*, vol. 389, no. 6653, pp. 829–832, 1997, 10.1038/39834.
- [155] Y. Kang, J. J. Walish, T. Gorishnyy, and E. L. Thomas, "Broad-wavelength-range chemically tunable block-copolymer photonic gels," *Nat Mater*, vol. 6, no. 12, pp. 957–960, 2007, 10.1038/nmat2032.
- [156] A. G. Mayes, J. Blyth, R. B. Millington, and C. R. Lowe, "Metal ion sensitive holographic sensors," *Anal. Chem.*, vol. 74, pp. 3649–3657, 2002.
- [157] M. D. Cathell and C. L. Schauer, "Structurally colored thin films of  $Ca^{2+}$ -cross-linked alginate," *Biomacromolecules*, vol. 8, pp. 33–41, 2007.
- [158] K. Busch and S. John, "Photonic band gap formation in certain self-organizing systems," *Phys. Rev. E*, vol. 58, no. 3, pp. 3896–3908, Sep 1998.
- [159] S. A. Holmstrom, L. V. Natarajan, V. P. Tondiglia, R. L. Sutherland, and T. J. Bunning, "Mechanical tuning of holographic polymer-dispersed liquid crystal reflection gratings," *Applied Physics Letters*, vol. 85, no. 11, pp. 1949–1951, 2004. [Online]. Available: <http://link.aip.org/link/?APL/85/1949/1>
- [160] D. R. Cairns, C. C. Bowley, S. Danworaphong, A. K. Fontecchio, G. P. Crawford, L. Li, and S. M. Faris, "Optical strain characteristics of holographically formed polymer-dispersed liquid crystal films," *Applied Physics Letters*, vol. 77, no. 17, pp. 2677–2679, 2000. [Online]. Available: <http://link.aip.org/link/?APL/77/2677/1>
- [161] J. D. Joannopoulos, P. R. Villeneuve, and S. Fan, "Photonic crystals: Putting a new twist on light," *Nature*, vol. 386, pp. 143–149, March 1997, erratum: *ibid.* vol. 387, p. 830 (1997).
- [162] M. Campbell, D. N. Sharp, M. T. Harrison, R. G. Denning, and A. J. Turberfield, *Nature*, vol. 404, p. 53, 2000.
- [163] J. Radford, T. Alfrey, and W. Schrenk, "Reflectivity of iridescent coextruded multilayered plastic films," *Polymer Engineering and Science*, vol. 13, pp. 216–221, 1973.
- [164] Y. Fink, J. N. Winn, S. Fan, C. Chen, J. Michel, J. D. Joannopoulos, and E. L. Thomas, "A dielectric omnidirectional reflector," *Science*, vol. 282, no. 5394, pp. 1679–1682, 1998. [Online]. Available: <http://www.sciencemag.org/cgi/content/abstract/282/5394/1679>
- [165] D. Gabor, "A new microscopic principle," *Nature*, vol. 161, pp. 777–778, 1948.
- [166] E. Leith and J. Upantnicks, "Wavefront reconstruction with diffused illumination and three-dimensional objects," *J. Opt. Soc. Am.*, vol. 54, pp. 1295–1301, 1964.

- [167] Y. N. Denisyuk, "Photographic reconstruction of the optical properties of an object in its own scattered radiation field," *J. Opt. Soc. Am.*, vol. 53, pp. 1377–1381, 1962.
- [168] M. J. Escuti and G. P. Crawford, "Holographic photonic crystals," *Opt Eng.*, vol. 43, no. 9, pp. 1973 – 1987, 2004.
- [169] M. Born and E. Wolf, *Principles of optics*. Cambridge University Press, 1999.
- [170] V. Berger, O. Gauthier-Lafaye, and E. Costard, "Photonic band gaps and holography," *J. Appl. Phys.*, vol. 82, pp. 60–64, 1997.
- [171] A. Turberfield, "Photonic crystals made by holographic lithography," *Mat. Res. Soc. Bulletin*, pp. 632–636, 2001.
- [172] W. S. Colburn and K. A. Haines, "Volume hologram formation in photopolymer materials," *Appl. Opt.*, vol. 10, p. 1636, 1971.
- [173] J. Margerum, A. Lackner, E. Ramos, G. Smith, N. Vaz, J. Kohler, and J. Allison, "Polymer dispersed liquid crystal film devices and methods of forming the same," US Patent 4938 568, 1990.
- [174] R. Sutherland, L. Natarajan, V. Tondiglia, T. Bunning, and W. Adams, "Electrically switchable volume gratings in polymer dispersed liquid crystals," *Appl. Phys. Lett.*, vol. 64, pp. 1074–1076, 1994.
- [175] W. K. Smothers, B. M. Moroe, A. M. Weber, and D. E. Keys, "Photopolymers for holography," *SPIE Proc.*, vol. 1212, p. 20, 1990.
- [176] R. Ingwall and M. Troll, "Mechanism of hologram formation in dmp-128 photopolymer," *Opt. Eng.*, vol. 28, pp. 586–589, 1989.
- [177] W. J. Gambogi, A. M. Weber, and T. J. Trout, "Advances and applications of dupont holographic photopolymers," *SPIE Proc.*, vol. 2043, p. 2, 1994.
- [178] R. Sutherland, L. Natarajan, V. Tondiglia, and T. Bunning, "Bragg gratings in an acrylate polymer consisting of periodic polymer dispersed liquid crystal planes," *Chem. Mater.*, vol. 5, pp. 1533–1538, 1993.
- [179] K. Tanaka, K. Kato, S. Tsuru, and S. Sakai, "A liquid crystal polymer optical device formed by holography for reflective color display applications," *Proc. SID*, vol. 24, pp. 109–111, 1993.
- [180] C. Bowley and G. Crawford, "Diffusion kinetics of formation of holographic polymer dispersed liquid crystal," *Appl. Phys. Lett.*, vol. 76, pp. 2235–2237, 2000.

- [181] R. L. Sutherland, V. P. Tondiglia, L. V. Natarajan, and T. J. Bunning, "Phenomenological model of anisotropic volume hologram formation in liquid-crystal-photopolymer mixtures," *Journal of Applied Physics*, vol. 96, no. 2, pp. 951–965, 2004. [Online]. Available: <http://link.aip.org/link/?JAP/96/951/1>
- [182] L. V. Natarajan, C. K. Shepherd, D. M. Brandelik, R. L. Sutherland, S. Chandra, V. P. Tondiglia, D. Tomlin, , and T. J. Bunning, "Switchable holographic polymer dispersed liquid crystal reflection gratings based on thiol-ene photopolymerization," *Chem. Mater.*, vol. 15, pp. 2477–2484, 2003.
- [183] G. W. Smith, "Cure parameters and phase behavior of an ultraviolet cured polymer dispersed liquid crystal," *Mol. Cryst. Liq. Cryst.*, vol. 196, pp. 89–102, 1991.
- [184] J. Brandup, E. Immergut, and E. Grulke, *Polymer Handbook*. John Wiley, 1999.
- [185] A. M. Fox, *Optical Properties of Solids*. Oxford University Press, 2001.
- [186] D. B. Williams and C. B. Carter, *Transmission Electron Microscopy: A Textbook for Material Science*. Plenum, 1996.
- [187] [Online]. Available: <http://eml.masc.udel.edu/>
- [188] J. S. Trent, J. I. Scheinbeim, and P. R. Couchman, "Ruthenium tetraoxide staining of polymers for electron microscopy," *Macromolecules*, vol. 16, no. 4, pp. 589–598, 1983. [Online]. Available: <http://pubs.acs.org/doi/abs/10.1021/ma00238a021>
- [189] A. Guinier, *X-Ray Diffraction in Crystals, Imperfect Crystals and Amorphous Bodies*. Dover Publication, Inc., 1994.
- [190] B. Chu and B. Hsiao, *Chemical Reviews*, vol. 101, pp. 1727–1761, 2001.
- [191] J. Ingham and D. Lawson, "Refractive index-molecular weight relationships for poly(ethylene oxide)," *J. Polym. Sci.*, vol. 3, pp. 2707–2710, 1965.
- [192] L. Zhu, B. H. Calhoun, Q. Ge, R. P. Quirk, S. Z. D. Cheng, E. L. Thomas, B. S. Hsia, F. Yeh, L. Liu, and B. Lotz, *Macromolecules*, vol. 34, p. 1244, 2001.
- [193] B. Wunderlich, *Thermal Analysis*. Academic Press, 1990.
- [194] B. Wunderlich, *Macromolecular Physics*. Academic Press, 1980.
- [195] Y.-L. Loo, R. A. Register, A. J. Ryan, and G. T. Dee, "Polymer crystallization confined in one, two, or three dimensions," *Macromolecules*, vol. 34, pp. 8968–8977, 2001.

- [196] Z.-M. Huang, Y.-Z. Zhang, M. Kotaki, and S. Ramakrishna, "Confinement size effect on crystal orientation changes of poly(ethylene oxide) blocks in poly(ethylene oxide)-b-polystyrene diblock copolymers," *Compos. Sci. Technol.*, vol. 63, p. 2223, 2003.
- [197] M. H. Vainio, P. Varpomaa, J. Seppala, and P. Tormala, "Modification of poly(l-lactides) by blending: mechanical and hydrolytic behavior," *Macromolecular Chemistry and Physics*, vol. 197, pp. 1503–1523, 1996.
- [198] H. Bittiger, R. H. Marchessault, and W. D. Niegisch, *Acta Crystallogr., Sect. B: Struct. Sci.*, vol. 26, p. 1923, 1970.
- [199] R. M. Ho, P. Y. Hsieh, W. H. Tseng, C. C. Lin, and B. Lotz, *Macromolecules*, vol. 36, p. 9085, 2003.
- [200] C. L. He, J. R. Sun, T. Zhao, Z. K. Hong, X. L. Zhuang, X. S. Chen, and X. B. Jing, *Biomacromolecules*, vol. 7, p. 252, 2006.
- [201] R. Jakubiak, V. Tondiglia, L. Natarajan, R. Sutherland, P. Lloyd, T. Bunning, and R. Vaia, "Dynamic lasing from all-organic two-dimensional photonic crystals," *Advanced Materials*, vol. 17, p. 2807, 2005.

## Vita

---

### Michael J. Birnkrant

#### Education

**Ph.D.** Material Science & Engineering, Drexel University, Philadelphia, PA 2009

**B.S.** Chemical & Biochemical Engineering, Rutgers University, New Brunswick, NJ 2004

#### Professional Experience

- **Graduate Research Assistant**, Drexel University, 10/2004 - 12/2008
- **Undergraduate Research Assistant**, Rutgers University, 05/2001 - 05/2004

#### Awards

- National Research Council Postdoctoral Fellowship, 2009
- National Science Foundation GK-12 Fellowship, 2006 - 2008
- Drexel University Research Excellence Award, 2007
- Sigma Xi Grants-in-Aide of Research Recipient, 2005 - 2006
- Dean's Fellowship, Drexel University, 2005 - 2007
- National Science Foundation IGERT Fellowship, 2004 - 2006
- Drexel University Research Day Dean's Award, 2005
- James J. Slade Scholar, 2003 - 2004
- Scholar Athlete Award, 2002 - 2003
- Rutgers University President's Award, 2002 - 2003

#### Selected Publications

- Birnkrant, Michael J.; Li, Christopher Y.; Natarajan, Lalgudi V.; Tondiglia, Vincent P.; Sutherland, Richard L.; Lloyd, Pamela F.; Bunning, Timothy J. *Layer-in-Layer Hierarchical Nanostructures Fabricated by Combining Holographic Polymerization and Block Copolymer Self-Assembly*. **Nano Letters** (2007), 7(10), 3128-3133.
- Birnkrant, Michael J.; McWilliams, Hilary K.; Li, Christopher Y.; Natarajan, Lalgudi V.; Tondiglia, Vincent P.; Sutherland, Richard L.; Lloyd, Pamela F.; Bunning, Timothy J. *On the Structure of Holographic Polymer-Dispersed Poly(ethylene Glycol)*. **Polymer** (2006), 47(24), 8147-8154.
- Li, Christopher Y.; Birnkrant, Michael J.; Natarajan, Lalgudi V.; Tondiglia, Vincent P.; Lloyd, Pamela F.; Sutherland, Richard L.; Bunning, Timothy J. *Polymer Crystallization/Melting Induced Thermal Switching in a Series of Holographically Patterned Bragg Reflectors*. **Soft Matter** (2005), 1(3), 238-242. (Highlighted in Royal Society of Chemistry, Chemical Technology News, Sept. 2005, 2, T33)

